

Alma Mater Studiorum – Università di Bologna

DOTTORATO DI RICERCA IN
INGEGNERIA DEI MATERIALI

Ciclo __XVI__

Settore Concorsuale di afferenza: __08/B2__

Settore Scientifico disciplinare: __ICAR/08__

EXPERIMENTAL ASSESSMENT OF ENVIRONMENTAL DECAY EFFECTS
IN MASONRY
VIA NON DESTRUCTIVE DIAGNOSTIC TECHNIQUES
AND
MECHANICAL TESTS

Presentata da: __Elena Gabrielli__

Coordinatore Dottorato

Prof. Ing. Giorgio Timellini

Relatori

Dr. Arch. Camilla Colla

Prof. Ing. Giorgio Timellini

Esame finale anno __2014__

Index

1. Introduction.....	1
1.1 Background and research needs	
1.2 Aims	
1.3 Phases of research work	
1.4 Definitions and clarifications	
1.5 First overview of masonry specimens built in the laboratory	
2. Weathering effects in masonry materials due to salt transport and crystallisation	7
2.1 Moisture transport and capillary rise phenomenon	
2.2 Effects of salts on porous masonry materials	
2.3 Evaluation of decay effects in masonry	
2.4 Conclusions	
3. Non-destructive techniques used in the experimental work	11
3.1 Ultrasonic tests	
3.2 Sonic tests	
3.3 GPR ground penetrating radar	
3.4 Infrared thermography	
3.5 Laser scanner	
3.6 Digital image correlation	
4. Materials and masonry specimens for experimental activity	33
4.1 Material characterization	
4.2 Single units of construction materials: testing arrangement	
4.3 Small walls and masonry assemblies for mechanical testing after natural and accelerated ageing	
4.4 Procedure for natural ageing	
4.5 Procedure for accelerated ageing	

5. Non destructive and mechanical evaluation of natural weathering in single units of masonry components materials.....	61
5.1 Mortar prisms: results of the long-term monitoring	
5.2 Fired-clay brick: results of the long-term monitoring	
5.3 Conclusions	
6. Non-destructive evaluation of outdoor full scale walls: moisture and salt transport, decay.....	87
6.1. Sonic tests	
6.2. Infrared thermography	
6.3. GPR radar	
6.5. Wireless electric potential monitoring & ion-chromatography analyses	
6.6. Laser scanner	
6.7. Digital image correlation	
6.8. Discussion	
7. Non destructive sonic evaluation of masonry specimens subjected to natural or accelerated ageing.....	163
7.1. Sonic evaluation: data acquisition and analysis procedure	
7.2. Small walls	
7.3. Six-brick columns	
8. Mechanical evaluation of small masonry walls subjected to natural or accelerated ageing.....	185
8.1 Preparation of the wallets	
8.2 Mechanical tests: equipment, set-up and testing procedure	
8.3 NDT monitoring of the mechanical tests: equipment and testing procedure	
8.4 Data analysis and visualization of results	
8.5 Discussion and conclusions	
9. Mechanical evaluation of masonry assemblies subjected to accelerated ageing.....	221
9.1 Six-brick columns: mechanical compression tests	
9.2 Six-brick columns: NDT evaluation of the mechanical tests	

- 9.3 Example of data analysis and visualization
- 9.4 Compression tests: discussion of the results and comparison
- 9.5 Shear tests

10. Discussion and conclusions.....275

11. References.....279

Annex I- List of publications

1. Introduction

1.1. Background and research needs

Environmental decay in porous masonry materials, such as brick and mortar, is a widespread problem concerning both new and historic masonry structures. These materials, because of their micro-structural characteristics are particularly vulnerable to aggressive agents and, when exposed to the environment, inevitably undergo aesthetical or substantial changes in character due to physical, chemical and mechanical processes. The decay mechanisms are quite complex, as they depend upon several interconnected parameters and result from the interaction between the structure itself and the specific micro-climate conditions to which it belongs.

In the last decades, very many studies have been carried out on this topic because of the complexity, diffusion and economic implications of such degradation phenomena. These investigations largely have regarded specific aspects of the different decay processes such as the characteristics of the controlling mechanisms, the physical-chemical reactions occurring or the deterioration susceptibility of various materials in different environments. With regard to the decay caused by aggressive agents and salts in brick masonry – at the focus of this thesis - more recent studies have paid attention to some of the damaging effects (i.e. appearance of the decay, changes in the material pores, variations of the chemical composition of the materials, ...) but yet very little is known about the consequences of such decay on the masonry's mechanical properties. This aspect is of true importance from the structural viewpoint.

Funnily enough, this side has been ignored so far even in standard documents on the topic, which restrict evaluation of the process in construction materials to qualitative, visual inspection. Further, attention in existing documents has been confined to single construction materials and not extended to the masonry composite. Even when accelerated ageing procedures have been proposed, the relation between the level of damage reached and the corresponding load of natural decay has been left undefined. An ulterior evanescent point is the efficacy of the artificial ageing and if it can be retained to cause to the material a similar decay process as it happens in un-constrained natural conditions.

As seen from the above brief discussion, a quantitative assessment of the masonry material degradation and how it affects the load-bearing capacity of masonry structures is still missing, whilst a number of points need deep probing.

1.2. Aims

In order to better investigate and understand the complex relation between material degradation caused by environmental agents and the implications on the resistance of the masonry material and structural element, a research work was planned, limiting the attention mainly to brick masonry wall structures, these being more typical of the Bologna area and Northern part of Italy.

To address this issue, an experimental approach was conceived, considering different integrated testing procedures, both non-destructive and mechanical, together with monitoring methods. The attention was focused on the phenomena related to the presence and transport of moisture and salts in masonry materials and on the damaging effects caused by the crystallization of two different salts, sodium chloride and sodium sulphate.

To confront some of the open, delicate questions reported above, given the already mentioned complexity of the phenomenon, it has been thought of tackling it in the laboratory, facing it from diverse perspectives, through many series of masonry specimens, very different in size and purposes but all made of the same brick units and lime mortar. These new-built specimens on one hand would allow to track the damage process in the materials since its beginning and to strictly monitor its evolution over a number of seasons or years (both the detection of the start of this damage and the long-term monitoring are unaccounted for in the technical literature. Related to this aspect is the validation study/applicability of suitable testing techniques, non-destructive, mini-invasive, analytical, of monitoring, to be used at discrete timings or continuously for this specific field of use), on the other hand they would allow a number of comparisons considering for example different exposure to aggressive agents (in terms of type of salt, of brine concentration, of artificial vs. open-air natural ageing, ...), different means of testing (qualitative vs. quantitative, non destructive vs. mechanical testing, punctual vs. wide areas, ...), different size of masonry element (1-, 2-, 3-header thick walls, full-scale walls vs. small size specimens, brick columns and triplets vs. small walls, masonry specimens vs. single units of brick and mortar prisms, ...).

The combination of different advanced testing methods, also taking into account novel monitoring techniques in an integrated holistic approach, is intended to enhance the current available diagnostic procedures in the field of assessing environmental decay in masonry structures, both in the direction of quantitative assessment of masonry and whole diagnose of the phenomenon. Hence, the experimental laboratory work has had two main aims: 1) improving knowledge of this decay process and its state of advancement, combining meso- and macro-scale investigations so to improve the assessment of decay effects due to aggressive environmental agents in brick masonry (in line with state of the art research, preference has always been given, where possible, to image diagnostic and monitoring techniques) and 2) validate holistic approaches and methodologies also in view of transferring the carried out validation on-site on real cases.

1.3. Phases of research work

This thesis starts with a short introduction to the mechanisms responsible for environmental decay in porous masonry materials and a literature review on previous investigations about the evaluation of weathering effects in masonry materials and structures due to salt transport and crystallization (Chapter 2). From a structural viewpoint, this literature review has pointed to the needs to assess the possible consequences of environmental decay on the physical and mechanical properties of masonry (i.e. the load-carrying capacity) and to better investigate the degradation effects on real cases in their specific microclimatic, by testing and monitoring tools capable of following the evolution over time of the decay processes since their beginning.

Thus, a review of the state-of-the-art in non-destructive diagnostic techniques (NDT) and mechanical methodologies available for repeated/single testing of masonry elements and structures was carried out prior to planning the measurement phases and designing the specimens. Among these, some experimental techniques suitable for evaluating environmental-driven problems in masonry structures were selected for this work. Hence, their basic principles and the testing equipment used are presented together with a description of the on-purpose testing procedures implemented, often with a number of innovative aspects (chapter 3).

Taking into account the testing aims, the selected testing techniques and the planned work's phases, several brick masonry walls and assemblies of different dimensions were on-purpose designed and built in the laboratory. After the physical-chemical and mechanical characterization of the constituent materials, the different series of masonry specimens for NDT and/or mechanical tests are described. In addition, the design and implementation phases of the two ageing procedures used to replicate the environmental damages are illustrated (chapter 4). For accelerated ageing, only sodium sulphate contamination has been foreseen.

Following, the results derived from this vast laboratory campaign made of ageing, data acquisition, data elaboration and visualization carried out since 2010 are presented in separated chapters in function of the different series of specimens and ageing treatments considered.

First of all, the damaging effects of the diverse natural ageing contaminations are investigated on several tens of single units of masonry building materials. Thus, in chapter 5 the results of the monitoring and the assessment of the weathering consequences on the physical and mechanical parameters of the materials are reported, These effects were evaluated via visual and photographic inspections, and assessed by gravimetric and dimensional surveys, non-destructive (ultrasound) and destructive tests, repeated at the end of each ageing season.

In chapter 6, the same problematics are qualitatively and quantitatively investigated with reference to naturally aged full-scale walls by means of repeated non-destructive (such as sonics, IR thermography, GPR radar, ...), micro-destructive and advanced monitoring techniques (wireless sensors for electrical impedance of dissolved chloride salt movements), also in order to evaluate the sensitivity of the non-destructive imaging diagnostic techniques to moist and salt decayed areas. In perspective, this work is valuable for transferability and further applications on real structures on-site.

In the next chapter it is reported of non-destructive sonic tests carried out on the sets of small walls and masonry assemblies, either subjected to natural or accelerated ageing, in order to evaluate differences/similarities of the effects and evolution of the environmental decay in masonry which is replicated by means of the two different treatments (chapter 7).

For the same series of specimens, the mechanical evaluation of the degradation effects is reported first with reference to the uniaxial compression tests carried out on small walls subjected either to natural or artificial ageing, at increasing decay levels prior to the mechanical testing (chapter 8) and, secondly, with reference (chapter 9) to axial and eccentric compression tests (2 grades of eccentricity) or shear tests performed on six-brick columns and

triplets respectively. Again, brick columns and triplets had all undergone accelerated ageing, and 4 series were mechanically tested after being subjected to increasing number of crystallization cycles. Main aim of the activities described in these two chapters was to assess the variations of masonry characteristic mechanical properties caused by aggressive environmental exposure. On the occasion of these mechanical tests an innovative non-destructive image monitoring procedure was on-purpose implemented, via digital image correlation. In the future, it is hoped to transfer this application in-situ on historic masonry.

Finally, a comparative analysis of the results is proposed and the outcomes discussed (Chapter 10).

1.4. Definitions and clarifications

For clarity of reading the remaining text and also as a preview, some proposed definitions that are worth at least in the context of this thesis are herein reported.

- Natural weathering or natural ageing: outdoors exposure to real weather during the summer seasons only, including rain water, in addition to water or low-concentrated sodium chloride or sodium sulphate brine artificially supplied at the base of specimens and naturally sucked in masonry by capillary rise.
- Ageing summer/season/year: used here as synonyms, they refer to a single period of natural weathering by outdoors exposure of the samples, usually lasting 5-6 months.
- Artificial or accelerated weathering/ageing: the masonry specimens undergo cycles of total immersion in tanks of highly-concentrated sodium sulphate brine followed by treatment in climatic cell while varying the boundary conditions (air temperature and relative humidity) to force salt crystallization.

I would like to acknowledge that my Ph.D. activity has started in the framework of a collaborative 7FP EU research project – SMooHS, Smart Monitoring of Historic Structures - concluded in November 2011 and it has afterwards continued up to now. This aspect is underlined in order to explain why some experiments presented herein had external collaborations.

1.5. First overview of masonry specimens built in the laboratory

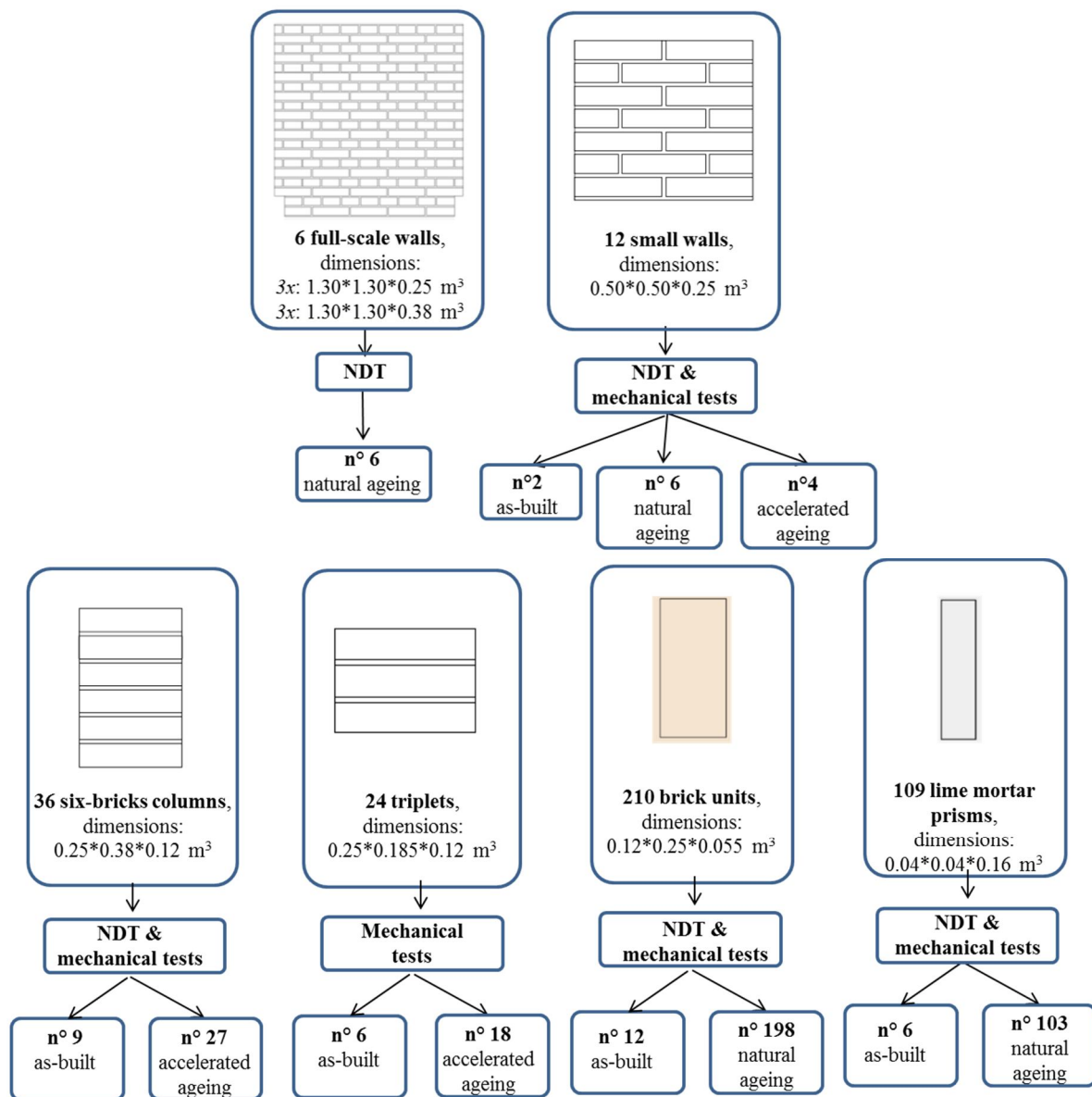


Figure 1.1: Overview of the series of specimens used for the experimental research.

2. Weathering effects in masonry materials due to salt transport and crystallization

Porous masonry materials such as stone, brick and mortar exposed to the environment inevitably undergo aesthetical or substantial changes in character due to physical, chemical or mechanical processes. Architects, restorers and experts in the field of buildings' conservation commonly used the word weathering to refer to all such changes.

More specific words as decay, deterioration or degradation are then used, respectively, when these modifications affect the intrinsic properties of a material or when they are associated with a worsening of the material's characteristics or a decline in its condition or functional capacities (ICOMOS 2010).

These changes are very common in historic or existing masonry structures outdoors exposed and they are strictly related with the presence and movements of water in all its status forms (liquid, gaseous and solid) into the material pores.

The mechanisms responsible for such damages in construction materials represented a topic of continuous research since the 1960's (Watt 2000, Larsen 1990) because of their complexity, as they involve a large number of parameters usually inter-connected, and because of their economic implications.

Weathering processes, indeed, are the results of a complicated interaction between the structure itself and the specific micro-climate conditions to which it belongs; it is thus necessary to know and fully understand the basics of the controlling mechanisms of the weathering processes, prior to study any method or technique for evaluating, preventing or repairing these damages (Scherer, internal stress).

This chapter is aimed at giving a brief overview on the literature on this topic. It deals first with the basic causes and the physical-chemical principles related to the weathering of masonry, especially in presence of water and salts. The salt-water systems are then described, with particular attention to the behaviour of two salt solutions which are frequently involved in masonry deteriorations: sodium chloride and sodium sulphate solutions. Finally, a description of the decay effects due to environments and of the available tests and existing standards for their evaluation is reported.

2.1. Moisture transport and capillary rise phenomenon

Water plays an important role on weathering of masonry construction materials being the principal responsible or the promoting agent of different types of decay such as:

- chemical decay, like corrosion, hydration or oxidations which may occur i.e. in presence of aggressive pollutants;
- physical decay, due to mechanical stresses induced into the material pores i.e. by freeze-thaw cycles, thermal expansion or salts crystallization/hydration;
- biological decay, as mould growth or biological colonization (ICCROM 99, Guerra 2011).

Water may penetrate into the material pores in different ways such as by capillarity, percolation or vapour.

The capillary rise process is one of the most common processes and it is responsible for salts' transport and crystallization.

2.2. Effects of salts on porous masonry materials

Salts, typically chlorides, sulphates and nitrates, can derive from different sources i.e. they can be already in the building materials or in the water used for the mortar mix, they can be absorbed from the ground through capillarity, they can enter into the structure from the atmosphere, especially in high-industrialized areas or near the sea. In the case of capillary rise, phenomenon of our present interest, the damaging mechanism follows this process: the dissolved salts are moved by water into the material pores until a certain height, function of the capillary and hydrostatic pressure; then, in presence of water evaporation and in certain specific microclimatic conditions, different for the diverse types of salt, they may crystallize on the surface or beneath it.

In the first case, the salt crystals become visible as white depositions, called efflorescences and may seriously affect the conservation of the surfaces, also if plastered; in the second case of salt crystallization, known as sub-efflorescence the crystals' volume increase may generate internal pressure greater than the resistance of the pore walls and thus cause material degradation, such as blistering, delamination, formation of cracks, etc. Repeated cycles of salt hydration/crystallization may worsen the process and terribly increase the amount of decay.

2.3. Evaluation of decay effects in masonry

Much has already been done with this respect to the evaluation of decay effects but much has to be done. As an example, there is still a strong interest in finding reliable and repeatable ways of determining the macroscopic hydraulic properties of porous media as stated by different authors [4-5]. In order to achieve this aim and obtain a detailed knowledge about the damp rise and the diffusivity mechanisms in masonry, the characteristic hygrothermal properties of the single building construction materials, such as brick units and mortar samples, as well as the properties of masonry assemblies have to be known. This information would be important both from an experimental view point as it would allow a deeper understanding of the degradation processes, helping in finding proper methods for diagnosis and for appropriate treatment solutions, and from a numerical point of view in order to assess and calibrate ad-hoc models able to i.e. estimate the evolution of the decay mechanisms in historical masonry.

At this regard, few international testing standards are available and they are concerned with the behaviour of single masonry constituent materials in contact with water. As a matter of fact, the dangerousness of the presence of water in a structure, which may cause modifications or decay in the materials, has been recognized from International Technical Committees and, i.e. it has been found that an increase in the value of the water absorption coefficient can be related to an alteration process [6]. Thus, the norms mainly describe water absorption tests to be performed on sets of small samples (typically 3 or 6 cubes with 50 mm side) of hardened mortars [7, 8], natural stones [9,10] and, not well specified specimens of porous inorganic materials used for and constituting cultural properties [11]. In detail, for both mortars and natural stones, the laboratory tests consist in positioning a specimen, previously dried to constant mass, into an uptake container with a constant level of tap water at room temperature (and atmospheric pressure) and in measuring its weight at different time periods (according to the type of material or the speed of water absorption) until constant mass. Thus, the water absorption coefficient can be determined. This parameter is defined as the amount of water absorbed per unit area (expressed in grams/cm²) as a function of time from a sample with one surface in contact with deionised or tap water [11, 12] or as percentage obtained by the ratio of the mass of the saturated sample to the mass of the dry specimen [9].

A slight difference has been found in [11] as this European Standard specifies a method, that may be applied to porous inorganic materials (either untreated or subjected to treatment or ageing) to determine both the amount and the rate at which a specimen absorbs water by capillarity through a surface in contact with water. Thus, it allows the evaluation of the water absorption coefficient as well as of the capillary water penetration coefficient, defined as “the slope of the curve obtained reporting the height of the water front migration versus the square root of time, calculated by linear regression”.

The behaviour of assemblies of 2 or more construction materials (i.e. brick masonry) in contact with water is not considered at all in the norms. In addition, the effects of dissolved salts within porous media has not yet been included in these types of tests. The only references to salts are to be found in the few standards available in the field of accelerated

ageing tests of materials [13-15], which, anyhow, refer to very small specimens of stones, marbles or brick units and do not really explain the relationship between the obtainable results in the case of accelerated ageing and the ones to be achieved by natural environmental ageing.

2.4. Conclusions

Although many characteristics of the salt damaging processes as well as some of their effects are well-known (i.e. appearance of the decay, changes in the material pores, sensitivity of different materials to this decay process ...), very little is known on the variations of the resistant capacity of masonry structures when subjected to prolonged salt capillary rise. Understanding better this complex correlation would be very important from a structural viewpoint.

3. Non-destructive techniques used in the experimental work

The experimental work has foreseen the application and validation of several on-site applicable non-destructive techniques (NDT) and laboratory destructive, mechanical, tests. According to the testing aims, these methods have been chosen after a state-of-the-art review, prior to the beginning of this PhD, during the 7th FP EU project SMooHS, because suitable for diagnose and assessment of masonry structures and for the evaluation of environmentally driven problems considering structural and materials parameters.

The non-destructive imaging techniques employed exploits different physical principles (i.e. acoustic or electromagnetics) and are aimed at evaluating qualitatively and quantitatively the effects and evolution over time of replicated weathering process in on-purpose designed brick walls and masonry assemblies as well as on the single units of building constituent materials.

The different types of laboratory mechanical tests (concentric and eccentric compression, shear tests) are aimed at addressing the variations on the principal mechanical characteristic parameters of masonry caused by environmental degradation.

In the following, the basic principles, the testing equipment used and the on-purpose developed testing procedures are described first with reference to the NDT tests and then for the mechanical methods.

3.1. Ultrasonic tests

Ultrasonic (US) tests are a well-known non-destructive acoustic technique based on the propagation of high-frequency waves, typically between 20 and 100 kHz, inside a material. In the field of civil engineering, these tests are largely used to estimate the elastic and mechanical properties of concrete, to detect the presence of defects such as cracks, voids, inhomogeneities in concrete, stone and masonry elements and structures and, also in combination with other techniques, to assess the health-state conditions of structural elements. The ultrasound tests are a well-established non-invasive diagnostic techniques for concrete structures, as testified by several available standards (EN 12504-4:2005, ASTM C 597:02, EN 13791:2007) and natural stone (EN 14579-4:2005). Anyhow, researches are still on-going with reference to concrete structures in order to better investigate the accuracy of this technique, i.e. by performing comparison with other NDT methods (Pascale e Colla, 2006) or to improve the analysis of wave propagation (Garnier V. et al., 2006). Instead, other researches were aimed at evaluating the potentiality of ultrasound tests in characterizing and locating defects in inhomogeneous materials such as wood (Bucur V., 1999; Maack e Krause, 2008) or masonry (Musolino et al., 2007). With reference to masonry materials, the US assessment of porosity and strength of mortars have also been studied (Voigt et al, 2006; Goueygou et al., 2009) and a more recent work has proved the reliability of ultrasound tests as a tool for determining textural characteristics of lime-mortars (Arizzi et al., 2013). On-site

applications with good results have been carried out also in historic masonry constructions (Dilek, 2007; Brozovsky et al. 2008, Camplani et al., 2008; Pascale 2008; Salazar et al., 2012).

Basic principles and types of tests

Short vibration pulses are generated by an electro-acoustical transducer (emitter) held in contact with the surface of the investigated element. The so-generated longitudinal or transverse stress waves, after travelling through the material, are then recorded by one or more transducers (receivers) positioned in the opposite or same surface of the element according to the data acquisition mode. The vibration is then converted into an electric signal, which is suitably amplified and continuously visualized on a CRT (Cathode Ray Tube) oscilloscope.

From ultrasound tests, the travelling time, Δt [μs], is measured, and knowing the ideal path length, L , the pulse velocity V [m/s], which is the velocity of the P- or S-waves propagation, is calculated:

$$V = \frac{L}{\Delta t} \quad 3.1$$

This velocity, is a function of the characteristic parameters of the material crossed:

$$V_l = \sqrt{\frac{E_d(1-\nu)}{\rho(1+\nu)(1-2\nu)}} \quad 3.2$$

where: E_d = dynamic modulus of elasticity of the material, ν = coefficient of Poisson of the material and ρ = density of the material.

Thus, from this equation, knowing the values of ν and ρ of the specific material tested and measuring V , it is possible to evaluate E_d . Then, from the dynamic modulus, an estimation of the static modulus of elasticity, E , could be performed, by reducing the first value of about a 30%.

In ultrasound tests, the wave attenuation is also measured. The attenuation is the decrease in the wave amplitude during its propagation within a material and it is due to the divergence of the radiation pattern (geometrical attenuation) or to absorption and scattering phenomena depending upon the characteristics of the crossed material.

The structural attenuation, A [dB], has usually the greater influence and depends upon the acoustic pressure (Figure 3.1):

$$A = 20 \log_{10} \frac{P_0}{P} \quad 3.3$$

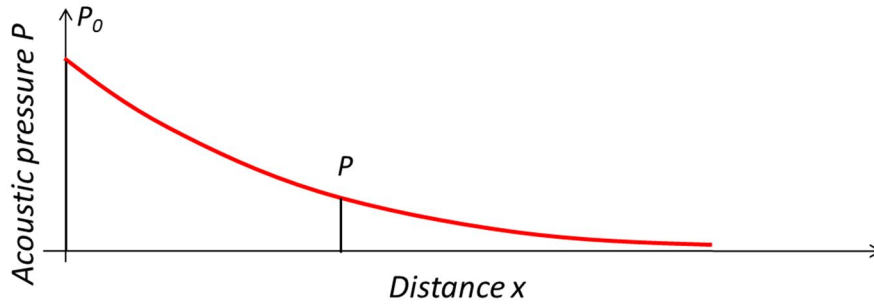


Figure 3.1: Amplitude of the emitted (P_0) and receive signal (P)

For each specific test, it is recommended to evaluate the obtainable resolution, R . This is the minimum detectable dimension of a defect and it is a function of the wavelength, λ , usually defined as a half or a third of the wavelength itself, was calculated for this specific case (Pascale, 2008). The signal wavelength, indeed, depends upon the velocity of the P-waves, V_p , into the specific material considered and the maximum signal frequency, f , according to Eq. 3.4:

$$\lambda = \frac{V_p}{f} \quad 3.4$$

Testing equipment

In this experimental work, ultrasound tests were performed by means of a commercial Olympus EPOCH 1000 available at the LAGIRN laboratory of our department and made of a portable unit and a signal amplifier was employed. This system is characterized by a pulse rate frequency up to 6 kHz, an equivalent measurement rate for the receiver, a gain range from 0 to 110 dB and full EN 12668-1 compliance [3]. A couple of 1MHz frequency probes for P-wave detection, 13mm in diameter, were used. These probes were chosen taking into account on the one hand, the small dimensions of the specimens to be tested (single units of bricks and mortar prisms, see chapter 5) and on the other hand the high resolution signals required which were capable of detecting also small anomalies and/or differences between the mortar prisms belonging to diverse sets.



Figure 3.2: Ultrasonic tests: testing equipment and probes (left and centre), calibration bars (right)

Testing procedure

Ultrasound tests can be performed in three types of signal transmission mode, according to the relative positions of the emitter and the receiver: direct, semi-direct or superficial transmission tests (Figure 3.3).

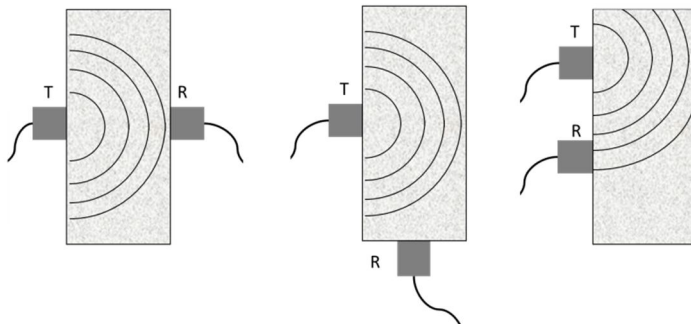


Figure 3.3: Ultrasonic tests, data acquisition mode: direct transmission (left), semi-direct transmission (centre), superficial transmission (right)

In this thesis, only US in direct transmission mode were considered to study brick units and lime mortar prisms in different ageing conditions. Longitudinal and transversal paths on the samples were considered.

The measurements were carried out by positioning the transmitting and receiving probes on each reading stations of the samples by means of a plastic clamp in order to ensure the same contact pressure, independently from the operator. In addition, a dry coupling of the transducers was obtained by interposing a latex sheet, 0.5 mm thick, between the surfaces of the probes and the sample, in order to ensure air removal and, in the same time, avoiding that remaining traces of coupling agents (usually gel or greasy pastes) would enter the material pores and alter the suction/evaporation mechanisms.

Prior to start with the data acquisition, for each set of samples, a calibration of the US signal was performed, by using a specific metal or plexiglas calibration bars with the aim of determining the reference values of time of flight and signal attenuation to be detracted from the single US measures.

3.2. Sonic tests

Sonic tests are an acoustic non-destructive technique, based on the variations of signal velocity and attenuation of low-frequency waves generated by means of an instrumented hammer and received by a transducer, generally an accelerometer after having crossed a material section. These tests are suitable for the detection of defects such as cracks, voids and inhomogeneities, the evaluation of the morphology of the structure and of its characteristics mechanical properties as well as assessment of the health-state of structures like brick, stone masonry and natural stone elements. Sonic tests are used for the damage detection and evaluation of material properties also in historical buildings. They are preferred to ultrasonic tests in cases of large and inhomogeneous elements because of their highest penetration depth.

In the fields of civil engineering as well as in cultural heritage sites, many researches and studies carried out in the last twenty years, have proved the reliability of sonic tests in recording useful information about hidden details and defects of a structural element and internal geometry, giving an overall qualitative view on the health-state conditions and structural integrity of the investigated structures and buildings.

Moreover, several studies have proved, by comparing this methods with other diagnostic techniques such as GPR radar, the feasibility and accuracy of the sonic tests for assessing the effectiveness of repair techniques or grout injections on structural masonry walls, i.e. performing the tests before and after the injection it was possible to estimate whether the grout is diffused inside the masonry or not (Binda et al. 2001; Russo et al., 2004; Anzani et al., 2006). Promising results were also obtained with regards to the evaluation of damages in historic stone elements (Cappabianca et al. 2008) Recent advancements on the data acquisition in superficial transmission mode and data analysis procedures allowed to visualize the values of sonic velocity and signal attenuation as 2D images (sonigrams), easing the data interpretation (Colla e Pascale, 2007; Colla et al. 2008). On-site experimental campaigns were successfully carried out also for the assessment of the mechanical properties of the masonry a cultural heritage, historic masonry tower (Colla e Pascale, 2010).

Basic principles and types of tests

In sonic tests low-frequency elastic waves (20Hz – 20KHz) are generated by an instrumented hammer on the surface to be investigated. The elastic shock excitation generates stress waves that propagate inside the material, as longitudinal or transverse waves. A receiver transducer, usually a piezo-electric accelerometer receives the pulses. The vibration is then converted into an electric signal, which is visualized on a CRT oscilloscope or on the screen of a personal computer.

For each measurement path, a pair of waveforms is recorded by a data acquisition unit: the signal generated by the hammer and the received signal after propagation in the material.

Sonic investigations can be performed in different ways, depending on the relative position between the hammer and the receiver: direct, semi-direct or surface transmission may be carried out (Figure 3.4). In direct transmission mode, or transparency, the hammer and the receiver are placed on two opposite surfaces of the structural element, on the same axis, so that the direction of transmission pulse is perpendicular to these surfaces. Instead, in the

surface method, or indirect transmission, both hammer and accelerometer are placed on the same surface, and measurements are taken along a straight line, vertical, horizontal or diagonal. Finally, in the semi-direct transmission mode, the stations of signal emission and reception belong to adjacent faces, but in some cases even opposite.

As for ultrasound tests, the so-called time-of-flight, ToF, in μs is measured (Figure 3.5) and the apparent pulse velocity, in m/s, is calculated, by knowing the ideal length of the wave path (Eq. 3.1). The wave attenuation, A (Figure 3.6) is also measured and reported to a dimensionless value with respect to the amplitudes of the transmitting (A_{maxTx}) and receiving signals ($A_{\text{maxRx}} - A_{\text{minRx}}$) by means of:

$$A = 20 \log_{10} \frac{A_0}{A} \quad 3.5$$

where $A_0 = A_{\text{maxTx}}$, and $A = A_{\text{maxRx}} - A_{\text{minRx}}$.

The variations on the values of the pulse velocity which are related to the density and the mechanical properties of the material, also in combination with the changes in the values of attenuation, for more accurate results, allows evaluating the homogeneity of the investigated material.

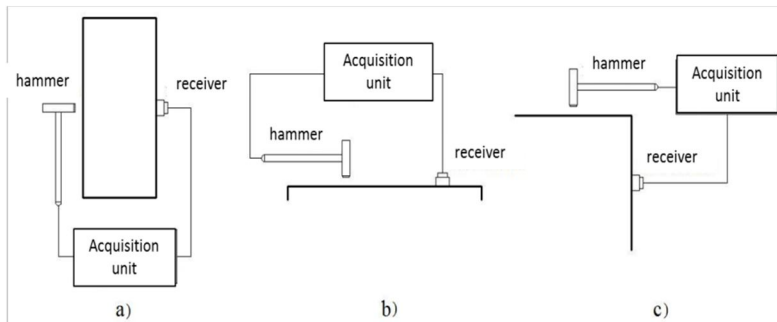


Figure 3.4: Sonic tests, data acquisition mode: direct transmission (left), surface transmission (centre), semi-direct transmission (right)

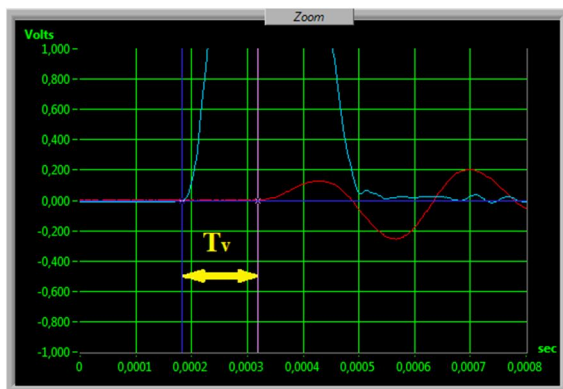


Figure 3.5: Sonic tests, measurement of the time-of-flight



Figure 3.6: Sonic tests, measure of the amplitude of transmitting (left) and receiving signals (right)

Testing equipment

The sonic tests instrumentation consisted in an

Hammer with a beryllium tip,

Micro-accelerometer



Figure 3.7: Sonic tests, testing equipment, hammer and receiver

Testing procedure: data acquisition and analysis

Prior to start with the data acquisition, the measurement stations have to be selected, usually by tracing rectangular grids on the surface/s to be investigated. The measurements positions and/or grids have to be chosen according to the testing aims and traced on the studied elements. No other surface treatments/preparation are required.

In this thesis, sonic tests were carried out in direct-through transmission mode and surface modes on naturally aged full-scale brick walls and naturally or artificially aged small walls and masonry assemblies.

The small walls and masonry assemblies were tested only via direct sonic tests and the measurements performed by placing the hammer and receiver on opposite positions, on the

lateral faces of the specimens, in order to carry out measures along the plane of the wall. Variations in sonic velocity and attenuation are measured.

On full-scale walls a rectangular grid of measurement points was marked on both main wall surfaces prior to perform direct sonic tests (Figure 3.8). The instrumented hammer and the receiver were progressively moved along the stations of the grid but always facing each other, starting from the top left corner of the wall front face.

On each position, the values of time-of-flight, signal velocity and signal attenuation were evaluated. The results beyond being visualized in graphs reporting the parameters as a function of the measurement stations, are post-processed together with the geometrical (x, y) coordinates of each station, by using a mapping SW in order to obtain grey-scale or coloured 2-D images which allows an easier visual interpretation and comparison of such results.

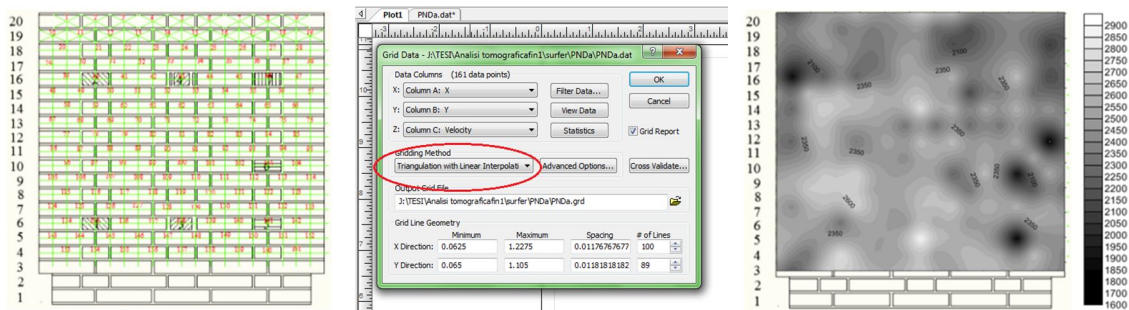


Figure 3.8: Example of measurement grid for direct sonic tests in full-scale walls (left), “Surfer” command window for plotting sonic results as coloured or greyscale maps (centre), example of a 2D direct velocity maps

To perform sonic tests in superficial transmission modes on the full-scale walls, both the hammer and the receiver (micro-accelerometer) are placed on the same wall surface (front side). In this case, the grid selected was not rectangular, but instead the stations were positioned at the intersection between 8 concentric circumferences of radius varying from 0.1m to 0.8m and 16 diameters with different angles, with the receiver staying still at the center of the grid and the transmitter moving on each station (Figure 3.9). Also in this case, data were analysed in terms of time of flight and signal velocities.

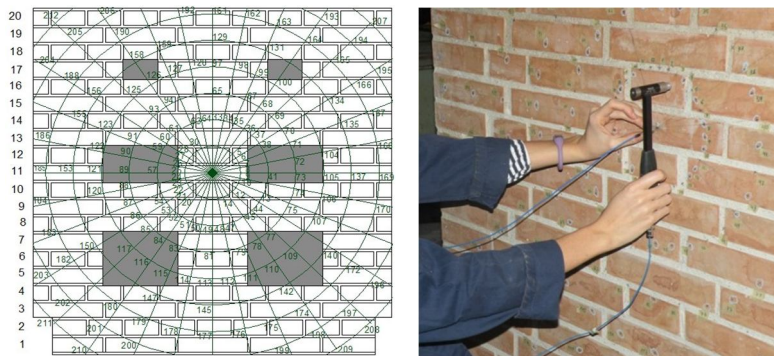


Figure 3.9: Example of measurement grid for surface sonic tests in full-scale walls (left), data acquisition phase

3.3. GPR ground penetrating radar

The GPR radar is a non-destructive technique based on reflection of electromagnetic signals born in the 50's in the geophysical field with specific tasks of soil investigation and only since the '80 has started to be use in the field of civil engineering. It is a global and fast technique, on-site applicable, which allows to scan large areas of walls, pavements and other elements, including historic constructions and thick stone or brick masonry. Among other applications, it is suitable to evaluate element and layer thickness, also in case of multi-whyte walls and to detect inner defects such as voids, inclusions, detachments, cracks and in-homogeneities in structural elements made of several different materials, like natural stones, stone and brick masonry, concrete. GPR allows also to assess the health-state conditions of new and historic structures and the presence of moisture and salts within walls.

This method is suitable for testing concrete and masonry structures also of large dimensions like bridges (McCann, et al. 2001).

Although it is a rapid, no-contact high resolution method for detecting and mapping features in engineering applications but it cannot be used for high resolution soundings in great depth ranges or in environments with high electrical conductivity. The range and resolution of GPR decreases with the presence of conductive materials like brine or conductive pore water. At saline contents of 0.05% by weight 900 MHz bow tie antenna were significantly attenuated. When testing through soil, the best results were obtained when using radar through dry soil. (Colla et al. 1997)

Successful results were obtained Detail knowledge obtained about the construction has a positive fall back on the structural model and on the analyses aimed at evaluating the load carrying capacity and safety of the object. It seems very promising the possibility of merging the GPR data about the hidden wail geometry with the impact-echo and sonic data about the time of flight of stress waves in different masonry patterns, in order to estimate homogeneity and constitutive parameters of a mechanical model of the masonry. Thermography inspection have also shown to be very useful in this case of archaeological cultural heritage benefiting from high protection, providing useful information about the health and patterns of superficial material layers.

Colla, C., De Miranda, S., Ubertini, F., 2008, On site diagnostic investigations for the assessment of the House of the Wooden partition, in Herculaneum, in On site assessment of concrete, masonry and timber structures SACoMATiS 2008. Proceeding of the First International RILEM Symposium, L. Binda, M. di Prisco, R. Felicetti, Vol. 2, 945-954.

The applied diagnostic procedure has served to identify the characteristics of the elements that determine the structural behaviour. The

Basic principles

Short electromagnetic pulses (frequency range 500-2500 MHz) are propagated into the structure thanks to an antenna moved on the surface, along survey lines. In reflection mode, the reflected signals are picked up by a receiving antenna moving on the same surface as the transmitter; in transmission mode, the receiver is placed on the rear surface of the element

(this operating mode is less frequently adopted). The propagation of the radar signal depends on the condition and dielectric properties of the materials encountered. The signal velocity and attenuation are the factors that describe the propagation of the radar waves into the materials. These parameters are a function of the relative permittivity, conductivity and magnetic permeability of the materials, which also determine the signal power reflected at boundaries where the dielectric properties vary.

Testing equipment

Signal generator and control unit with data storage functions and monitor for real-time data visualisation. One or more antennae boxes containing a transmitting and a receiving antenna (usually dipole antennas). Survey wheel can be attached to antenna for precise recording of survey length. After data acquisition, data elaboration is performed on a PC with appropriate SW

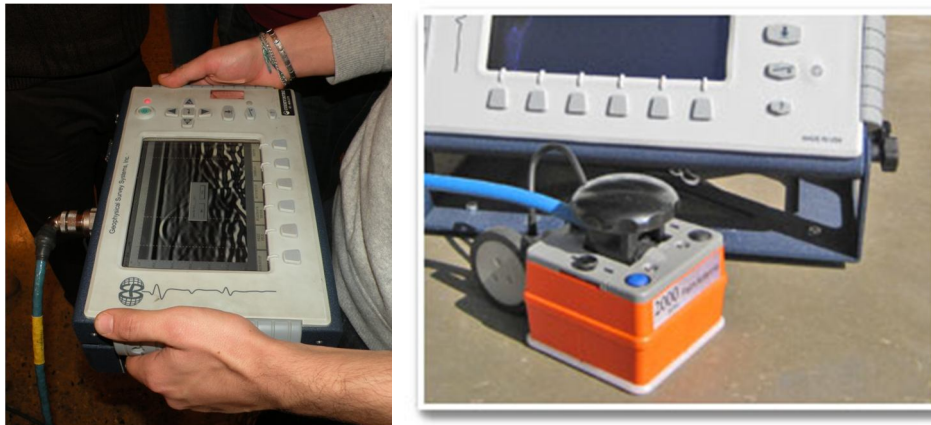


Figure 3.10: GPR testing equipment and antenna

Testing procedure: data acquisition and analysis

Choice of antenna frequency must be suited to characteristics and thickness of materials investigated, dimensions and location of defects sought. Necessity to access a sufficiently wide testing surface in function of penetration depth and antenna dimension.

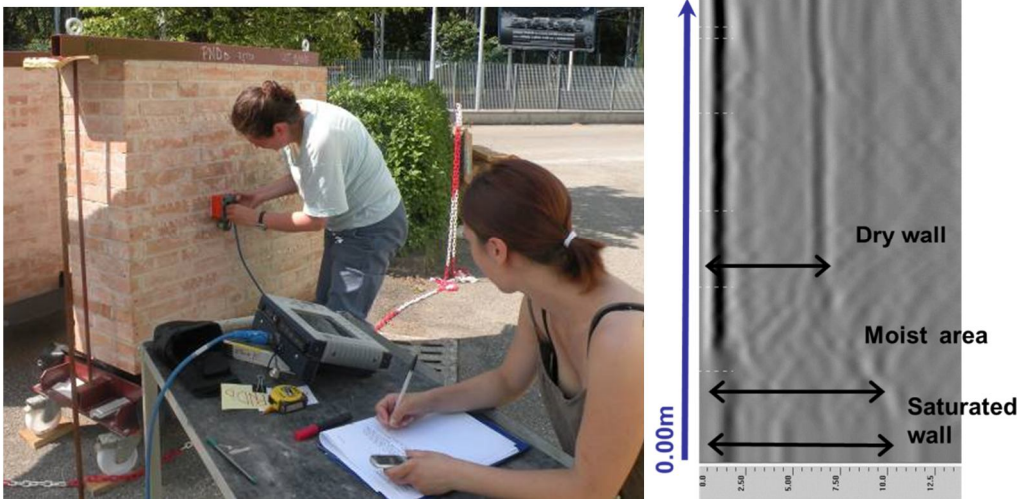


Figure 3.11: Data acquisition and example of radargram

3.4. Infrared thermography

Infrared thermography (IRT) is a non-destructive investigation technique, which is becoming more frequently employed in civil and architectural inspections, in the diagnostic phase, in preventive maintenance or to verify the outcome of interventions. On historic structures, it allows investigating details of construction (e.g. hidden structure or masonry texture behind the plaster), damage and material decay (e.g. moisture, plaster detachment from a wall, detachment within a fresco, cracks pattern evolution, temperature pattern evolution,

Infrared thermography is a non-destructive investigation technique, which is becoming more frequently employed in civil and architectural inspections, in the diagnostic phase, in preventive maintenance or to verify the outcome of interventions. On historic structures, it allows investigating details of construction, damage and material decay. In order to obtain more detailed information IRT can be used with other NDT techniques (e.g. ultrasound, radar etc.)

Applications of infrared thermography in civil engineering are not limited to the identification of heat losses in building envelopes; infrared thermography methods enable localisation of voids and other irregularities in the near surface region, localisation of plaster delaminations, detection of moisture in the near surface region etc.

Masonry and especially historic masonry has a very inhomogeneous structure containing several different materials (brick, stone, mortar, plaster, wood, metal etc.) with different thermal properties; in this cases thermography is a very reliable method to assess the following testing problems in the surface near region: detection of plaster and tile delaminations, location of mounting parts behind plaster, characterisation of masonry structure behind plaster, location of empty joints, detection of enhanced moisture, location of delaminations of strengthening materials.

In the following, some relevant information arising from literature review are summarized.

Very interesting is the case of the massive masonry of the Historical Arsenal of Venice (Grinzato et al., 2002 [5]) where IR thermography has been applied successfully for the knowledge of wall bonding, moisture mapping and the measure of the thermal diffusivity of bricks and plaster.

A review of results (hidden structure identification, adhesion of frescoes testing, cracks mapping and air flows study) given by thermography applied for the conservation and monitoring of the Scrovegni Chapel at Padova, frescoed by Giotto, is presented in [6] (Grinzato et al., 2002).

Different thermographic techniques for frescoes NDT were compared by Carlomagno et al. and reported in [7] (2002). The authors evidenced how the choice of the most appropriate thermographic technique, for non-destructive evaluations, depends on several considerations linked on both material characteristics and test objectives.

The application of infrared thermography to the non-destructive testing of concrete and masonry bridges was evaluated by Clark et al. ([8], 2003), while Avelidis et al. ([9], 2003) evidenced the importance of proper emissivity values for building diagnostics. Since in

literature there is little work that has been published on emissivity values for building materials (mostly historical buildings) at a range of temperatures, the results that arise from this research work, provide valuable information to the thermograph whose investigation is concerned with buildings and historic complexes (however the best approach, whenever possible, is to measure emissivity on site).

Some others interesting applications of infrared thermography for the investigation of historic structures by Avdelidis et al., 2004 are reported in [10]; the authors concluded that infrared thermography provides significant information for the assessment of materials and techniques for the protection of cultural heritage. In particular, it can be used efficiently for the assessment of conservation materials and techniques on the subject of surface cleaning, stone consolidation, restoration of masonry by repair mortars, as well as to disclose any substrate features, such as tesserae on plastered mosaic surfaces.

Rosina et al. ([14], 2004) developed an IRT procedures for the monitoring of restoration interventions on ancient building surfaces (i.e. application of protective films, water repellent, restoration of plaster delamination), the surveillance of the risks areas (i.e. risk for dew, infiltration, thermal bridges, window frames).

The use of infrared thermography for non-destructive evaluation of one- and two-layer masonry structures has been examined by Meola and reported in [19] (2007)

Remarkable is also the investigation by IR thermography of Roman archaeological stone masonry structures with thick plaster overlay (Colla et al., 2008 [24]). Particular aims have been to investigate the state of bonding between the plaster and its support, to locate moist areas in a façade wall highly inhomogeneous in terms of plaster materials, surface roughness and plaster thickness, and to unveil construction details hidden under the finishing layer, such as the shape and layout of the masonry units or the inclusion of metal elements. The authors concluded that the information provided by IR inspections outcome is of great significance in terms of acquired knowledge about the archaeological masonry construction and has positive consequences on structural evaluation.

Basic principles

The presence of a subsurface defect modifies the diffusion rate of thermal propagation. Infrared thermography is a contactless NDT technique able to record the distribution of surface temperatures and thus to unveil details of what is under the surface, within shallow depths, or its thermal behaviour.

Passive and active thermography testing procedures can be differentiated. In passive thermography, abnormal temperature profiles indicate a potential problem, and an important measurement parameter is the temperature difference with respect to a reference. Generally, passive thermography is rather qualitative since the goal is simply to pinpoint anomalies. In active thermography it is necessary to bring some energy to the area inspected, in order to obtain significant temperature differences witnessing the presence of subsurface anomalies.

Testing equipment

Infrared thermo camera with a specific wavelength window (depending on the material to be tested), different kinds of lens (depending on the distance from the analyzed surface, on the surface dimensions and on the minimum dimensions of the expected defect), PC, post-processing software.



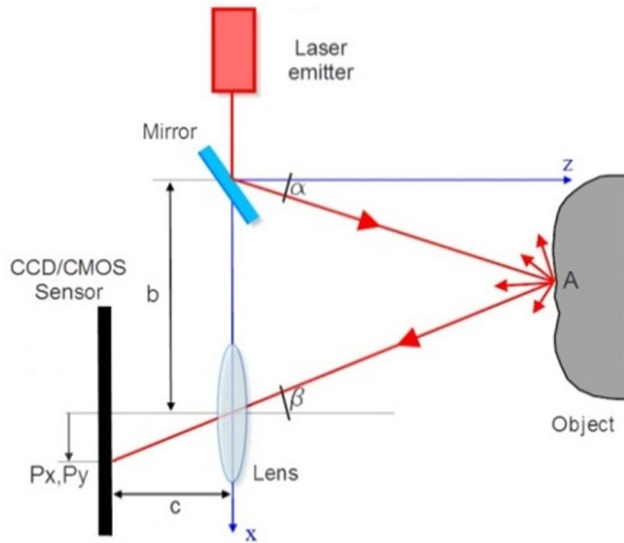
Figure 3.12: Data acquisition

3.5. Laser scanner

In this thesis, a triangulating desktop laser scanner was used, which is proven to be a reliable technology for non-contact surface measurements. The technique is called triangulation because the laser spot, the camera and the laser emitter form a triangle. Exploiting the principle of the topographic forward intersection it is possible to determine the position of a point in the 3D space defined by the instrumental reference system (Fig. 2). The distance between the laser emitter and the camera sensor (representing one side of the triangle) is known by the constructor specification, and it is called “baseline” (b). The out-coming angle (α) of the laser beam is also known by a prior calibration of the rotating mirror. Then the laser beam undergoes a reflection on the targeted surface, and its footprint on the receiving sensor (usually a CCD or CMOS) makes it possible to calculate the angle (β). These three informations (α , β , b) combined with the trigonometric formulas (1) and (2) fully determine the coordinates of the points cloud in which the surface can be discretized.

Following a process of triangulation, the points cloud can be converted into a mesh of triangles, which constitute the 3D surface of the object. If the device is able to capture also the color RGB information

Basic principles



X, Y, Z) coordinates of a single point

$$x_A = \frac{b}{1 + \frac{\tan \beta}{\tan \alpha}} \quad y_A = \frac{b}{\frac{\tan \alpha}{\tan \gamma} + \frac{\tan \beta}{\tan \gamma}} \quad z_A = \frac{b}{\tan \alpha + \tan \beta}$$

Testing equipment

The laser scanner used in this work is produced by NextEngine Inc. and is based on Multi-stripe Laser Triangulation (MLT) technology. The laser scanner acquires the data in two different modes corresponding to two different baselines: Macro mode and Wide mode. Some constraints on the distance between the object and the scanner are given for each mode (Tab. 1). The choice of the scan mode depends on the object's size and the desired output accuracy.



NextEngine HD

(desktop triangulation scanner)

Table 1. NextEngine laser scanner specifications.

Dimensions	224 x 91 x 277 mm	
	Macro Mode	Wide Mode
Field of View	13x10 cm	35x25 cm
Working distance	18 cm	40 cm
Accuracy	$\pm 127 \mu\text{m}$	$\pm 381 \mu\text{m}$
Resolution	200 DPI	75 DPI
Texture density	400 DPI	150 DPI
Points/sec	50000	50000

The scanner mounts a couple of twin arrays of Class four 1M 10-mW solid-state lasers with custom optics at a 650-nm wavelength. The scanner also features twin 3 MP CMOS RGB image sensors, and built-in white light texture illuminators [7, 8] This technique was chosen because it is contactless, rapid and capable of providing quantitative information, thus it could be helpful in order to monitor the degradation processes caused by moisture and salt movements since their beginning.

3.6. Digital image correlation

Finally, an additional innovative non-destructive procedure was considered to evaluate the decay progress and evolution in outdoor walls based on the digital image correlation technique.

The Digital Image Correlation (DIC) is a non-destructive, contactless, optical technique which allows the determinations of high-definition full-field maps of displacements and strains of a surface object subjected to an external force. The method, 2D or 3D, exploits the principles of photogrammetry, digital image processing and stereo-images and it allows a continuous data acquisition. It employs a mathematical algorithm to compare digital images taken at different deformation states of a specimen by means of 1 or 2 digital cameras. This comparison is based on tracking the position in the consecutive, subsequent images of a random speckle pattern applied to the investigated surface prior to the test by using appropriate patterning techniques (spray painting, cotton swab, stencil, speckle patterning, air brush, etc.) [...3Vancouver, + general?] (Fig. 1). The results obtained by means of the DIC technique, in terms of displacement, deformation and strain fields are displayed as greyscale or coloured maps [21 8*]. 38, 40–46].

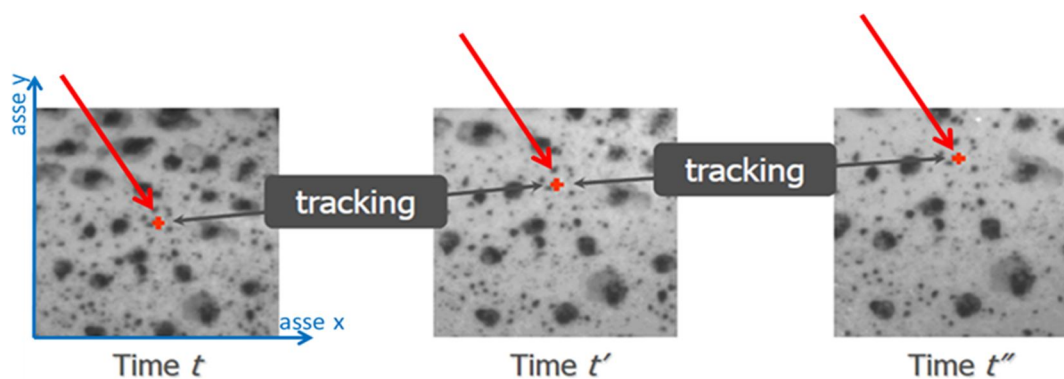


Figure 3.13: Monitoring over time of the displacement of 1 point [...] cambiare scritta assi

1.1. Basic historic information and principle of DIC

The DIC technique was developed in the early '80s at the University of South Carolina as a 2D method to measure the in-plane displacement field of an object while it is undergoing a deformation or a movement. In this case, one digital camera acquires the images and dedicated software compares the reference, non-deformed image with the subsequently recorded deformed images (Fig. 2 left). This process follows different steps: firstly, the reference image is divided into sub-images, or square subsets, which are centred on a point of interest –where the displacements will be calculated-. Each sub-image is then used to track the corresponding location of each control point in the deformed image, by means of a correlation function, until reaching the maximum correlation coefficient between the reference subset and the “deformed” subset, obtaining the displacement of the considered point (Fig. 2 right). Then, the same procedure is repeated to calculate the displacements for all points and images [tesi scaric 12/11; H. Song et al. / Tectonophysics xxx (2013) xxx–xxx &

(Pan et al., 2009b; Sutton et al., 2009; Zhang et al., 2006)]. Fig. 2 di H.Song??? W.H. Peters and W.H. Branson [50].

This simple methodology is appropriate for planar specimens and it gives accurate results only if the specimen is parallel to and at a constant distance from the digital camera for the entire duration of the experiment in order to discard or at least minimize the effects of out-of-plane displacements. In this case, indeed, the monocular vision of the sample allows detecting only in-plane displacement (u , v) and corresponding deformation fields (ϵ_x , ϵ_y , γ_{xy}).

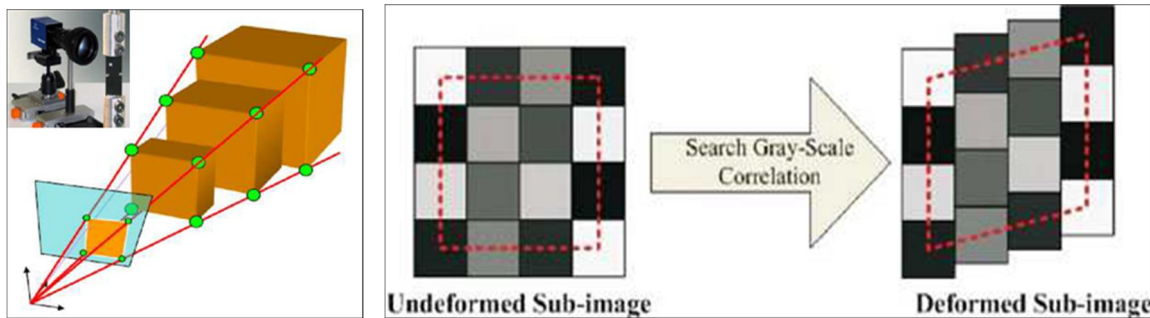


Figure 3.14: Digital camera and relative monocular vision (left); greyscale correlation between un-deformed and deformed sub-image (right) [DICmanual & Tung et al 2010]

A 3D version of the DIC method has been implemented at the beginning of this century, in order to measure the out-of-plane motion [...]. This procedure is based on the simultaneous acquisition of pair of images, by means of two CCD cameras, placed in front of the investigated object with different angles (Fig. 3). The post-processing software analyzes and compares each couple of deformed images to the pair of reference images by applying first a stereo imaging equation and then a correlation algorithm (comparison of images pixel by pixel). For an accurate determination of the 3D coordinates (x , y , z) and the 3D displacement vector [$u(P)$, $v(P)$, $w(P)$] of each point P of the images, it is required to calibrate the DIC system prior to the test, in order to calculate the intrinsic and extrinsic parameters of the digital cameras set-up (distortion of the lens, relative distance of the cameras, orientation of the cameras with respect to the object surface, ...) which are characteristics of the specific stereoscopic configuration used [A; vet spost???]. The calibration procedure consists in recording simultaneously a set of images with the two cameras while the position and inclination of a calibration target is changing in front of the specimen to be investigated. The calibration target is usually a white flat plate with a grid of black dots of known dimension and distribution (Fig. 4). The calibration images acquired are used by the software to calculate the coordination system of axis and establish the ideal working plane. The result of the calibration indicates the quality of the adopted configuration and allows selecting the best stereovision system for this specific experiment, which is the one with the least error [A].

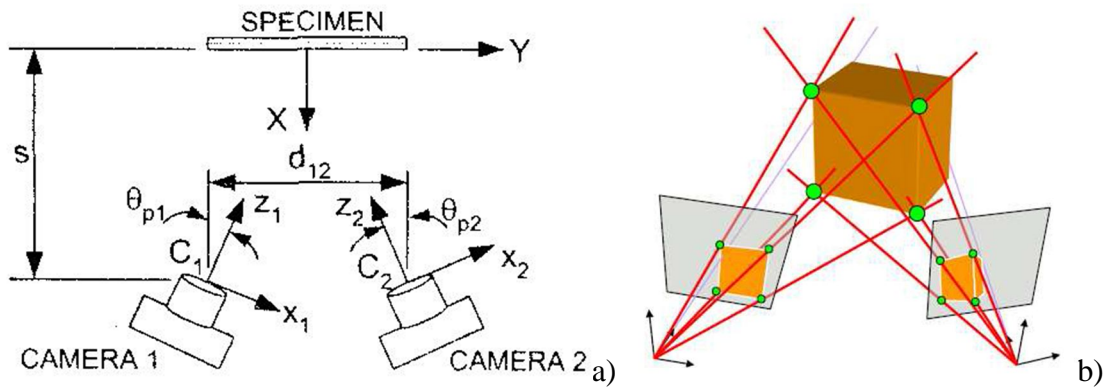


Figure 3.15: a) Set-up of the 3D DIC method, acquisition of stereoscopic images, b) 3D vision [Zafar, DICmanual]

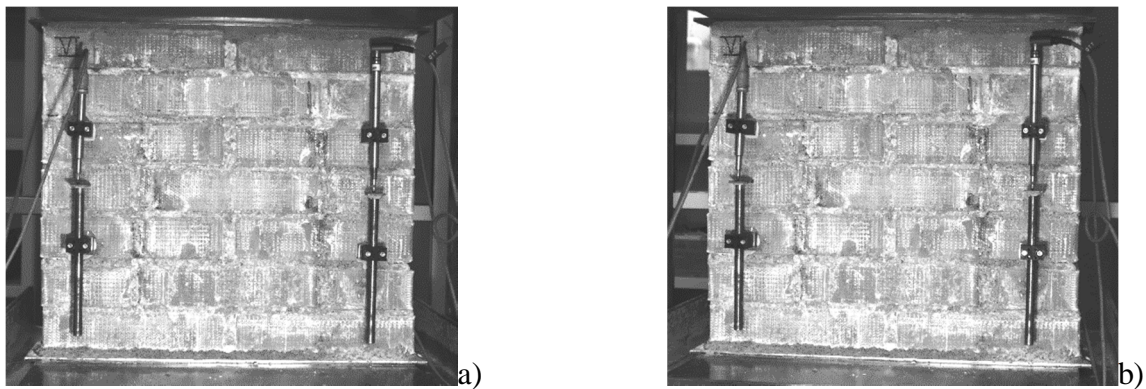


Figure 3.16: Simultaneous acquisition of couple of reference images, a) from the left camera, b) from the right camera

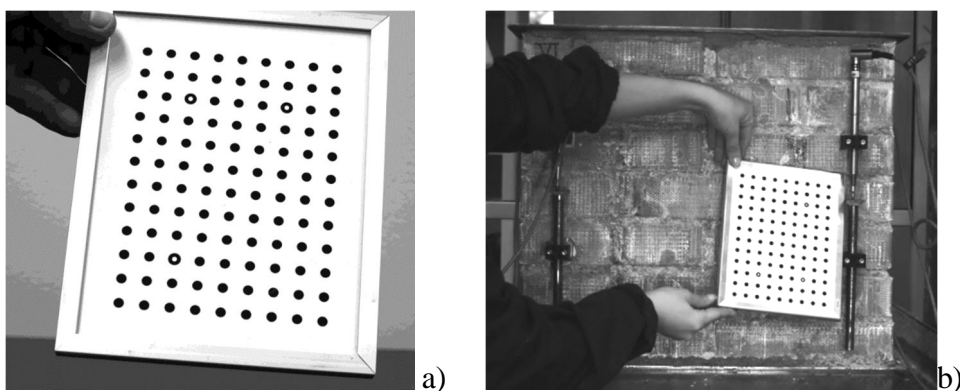


Figure 3.17: a) a calibration target, b) example of calibration procedure

The accuracy of this non-destructive monitoring technique relies upon several factors including the interpolation and correlation algorithms, the distortion of the lenses, the light distribution uniformity and the quality of the superficial speckle pattern. The first two parameters are distinctive of the equipment selected for the measurements, while the dot

pattern and brightness are defined and controlled by the operator before and during the test. In particular, since a fundamental assumption of the DIC method is that the light intensity field defined on the surface as a digital greyscale does not change during deformation, the operator should guarantee the steadiness and uniformity of the brightness throughout the experiment. Last but not least, the surface preparation plays an important role on the precision of the measurements, thus, the surface has to be treated (Fig. 5) in order to show a random pattern of dots, as much as possible non-repetitive, isotropic and with high-contrast chromatic areas, so that each point of the surface could be recognized and tracked by the DIC [V3 + ...].

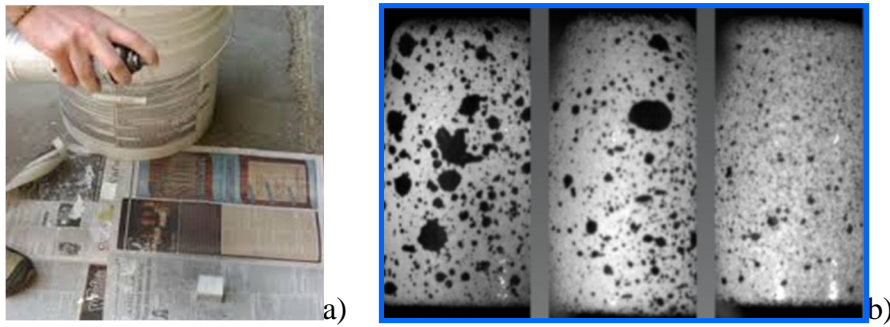


Figure 3.18: a) surface preparation by spray [...], b) examples of pattern [...]

4. Materials and masonry specimens for experimental activities

In this experimental research, different series of professionally made full-scale walls, wallets, masonry assemblies (brick columns and triplets) were considered as well as new units of porous building materials (bricks, mortar) (Figure 4.1). After design and construction, firstly they underwent natural or accelerated ageing according to on-purpose developed procedures aimed at reproducing the effects of the decay due to environmental agents such as moisture and salt. Given that the main aim of this thesis was to study the controlled evolution over time of this degradation and hence its effects on the physical and mechanical properties of masonry materials, in a second step they were characterized by means of repeated non-destructive and mechanical tests.

In this chapter it is described the physical-chemical and mechanical characterization of the masonry constituent materials. Following, for the different series of specimens, the design and construction phases, the dimensions, numerosity and aims of test o are reported. Finally, the two implemented ageing procedures are illustrated.

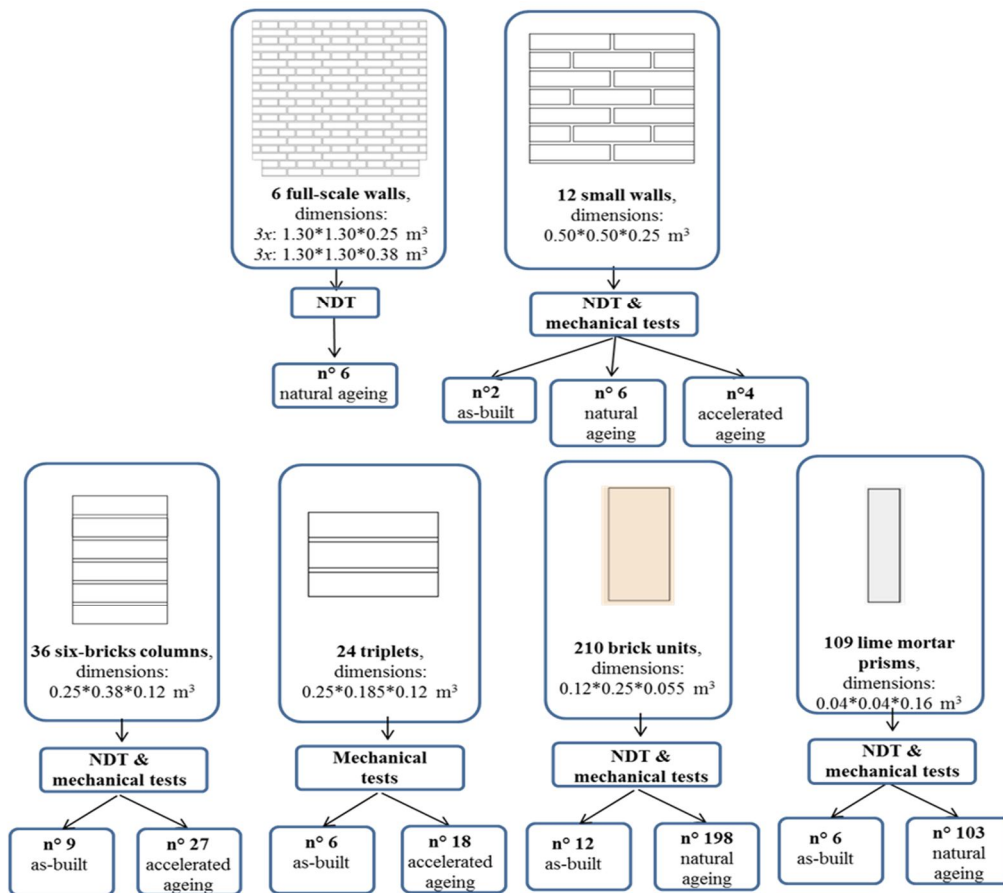


Figure 4.1: Main characteristics of the different series of specimen studied

4.1 Material characterization

Given that one of the main focus of the planned experimental work was to follow the decay evolution in masonry since its beginning, new porous construction materials were selected, that is fired-clay bricks and natural hydraulic lime mortar (Figure 4.1). The outdoors phases of the foreseen experiments being undertaken in the Bologna climate, a market search was made for locally produced materials. This search was not successful for the mortar mix.

First of all, as the durability of masonry structures subjected to weathering is function, among other factors of the characteristics of its individual component materials, the physical-chemical and mechanical properties of both bricks and lime mortar were studied by means of several laboratory testing techniques. The main aim of these preliminary tests was to determine with a detailed level of information the starting, undamaged, conditions of the 2 porous materials in terms of characteristic properties. Special attention was paid to those physical properties connected to water and salt transport phenomena. The lab tests described in the following paragraphs were partly carried out at the MPA laboratory of the University of Stuttgart, thanks to a collaboration started in the framework of the 7FP EU research project SMooHS (D5.2-5, SMooHS), and partly at the LISG laboratory of the DICAM Department of the University of Bologna. When possible, standard procedures were followed in order to obtain reliable and replicable results, otherwise, on-purpose procedures partly based on previous research experiences available in literature were developed.

Water would have been important in the experiments, both in the specimens construction stage (mortar mix, wetting of bricks) and in the ageing stage (water and brine sorption/immersion). Therefore, parallel to test the two single building materials, ion-chromatography analysis was carried out in MPA also on to the tap water of the Bologna aqueduct to quantify its salt content and thus, to determine a possible initial value of salt contamination. The results, in terms of anions and cations concentrations, show a low initial amount of chlorides and nitrates but high concentrations of sulphates, equal to 0.0138% -wt. (Table 4.1, Table 4.2). This not negligible initial sulphate content has to be kept into account because it may influence the material's ageing processes, especially the natural one (§4.5).

Table 4.1: Tap water from Bologna, ion-chromatography analysis: concentrations of anions (D5.2 part5, SMooHS)

	F ⁻		Cl ⁻		NO ₃ ⁻		SO ₄ ²⁻	
	mg/l	% -wt	mg/l	% -wt	mg/l	% -wt	mg/l	% -wt
tap water	not detected		37.2	0.004	10.3	0.001	138	0.014

Table 4.2: Tap water from Bologna, ion-chromatography analysis: concentrations of cations (D5.2 part5, SMooHS)

	Na ⁺		NH ₄ ⁺		K ⁺		Mg ²⁺		Ca ²⁺	
	mg/l	% -wt	mg/l	%-wt	mg/l	% -wt	mg/l	% -wt	mg/l	% -wt
tap water	27.1	0.003	not detected		3.13	0.0003	25.9	0.002	129	0.013

4.1.1 Mortar mix

A commercial ready-mix hydraulic lime mortar was selected. The binder in pure NHL5 while maximum size of aggregates is 4 mm (Figure 4.2). The fresh lime mortar was prepared adding tap water of the Bologna aqueduct to the commercial mix with pure NHL5 binder in the proportions water-to-mortar-mix 0.16 l/Kg. In the experiments, the mortar was used both for construction of the masonry specimens and for casting a high number of mortar prisms of standardized dimensions (b x s x h) 4 x 4 x 16 cm³. These were prepared in the Bologna lab, according to (EN 1015-11): the fresh mix was poured into moulds, in two layers each one compacted with a pestle and then, let to cure in a climatic chamber for 28 days, 7 days at 20°C and RH=95% and 21 days at the same temperature but reduced RH (65%).

To determine the undamaged conditions of the specific mortar used, a complete laboratory testing procedure was carried out, although some physical-mechanical properties of the commercial binder selected were already known from the available technical data sheet, i.e. for the compression strength, it is classified as a class III mortar (UNI EN 1015-11) (Figure 4.2). According to the indications of each specific standard, the different measurements were carried out directly on dust samples of the commercial mortar or on prisms.

T30V

MALTA
pronta a base di FEN-X/A



T30V è un malta per intonaco, rinzaffo, riempimenti e tamponature, realizzazione di giunti in murature faccia a vista e allettamento mattoni a base di calce idraulica naturale FEN-X/A ed inerti selezionati con granulometria massima di 4 mm.
T30V è una malta a medio alta resistenza, a basso contenuto di sali idrosolubili e ribro controllato particolarmente adatta negli interventi di ristrutturazione e risanamento.
T30V è conforme alla UNI EN 998-1 riguardo le "Specifiche per malte per opere murarie - Malte per intonaci interni ed esterni" e soggetta a marcatura CE secondo la normativa vigente.

Fornitura: in sacchi da 30 kg

DATI TECNICI

Granulometria (UNI EN 1015-1)	da 0 a 4 mm
Acqua d'impasto	ca. 0,16 l/Kg (ca. 5 l/sacchetto)
Peso specifico (UNI EN 1015-10)	1750 + 1850 Kg/m ³
Resa (per intonaco)	ca. 18 Kg/(m ² x cm)
Resistenza a compressione (UNI EN 1015-11)	Classe CS III (3,5 + 7,5 N/mm ²)
Resistenza alla diffusione del vapore (UNI 9233)	μ = 12
pH	> 10,5
Classe di reazione al fuoco	A1

I dati tecnici sono stati ottenuti da una malta preparata in laboratorio mediante miscelazione con miscelatore conforme alla EN 106-1 per 75 secondi a bassa velocità.

VOCE DI CAPITOLATO

Malta pronta a base di calce idraulica naturale conforme alla UNI EN 459-1, classificata NHL5 e soggetta a marcatura CE secondo la normativa vigente ed inerti selezionati con granulometria da 0 a 4 mm tipo TASSULLO T30V, adatta alla realizzazione di intonaci, rinzaffi, riempimenti e tamponature, realizzazione di giunti in murature faccia a vista e allettamento mattoni, di peso specifico di 1750 + 1850 Kg/m³, di classe CS III di resistenza a compressione (classificazione secondo UNI EN 998-1), resistenza alla diffusione del vapore (μ) pari a 12, pH > 10,5 e di classe A1 di reazione al fuoco.

Tassullo s.p.a.
via Nazionale, 157 38010 Tassullo (TN)
Tel: 0463/451506 Fax: 0463/451403
www.tassullo.it tassullo@tassullo.it



L'uso del prodotto implica la verifica della sua idoneità all'impiego previsto e l'assunzione delle responsabilità derivanti dall'utilizzo. I dati riportati sono ottenuti da misure di laboratorio. La TASSULLO S.p.A. si riserva di apportare in qualsiasi momento e senza preavviso le varianti ritenute più opportune ai dati tecnici riportati.

Figure 4.2: Commercial ready-mix hydraulic lime mortar: technical sheet

The physical-chemical characterization of the hydraulic lime mortar consisted in measuring the following properties:

- bulk density, by means of He-pyknometry;
- apparent density, according to (DIN EN 1936);
- open porosity and pore size distribution, via mercury intrusion porosimeter (MIP);
- mineralogical composition, by means of X-ray diffraction analyses;
- water absorption and capillary uptake via hydric test methods (DIN EN 13755, 2002; DIN EN 1925, 2000).

In addition, the salt contamination of this mortar mix in sound conditions was evaluated by ion-chromatography analyses.

The main resulting physical properties are summarized in Table 4.3.

Table 4.3: Main physical properties of the mortar determined on cured samples (D5.2-5, SMooHS)

Material	Bulk density [kg/dm³]	Apparent density [kg/dm³]	Porosity [Vol.-%]
NHL - mortar	2.06	2.60	20.6

The pore size distribution was determined by means of a Carlo Erba mercury intrusion porosimeter. This test allowed to quantify with a good accuracy, the percentage and dimensions of voids within the material. The main limitation of this techniques relies on the high-pressures used which may break weak pores recording false data, especially in the case of fragile or damaged materials [D5.1]. Anyhow, in this study, the parameters determined by MIP on undamaged mortar samples were highly-accurate. Their knowledge is very important as the porosity and pore distribution strongly influences the absorption and drying behaviour of the material as well as its vulnerability to salt attack. Although this latter topic is still object of discussion, numerous experimental researches indicated that the more sensitive pores to the decay phenomena caused by water movements and salt crystallization are those with radius ranging between 0.1 and 10 μm (Larsen et al. 1990; Rodriguez-Navarro et al. 2000; Arnold et al., 1990; Lubelli et al., 2004. Cultrone et al. 2008; Theoulakis et al. 1997). The mortar mix showed a rounded and quite wide curve of pore size distribution with the majority of pores roughly concentrated between 0.1 and 2.3 μm (Figure 4.3 left). This aspect indicates that the quasi-totality of its micro-pores are accessible to water and vulnerable to salt attack.

Then, by means of a Bruker AXS D8 X-ray diffractometer, the mineralogical phase composition was determined considering a mortar prism 9 months after casting. The results showed that this mortar is essentially composed of dolomite, calcite (carbonate) and quartz (mainly in the fine grained components) with minor amounts of vaterite, mica minerals, clay minerals and ca-silicates (Figure 4.3 right). This composition and in particular the presence of calcium carbonate suggests a vulnerability of the mortar mixture to degradation processes caused by chemical reactions which may occur in presence of water and sulphates with the production of gypsum [16-18].

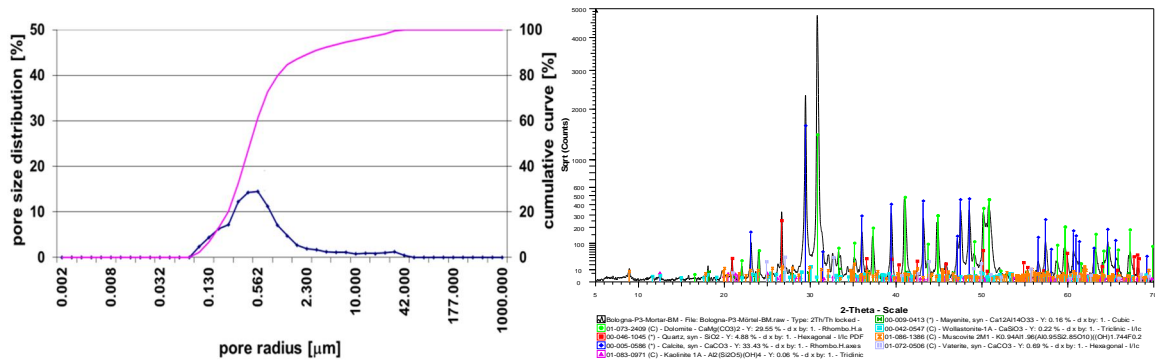


Figure 4.3: Hydraulic lime mortar pore size distribution and cumulative curve of pore volume by MIP (left) and mineralogic composition by X-ray diffraction analysis (right) (A1.8)

Additional physical characterizations were performed by means of a series of non-standardized damp rise tests considering mortar prisms in contact to distilled water or sodium chloride solutions at different concentrations (A1.16). These tests were carried out in climatic chamber in stable and controlled environmental conditions ($T=20^{\circ}\text{C}$, $R_H=60\%$) in order to restrict the effects of the boundary conditions on the diffusivity properties of the material. Each test consisted in placing vertically a specimen into a tray lined with a layer of cotton wool, soaked by water or salt brine and measuring the visible and IR level of capillary rise on one face of the specimen, thanks to a graduated 5-mm scale, marked by pencil on the faces of the prism. The level of brine or water in the tray was kept constant, about 3mm high, during each capillary rise test. This suction procedure, partly suggested in (EN ISO 15801:2010) was put in place because of laboratory constrictions which made impossible to perform subsequent weightings of the specimens as required by the procedure in (DIN EN 13755, 2002).

The values of capillary rise speed were determined as the slope of the absorption curve (rising damp levels in cm vs. square root of time expressed in hours). Following, the capillary suction rates were estimated considering the measured open porosity (upper limit for the water-accessible pore space) and the from available data banks by knowing the brine concentration. This intrinsic parameter, density, is almost proportional to the suction velocity but small discrepancies are expected due to some unavoidable variability of the mortar mix characteristics. The measured suction velocity varied with the used solution and decreased in an inversely proportional manner with increasing salinity of the solution (Table 4.4). This probably occurs because the presence of dissolved salts tends to occlude the micro-pores and to slow the moisture rise within the material (A1.16).

Moreover, ion-chromatography analyses were performed on the mortar mixture prior to mixing with water to evaluate the possible salt contaminations of this material. Indeed some salts may be contained into the mortar mix (§ 4.1). These results showed a small but not negligible amount of sulphates (Table 4.5, Table 4.6).

Table 4.4: Capillary rise velocity measured in mortar prisms in different conditions (A1.16)

Sample code	Contamination agent	Test duration [h]	Suction velocity [cm/h ^{1/2}]	Capillary suction rate [kg/m ² h ^{1/2}]
1M1	Distilled. Water	6	6.70	14.31
1M3	NaCl 10% wt	11	5.28	11.67
1M4	NaCl 30% wt	24**	5.03	12.32
1M5*	Distilled water	24**	6.56	13.51

* previously dried in oven to constant weight; ** this value corresponds to the time at which the operator saw the end of the test and stopped it, not to the real duration

Table 4.5: Mortar, concentrations of anions (mg/l) (D5.2-5, SMooHS)

Material	F ⁻	Cl ⁻	NO ₃ ⁻	SO ₄ ²⁻
NHL- mortar	<0,01	<0,01	<0,01	0,17

Table 4.6: Mortar, concentrations of cations (mg/l) (D5.2-5, SMooHS)

Material	Na ⁺	NH ₄ ⁺	K ⁺	Mg ²⁺	Ca ²⁺
NHL- mortar	0,01	<0,01	0,02	<0,01	0,08

Finally, to complete the characterization of the selected mortar, some non-destructive (by high frequency ultrasonic signal direct transmission) and mechanical destructive tests were carried out. For the details of testing and outcome of ultrasound results, please see chapters 3 and 5. In detail, bending tests and subsequent compression tests on the 2 stumps obtained from bending were undertaken on a statistically representative number of 4x4x16 cm³ hardened mortar prisms determining the values of flexural strength, f , and compressive strength, f_j (EN 1015-11:2007). Longitudinal compression tests were carried out on additional prisms after instrumenting them with 2 strain gauges (Tok.Sok. 10mm length, $k=2.13$) to evaluate the modulus of elasticity, E_j (EN 13412-2006) (Table 4.7). For this latter test, an example of the testing set-up and of the determined stress-strain curve is reported (Figure 4.4).

Table 4.7: Average mechanical properties of the hardened and cured mortar

Material	f_j [N/mm ²]	f [N/mm ²]	E_j [N/mm ²]
NHL - Mortar	3.17	1.19	4817.76

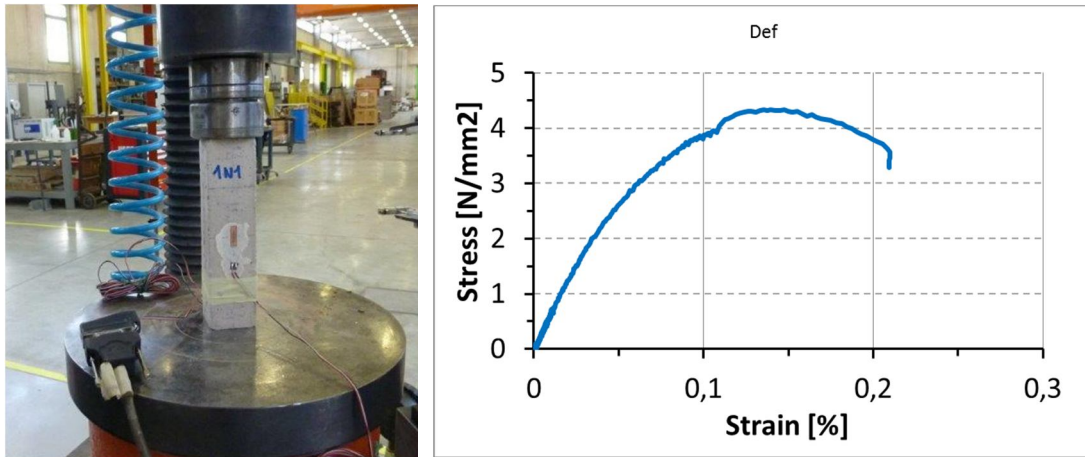


Figure 4.4: Longitudinal compression test of an undamaged mortar prisms: set-up (left) and example result in term of stress-strain curve (right)

4.1.2 Brick units

With regard to the chosen brick units, these were of local production (Figure 4.5).

The fired-clay full bricks of UNI standard dimensions 25 x 12 x 5.5 cm³ were fully characterized by means of several laboratory tests. Similarly to the mortar, first, the physical-chemical parameters were determined, following standard procedures (Table 4.8).

				IBL spa Sede legale ed amministrativa/Registered address via Ponte Pietra, 11 - 48010 Cotignola (RA) Tel. +39 054 540 123 - Fax. +39 054 542 067 www.iblspa.it - e-mail: ibl@iblspa.it Stabilimento/Factory: BENTIVOGLIO (BO)	
0948					
11					
0948-CPD-0090		MATTONI ESTRUSI		da Intonaco	
UNI EN 771-1		EXTRUDED BRICKS			
Tipo/Type: HD		Code art.: 601		Mattone	
Elemento in laterizio per muratura portante anche per zona sismica/Clay unit for structural masonry		UNI (12x25x5,5)			
		N. Pezzi/pacco: 272		N. Pezzi/m ² : 60	
		N. Unit/pack:		N. Unit/m ² :	
rev. 1_ 02 - 8 aug 11					
Dimensioni/Dimensions				Tolleranze/Tolerances	
Lunghezza <i>Length</i>		mm	250	T1 = +/- 6	
Larghezza <i>Width</i>		mm	120	T1 = +/- 4	
Altezza <i>Height</i>		mm	55	T1 = +/- 3	
R2					
Configurazione e forma: Mattone Pieno in laterizio come da disegno <i>Configuration and shape: Clay solid unit as in drawing</i>					
Massa volumica lorda <i>Gross dry density</i>		kg/m ³	1.750	Tolleranza/Tolerance D1 = +/- 10%	
Resistenza alla compressione <i>Compressive strength</i>				Categorial/Category	
Valore medio faccia base ⊥ <i>Mean value bed surface ⊥</i>		N/mm ²	28,0	I	
Valore medio testa 1 [lunghezza x altezza] ⊥ <i>Mean value face surface [length x height] ⊥</i>		N/mm ²	10,0		
Valore medio testa 2 [lunghezza x altezza] ⊥ <i>Mean value header surface [width x height] ⊥</i>		N/mm ²	10,0		
Durabilità al gelo-disgelo <i>Freeze/thaw resistance</i>		Categorial/Category		F0	
Contenuto di sali solubili attivi <i>Active soluble salts content</i>		Categorial/Category		S0	
Reazione al fuoco <i>Reaction to fire</i>		Classe/Class		A1	
Assorbimento d'acqua <i>Water absorption</i>		%		Da non lasciare esposto <i>Not to be left exposed</i>	
Tasso iniziale di assorbimento d'acqua <i>Initial rate of water absorption</i>		kg/(m ² .min)	3,5		
Coefficiente di diffusione del vapore acqueo <i>Water vapour permeability</i>		-	μ = 5 / 10	Valori tabulati in UNI EN 1745 <i>Tabulated values in EN 1745</i>	
Adesione malta↔laterizio <i>Bond strength</i>		N/mm ²	0,15 - 0,30	Secondo EN 998-2, All. 2 <i>According to EN 998-2, Annex 2</i>	
Conduttività termica [lunghezza x altezza] ⊥ <i>Thermal conductivity [length x height] ⊥</i>		W/(m.K)	0,530	Calcolo secondo UNI EN 1745 <i>Calculated according to EN 1745</i>	
Conduttività termica [larghezza x altezza] ⊥ <i>Thermal conductivity [width x height] ⊥</i>		W/(m.K)	0,530	Calcolo secondo UNI EN 1745 <i>Calculated according to EN 1745</i>	

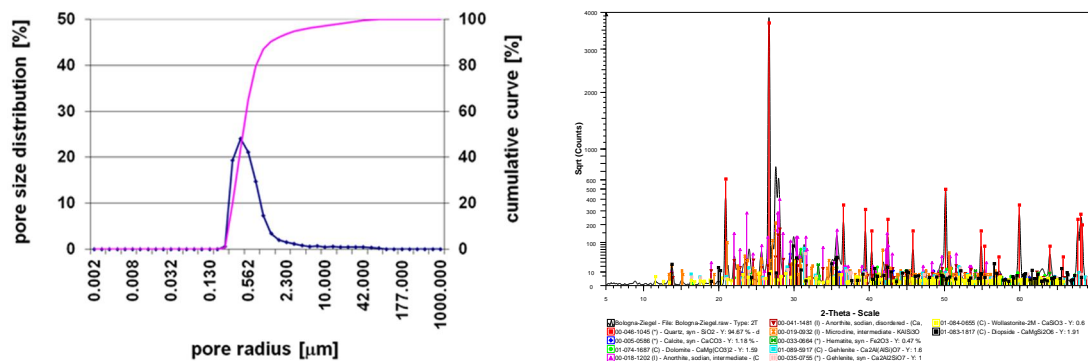
Figure 4.5: Fired-clay full bricks, technical data sheet

Table 4.8: Main physical properties of the red full bricks (D5.2-5, SMooHS)

Material	Bulk density [kg/dm ³]	Apparent density [kg/dm ³]	Porosity [Vol.-%]	Water absorption coefficient [kg/m ² h ^{-0.5}]
Brick	1.79	2.33	23.2	7.15

This porous material shows a total porosity higher than the mortar total porosity but with a sharper, narrower pore size distribution (0.3 – 2 μm); thus, the vulnerability to salt decay is almost the same as for the hydraulic mortar (Figure 4.6 left).

The main mineralogical constituents of the brick units were quartz, feldspar (anorthite, microcline/orthoclase), ca-silicates (gehlenite, diopside, wollastonite), and in minor amounts hematite, calcite and dolomite (Figure 4.6 right). From the X-ray diffraction analyses, other considerations are arising: the presence of remaining carbonates means that the firing conditions during manufacturing of the bricks were low to medium temperatures. The knowledge of this latter aspect is very important as the firing cooking temperature of the bricks significantly changes their final chemical and mineralogical composition and thus influences the pores distribution and the value of the characteristic compression strength (Elert et al., 2003; Cultrone et al. 2008).

**Figure 4.6:** New fired-clay brick: pore size distribution (left) and mineralogy composition (right)

Water and brine uptake experiments carried out on the brick units (A.1.16) similar to those reported from the mortar prisms (§4.1.1) highlighted also a decrease in suction velocity with increasing concentration of chloride brines, but with some discrepancies, mainly due to the statistical spread of porosity of bricks (Table 4.9). By comparing the results obtained for the two constituent materials tested, it is noted that the suction velocity determined for the mortar samples was almost 1.6 times higher than for the brick units tested in the same conditions. This lower suction velocity of bricks, evident for all the tested brines, is explicable taking into account the different pore distribution of the two building materials.

Table 4.9: Capillary rise velocity measured in different brick units (A.1.16)

Sample code	Contamination agent	Test duration [h]	Suction velocity [cm/h ^{1/2}]	Capillary suction rate [kg/m ² h ^{1/2}]
1B1	Distilled. Water	168**	3.22	7.47
1B3	NaCl 10% wt	69.5	3.14	7.82
1B4	NaCl 30% wt	168**	2.69	7.42
1B5*	Distilled water	94	3.25	7.54

* previously dried in oven to constant weight ;** this value corresponds to the time at which the operator saw the end of the test and stopped it, not to the real duration

As for the mortar mix, the initial content of salts in new undamaged bricks was determined by means of ion-chromatography analyses. Concentrations of soluble sulphate and calcium ions were found also in this material (Table 4.10, Table 4.11).

Table 4.10: New bricks, concentrations of anions (mg/l) (D5.2-5, SMooHS)

Material	F ⁻	Cl ⁻	NO ₃ ⁻	SO ₄ ²⁻
Brick	<0.01	<0.01	<0.01	0.11

Table 4.11: New bricks, concentrations of cations (mg/l) (D5.2-5, SMooHS)

Material	Na ⁺	NH ₄ ⁺	K ⁺	Mg ²⁺	Ca ²⁺
Brick	0.02	<0.01	0.03	<0.01	0.22

Finally, after non-destructive characterization by ultrasounds (please see §5 for the outcome) uniaxial compression tests on brick cubes (UNI EN 772-1:2002, UNI EN 14580: 2005) were carried out to evaluate the mechanical characteristic behaviour of this material in sound conditions. In detail, the compressive strength f_b , and the modulus of elasticity, E_b , were determined (Table 4.12). A typical testing set-up and resulting stress-strain graph is herein reported (Figure 4.7).

Table 4.12: Mechanical properties of the hardened mortar

Material	f_b [N/mm ²]	E_b [GPa]
Brick	79.96	16.01

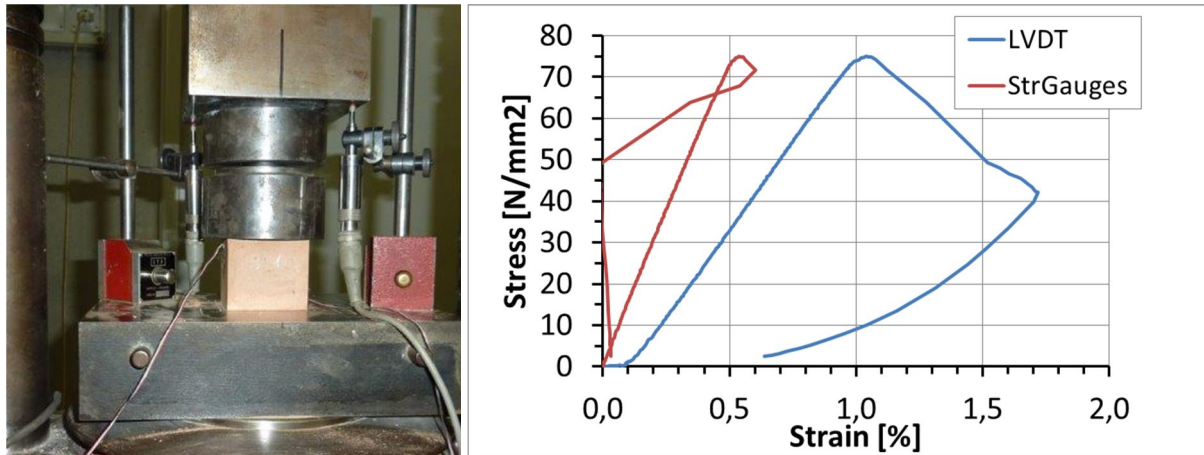


Figure 4.7: Set-up of uniaxial compression test on a brick cube (left) and resulting stress-strain graph (right)

4.2 Single units of construction materials: testing arrangement

In addition to studying weathering in masonry specimens, in the research it was foreseen to undergo single units of construction materials to natural ageing. Therefore, large sets of bricks and mortar prisms were prepared for a total of 103 mortar prisms and 198 fired-clay bricks.

The weathering on these constituent materials was reproduced by means of long-term natural ageing, which consisted in outdoors exposure of the samples together with water or salt solution capillary rise from the base §4.5.

The single units of porous materials were divided into different basins according to the material type and the contamination agent used: water, sodium chloride or sodium sulphate brine. The salt concentrations in the brine are reported in Table 4.13 as a weigh percentage of the solution. The low percentage of salts used are devised to reproduce real general conditions of salt contamination in masonry. Thus, 3 pools for the bricks and 3 basins for the mortars were prepared (Figure 4.8). The bricks were divided into 3 series of 66 units each and the mortars into 3 sets of 30 prisms each. In addition, a 4th set made up of only 13 mortar prisms defined “dry”, was subjected solely to weathering by atmospheric agents, without any damp rise. In the basins, the samples were standing vertically. The plastic basins containing the specimens had sides of limited height to allow maximum exposure to direct sun rays and maximize water/brine evaporation. Throughout each summer, To reproduce the phenomenon of damp rise from the base, a thin layer of about 2 cm, of tap water or salt solution was poured into the different tubs and kept constant as much as possible. In the right climatic conditions depending also on the salt type it was expected that salt crystallization would take place by brine evaporation in the form of efflorescence and sub-efflorescence in the upper part of the specimens. Because of this, at mid-season during each ageing period, all the brick units and mortar prisms were overturned in order to provoke a decay as homogeneous as possible along the specimens heights and allow the formation of salt crystals on both specimen’s heads.

It is to be noted that each year, the outdoors exposition of the single materials units was limited to the summer months, roughly between June and November, in order to reproduce

only the decay caused by salt contaminations and avoid other environmental-related effects such as those caused by freeze-thaw cycles. The natural ageing procedure described in §4.5, was repeated for three summers (2010, 2011 and 2012), which are identified as 1st, 2nd and 3rd ageing season (or year) respectively. At the end of each summer, capillary rise was suspended and the specimens were transported inside the lab and stored in stable, not controlled, environmental conditions until the following summer when after outdoors placement, their capillary suction would newly begin.

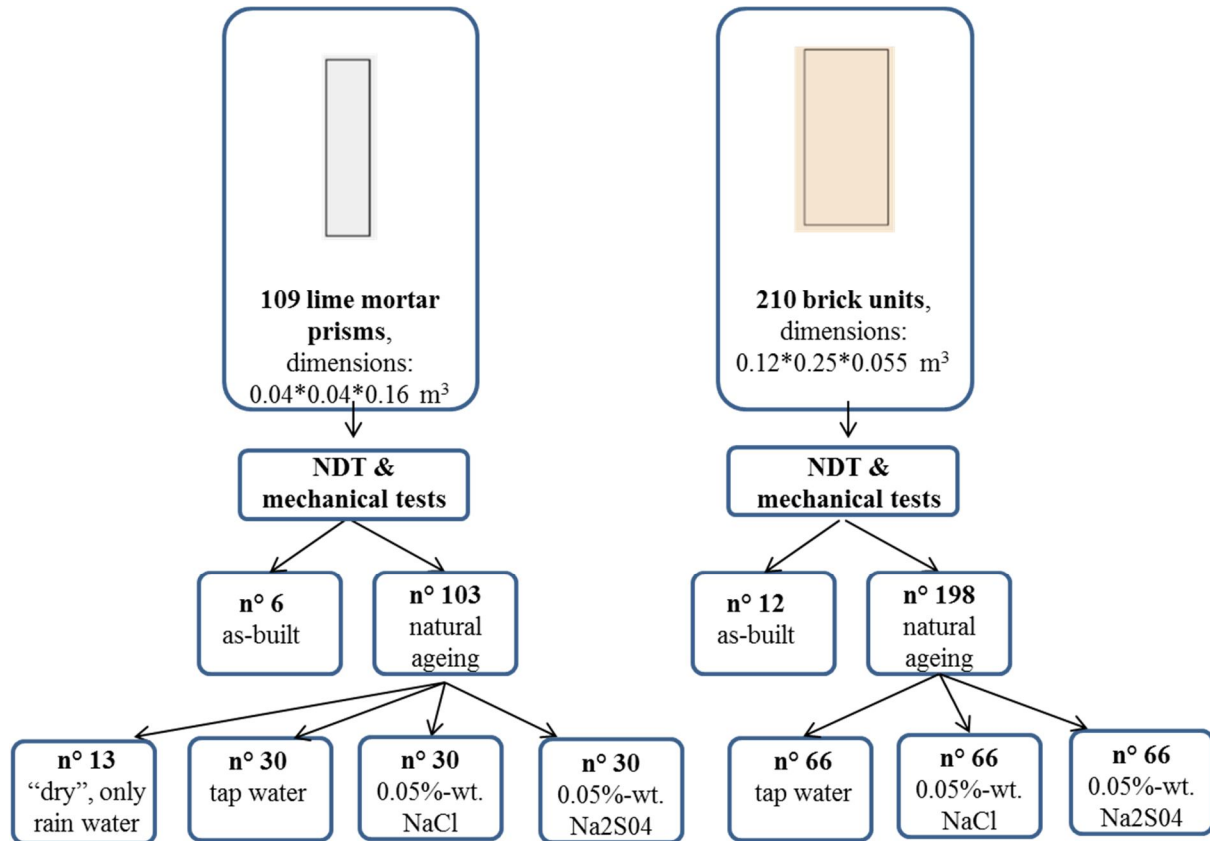


Figure 4.8: Numerosity of the single units for natural ageing

Table 4.13: Numerosity of the series of single units of porous materials subjected to natural ageing and to various contamination agents

Material	Solution			
	Water (H)	NaCl 0.05%-wt (C)	Na ₂ SO ₄ 0.05%-wt (S)	Dry (D)
Brick (n°)	66	66	66	0
Mortar (n°)	30	30	30	13

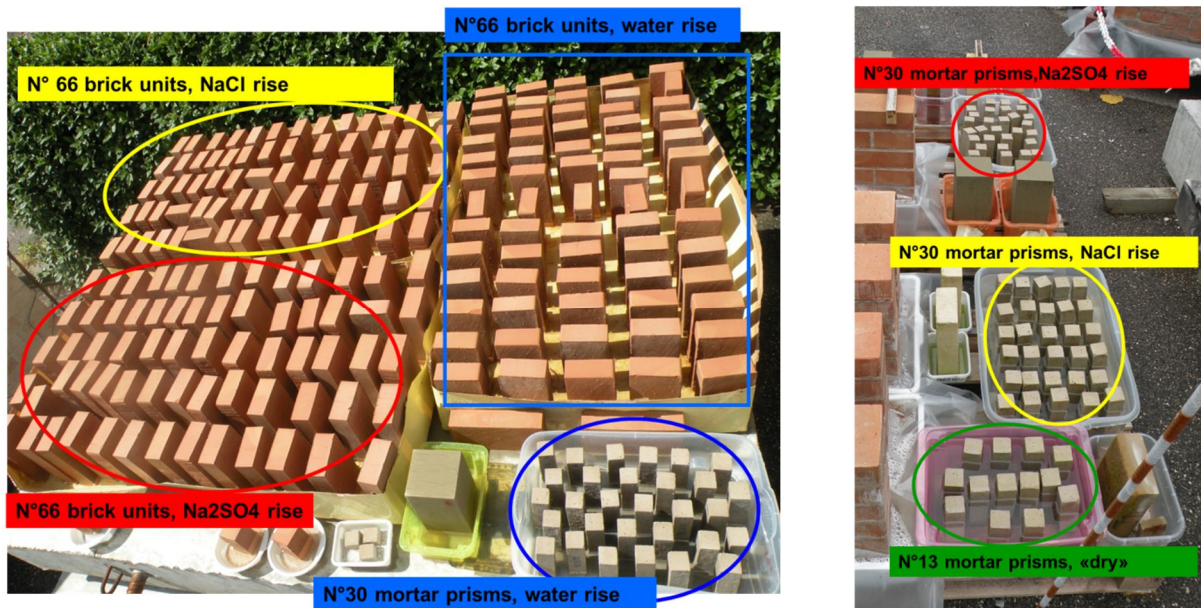


Figure 4.9: Brick units and mortar prisms outdoors exposed; in blue the samples subjected to water rise, in yellow those subjected to NaCl rise and in red the specimens subjected to Na₂SO₄ rise; the “dry” samples are indicated in green.

4.3 Full-scale walls for NDT

Six full-scale brick masonry walls were on-purpose designed and built to study via non-destructive testing techniques the effects of weathering process, simulated by means of a natural ageing procedure (§4.5), on real masonry elements.

These walls were designed taking into account two particular aims: 1) evaluate the feasibility of several non-destructive testing techniques such as sonic tests, IR thermography and GPR radar in qualitatively and quantitatively detecting defects, inhomogeneities, moisture content or decay in the walls caused by ageing; 2) evaluate the ability of the same methods in detecting the beginning of damage and in monitoring over the time the progressive variations in structure and material due to same environmental ageing procedures.

The construction materials used in the six full-scale walls, alphabetically named from PNDA to PNDF, are the same described in §4.2: fired-clay bricks and hydraulic lime mortar (nominal thickness of vertical and horizontal joints, 1 cm). The walls, which are 20 brick courses high present two thicknesses: 2-headers thick -25 cm- (PNDA, PNDB, PNDC) and -3-headers thick -38cm (PNDD, PNDE, PNDF). The two different brick layouts chosen are typically employed in historic and existing brick masonry structures of the Northern and central Italy. All the walls were left unplastered except for the rear face of wall PNDA where for the render (1 cm thick) the same mortar was used.

In the front face of the 2-headers walls, stone inclusions were added during the construction and reached half of the wall thicknesses. These stone units differ in type and origin, varying from the Varignana sandstone of the Bolognese Apennine, to a dolomite limestone from Palestine, Leccese limestone from South Italy and Schilfsandstone from a quarry near

Swabish Gmund – Southern Germany. Instead, in the thicker walls, voids of different depth and lateral dimensions were left and positioned at various heights from the ground and at various depths from the wall front surface. These voids were simulated by means of polystyrene blocks and remain not visible.

The detail geometrical characteristics are reported in Figure 4.10 and

Figure 4.11.

For the purpose of simulating moisture and salt supply at the base of the specimens during a later weathering exposure, the walls were built into metal basins. The basins are part of more complex, on-purpose designed, steel frames in which the basins on one hand support the weight of the walls and on the other hand contain water or salt solutions to be added for simulating the capillary rise phenomenon. Thus, these basins are slightly larger than the brick wall base areas but of limited height to allow water evaporation (dimensions l x w x h: 160 x 60 x 10 cm³). They were lined with a waterproof and acid proof sheet, few millimeters thick, as a protection to the metal and separation between metal and masonry. Moreover, the basins were equipped below with four castor wheels to allow the movements of the walls which were intended to be stored outside the lab after a proper period of curing indoors. In addition to the basin, each steel frame consisted in a superior plate, designed to protect the top part of the walls from rain water intrusion, and in two vertical metal tie bars to connect top and bottom plates with eyelets as extra rigid transportation possibility (Figure 4.12).

In June 2010, after approx. 4 months of curing indoors, the six walls were moved outside the lab, in a dedicated area, to be exposed to the real microclimatic conditions of Bologna. This outdoors exposure continued up to now. In this thesis, only the outcome of the first 3 years (2010-2012) will be reported. The wall main face was South-oriented in order to receive direct sun rays. Some space was left between the walls to allow the movements of the operators which would perform NDT and other tests.

As stated before, the walls were intended to be subjected to the brine damp rise phenomenon in addition to the effects caused by this outdoors exposure, including rain water. For the capillary rise simulation, two different salt types were considered. The salts were chosen among the most common and damaging salts for existing masonry structures: sodium chloride and sodium sulphate (§2.3). For both salt solutions, two low concentrations (0.05% and 0.1%-wt.) were selected with the aim of obtaining salt contents similar to those present in low-salinity groundwater. Thus, two walls (PNDA and PNDB) were undergone to NaCl contamination and two (PNDD and PNDE) were undergone to Na₂SO₄ contamination. The two remaining walls were used as “references”: one was subjected to rain water only (PNDC, 25 cm thick), while the other was regularly supplied with tap water (PNDF, 38 cm thick) (Figure 4.13)

Capillary rise was performed on these walls only during the warm season. For the rest of the year, the basins were drained and the walls were covered with water-proof sheets to avoid rain, snow and ice to cause other types of damage to the specimens. This continuous outdoors

storing was compulsory because of difficulty in repeated transport of these large elements between in and out of laboratory which would have required a vehicle with crane.

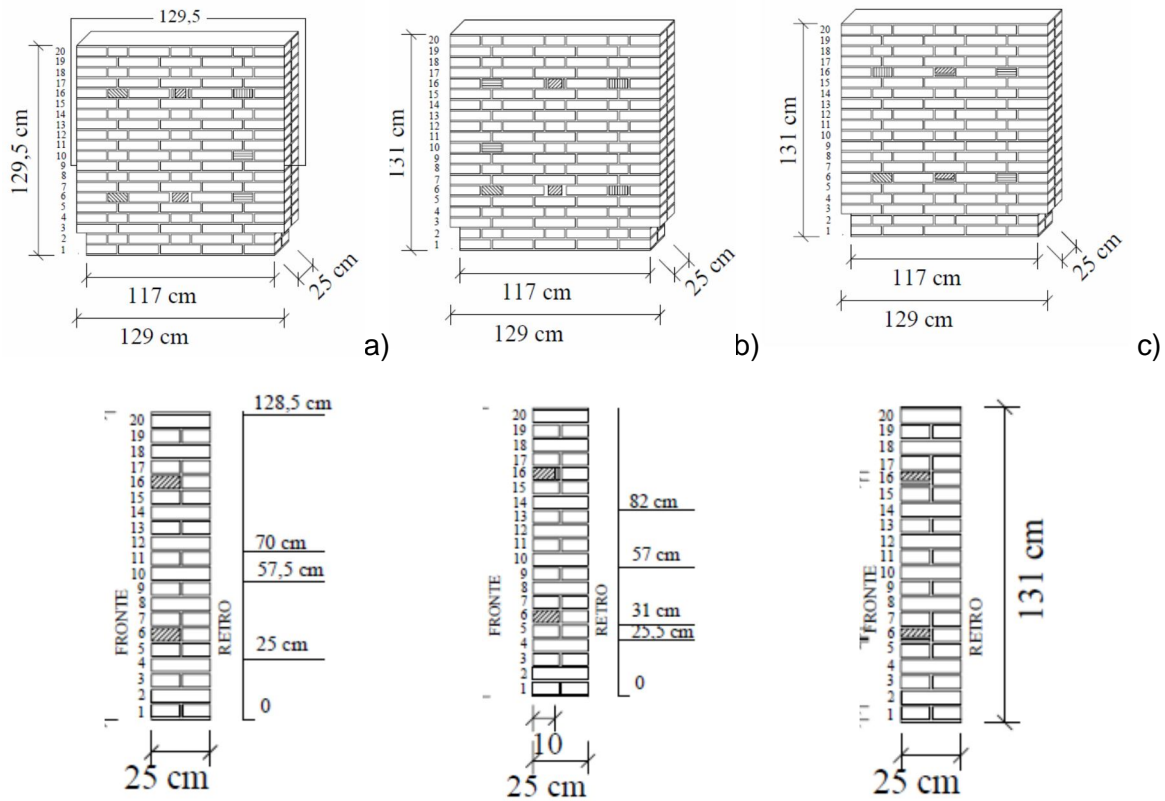


Figure 4.10: Full-scale 2-header walls brick masonry walls, with stone inclusions. From left to right side PNDA, PNDB, PNDC: wall masonry layouts (top) and vertical centre sections (bottom)

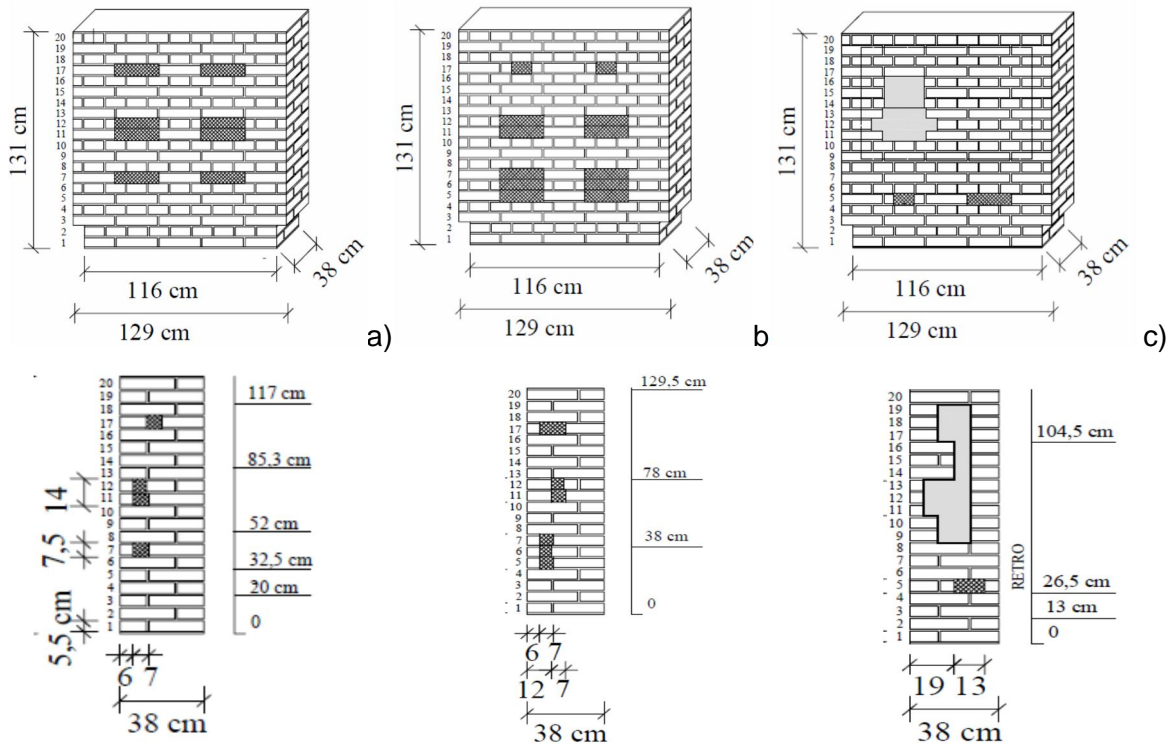


Figure 4.11: Full-scale 2-header walls brick masonry walls, with voids inclusions. From left to right side PNDD, PNDE, PNDF: wall masonry layouts (top) and vertical centre sections (bottom)



Figure 4.12: Steel metal tub with black waterproof and acid-proof lining for later pouring of the brine (left), manufacturing of one brick course in wall PNDE with 2 voids simulated by polystyrene blocks (left side).

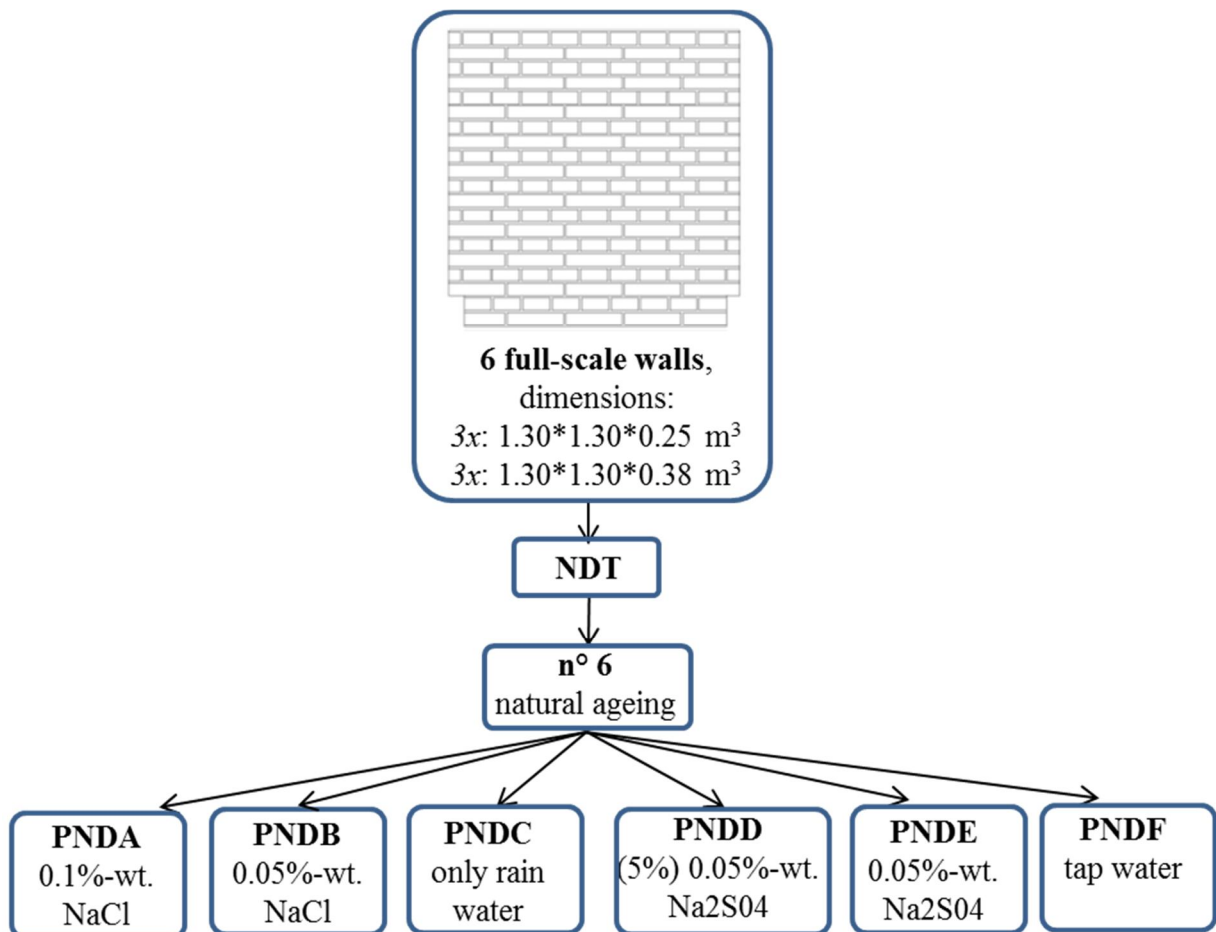


Figure 4.13: Full-scale walls, natural ageing procedure

4.4 Small walls and masonry assemblies for mechanical testing after natural and accelerated ageing

To evaluate the effects of weathering simulated by means of natural (§4.5) or accelerated (§4.6) ageing procedures on the mechanical properties of masonry structures, additional sets of specimens of limited dimensions were designed and built with the same porous construction materials. Overall, 12 one-header small walls, 36 six-brick columns and 24 triplets were realized (

Figure 4.15).

4.4.1. Masonry wallets

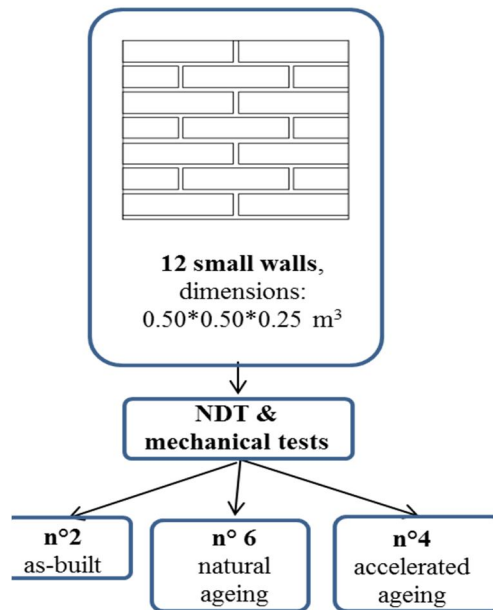
The 12 small walls are made of 7-brick courses, one-header thick (12 cm) and were designed to be undergone to uniaxial compression tests. Prior to be evenly loaded, they were subjected to different ageing treatments. Thus, the mechanical tests were carried out in order to assess the variations of the characteristic compressive strength of masonry at varying levels of environmental decay. These small walls were divided into 3 subsets: the 1st was made of two wallets in sound conditions to be used as reference, the 2nd set included 4 specimens designed for the accelerated ageing treatments and the last set was composed of 6 wallets, intended to undergo natural ageing treatments. They were numbered by using Roman numeral, from I to XII (Table 4.14).

The small walls of the 2nd subset, after a period of curing in stable environment (into the lab) were placed outdoors, in 3 different plastic basins (in pairs). Two were to be contaminated with water, two with NaCl (0.05%-wt.) and two with Na₂SO₄ (0.05%-wt.)

As for the single units of masonry materials the plastic basins were of limited height to facilitate the sun exposure and water evaporation.

Instead, the 2nd set of 4 small walls were subjected to a diverse number of accelerated ageing cycles simulated by means of a complete immersion in high-concentrated sodium sulphate solution followed by an on-purpose designed treatment in climatic chamber (§4.6). These wallets, after the constructions were mounted into steel frames, later described, and realized to facilitate their movements.



Figure 4.14: Manufacturing of small walls of nominal dimensions 50 x 12 x 50 cm**Figure 4.15:** Numerosity and set-up of the series of small walls**Table 4.14:** Subdivision of the small walls for NDT and mechanical tests

Specimen code	Ageing treatment	Salt solution
I	None, as-built	/
IV	None, as-built	/
II	Accelerated ageing	Na ₂ SO ₄ 10%-wt.
III	Accelerated ageing	Na ₂ SO ₄ 10%-wt.
V	Accelerated ageing	Na ₂ SO ₄ 10%-wt.
VI	Accelerated ageing	Na ₂ SO ₄ 10%-wt.
VII	Natural ageing	Tap water
VIII	Natural ageing	Tap water
IX	Natural ageing	NaCl 0.05%-wt.
X	Natural ageing	NaCl 0.05%-wt.
XI	Natural ageing	Na ₂ SO ₄ 0.05%-wt.
XII	Natural ageing	Na ₂ SO ₄ 0.05%-wt.

4.4.2. Masonry assemblies: columns and triplets

The six-brick columns and triplets were designed exclusively to undergo accelerated ageing treatments and later being subjected to compression or shear tests respectively. They were professionally realized with units of fired-clay bricks and 1cm thick lime mortar joints, according to the indications reported in (20-21).

After a 28 days of curing in stable but not controlled environmental laboratory conditions, the masonry assemblies were directly mechanically tested or prepared for the accelerated ageing

procedure. Indeed, these specimens were divided into 4 subsets, each of them composed by 9 columns and 6 triplets. The 1st set, indicated as “0”, was used to determine the reference, characteristics mechanical properties of the masonry and thus, all the specimens were in their as-built, sound conditions when subjected to the corresponding mechanical test. Instead, the other three sets were decayed by means of a different number of repeated accelerated ageing cycles consisting in full immersion into a high-concentrated sodium sulphate solution and treatment in climatic chamber (more detail are reported in paragraph §4.6).

The number of assemblies considered to prepare each set was chosen in function of the organized mechanical tests, in order to have at disposal, for each experiment, a representative number of specimens. In detail, the 9 six-brick columns of each subset were intended to be tested at compression, applying a concentrated load at three different eccentricities (3 specimens for type of tests) while the number of triplets (6 per set) used to evaluate the masonry shear strength was chosen according to [20].

Furthermore, it has to be reminded that, in this case, the design phase has then foreseen the design and construction of light but resistant steel frames to ease the movements of the specimens placed in vertically (from the tubs to the climatic chamber and vice versa) during the ageing treatment. These frames were made of a rigid base realized with two metal strips to support the weight of each six-brick column or triplet without preventing the brine absorption from their bases and a removable structure realized with two Φ 6 steel elbow pipes (Figure 4.17).

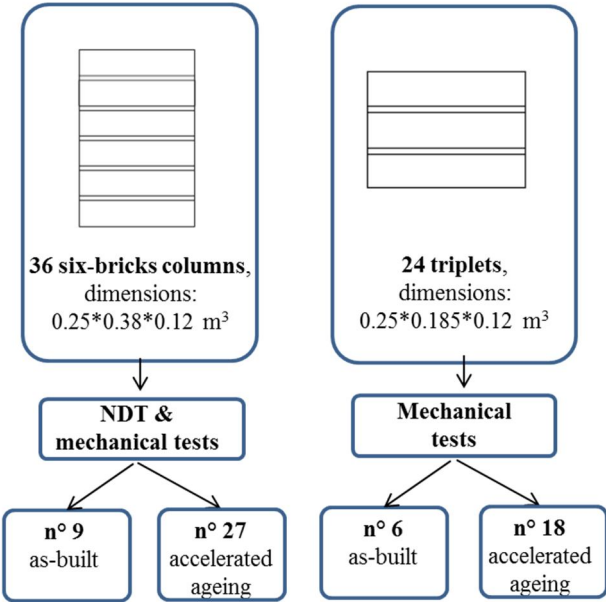


Figure 4.16: Numerosity and set-up of the series of columns and triplets

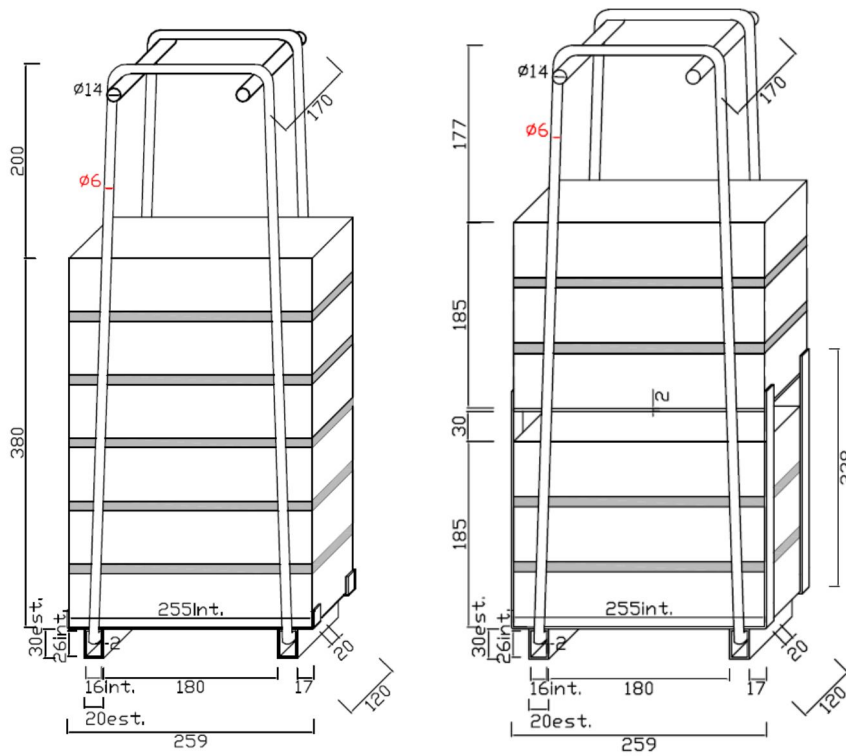


Figure 4.17: On-purpose realized steel frame for six-brick columns (left) and triplets (right)



Figure 4.18: Phases of the construction of six-brick columns (left) and triplets (right)

4.5 Procedure for natural ageing

The so-called “natural” ageing procedure consisted in the outdoors exposure and simulation of capillary rise from the base by means of water or low-concentrated brines (sodium chloride and sodium sulphate). The salt solutions were prepared with the tap water of the Bologna aqueduct.

In order to reproduce only the decay caused by salt contaminations and avoid other effects such as those caused by freeze-thaw cycles, the outdoors exposition of the walls and samples has been limited to the summer months, roughly between June and November each year and it has been repeated for three years (2010, 2011 and 2012).

In the following sections these periods are called, respectively, 1st, 2nd and 3rd ageing seasons. During the three ageing seasons, the amount of brine into the tubs, prepared by using tap water, has been kept constant at a level of about 2 cm.

This thin layer of solution allowed the capillary rise from the base and, during evaporation, in certain microclimatic conditions depending also on the salt type, the crystallization of salts on the upper part of the specimens themselves.



Figure 4.19: General view of the outdoor exposed full-scale walls

Monitoring of the microclimatic conditions

It is known from literature that the effects of the natural ageing in porous building materials (§3.2) and their evolution over time, are the results of a complicated interaction between the materials themselves and the specific microclimatic conditions to which they belong. Thus, the boundary thermodynamic conditions characterizing the environment surrounding the tested materials are to be known in order to fully understand the existing weathering mechanisms. In this case, the daily climate parameters (min, max and average air temperature and average relative humidity) were collected partly from the meteorological station at Borgo Panigale, located 5 Km away from the laboratory, and partly from a wireless monitoring system installed on one large wall, placed near the tubs containing the single material units [10]. Additionally, thanks to the collaboration with the LIDR laboratory of the University of Bologna, the rainfall was monitored by a rain gauge (ISCO 6712, ± 5 ml repeatability) installed on the laboratory roof; this parameter is important to discriminate between days in

which the salt crystallization is allowed or not. The average daily values of air temperature, relative humidity and rainfall are reported in Figure 3 for the 3 ageing seasons.

These parameters are important to roughly estimate the number of possible salt hydration/crystallization cycles occurred in the different time periods and thus to better understand the evolution and appearance of the degradation processes. This estimation, however, could be done only after having established the critical conditions, at least in terms of air temperature and relative humidity, which cause the crystallization of the two different salts considered in this study. At this purpose, different research studies were already carried out with reference to either sodium chloride or sodium sulphate. From the literature review [4, 16, 17], it appears reasonable to set the following threshold: air temperature above 20°C and RH below 75%, as critical conditions for the crystallization of sodium chloride. As the main cause of degradation in presence of sodium sulphate, has been demonstrated to be the change from mirabilite ($\text{Na}_2\text{SO}_4 \cdot 10\text{H}_2\text{O}$, large crystals) to thenardite (Na_2SO_4 , small and compact crystals) [18, 19], the critical conditions have not been defined as a fixed threshold but as those values of air temperature and relative humidity which allow the passages between these two phases of the salt, by using the diagram of Steiger [20], as already shown in [11].

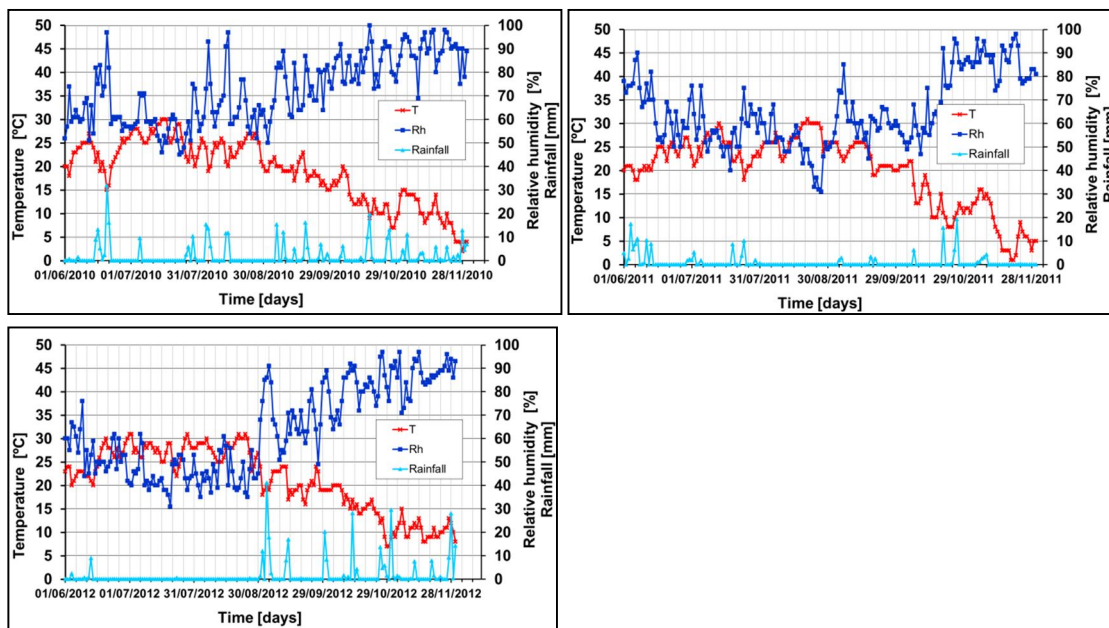


Figure 4.20: Environmental parameters monitored during the 1st (top, left), 2nd (top, right) and 3rd ageing season (bottom)

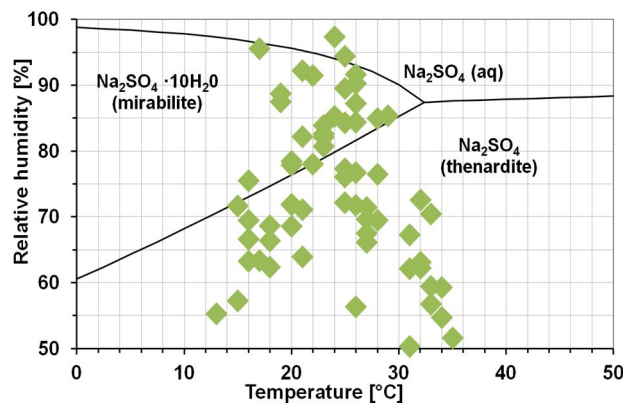


Figure 4.21: Example of calculation of occurred phase changes of sodium sulphate (20th July – 20th September 2010) (after Steiger 1996, modified)

According to the previous statements, the monitored climatic data were elaborated to determine the number of crystallization cycles for each salt and each ageing season, considering the real number of days of outdoors exposure of the brick and mortar samples and the numbers of rainy days and amount of rainfall. Moreover, each day with favourable conditions to the salt crystallization has been counted a single crystallization cycle in order to take into account the disappearance of that conditions during the night due to the daily fluctuations of the environmental parameters considered. These estimated values have been then reduced to a half considering the fact that the specimens have been overturned during each ageing season (Table 4.15). This evaluation clearly indicates that the specific environment chosen, that is the microclimate of Bologna, is always more favourable to the crystallization of sodium chloride than to the crystallization of sodium sulphate, and the difference was more pronounced in the 2nd ageing season.

Table 4.15: Number of possibly occurred salt hydration/crystallization cycles in the three summers (referred to single units of building materials)

Type of salt	1st ageing season, 2010	2nd ageing season, 2011	3rd ageing season, 2012
Sodium chloride	38	117	112
Sodium sulphate	33	41	83

4.6 Procedure for accelerated ageing

Laboratory accelerated ageing tests were carried out on some masonry wallets, six-brick columns and triplets (§4.4) in order to reproduce the decay due to salt contamination in masonry, on a shorter time period than the one necessary for the natural ageing. Overall, 4 wallets, 27 columns and 18 triplets, were divided into 3 series and tested in order to obtain three different levels of decay.

The testing procedure was accurately designed taking into account the testing aims, the specimens dimensions and the laboratory facilities and constraints. These tests consisted in a time period of full immersion of the specimen in a high-concentrated sodium sulphate solution (10% -wt.) followed by a drying treatment in climatic chamber; the duration of each phase as well as the values of air temperature and relative humidity inside the chamber were chosen in order to accelerate the ageing process by maximizing the number of phase changes of the specific salt, chosen due to its damaging nature towards porous materials, well-known from literature (§2.3).

As there was a lack of suitable standard procedure to be followed, an on-purpose procedure was developed. Anyhow this was influenced by existing guidelines related to accelerated tests on single units of porous materials

Some numerical simulations were also carried out in order to define the boundary conditions able to maximize the formation of mirabilite crystals [22]

Thus, the single cycle of the accelerated ageing test proposed, consisted in a short-time bath in solutions followed by .. hours of treatment in climatic chamber:

- 3 hours of total immersion in high-concentrated sodium sulphate solution;
- 8 hours of heating, changing gradually the air temperature from 20°C to 60°C and decreasing the relative humidity until the 15%;
- 18 hours at constant temperature (60°C) and constant relative humidity (50%);
- 8 hours of cooling, reducing gradually the air temperature from 60°C to 20°C at the same constant RH;
- 4 hours of final cooling by switching off the climatic chamber.

Instead of considering a 41 hours-cycle, the duration of the single cycle was established in 43 hours because 2 additional hours were added for the relative movements of the masonry assemblies, performed by means of a forklift, thanks to the aid of the steel frames. In detail, 1 hour after the end of the immersion phase was considered to let the specimens dry before inserting them into the climatic chamber, and 1 hour at the end of the treatment in climatic chamber, before starting again the immersion, was considered to have time to perform visual inspections and collect photographic documentations.

This cycle was repeated several times to obtain a different decay: 18, 28 or 38 times for the 2nd, 3rd and 4th series of masonry assemblies respectively (**Errore. L'origine riferimento non**

è stata trovata.) Each series, as explained in §4.4, was composed by 9 columns, 6 triplets and 1 wallet, with the exception of the 3rd (2 wallets).

To allow the complete immersion of the specimens, two plastic tanks of internal dimensions (b x l x h) 100 x 60 x 80 cm³ were used, placing half of the steel frames into one tub and half into the second. The salt solution was prepared with tap water .

After the immersion and the drain phases, the specimens were inserted into the climatic chamber available in the lab. This was an “Angelantoni” of dimensions 140 x (150h x 100 depth cm³ range -20°C + 60°C. RH 0-100% (door open) In order to limit the salt dispersions into the testing machine, the frames were not put in contact directly with the plates of the machine but positioned into two thin steel basins, on-purpose inserted.

To monitor the appearance and evolution of decay, the 16 specimens of each series were visually inspected, roughly every 2/3 cycles and the damages, in terms of cracks, salt deposition, types of salts efflorescences were recovered in hand- made notes and photographically documented by means of a Nikon Coolpix digital camera

This procedure allow detecting the appearance of salt efflorescences on both bricks and mortar joints as well as degradation. Diverse salt efflorescences where noticed (varied from soft to hard). Evident decay appeared since the first cycles of ageing as brick delaminations, pitting, formation of cracks (or development of existing cracks) and material losses

At the end of the ageing tests, a crack pattern survey was performed and prior to the execution of the mechanical tests Main aim of this survey was to estimate the amount of decay caused by accelerated sgeing treatments



Figure 4.22: Tanks for the complete immersion of the masonry assemblies (left) and positioning of six-brick walls into the tanks.



Figure 4.23: Climatic chamber used for the accelerated ageing tests



Figure 4.24: Appearance of a six-brick column at the end of

5. Non-destructive and mechanical evaluation of natural weathering in single units of masonry components materials

This chapter reports on the results of the monitoring of simulated weathering processes on single units of masonry building materials and on the evaluation of their effects and evolution over time.

Two porous construction materials were considered: fired-clay brick units and lime mortar prisms (§4.1). Overall, 198 bricks and 103 mortar prisms exposed outdoors to real weather and additionally subjected to water or low-concentrated brine capillary rise were studied over three summers (2010-2011-2012). Thus, the reproduced ageing of the materials is in reality the combination of 1) a natural, outdoors exposure to real weather, but only during the “summer” season (to introduce moisture evaporation and damage by salt crystallization but to avoid damage by freezing-thaw cycles), including rain water and 2) “artificial” water/brine suction from the specimens’ base, thanks to solutions frequently provided to the specimens’ containers. Notwithstanding this second point, in this thesis, this weathering procedure is defined as “natural” to distinguish it from the accelerated ageing of other series of masonry specimens (see chapters 8 and 9), defined as artificial ageing.

The specimens were divided into different series according to the material type and the contamination agent used to reproduce the capillary suction from the base: water and sodium chloride or sodium sulphate brines at 0.05% -wt. concentration. Hence, 3 basins for the bricks and 3 basins for the mortars were prepared. In addition, a 4th set of mortar prisms was considered. It was defined “dry” as these samples were subjected to outdoors exposure only, without the addition of any solution to simulate the brine rise.

The two types of brines considered were chosen because recognized as common damaging agents for masonry structures which are usually present i.e. in the groundwater or in the environment. Similarly, the very low concentration of the same two solutions was selected because it is comparable to the one characterizing limitedly salted groundwater (§4.2)

The spread and effects of the diverse natural ageing contaminations on the characteristic physical and mechanical parameters of the materials were investigated by means of visual and photographic inspections, non-destructive and mechanical or destructive tests, repeated at the end of each ageing season (**Errore. L'origine riferimento non è stata trovata.**).

The various testing procedures followed, as well as the testing equipment and set-ups are presented first with reference to the mortar prisms and then to the fired-clay brick units. In addition, the main observations and results are reported and finally compared and discussed.

Table 5.1: Numerosity distribution of the mortar units per year

Material (initial number of units)	Ageing season	Brine			
		Dry (rain water only)	Water	NaCl 0.05%-wt	Na ₂ SO ₄ 0.05%-wt
Mortar prims (103)	1 st year	13	30	30	30
	2 nd year	13	30	30	30
	3 rd year	10	24	24	24
Brick units (198)	1 st year	/	66	66	66
	2 nd year r	/	66	66	66
	3 rd year	/	60	60	60

5.1. Mortar prisms: results of the long-term monitoring

Repeated non-destructive and mechanical tests were carried out to check over the time the variations on the appearance and on the properties of the 4 sets of hydraulic lime mortar prisms during ageing. Before these tests, the samples were conditioned to the same moisture content and visual, gravimetric and dimensional surveys were undertaken. Thus, these results are first described. Following, the non-destructive and main mechanical procedures and outcomes are reported.

5.1.1. Visual inspection

Visual inspections and photographic observations were repeated periodically during the four years of weathering in order to monitor the visible changes in appearance of the mortar prisms at the surface.

Since the very beginning of the ageing, some effects of brine evaporation, in terms of colour changes and superficial deposition were clearly visible on the three sets of mortars subjected to water or salt capillary rise, while they were less evident on the “dry” prisms, which were exposed outdoors without any addition of liquids except rain.

As an example, from the photos taken 1 month after the beginning of the ageing procedure, colour changes were already well visible (**Errore. L'origine riferimento non è stata trovata.**). The colour variations of the mortar prisms' surfaces allow to distinguish the wet areas (darker areas) as well as the level at which brine evaporation occurred. At this level, in the upper part of the specimens, salt crystallization in the form of efflorescences, appeared as white superficial depositions. These were more evident on the top corners of the prisms contaminated with sodium sulphate than with sodium chloride. Nonetheless they were recognizable also in the prisms in contact with tap water because of the percentages of salts contained in it (§4.2). The greater amount of salt depositions visible on the samples contaminated with sulphates suggests that the climatic conditions were more favourable to the occurrence of sodium sulphate efflorescences than sodium chloride's.

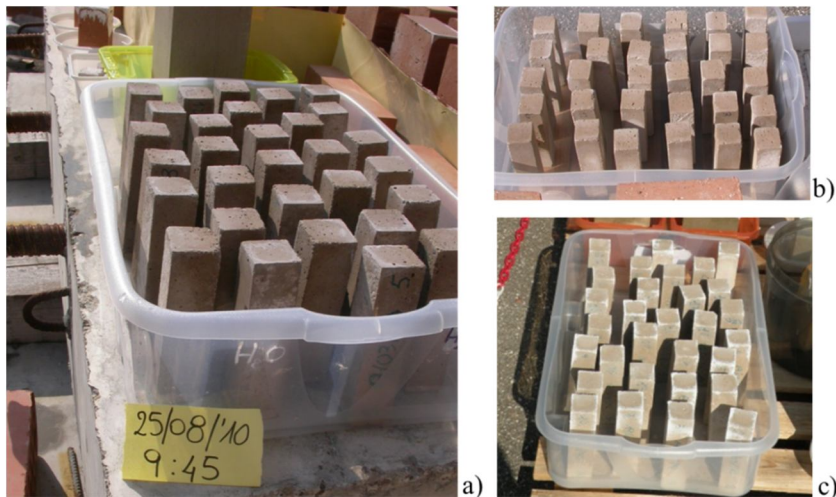


Figure 5.1: Mortar prisms appearance in a morning of an August day during the 1st ageing season: a) water contamination, b) sodium chloride, c) sodium sulphate

With the passing of time, on all the sets of mortar prisms, other effects of the weathering process started to appear. These were mainly surface discoloration, powdering, scaling, surface erosion as well as material losses. The latter effect was testified by the substantial amount of dust collected from the basins bottom at the end of each ageing season (§5.1.2). Nonetheless, the spreading and seriousness of the decay effects was different for the different sets of prisms. As a further example, the “dry” mortar prisms appeared the healthiest after 3 ageing seasons, followed by those subjected to water rise (Figure 5.2). On the contrary, the prisms contaminated with sodium chloride brine were more degraded than those in contact with sodium sulphate brine (Figure 5.3, Figure 5.4). This is in line with the estimations made from the monitoring of real environmental conditions about the possible number of salt crystallization cycles occurred for the two types of salt considered (§4.4): over the whole ageing period of three summers a number of sodium chloride crystallization cycles almost double than for sodium sulphate was estimated (133.5 cycles vs. 78.5).



Figure 5.2: Visual decay on mortar prisms during the 3rd ageing season: dry (left) and water (right)



Figure 5.3: Visual decay on mortar prisms during the 3rd ageing season. Sodium chloride contamination: general view (left) and detail (right)



Figure 5.4: Visual decay on mortar prisms during the 3rd ageing season, subjected to sodium sulphate rise: general view (left) and detail (right)

The effects of the natural ageing continued to spread and became really pronounced at the end of the 3rd ageing season, as testified by new detailed photos (Figure 5.5). Both mortar prisms reported in these images, each contaminated with one of the two salt solutions, showed evident signs of degradation especially on their top and bottom faces, see §4.2. These faces appeared rougher than the lateral faces and with smoothed angles caused by consistent material loss. At this time period, salt efflorescences, visible as soft white depositions, and material powdering were visible only on the top surface of the mortar prism subjected to sodium sulphate contamination (Figure 5.5 b).

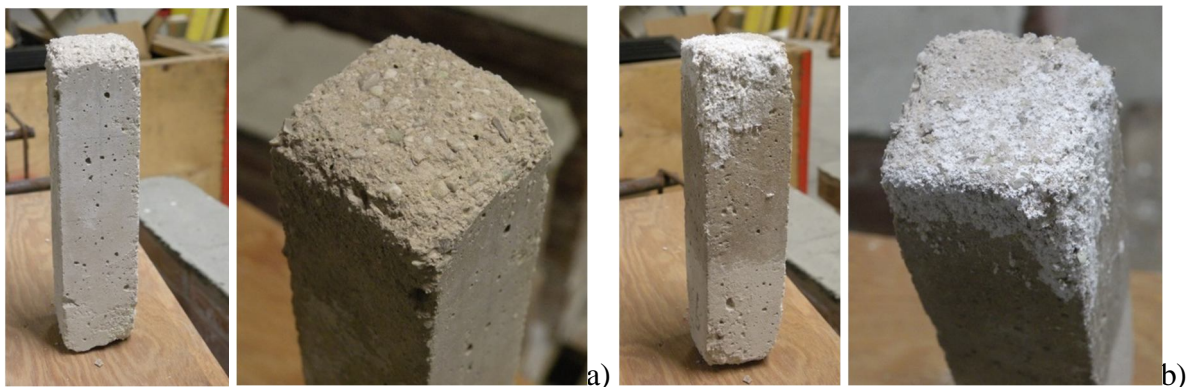


Figure 5.5: Lateral and top face of one mortar prism subjected to sodium chloride (a) and one to sodium sulphate rise (b) rise after 3 ageing seasons

5.1.2. Gravimetric and dimensional analysis

The visual observations showed that material losses were one of the major and more evident effects of the natural ageing process to which the mortar prisms were undergone. In order to quantify this degradation, a simple procedure was derived. It consisted on one hand, in collecting and weighting the powder recovered from each of the 4 basins' at the end of each ageing season and on the other hand, in measuring the dimensions and weighting all the mortar prisms contained into each basin at the same time period.

Preliminarily to these recognitions, after having interrupted the ageing process of the mortars before winter (§4.5), the prisms were stored indoors for at least one month, and finally in a stable environment ($T \sim 22^{\circ}\text{C}$, $R_H \sim 40\%$) for a few more days. Specimen' dimensions for each prisms were obtained as the average value of two measurements across the 3 directions by means of a digital calliper with accuracy of ± 0.01 mm. The single samples weight was recorded by using a digital scale with accuracy of ± 0.1 g.

The values of mass and volume calculated at the end of each summer and the corresponding density are reported for each set of mortar prisms (Table 5.2 to Table 5.4). Among these 3 parameters, the more reliable appears to be the mass as it refers to the whole mortar prism. On the contrary, the parameter most affected by error seems to be the volume given that, although the measurements of dimensions were accurate, they are punctual values and the material loss from the prisms edges is unaccounted for. As a consequence, a certain level of uncertainty has to be expected in the values of density.

Table 5.2: Mortar prisms, average values from gravimetric and dimensional analysis at the end of the 1st season

	Dry	H2O	NaCl	Na2SO4
Mass [g]	500.1	511.4	501.6	513.4
Volume [mm ³]	248928.2	250163.0	248485.3	253030.5
ρ [Kg/m ³]	2009	2044.3	2018.6	2029

Table 5.3: Mortar prisms, average values from gravimetric and dimensional analysis at the end of the 2nd season

	Dry	%	H2O	%	NaCl	%	Na2SO4	%
Mass [g]	500.2	0.02	511.9	0.10	503.1	0.30	513.2	-0.04
Volume [mm ³]	249192.1	0.11	247335.3	-1.13	246101.3	-0.96	251460.8	-0.62
ρ [Kg/m ³]	2007.3	-0.09	2069.7	1.24	2044.3	1.27	2040.9	0.59
Lost mass [g]	0.47		0.42		0.50		0.93	

Table 5.4: Mortar prisms, average values from gravimetric and dimensional analysis at the end of the 3rd season

	Dry	%	H2O	%	NaCl	%	Na2SO4	%
Mass [g]	504.6	0.89	516.5	0.99	505.9	0.86	514.1	0.13
Volume [mm ³]	249193.5	0.11	252081.8	0.77	249482.5	0.40	252956.3	-0.03
ρ [Kg/m ³]	2025.4	0.82	2048.9	0.22	2028.1	0.47	2032.1	0.15
Lost mass [g]	0.28		0.43		4.31		2.87	

In addition to those 3 parameters, for the 2nd and 3rd ageing season only, the average amount of lost material per specimen is shown. These figures were determined by dividing the total mass of dust recovered into each basin by the number of prisms contained inside (Table 5.3, Table 5.4). By looking at the single parameter changes with increasing ageing, some values seem contradictory, i.e. the comparison of mass with material loss.

As described earlier (§4.2), prior to begin the ageing process, the reference average value of such physical characteristics were determined on a limited number of prisms in their as-built undamaged conditions. Thus, the values from ageing can also be compared with the reference conditions.

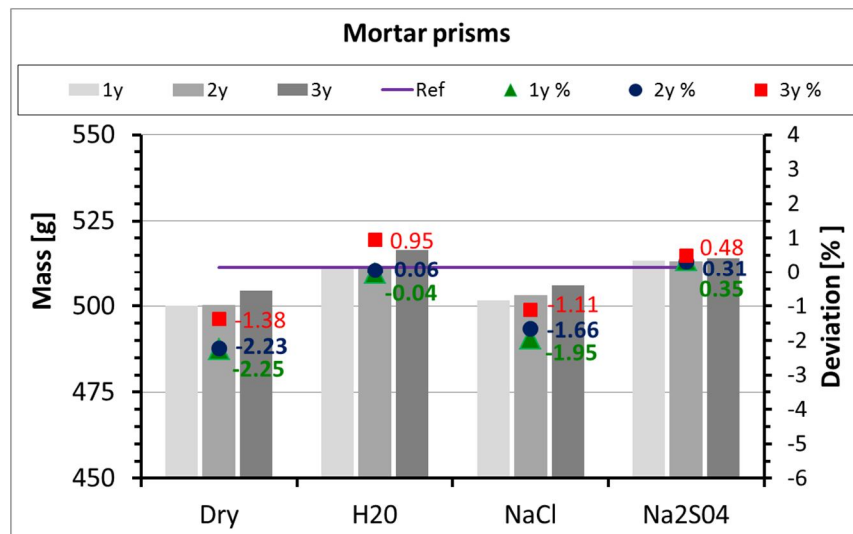


Figure 5.6: Mass variations on the 4 sets of mortar prisms at the end of each ageing season. The reference mass value measured on as-built specimens is reported as a violet continuous line and the deviations from this values is reported in %.

By looking at mass variations and taking into account the corresponding reference value, some differences are evident (Figure 5.6).

At the end of the first ageing season, the average weights of the different sets of mortar prisms were equal or lower than the reference weight. Then, all 4 sets of mortar prisms showed a slow increase in weight with increasing levels of ageing. Considering that powdering and blistering areas in specimens were clearly detected and a consistent amount of material dust was collected into each basin at the end of the seasons, this measured increasing trend, was unexpected. It may indicate that the air in the material pores was partly but increasingly

replaced by new matter, i.e. salts, which were introduced through the capillary rise process (including salts dissolved in the tap water) (§4.2.1). These salts, including sodium chloride and sodium sulphate, in their specific favourable microclimatic conditions will have deposited and crystallized within the prisms and this has probably caused the weight increase. Thus, the salt enrichment has influenced the mass values and partly hidden one of the most serious effects of the weathering decay process that is the weight loss due to powdering of the external layers of the mortar prisms. Hence, the variations of weight and dimension recorded at different ageing periods are still an index of the on-going deterioration process, but they are due to a combinations of two contrasting effects: enrichment of salts within the material pores together with loss of decayed material.

The weight changes of the mortar specimens are different according to the diverse contaminations undergone by the samples. The specimens belonging to the “dry” series, which underwent degradation by environmental agents only, resulted the lightest at the end of each ageing season while the heaviest specimens were from the series contaminated with sodium sulphate. This is well explainable considering the weight of salt crystals (§4.1.3): indeed sodium sulphate (142.02 g/mol; $\rho=2.66 \text{ g/cm}^3$) is heavier than sodium chloride (58.44 g/mol; $\rho=2.16 \text{ g/cm}^3$)! [ref.].

With the aim of determining the progress velocity of the decay process and the level of contamination reached [1, 2], the information recovered from the gravimetric and dimensional analyses was also associated with the calculated number of salt hydration/crystallization cycles occurred during each summer. As explained in §4.5 and summarized here for convenience, these numbers were roughly estimated taking into account the local climate conditions, in terms of air temperature and relative humidity, the critical crystallization conditions in terms of the same microclimatic parameters for each type of salt considered and the number of days of outdoors exposure of the samples. To perform a simple but as precise as possible estimation, another assumption was made, despite considering each favourable crystallization day as a single crystallization cycle: the estimated number of cycles was reduced to half due to the overturning of specimens performed at mid-season in order to obtain a uniform decay distribution (Table 5.5). These results show that in the specific microclimate considered, the summers’ weather was always more favourable to the crystallization of sodium chloride than to sodium sulphate and the greatest difference was recorded for the second ageing season (summer 2011). This is in line with the greater weight decrease detected for the prisms contaminated with sodium chloride.

Table 5.5: Number of possibly occurred salt hydration/crystallization cycles, mortar prisms

	1 st season, 2010	2 nd season, 2011	3 rd season, 2012	Tot
NaCl	19	58.5	56	133.5
Na₂SO₄	16.5	20.5	41.5	78.5

FINO QUI

Instead, with reference to the density, values greater than the reference one are measured at the end of each ageing season, for all the sets of mortar prisms (Figure 5.7). Throughout the natural ageing process, the samples subjected to water capillary rise appeared always more consistent than all the others, while the lightest mortar prisms were those belonging to the dry set. Instead, the samples of the two sets subjected to brine damp rise with two different salts presented the approximately the same consistency.

Looking at the same data for the different seasons, a density increase from the 1st to the 2nd year is measured for the majority of the mortar samples, followed by a decrease from the 2nd to 3rd one. This latter aspect, combined with the mass increase detected before, indicates a volume decrease caused by the huge loss of material from the external layers.

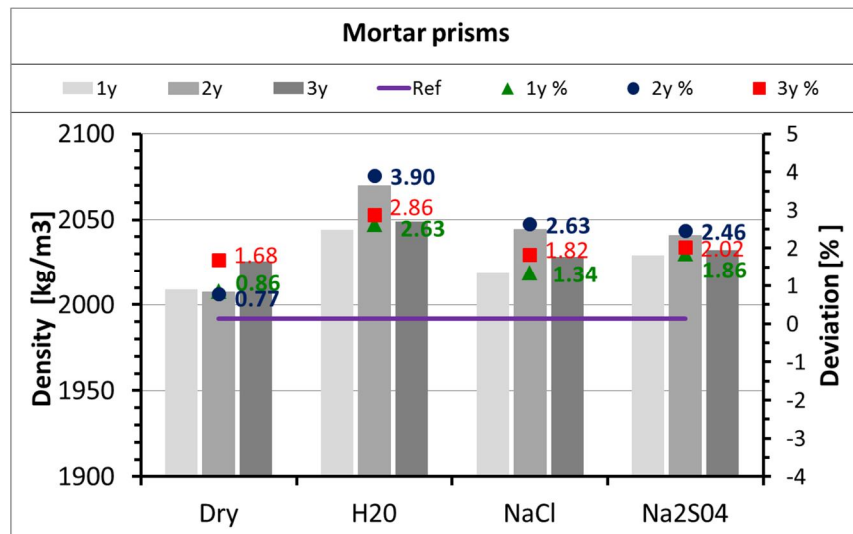


Figure 5.7: Variations of density on the 4 sets of mortar prisms at the end of each ageing season. The reference value is reported as a violet continuous line and the deviations from this values, measured in the different periods, are indicated in %.

5.1.3. Ultrasound tests

In order to achieve the testing aims and thus, to monitor and evaluate the spread and consequences of the weathering process on the physical properties of the diverse sets of mortar prisms, a well-known non-destructive, acoustic technique was employed. In detail, high-frequency ultrasonic measurements (§3.1) in direct transmission were repeated at different time periods - at different levels of decay - to monitor the evolution over time of the degradation effects caused by the simulated natural ageing procedure (Table 5.6).

Table 5.6: Mortar prisms, date of the ultrasound tests

Date of test	Ageing period
May 2011	end 1 st season
November 2011	end 2 nd season
May 2013	end 3 rd season

The US surveys were carried out by means of 1MHz frequency probes for P-wave detection (§3.1). Prior to start the acquisition campaign, some US measurements were carried out in

order to determine the reference velocity of the P-waves, V_p and the characteristic signal resolution, R .

Thus, these parameters were determined for both considered materials, hydraulic lime mortar prisms and fired-clay bricks, in their undamaged conditions (Table 5.7). As the estimated wavelengths are greater than the maximum size of the internal aggregates of the studied materials in sound conditions, the passage of the ultrasonic within them was guaranteed.

Table 5.7: Characteristic parameters of the US signal for the single units of masonry constituent materials

	Mortar	Brick
V_p [m/s]	2000	3400
R_{max} [mm]	2.0	3.4

Testing procedure

The non-destructive ultrasound measurements were repeated following the testing procedure explained in 3.1. The measures were carried out on all the mortar prisms of each set (§4.2) at the end of each ageing season, after a proper acclimatization period of the mortar prisms themselves in indoors stable conditions. This practice was aimed at obtaining fully comparable testing conditions between different years and at stabilizing the moisture content into the same prisms.

On each mortar prism, the ultrasound measures were performed in direct transmission along 4 paths: 1 longitudinal path (A-B), along the main dimension of the specimens which was nominally equal to 16 cm, and 3 transversal paths (1-1', 2-2', 3-3'), 4 cm long, at three different specimens' heights (Figure 5.8 left).

These 4 measurements paths were considered in order to evaluate possible variations of the material properties within the same material's unit, caused by the natural ageing process. The longitudinal path, crossing the whole specimen length and thus passing through areas subjected to different degradations, should provide an averaged estimation of the decay in the entire sample. Instead, the US measures along the transversal paths should gave more localized information in function of the position and distance of each path from the face in contact with the brine and from the brine evaporation level. Indeed, the central transversal path may present diverse conditions than the other two paths with the same length as the latters were located near or above the crystallization areas.

As explained in 3.1, a plastic clamp was used to set in place the probes and a dry coupling of them with the surfaces was ensured. Calibration was performed, for each set of samples, before starting the data acquisition.



Figure 5.8: Mortar prisms: US measurement paths (left), testing equipment (centre), detail of the position of the probes for ultrasound tests along a transversal path (right).

US data analysis and results

The ultrasonic measurements allow the direct determination of two parameters: the time of flight [μs], which is the time employed by the wave to pass through the material, that is to move from the transmitting probe to the receiving one and the attenuation [dB] which is the amount of signal amplification applied during data acquisition to bring the first peak of the received signal to a certain, established, amplitude. The signal velocity [m/s] is later determined from the time of flight and knowing the distance between the two probes, which is the length of the ideal straight path of the signal.

In order to have reference values for comparison, US tests with the same modality were performed on a representative number of mortar prisms in as-built, undamaged conditions, determining the average values of signal velocity and attenuation.

First of all, the averaged results obtained at the end of the three ageing periods along the longitudinal path, were reported for the 4 sets of mortar prisms in terms of signal velocity and attenuation. In both graphs, a continuous violet line is used to indicate the reference values of each parameters and percentages are used to indicate the deviations from that values (Figure 5.9, Figure 5.10).

On average, the signal velocity measured on the 4 sets of aged mortar prisms, at different levels of decay, is always greater than the reference one but there is a lowering tendency at the passing of time, that is moving from the 1st to 2nd and to the 2nd to 3rd ageing season (Figure 5.9). This behaviour is recognized on all the sets of mortars with the exception of the dry one. Indeed, the values of velocity measured on the latter set seemed to be almost stable with the changing of the years. This aspect indicated that the variations in velocity are mainly caused by the water/brine capillary rise instead of the outdoors exposure.

The greater velocities measured are coherent with the gravimetric and dimensional analyses. Indeed, they are explainable taking into account the mass increasing –and increasing densities- measured at the same time periods, which depended on the changes at the microstructural level. The mortar pores, indeed, since the first ageing periods, are no longer filled with air but with water and/or salt crystals. So, the US signals passing through a denser material, with a lower amount of voids, can move at greater velocities. The difference between sound mortars and aged ones is more pronounced at the end of the 1st ageing season. Later, with the passing of time a lowering in the averaged values of velocity was detected for

the samples contaminated with water and salt brines, although without reaching the reference value. This indicated that the decay was evolving. The effects of natural ageing, indeed, were the results of two contrasting processes: on the one hand, there was a salts enrichment into the material pores and on the other, degradation with delamination and material losses due to the increasing volume of the salt crystals into the same pores. Thus, the first process is visible since the beginning, while the latter appeared only from the 2nd ageing season and it depends upon the contamination agent used.

Additional observations can be drawn by comparing the behaviour of the two sets of mortar subjected to sodium chloride or sodium sulphate brines. On average, at the end of the three ageing seasons, the US velocity along the longitudinal path were lower for the mortar subjected to NaCl rise than for Na₂SO₄ rise. This is an index of the greater damage occurred on the mortars of the first set. Although it is known that, for porous construction materials, sodium sulphate is more aggressive than sodium chloride, this result is in line with the much higher (almost double) estimated numbers of possible chloride crystallization cycles over the three summers (Table 5.5).

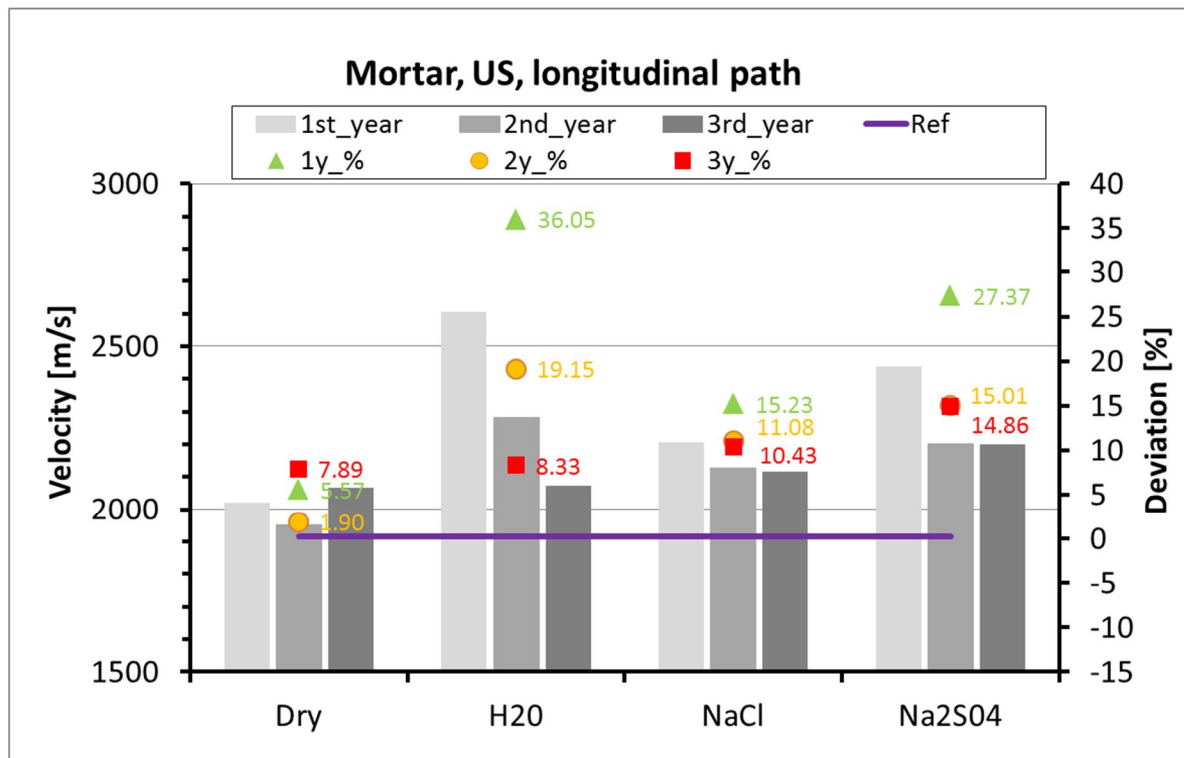


Figure 5.9: Mortar prims, US longitudinal measurements at the end of each ageing season: average values of velocity

The values of US signal attenuation for the measurements along the longitudinal path measured for the three sets of samples at the end of each season, confirmed the observations raised from the velocity values (Figure 5.10). Indeed, an increasing tendency in attenuation was detected with the passing of time for all the 4 mortar sets. Again, the greater values of attenuations recorded for mortar prisms subjected to NaCl rise than for those subjected to

Na_2SO_4 rise, suggested that a greater damage occurred on the first sets of samples, probably due to the greater number of hydration/crystallization occurred for this salt.

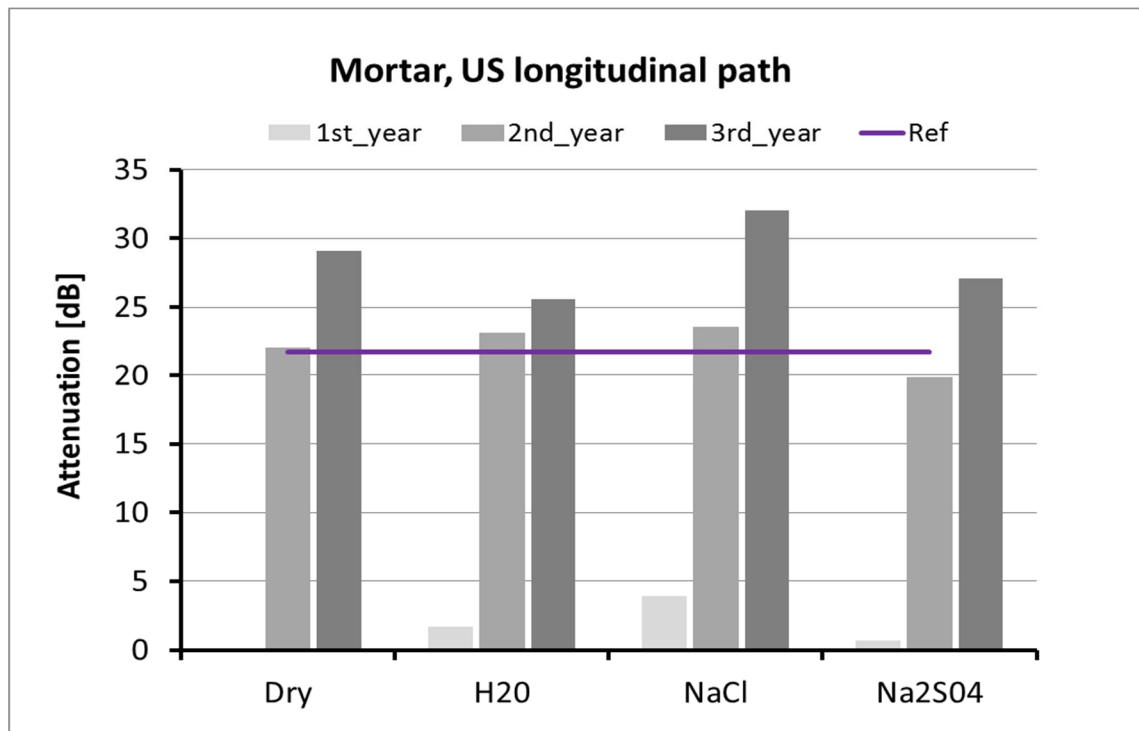


Figure 5.10: Mortar prims, US longitudinal measurements at the end of each ageing season: average values of attenuation

In order to better evaluate the evolution over time of the decay caused by natural ageing procedure, US results obtained from the measurements along the transversal path were also considered. In this case, the average values of velocity and attenuation measured at the end of each ageing period were shown for each set of prisms at each transversal position (Figure 5.11 - Figure 5.13).

At the end of the first ageing season, the tests were carried out for three of the four set of mortar prisms. No data for the dry mortars were available. Anyhow, in this case, values of velocity greater than the reference ones, were detected for both the set of mortar in contact with water and the set contaminated with sodium sulphate. Instead, the prisms subjected to sodium chloride rise presented lower values along the three transversal paths (Figure 5.11 left). This indicated that in the water and Na_2SO_4 samples the effects of the replacement of air into the pores with water or salt is predominant. On the contrary, the degradation caused by repeated salt hydration/crystallization cycles is predominant for the samples subjected to NaCl rise. These considerations are confirmed by the values of attenuation which are greater on these latter samples than for the other (Figure 5.11 right).

An analogous behaviour was detected both at the end of the 2nd and 3rd ageing season (Figure 5.12, Figure 5.13).

On the single set of mortar prisms, some differences are arising along the three transversal paths: lower values of velocities associated to greater values of attenuations are detected on the external paths (1-1' and 3-3') than in the central one (2-2'). This indicated a different spread of the decay along the mortar units which is more pronounced near the top and bottom faces, that is near the crystallization zone.

Thus, overall, it can be affirmed that the US technique was able to detect variations due to weathering since the beginning of the damaging processes.

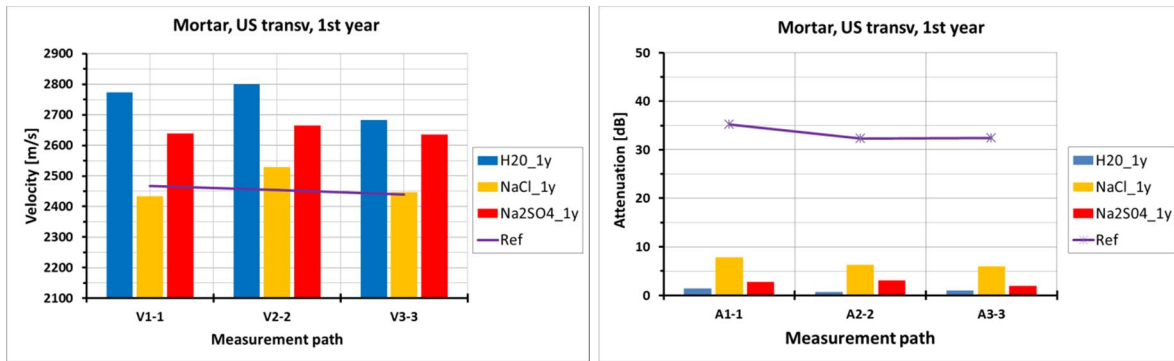


Figure 5.11: Mortar prisms, US transversal measurements at the end of the 1st ageing season: average values of velocity (left) and signal attenuation (right)

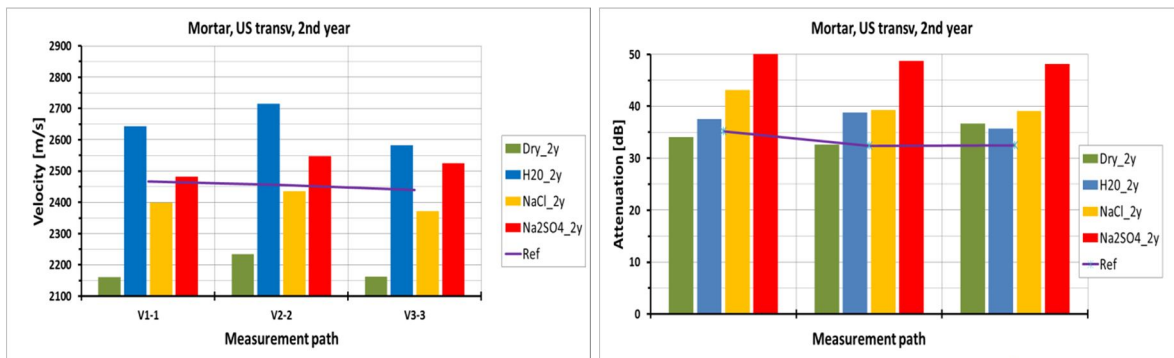


Figure 5.12: Mortar prisms, US transversal measurements at the end of the 2nd ageing season: average values of velocity (left) and signal attenuation (right)

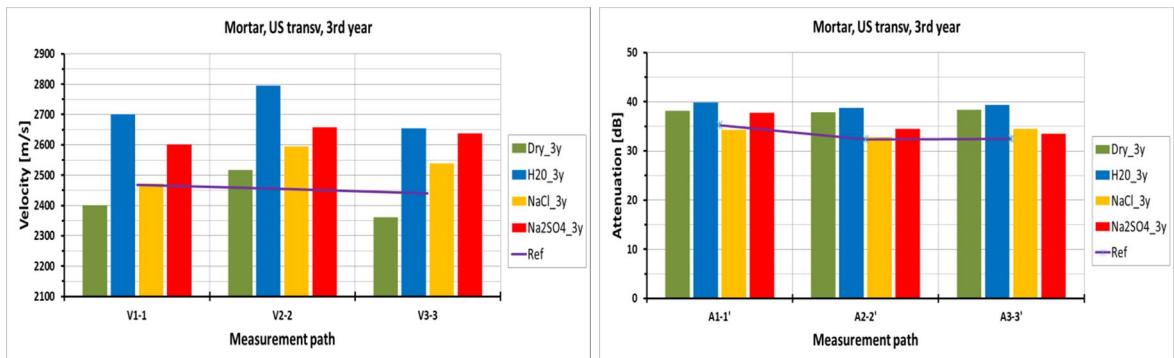


Figure 5.13: Mortar prisms, US transversal measurements at the end of the 3rd ageing season: average values of velocity (left) and signal attenuation (right)

5.1.4. Mechanical tests

The mechanical characteristic parameters of aged mortar prisms were determined by bending and compression destructive tests. These tests were carried out at the end of the 2nd and 3rd ageing season on a limited but representative number of mortar prisms belonging to the different series (Table 5.8). The results obtained in term of bending strength, f , compression strength, f_j and modulus of elasticity, E_j , were then compared with the values measured on reference, undamaged mortar prisms (§4.2).

Table 5.8: Mechanical tests on mortar prisms

Type of test	contamination agent				Ageing season
	Dry	water	NaCl 0.05%-wt	Na2SO4 0.05%-wt	
Bending tests [13]	2	3	3	3	2nd year
Complex post-bending [13]	4*	6*	6*	6*	
Modulus tests [14]	1	3	3	3	
Bending tests	2	3	3	3	3rd year
Complex post-bending	4*	6*	6*	6*	
Modulus tests	1	3	3	3	

*number of specimens obtained after the bending test

Testing equipment and set-up

Three types of mechanical tests, bending tests, compression tests on the stumps obtained from bending and longitudinal compression tests for the evaluation of the modulus of elasticity were performed in order to evaluate and measure possible changes due to natural ageing in the resistant capacity of the mortar.

The tests were carried out following the indication reported in international standards [13, 14]. The testing equipment and set-up procedure used were the same employed to tests the sound mortar prisms, see §4.2 (Figure 5.14). Anyhow, the principal characteristics of the set-up are herein summarized for convenience (Table 5.9).



Flex +

Figure 5.14: Mortar prisms: set-up of the mechanical tests: bending tests, compression tests and determination of the modulus of elasticity, from left to right

Table 5.9: Characteristics of the mechanical tests on mortar prisms

Type of test	Tot. n° of mortar prisms per year		Freq. of data acquisition [data/sec]	Load velocity [N/s]	Instrumentation
	2 nd year	3 rd year			
Bending	11	11	0.2	10-20	2 LVDTs
Compression post-bending	22	22	0.2	200	2 LVDTs
Modulus	10	10	0.2	100	2LVDTs & 2 strain gauges (Tok.Sok. 10mm lenght, k=2.13)

Results

The average values of the main mechanical parameters determined at the end of the 2nd and 3rd ageing season were reported for each set of samples (Figure 5.15, Figure 5.16).

Overall, at the end of both summers, an increasing strength was detected for all the sets of mortar, both from the bending tests and the subsequent compression tests, compared to the reference values. Analogously, a greater stiffness was measured on the aged samples than on the undamaged ones.

This improvement on the mechanical properties is in line with the greater US velocities measured along the longitudinal path and it is a consequence of the increased density due to the salt enrichment within the material pored.

Anyhow, passing from the 2nd to the 3rd ageing period, a certain decreasing trend was noted on the values of bending and compression strength. This tendency may indicate that the progress of decay due to repeated numbers of salt hydration/crystallization cycles and material losses with a consequent reduction of the resistant areas, started to affect the mechanical resistance. This is more evident on the mortar samples contaminated with sodium sulphate which appeared more aggressive than chloride and able to cause a greater inner decay, despite the less number of cycles occurred.

The progress of decay seemed to not affect the stiffness in the same way, as from the 2nd to the 3rd season an increase on the values of the modulus of elasticity is visible for all the mortar samples (Figure 5.16).

Thus, from a mechanical viewpoint, the natural ageing process simulated by outdoor exposure and water or salt capillary rise improved the characteristic properties of this porous materials, which, after three years of ageing appeared more strength and stiff than at the beginning of the process.

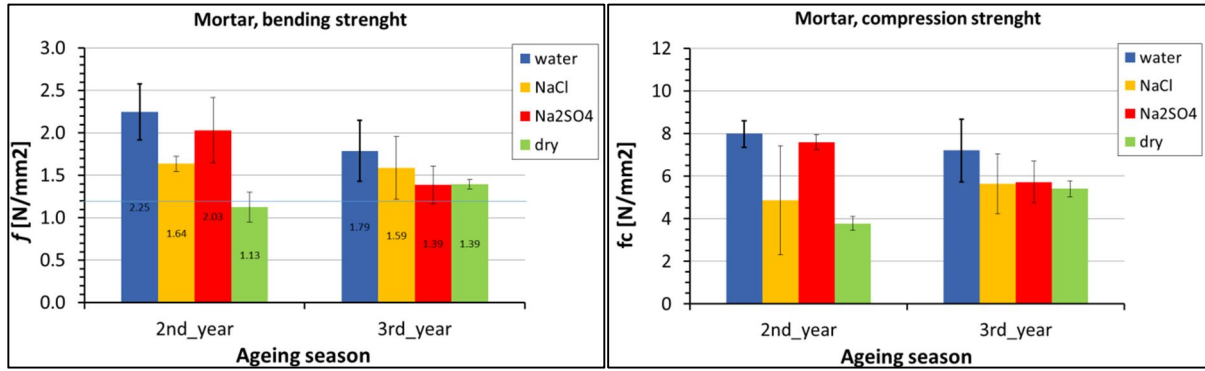


Figure 5.15: Mortar prisms: results of the bending (left) and compression tests (right)

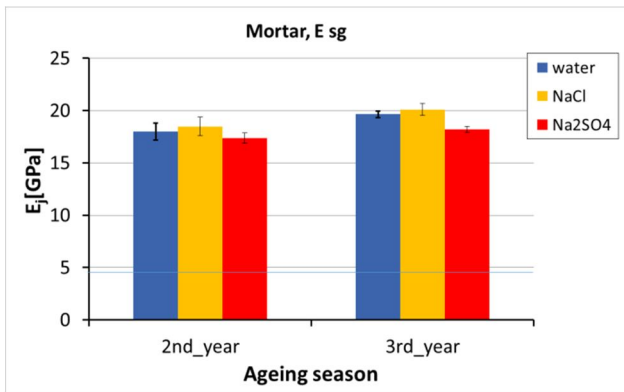


Figure 5.16: Mortar prisms: average values of modulus of elasticity determined at the end of each ageing season

5.2. Fired-clay bricks: results of the long-term monitoring

Similarly to what has been performed for the mortar prisms, the effects of the natural weathering on the three sets of brick units considered were monitored and evaluated via visual, non-destructive and mechanical tests.

5.2.1. Visual inspection

The repeated visual observation and photographic documentation taken showed the appearance of salt efflorescences as white superficial deposition in the upper part of the specimens since the beginning of the test on all the brick units of the three sets although with some differences. In the case of specimens contaminated with water, indeed, these salt depositions were softer and more similar to dust depositions than in the other two sets. In the bricks contaminated with sodium sulphate, these were more dense (Figure 5.17 left).

In addition, cracks on the top and bottom faces of the brick units were later recognized as a visible weathering effects. These were more evident on the set of bricks contaminated with sodium sulphate and at the end of the 3rd ageing season, despite the higher number of hydration/crystallization cycle of sodium chloride than sodium sulphate (Figure 5.17 right).

Instead, no signs of material delaminations, crumbling or powdering were identified and no dust was collected at the basin's bottom.

Thus, from the visual inspection, fired-clay brick units appeared less vulnerable than mortar prisms to weathering effects.



Figure 5.17: Appearance of the fired-clay brick sets during the first ageing season (left) and detail of one brick at the end of the 2nd ageing season (right)

5.2.2. Gravimetric and dimensional analysis

In this case, gravimetric and dimensional analyses were performed only twice: at the end of the 1st and 2nd season, while no data were available from the last ageing summer. Actually, not all the bricks were considered but only 10 per set which was a quite representative number.

Choosing the mass as the more accurate parameter as done for the mortar prisms, analogous differences arose. A decrease in weight indeed was recovered on all the aged bricks although, passing from the 1st to the 2nd an increasing tendency was then detected.

However, scarce variations were detected, approximately equal to 2%. Considering the large dispersion on the data characterizing this type of material, indeed, these values could not be considered as certain.

Analogous variations of density were measured, indicating a progressive replacement of the air contained within the material pores with water and/or salt crystals, heavier than air. As a result, at the end of the ageing period, bricks appeared more dense and homogeneous.

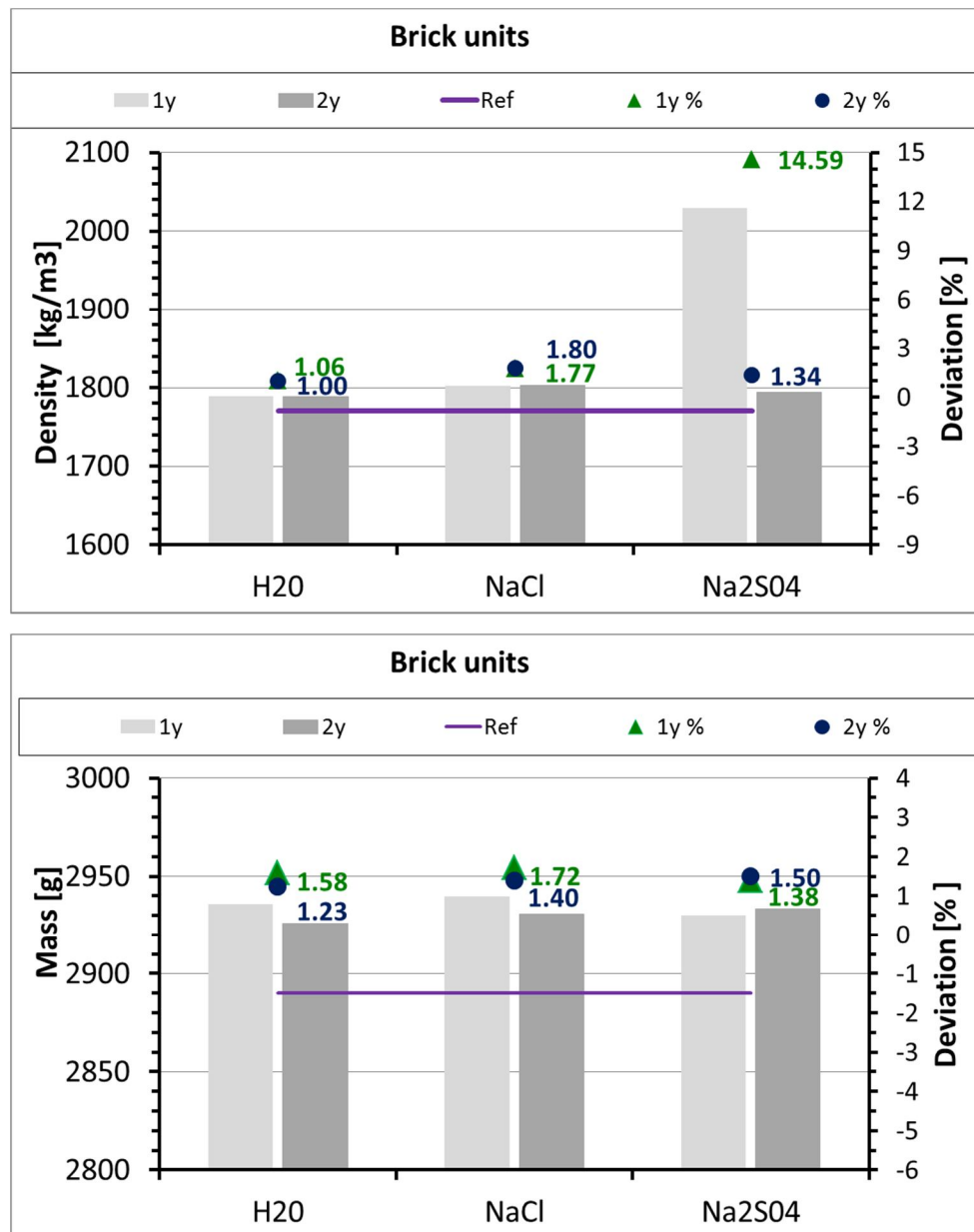


Figure 5.18: Fired-clay bricks: variations of density (top) and mass (bottom) per set per year

5.2.3. Ultrasound tests

The ultrasonic tests were repeated at the end of each ageing season on a representative number of solid brick units, equal to 10 for each basin per year, after, as in the case of mortar prisms a proper acclimatization procedure, in order to avoid undesirable effects due to different moisture content.

The same equipment and testing procedure followed for the evaluation of weathering effects on mortar prisms was employed for the brick units.

For each set of samples, the ultrasonic measurements were performed in direct transmission, along one longitudinal path (A-B) and three transversal paths (1-1', 2-2', 3-3'), according to the scheme reported in (Figure 5.19). This procedure was followed to evaluate possible variations in the different portions of the materials as may not be affected in the same way by the natural ageing. The three transversal paths, being placed at different distances from the areas in which crystallization occurs, could allow obtaining helpful information to describe the spread of damage along each specimen, while the longitudinal measure, crossing areas at different degradation level, provides an averaged estimation of the decay of the entire sample.

As in the case of mortar prisms shown in the previous paragraph, the results of the US measures are reported in terms of signal velocity and attenuation for the three sets of fired-clay bricks and for the three ageing season. The values obtained from US measures on undamaged bricks are considered as references and they are used to compare the values obtained from aged bricks in order to identify the weathering damages and their evolution over time. [5]



Figure 5.19: Brick units: scheme of the US measurements (left), longitudinal measure (centre) and transversal one (right)

The average values of velocity measured along the longitudinal path are quite similar in the three sets of bricks and overall, always greater than the value obtained for the brick units in sound conditions. In this case, differently to what was found for the mortar prisms, there is an increasing tendency of velocity with the passing of time (Figure 5.20).

The velocity improvements indicate that the aged bricks are more homogeneous and dense than the undamaged ones. This, as in the case of mortars, is probably due to the increasing presence of water and/or salt crystal within the material pores and to the presence of large areas of the units still not contaminated which causes a quite similar average behaviour.

Anyhow, the salt enrichment seems to govern the decay process for this material also after three ageing seasons. This aspect is also confirmed by the visual observation as no delaminations or material losses were detected and the only visible degradation effect noted was the presence of some cracks at the end-faces of the samples

Thus, the fired-clay bricks appeared to be less sensitive to the type of salt and probably less affected by the ageing process than the mortar prisms.

The values of attenuation measured (Figure 5.21) at the end of the 2nd and 3rd season, for the three sets of bricks confirmed the observations deriving from the velocity values. Instead, the attenuations recorded at the end of the 1st years, almost null, are not in line with the corresponding velocities and they are lower than expected.

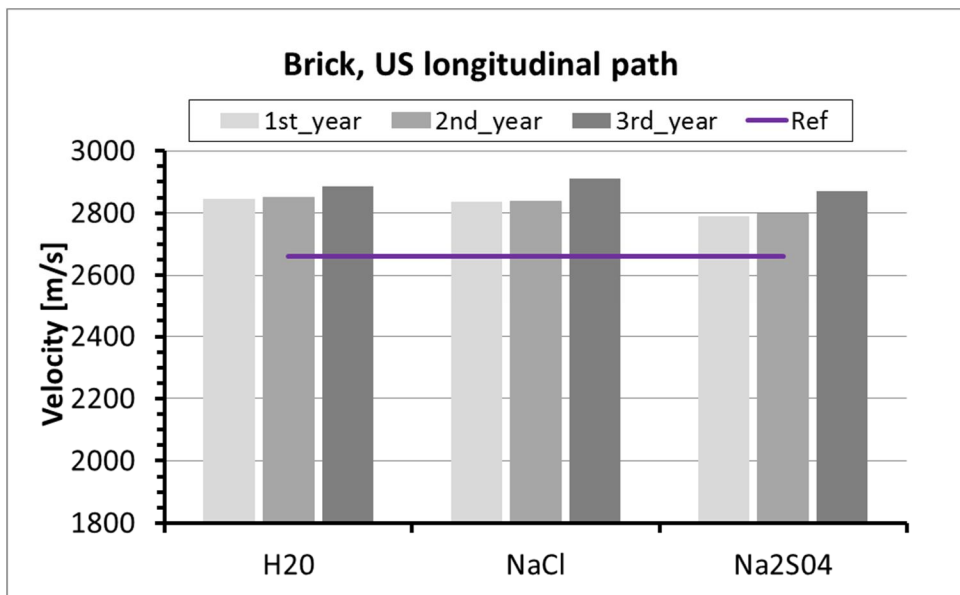


Figure 5.20: Fired-clay bricks: US velocity along the longitudinal path

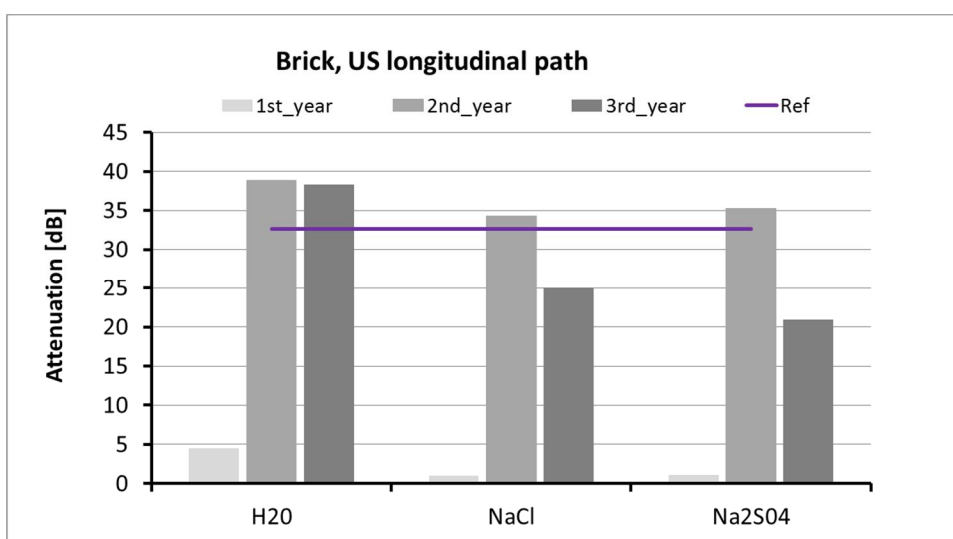


Figure 5.21: Fired-clay bricks: US signal attenuation along the longitudinal path

The US results obtained from the measurements along the three transversal paths are more inhomogeneous and quite dispersed. Variations in terms of velocity and attenuation, although of small entities, were found between the different ageing periods and between the diverse sets of samples (Figure 5.22, Figure 5.23, Figure 5.24).

At the end of the first ageing period, the measurements were performed only along the 1-1' transversal path. The values of velocity recorded were almost equal between the three sets of fired-clay bricks and taking into account the dispersion on the values measured, almost equal to the velocity determined for the reference bricks. The attenuations were very limited and almost equal on the three sets (Figure 5.22).

Similar results were found at the end of the second ageing season (Figure 5.23), while some differences were measured at the end of the 3rd (Figure 5.24). At this time period, seems that the decay process started to be appreciable at least on the samples contaminated with sodium chloride which had the more favourable environmental conditions for crystallization. Indeed, in this set of bricks, the values of velocities are significantly lower than those obtained in the previous year and for the reference samples.

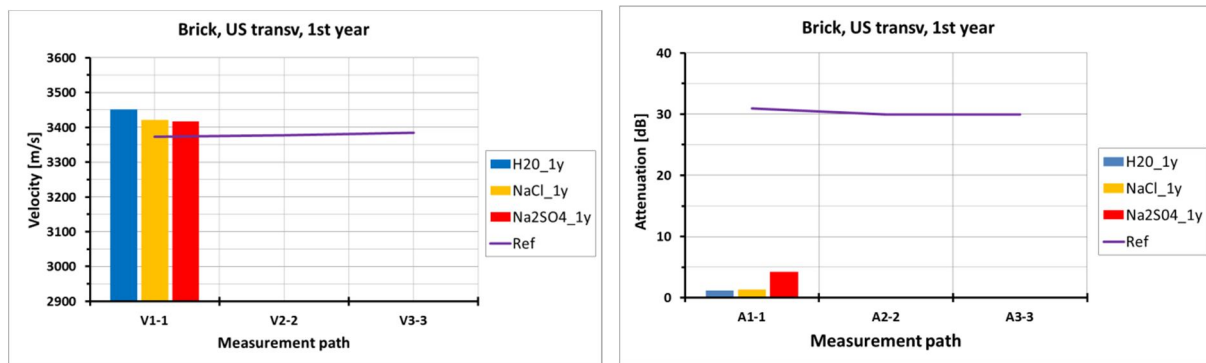


Figure 5.22: Fired-clay bricks: US velocity (left) and attenuation (right) measured at the end of the 1st ageing period

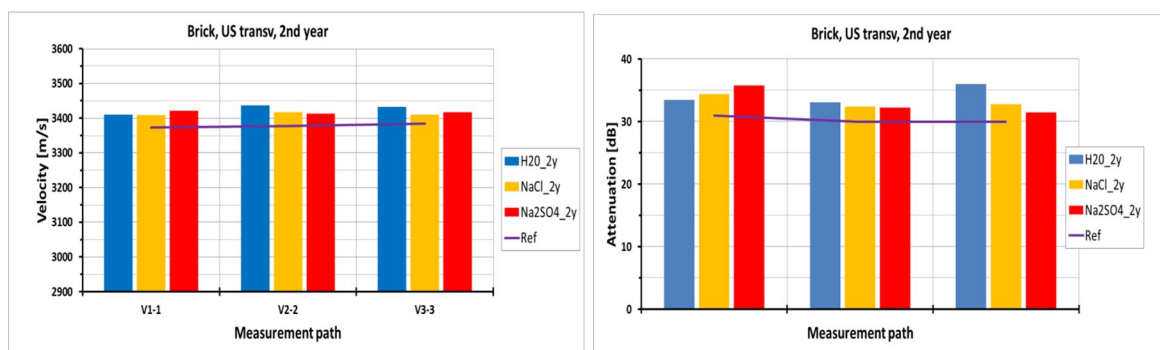


Figure 5.23: Fired-clay bricks: US velocity (left) and attenuation (right) measured at the end of the 2nd ageing period

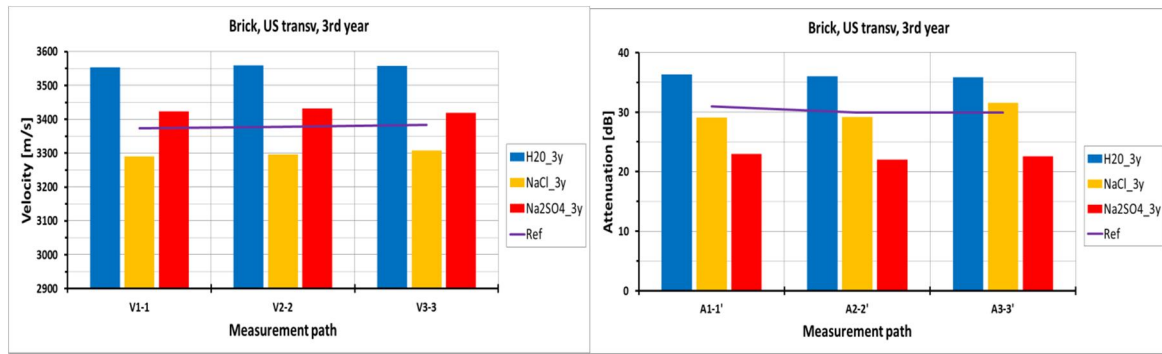


Figure 5.24: Fired-clay bricks: US velocity (left) and attenuation (right) measured at the end of the 3rd ageing period

5.2.4. Mechanical tests

In order to evaluate the effects of the decay caused by environmental agents such as water and salts on the mechanical properties of bricks, several cubes were subjected to compression tests. These tests were carried out according to [16], by means of the same testing equipment and set-up describe in §4.2 for brick units in sound conditions-

In detail, 24 cubes of 5 cm³ per set per year, were considered. These were obtained from 6 bricks for each set per year by cutting 4 cubes from each longitudinal half of a single brick in order to determine also possible differences along the height of the specimen.

From these 24 cubes, 18 were tested for strength according to [16] and the global displacements were monitored by LVDTs fixed at the plates of the testing machine; 2 cubes each instrumented with 2 strain gauges (Tok.Sok. 6 mm length, k=2.10), were tested for determination of axial deformation (Figure 5.25 left in blue) and 4 cubes (only 2 at the end of the 3rd year), each instrumented with strain rosettes (Tok.Sok. 6 mm length, k=2.10) were tested for axial and transversal deformations (Figure 5.25 left, in red).

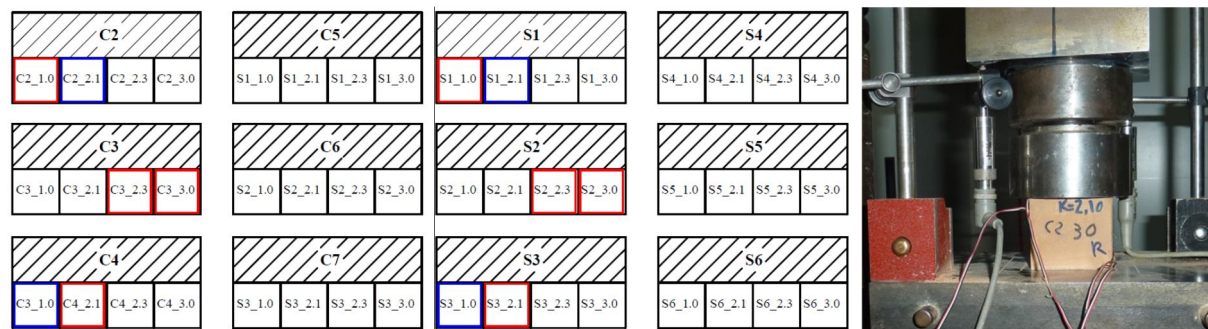


Figure 5.25: Scheme used to obtain the cubes from brick units (left) and set-up of the uniaxial compression test on brick cubes (right) [5]

First of all, the average results obtained at the end of the 2nd and 3rd ageing season, in term of compressive strength and modulus of elasticity (measured by strain gauges) were reported for the three sets of bricks (Figure 5.26, Figure 5.27).

The main variations can be summarized as an almost unchanged compressive strength and increase of the stiffness, associated to a decrease ductility and a more brittle failure observed during the same tests. These changes were detected for all the 3 sets of bricks. Actually, the values of compressive strength decreased at the end of the 3rd season but the statistical dispersion of the results is so high that these data could not be considered as certain.

Anyhow, these results seem corresponding to the results obtained from the US tests.

Similar observations are arising also looking at the data, dividing the results for the original positions of the brick cubes.

Thus, it seems that the decay process is still on-going and not so pronounced as in the case of mortar prisms as few effects are visible on the mechanical properties.

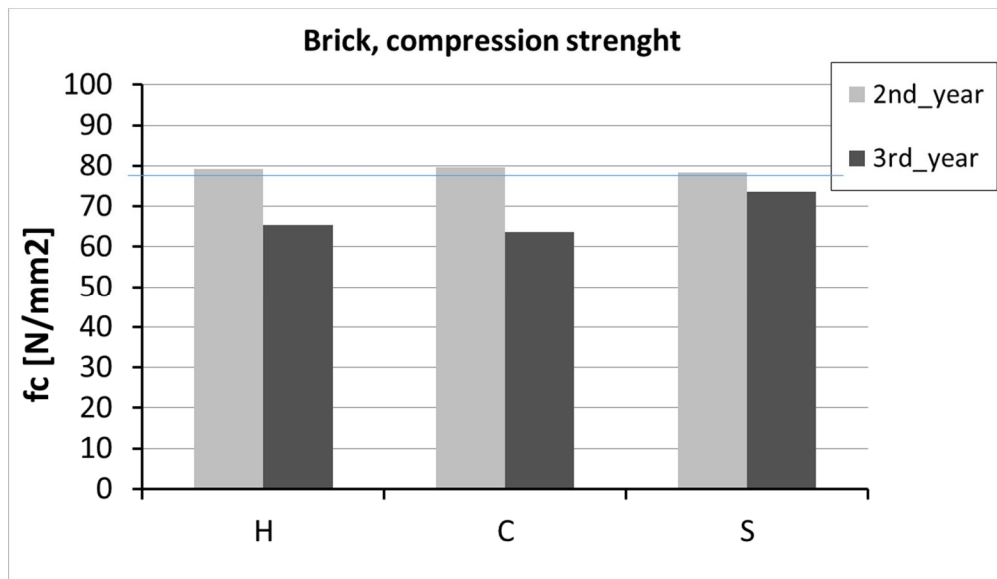


Figure 5.26: Fired-clay bricks: average values of compressive strength measured at the end of two different ageing seasons

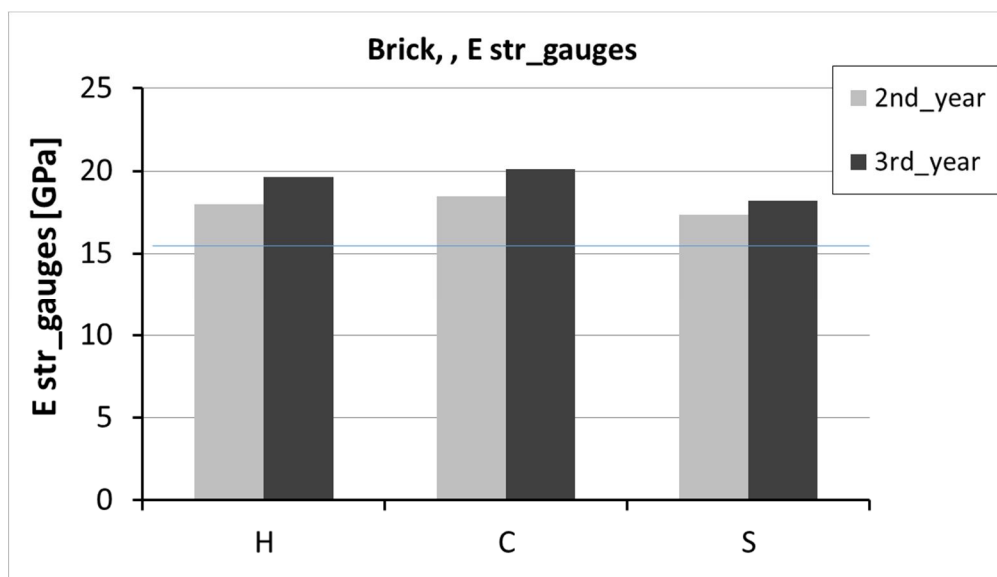


Figure 5.27: Fired-clay bricks: average values of modulus of elasticity measured at the end of two different ageing seasons

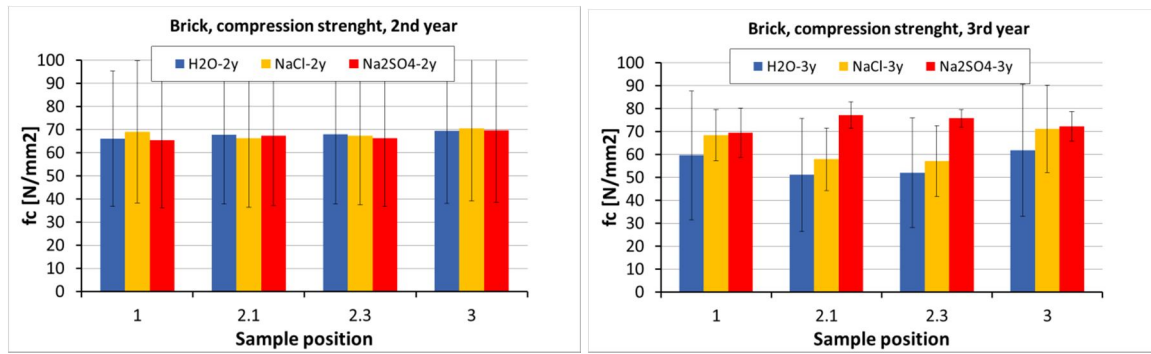


Figure 5.28: Fired-clay bricks: values of compressive strength measured at the end of the 2nd (left) and 3rd (right) ageing season, divided for position

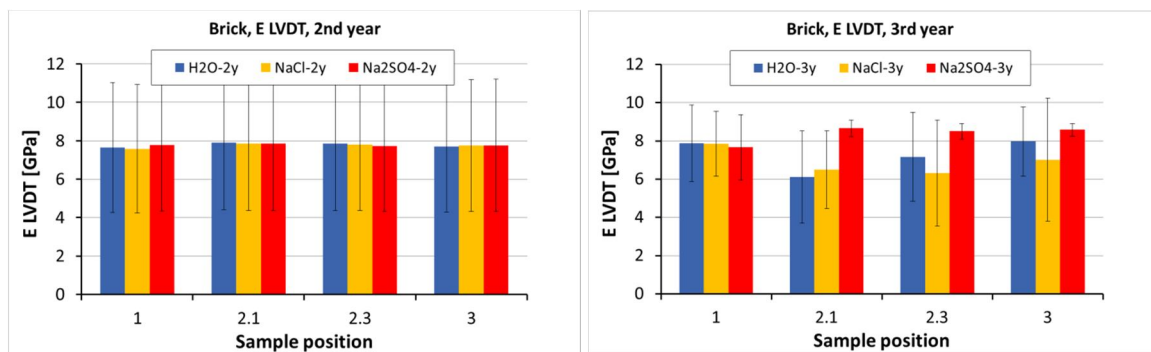


Figure 5.29: Fired-clay bricks: values of modulus of elasticity measured by means of LVDTs at the end of the 2nd (left) and 3rd (right) ageing season, divided for position

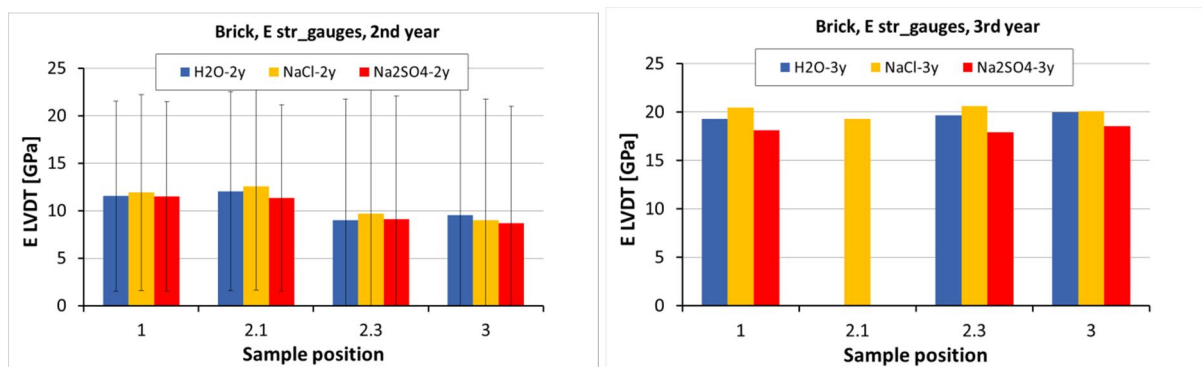


Figure 5.30: Fired-clay bricks: values of modulus of elasticity measured by means of strain gauges at the end of the 2nd (left) and 3rd (right) ageing season, divided for position

5.3. Conclusion

This chapter reported the results of the long-term ageing and monitoring of units of porous building materials naturally aged. All the samples were exposed outdoors and divided into 4 sets (in the case of mortar) or 3 sets (in the case of bricks) according to the contamination agent used to simulate the capillary rise from the base (none, tap water or low-concentrated sodium sulphate and sodium sulphate brines).

The evaluation of the spread and evolution over time of the decay process was performed both on the mortar prisms sets and on the brick ones by means of repeated visual inspections, gravimetric and dimensional survey, non-destructive ultrasound tests and mechanical tests.

First of all, it was found that the mortar prisms appeared more sensitive to the salt decay than the brick units. This was noted from the visual observation, as mortar prisms appeared, on average more damaged (rough surfaces, delaminations and material losses were detected) than the bricks (only cracks were detected), and also from the variations in the physical and mechanical properties, which were more accentuated for the mortar sets than for the bricks.

The variations in terms of ultrasonic velocity and attenuation have proved that this non-destructive technique is able to detect the evolution of the natural decay since its beginning, for both types of material. The increased velocity and reduced attenuation measured on the aged samples if compared to the undamaged ones, suggests an increased density and homogeneity of the aged materials. This was, on the one hand, confirmed by the gravimetric and dimensional analyses and on the other hand, this improvement was confirmed by the mechanical tests. The latter, indeed, show an increase in resistant capacity of the aged brick and mortar prisms, although visible superficial material decay (especially decohesion and powdering in the mortar and cracks in bricks) was observed and a reduction in sample section was measured for the mortar prisms.

This improved mechanical behaviour of the salt contaminated porous materials need to be studied more in depth and the evolution of decay should be monitored for a longer period in order to verify if this increase would be followed i.e. by a sudden decrease in the characteristic properties.

6. Non-destructive evaluation of outdoor full scale walls: moisture and salt transport, decay

This chapter deals with the results of the non-destructive diagnosis evaluation of the full-scale brick walls (§4.4) exposed outdoors to natural environment, over four summers (2010, 2011, 2012 and 2013), in addition to water or brine capillary rise (Table 6.1, Figure 6.1).

Several NDT methods were applied and repeated at different time intervals together with some minor-destructive and monitoring techniques in order to evaluate the spread and evolution over time, since the beginning, of the decay effects caused by weathering, as well as moisture content and salt transport, both at a superficial and in-depth level.

Table 6.1: Full-scale brick walls, type of brine added to simulate the damp rise phenomena

Full-scale wall	Type of solution and concentration
PNDA	0.1%-wt. NaCl solution
PNDB	0.05%-wt. NaCl solution
PNDC	only natural rain water
PNDD	0.1%-wt. Na ₂ SO ₄ solution
PNDE	0.05%-wt. Na ₂ SO ₄ solution
PNDF	tap water

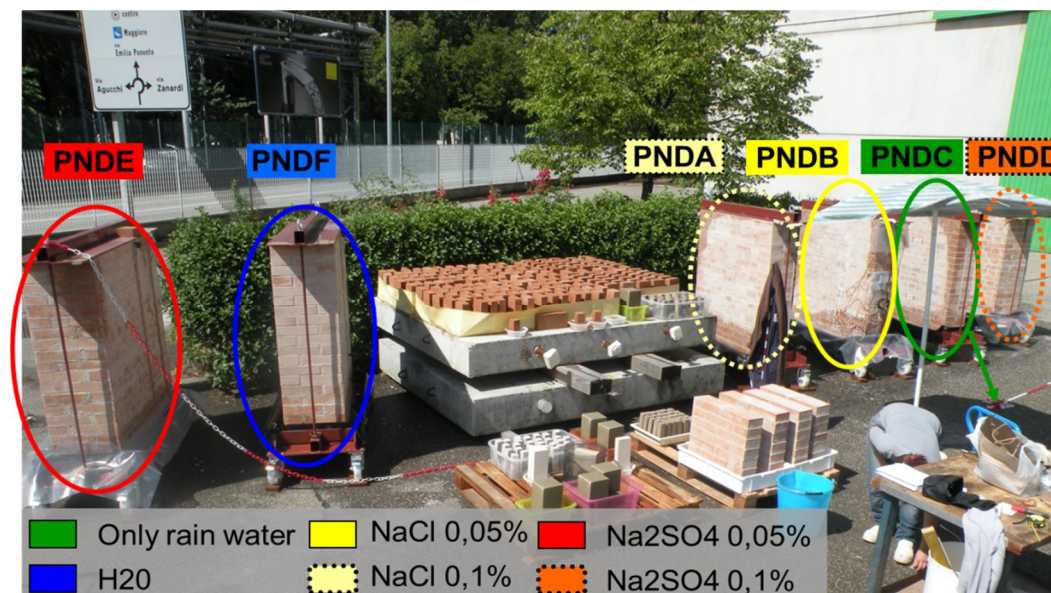


Figure 6.1: Overview of the full-scale walls, July 2010

The non-destructive diagnostic techniques selected are applicable on-site, exploit different physical principles (i.e. sound waves, electromagnetic waves) and belong to the user-friendly category of the imaging diagnostic techniques. In detail, visual inspection, sonic tests, IRT, laser scanner and DIC were used for the superficial monitoring, GPR radar and sonic tests to

obtain an in-depth monitoring and wireless sensor monitoring and micro-cores to define salt concentration profiles.

The chosen techniques, not-standardized, were employed by means of on-purpose developed procedures to obtain the best results and maximum performances, as well as properly established simplification to not causing damages to the masonry structures nor their surfaces and to ease the data acquisition or post-processing phase. Thus, first of all, the experimental campaign carried out was aimed at evaluating the effectiveness of the selected methods as well as their sensitivity and accuracy in detecting and following the evolution of one or more of the aspects connected to and resulting from the simulated weathering processes, in addition to, for example, their reliability in identifying the presence of artificial defects inserted into the same brick walls, although this issue is outside the scope of the present work.

Herein an overview on this extensive experimental campaign as well as on the integrated non-destructive diagnostic procedure followed and on the achieved outcomes is reported by means of exemplary results obtained at least for one full-scale wall.

6.1. Visual inspection and photographic documentation

First of all, to monitor the evolution of the degradation process due to aggressive environmental agents over different years, visual inspections were periodically carried out, during and at the end of each ageing season, collecting photographic documentation.

These simple visual inspections and observations allowed detecting the presence and variations of moist areas/levels thanks to the darkening of the brick walls' surfaces as well as the appearance of the effects due to salt contamination such as salt efflorescences, cracks, delaminations, pitting, mortar joint scarification, etc.

The following exemplary images were taken at different time periods of ageing and showed the variations on the surfaces' appearance of the six full-scale walls. For convenience, the precise duration of each natural ageing season, intended as the summer months in which brine/tap water has been poured into the tubs at the walls' base is reported in Table 6.2, in order to relate each image with the corresponding ageing summer.

Table 6.2: Natural ageing periods

Ageing season	
1 st	July 2010 – November 2010
2 nd	2011 – November 2011
3 rd	2012 – November 2012
4 th	2013 – November 2013

Report D5.2 part 3+ 15th IBMAC

6.1.1. Full-scale wall PNDA (0.1%-wt. NaCl)

The wall PNDA, 25 cm thick, presented one main surface unplastered and one plastered, with a layer of lime mortar, 1 cm thick and it was contaminated by a sodium chloride solution (0.1%-wt.). The effects of weathering and salt rise on both main surfaces are reported below with reference to the first two ageing seasons. After only 5 months of ageing, thin white salt efflorescences were visible both on the brick/stone surfaces as well as on the mortar plaster in correspondence of the brine evaporation band. The plastered rear side appeared more damaged than the front side presenting quite large areas with material losses (Figure 6.2, Figure 6.3) (report D5.2-part 1).



Figure 6.2: PNDA, front side at the end of the 1st ageing season (Nov. 2010)



Figure 6.3: PNDA, plastered rear side at the end of the 1st ageing season (Nov. 2010)

This decay worsened with the passing of time: at the end of the 2nd summer, some localized pitting phenomena and brick flakes detachments were visible in the front side while the extensions of degraded areas in the rear side increased (Figure 6.4, Figure 6.5).



Figure 6.4: PANDA, front side at the end of the 2nd ageing season (Nov. 2011)



Figure 6.5: PANDA, rear side status at the end of the 2nd ageing season (Nov. 2011)

6.1.2. Full-scale wall PNDB (0.05%-wt. NaCl)

Some effects of environmental degradation were visible since the very beginning of the natural ageing procedure. Indeed, 15 days after pouring the brine into the wall tub, the wet areas were clearly identifiable on both sides of the wall but the height of the moist level was different probably because of the different sun exposure of the two faces. In the rear side, some localized areas with salt efflorescences were visible (Figure 6.6).

After 5 months of ageing, in November 2010, salt efflorescences were uniformly distributed along the evaporation band on both sides of the wall. These soft salt depositions were mainly located on brick at masonry courses 6 and 7, as well as on the mortar joints between these courses (Figure 6.7).

Sparse salt subflorescences were detected on the front side, below the rise level, on bricks positioned near the wall's edges where the evaporation is more accentuated (Figure 6.8). These crystallizations were visible because they had already provoked material's expulsion or detachments (exfoliation). The presence of degradation on both masonry components is well in line with their properties, especially considering their similar values of porosity (15thIBMAC). Localized pitting phenomena on bricks were also observed.

Moreover, after 5 months of ageing, scaling on the Palestine stone inclusion located at masonry course 6 was evident. The progress of the degradation of this stone is faster than the decay on brick and mortar joints (Figure 6.9).



Figure 6.6: PNDB, July 2010, 15 days after pouring the brine: a) front, b) rear side



Figure 6.7: PNDDB, rear side at the end of the 1st ageing season (Nov. 2010)



Figure 6.8: PNDDB, front side at the end of the 1st ageing season (Nov. 2010)



Figure 6.9: PNDB, front side, progress of deterioration in the Palestine stone: a) November 2010, b) April 2012, c) August 2012, d) September 2013

6.1.3. Full-scale wall PNDC (only natural rain water)

Some salt efflorescences, probably due to the initial salt content of the porous construction materials, were visible since the end of the 1st ageing season also on this two-header wall which was not subjected to additional brine rise from the base, except of the rise of rain water which may have been recovered in the tub (Figure 6.10).



Figure 6.10: PNDA damage status of plaster on back side at the end of the second aging season (2011-11-08)

6.1.4. Full-scale wall PNDD (0.05%-wt. Na₂SO₄)

This three-header wall was contaminated with sodium sulphate, salt notoriously more aggressive than sodium chloride. The solution used to simulate the brine rise was at low-concentration with the exception of the 1st time of brine-pouring, when a medium concentration solution was employed.

Since the end of the first ageing period, both salt efflorescences and sub-florescences were visible as blistering and detachment of brick flakes occurred near the evaporation band of both sides of the wall (Figure 6.11, Figure 6.12). Mortar scarification was also quite evident, especially in the wall front side which was more exposed to sun radiations (report).

This degradation phenomena became more pronounced with the passing of time (Figure 6.13, Figure 6.14), causing consistent losses of materials portions both from brick surfaces and mortar joints, especially near the edges of the wall (Figure 6.15).

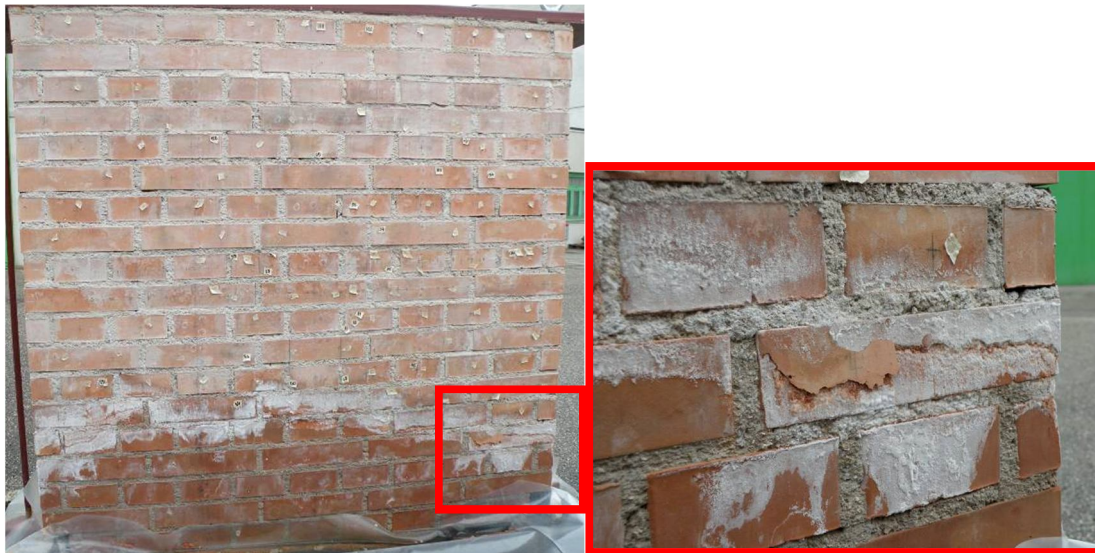


Figure 6.11: PNDD front side, at the end of the first ageing season (Nov. 2010)



Figure 6.12: PNDD rear side, at the end of the first ageing season (Nov. 2010)

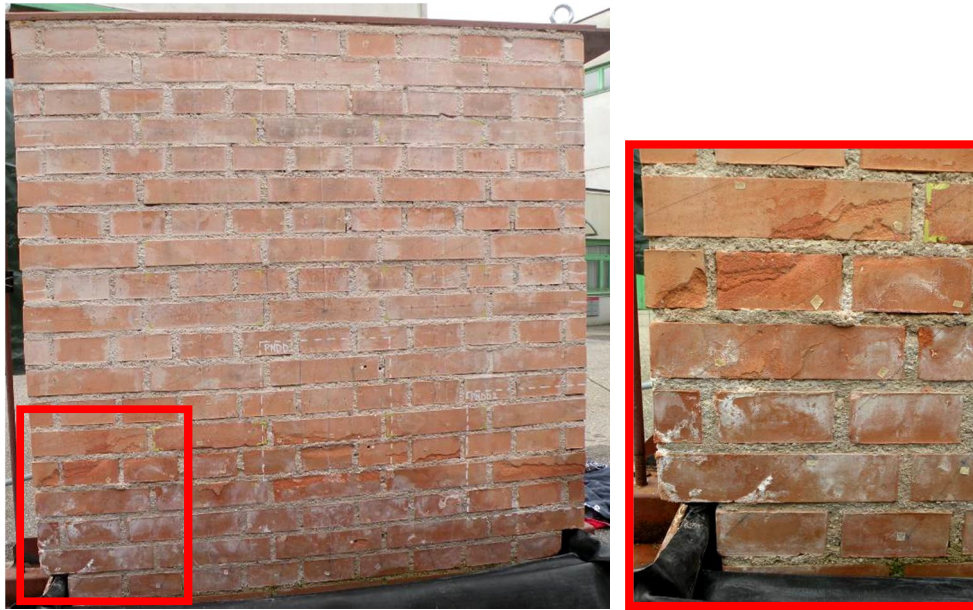


Figure 6.13: PNDD front side, at the end of the second ageing season (Nov. 2011)



Figure 6.14: PNDD rear side, Nov. 2011, evident blistering of bricks and losses of materials on the mortar joints



Figure 6.15: PNDD, rear side at the end of the 3rd ageing season (November 2012)

6.1.5. Full-scale wall PNDE (0.05%-wt. Na₂SO₄)

As seen for the previous walls, moist areas and salt crystallization on the surfaces or beneath them were visible since the very beginning of the ageing period (Figure 6.16). In this case, different white crystals correspond to the sodium sulphate phases were noted: some of them appeared as hard and persistent bubbles (subflorescences) whilst others, very thin and delicate, looked like a dust deposition (efflorescence). Probably because of the aggressiveness of the type of salt employed for the damp rise (sodium sulphate), the first detachment of brick flakes already occurred after 5 months of ageing (Figure 6.17). (Ibmac)



Figure 6.16: PNDE, front side, July 2010 (left) and November 2010 (right)



Figure 6.17: PNDE, Nov. 2010, rear side (left) and 2 brick degradation details (right)

6.1.6. Full-scale wall PNDF (tap water)

The exposition to the natural environment caused same damages also if it is not coupled with brine rise from the base. Indeed, to simulate the capillary rise only tap water was poured into the tub of this wall. Despite this, because of the initial content of soluble salt into the porous materials as well as in the tap water of the Bologna aqueduct, salt efflorescences were observed since the first ageing season. After 3 ageing season, blistering and detachment of brick flakes interested several bricks near the evaporation band and serious scarification of the mortar joints had already occurred (Figure 6.18).

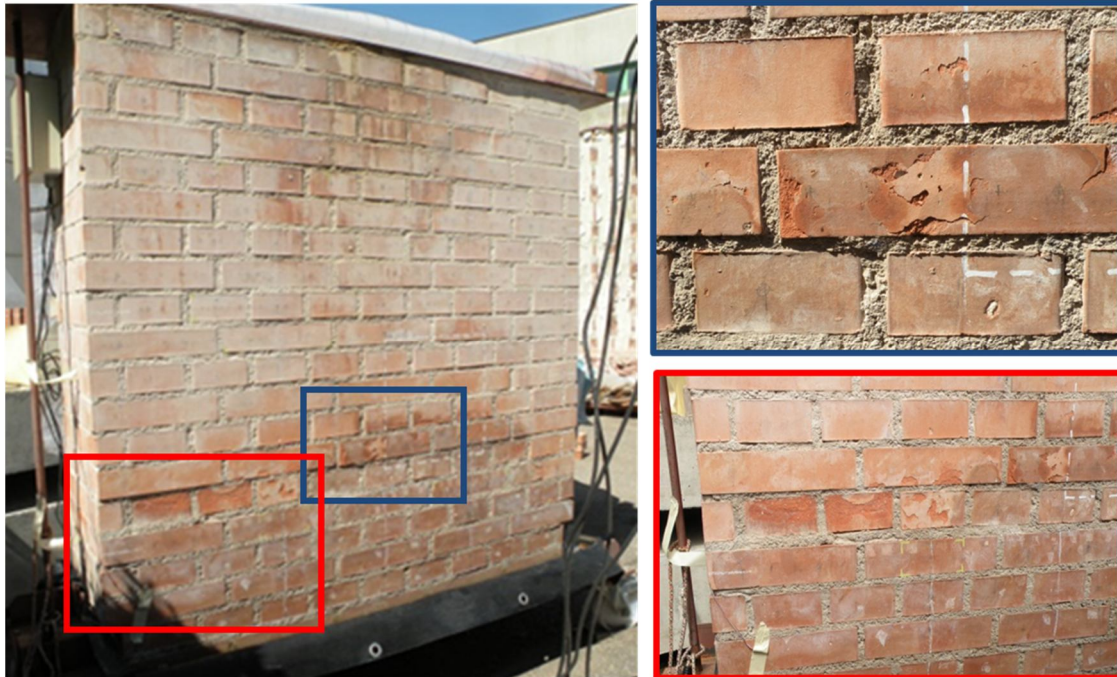


Figure 6.18: PNDF, front side, during the 3rd ageing season (June 2012)

6.1.7. Observations

The visual inspection and photographic documentation underlined the differences between the type and spread of decay caused by the two salt considered. All the walls showed an initial decay due to salt visible as salt depositions, delaminations and detachments on bricks and loss of material in mortar joints, although the degradation was more evident on wall PNDD and PNDE which were subjected to Na_2SO_4 rise (15Ibmac). This occurred in spite of the lower number of possibly occurred crystallization/hydration cycles of Na_2SO_4 with respect to NaCl (estimated in §4.3). This characteristic clearly confirms that the sodium sulphate action on masonry is more destructive than sodium chloride's, as already mentioned by other authors (Binda 1987, Van Hees 2004).

6.2. Sonic tests

Sonic tests were one of the non-destructive diagnostic methods used to evaluate the decay effects caused by natural weathering and their evolution over time. The measurements were repeated three times, at different levels of decay: prior to the beginning of the ageing procedure that is in the as-built conditions of the specimens, after 2 years and after 3 years of ageing. The reliability and accuracy of this acoustic technique were tested by employing two different testing procedures: direct-through transmission and superficial transmission §3.3.

In the following, after a brief recall on the data acquisition and analysis procedures, some exemplary results are reported.

6.2.1. Sonic tests in direct trough transmission

As mentioned in section 3.3, in direct-through transmission tests, the transmitting and receiving stations are facing each other on the opposite faces of the wall. A rectangular grid of measurement points was marked on both wall surfaces. The instrumented hammer and the receiver (§3.3.1) were progressively moved along the stations of the grid but always facing each other. On each position, 2 waveforms were recorded: one from the hammer and one from the receiving transducer. The time-domain data analysis consisted in determining, for each measurement, the so-called time-of-flight, ToF, in μs and evaluating the correspondent signal velocity, in m/s, by knowing the ideal length of the wave path which is, in our case, the walls' thickness. Moreover, the amplitudes of the transmitting and receiving signals were recorded and the signal attenuation evaluated.

For each full-scale walls and each time period, results are visualized in graphs reporting the parameters as a function of the measurement stations. Then, the outcomes, in terms of signal velocity and attenuation recorded on each position of the grid were post-processed together with the geometrical (x, y) coordinates of each station, by using a mapping SW in order to obtain grey-scale or coloured 2-D images which allows an easier, visual interpretation and comparison of such results. In order to simplify the data understanding, they were directly related to the geometry of the wall by superimposing the grey-scale 2D maps to the geometric layout of each brick wall. Some examples are reported in the following for all the walls, starting with wall PNDA, with reference to two or three ageing periods.

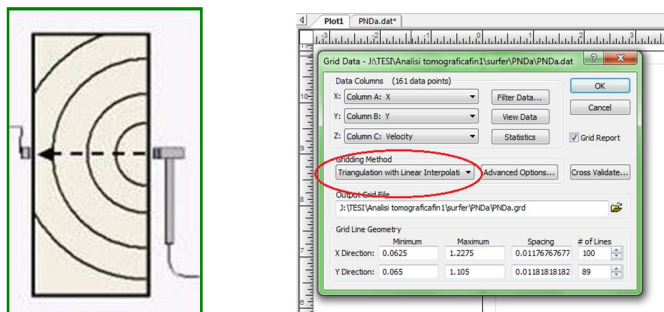


Figure 6.19: Scheme of sonic test in direct transmission mode (left), “Surfer” command window for plotting sonic results as coloured or greyscale maps (right)

PNDA

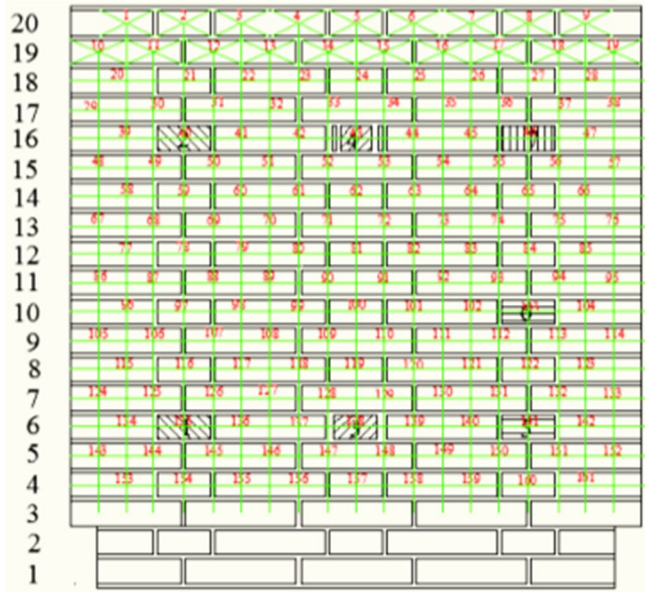


Figure 6.20: PNDA, measurement grid for sonic tests in direct transmission. The numbers in the grid refer to the transmitting (hammer) stations on the front side of the wall but a mirrored grid was marked also on the wall rear side for the identification of the accelerometer positions.

From the sonic tests in direct transmission in undamaged conditions of the wall carried out prior to the outside exposition of the same, the maximum obtainable resolution of the signal, R , was calculated from the time of contact, for a number of different measurement stations, as a function on the minimum wavelength, λ , in order to know the minimum dimensions of i.e. defects which are detectable in this specific testing conditions (Table 6.3). This analysis shows a signal resolution varying from 40 to 20 cm.

Table 6.3: PNDA, examples of evaluation of the wave maximum resolution R

Station	Tc [μ s]	fmax [Hz]	v [m/s]	λ_{min} [m]	R=1/2 λ_{min} [m]	R=1/3 λ_{min} [m]
10	276	3623	1984	0,55	0,27	0,18
34	316	3165	2083	0,66	0,33	0,22
88	334	2994	1953	0,65	0,33	0,22
91	336	2976	2193	0,74	0,37	0,25
107	302	3311	2118	0,64	0,32	0,21
108	414	2415	1923	0,80	0,40	0,27
120	352	2841	2272	0,80	0,40	0,27
134	320	3125	1893	0,61	0,30	0,20

In as-built conditions, the average value of signal velocity was approx. 2116 m/s, index of a good quality of masonry, without significant internal defects, i.e. voids. The velocity is correlated to the path crossed by the signal and, greater values were measured on the stations positioned on header bricks (avg. 2210 m/s) than on those crossing both the bricks and the internal vertical mortar layers (avg. 2104 m/s), indicating the sensitivity of the technique in discriminating between the two different patterns, although the difference is not so high (CoV =5%). It has to be noted, although outside the scope of this thesis, that the values more distant from the average signal velocity were measured on the stations positioned on the 7 stone inclusions (Figure 6.21). Low values of signal attenuation, quite uniformly distributed were recorded, confirming the good health-state of the wall, with the exception of one station, corresponding to the sandstone on the 6 brick course, left side of the wall (Figure 6.22).

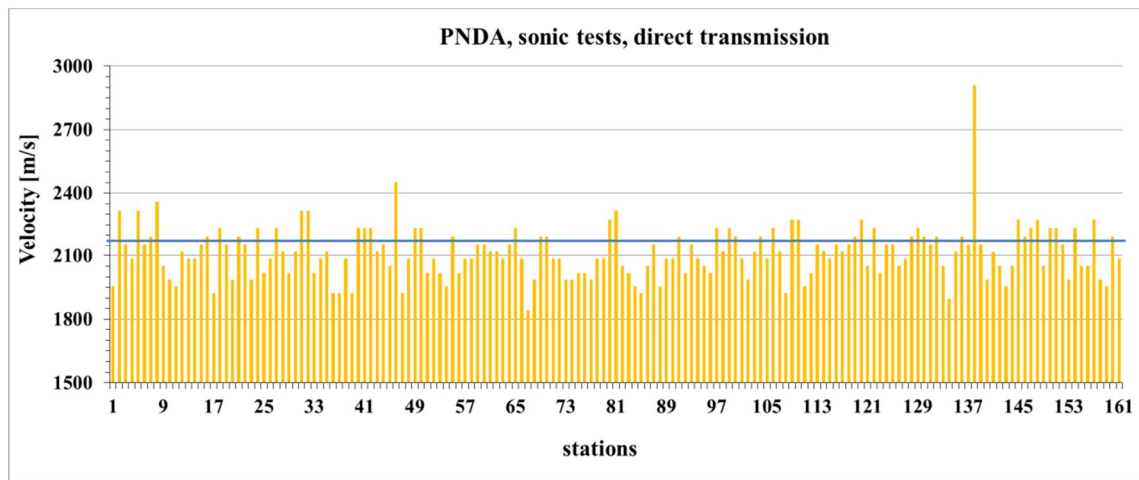


Figure 6.21: Wall PNDA in as-built conditions, sonic tests in direct transmission, signal velocity. The blue line represents the average velocity (2116m/s).

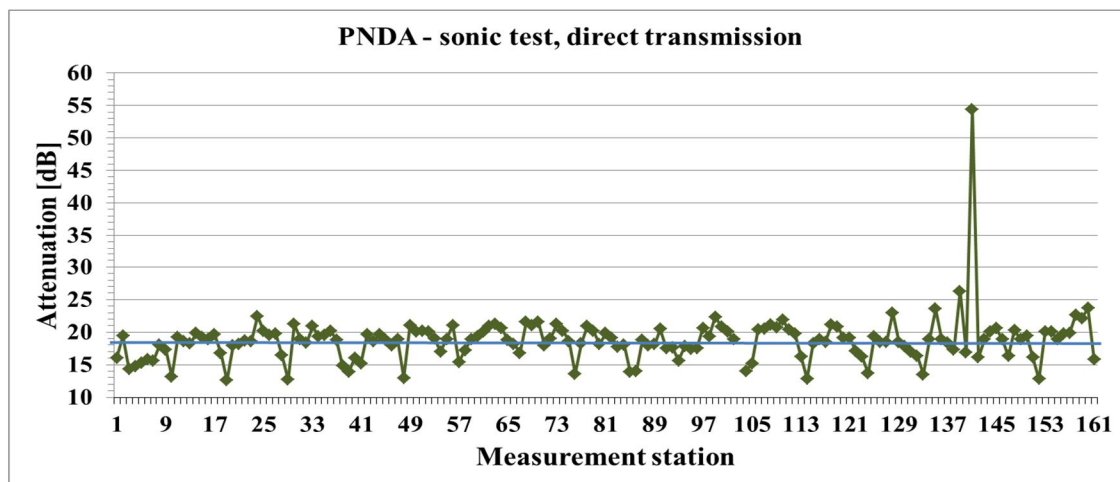


Figure 6.22: Wall PNDA, in as-built conditions, sonic tests in direct transmission, signal attenuation. The blue line represents the average signal attenuation (18.72 dB).

After two ageing summers the results obtained from the same measurements showed an increased velocity (avg. 2424 m/s) with more sparse data (C.o.V.=8.8%). The highest velocity

were measured from the stations located in the lower part of the wall, below masonry course 11 that is in correspondence of the moist areas (Figure 6.23).

In these positions, indeed, probably most of the pores of both brick and lime mortar (which composed also the plaster layer of the rear side) where, at this time period, filled with water or brine, easing the passage of the sonic signal, if compared with the previous situation in which the pores where filled with air.

Thus, apparently, the wall seemed in wealthier condition. Instead, the occurrence of some damages is visible from the values of signal attenuation, which, in average increased almost two times. The values of attenuation were not uniformly distributed and greatly deviated from the average value. The greater deviations were measured on the bottom part, below the evaporation band, indicating that some decays happened in this area (Figure 6.24).

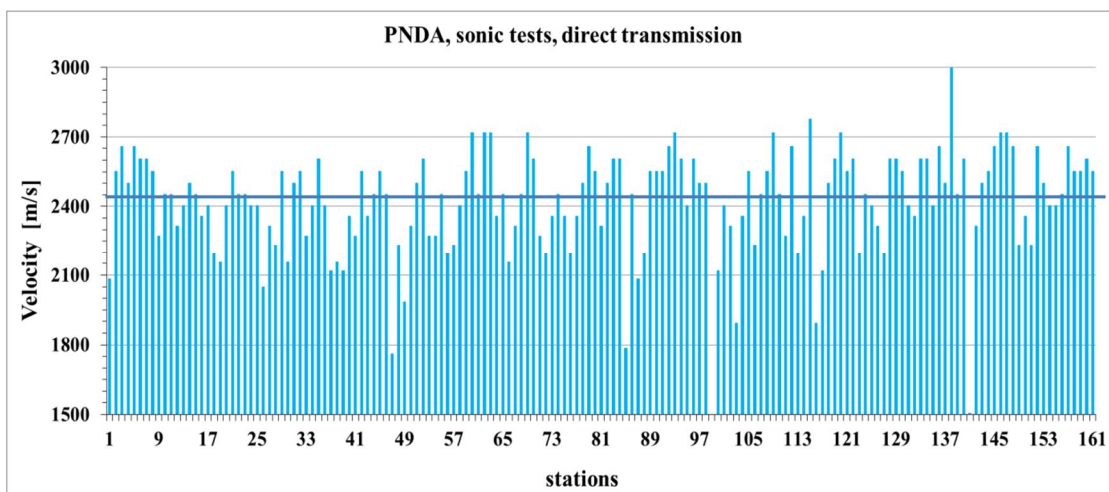


Figure 6.23: Wall PANDA, sonic tests in direct transmission after 2 years of natural ageing, signal velocity. The blue line represents the average velocity (2424 m/s).

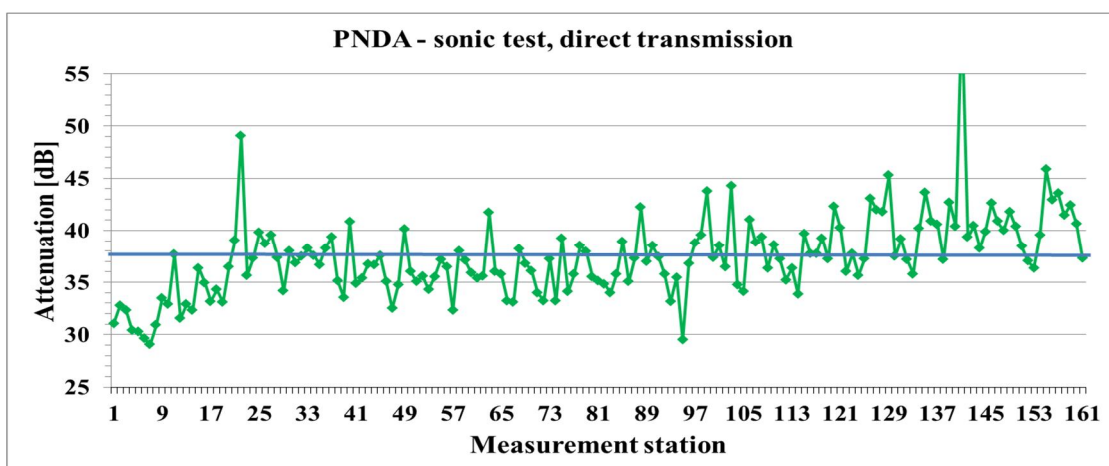


Figure 6.24: Wall PANDA, sonic tests in direct transmission after 2 years of natural ageing, signal attenuation. The blue line represents the average value (37 dB).

Finally, at the end of the 3rd ageing season, the values of signal velocity measured were still greater than those recovered in undamaged conditions (in average 2346 m/s vs. 2116 m/s) but lower than those obtained at the end of the 2nd season (Figure 6.25). This aspect, in addition to the high and sparse values of attenuation may suggest the progress of some degradation phenomena which started to be more relevant than the presence of moisture into the building materials (Figure 6.26).

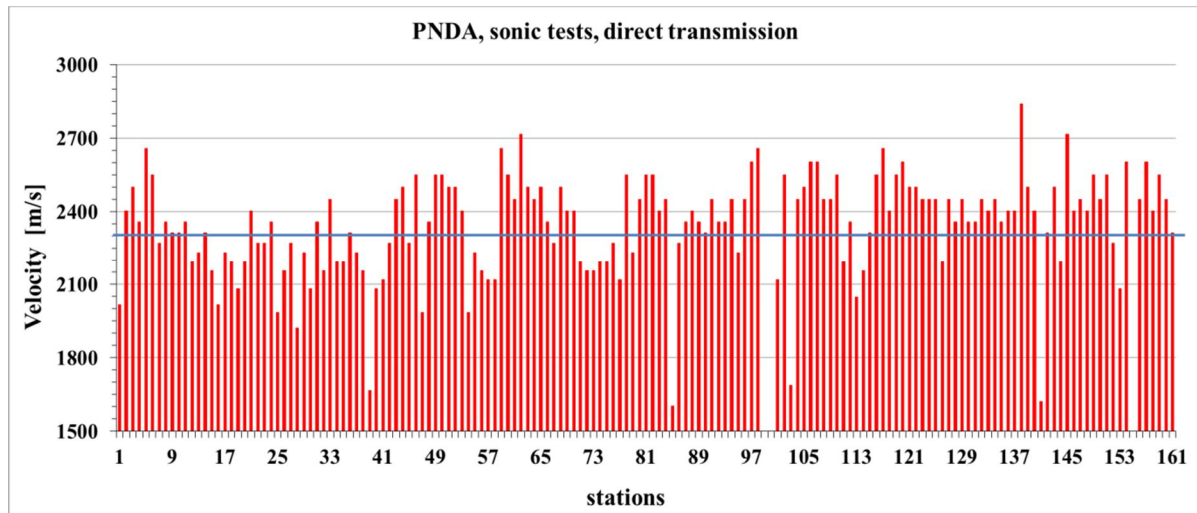


Figure 6.25: Wall PNDA, sonic tests in direct transmission after 3 years of natural ageing, signal velocity. The blue line represents the average velocity (2346 m/s).

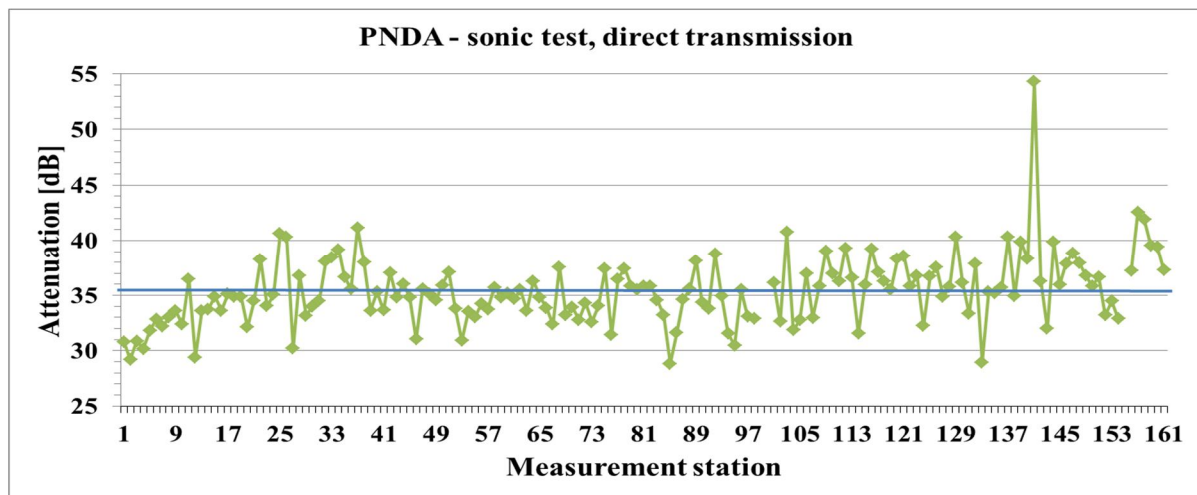


Figure 6.26: Wall PNDA, sonic tests in direct transmission after 3 years of natural ageing, signal attenuation. The blue line represents the average value (35.37 dB).

These considerations are clearly visible from the statistical evaluation of the averaged data (Table 6.4) and from the vertical profiles, along the height of the wall represented with the number of the masonry courses, obtained by averaging the values of signal velocity and attenuation on each course, respectively (Figure 6.27, Figure 6.28).

Table 6.4: PNDA, direct sonic tests, average values of signal velocity and attenuation for the three ageing periods

Full-scale wall PNDA	Undamaged	After 2 ageing summers	After 3 ageing summers
Velocity [m/s]	2116.26	2424.15	2346.02
<i>Dev.st.</i>	125.96	214.86	205.28
<i>CoV [%]</i>	5.95	8.86	8.75
Attenuation [dB]	18.73	37.3624	35.37
<i>Dev.st.</i>	3.74	3.88	3.12
<i>CoV [%]</i>	19.97	10.39	8.81

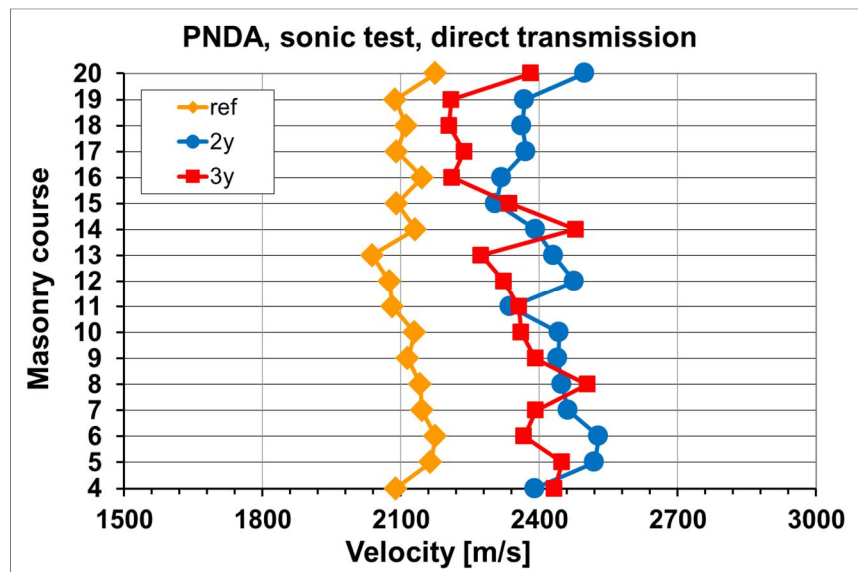


Figure 6.27: PNDA, sonic tests in direct transmission, average values of signal velocity vs. brick masonry courses for the three measurement campaigns

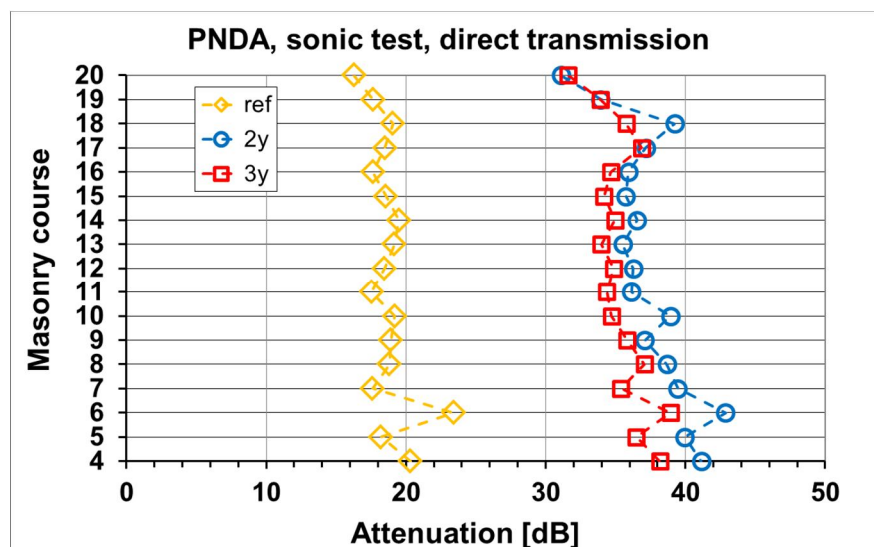


Figure 6.28: PNDA, sonic tests in direct transmission, average values of signal attenuation vs. brick masonry courses for the three measurement campaigns

Finally, in order to consider the sonic tests as a diagnostic imaging techniques, the outcomes of the punctual measurements were visualized as bi-dimensional maps superimposed to the geometry of the wall via a simple imaging processing software, Surfer®. The geometrical grid used to create such maps (b x h: 116.5 x 104 cm²) was greater than the real dimensions of the measurement grid as the origin of the reference system (x, y) was fixed on the external left border of the wall front side and at the middle height of the bricks of masonry course 3. This choice was made to simplify the post-processing procedure and to diminishing the disturbing border effects.

As an example, two grey-scale velocity maps obtained for the two extreme health-state condition of the wall, undamaged and after 3 years of ageing, are plotted with the same legend (Figure 6.29). Overall a shift towards greater values of velocity is evident after the three ageing summers, although the upper part of the wall seemed to have maintained almost the same values measured when the wall was in undamaged conditions. The undamaged maps appeared more homogeneous with the exception of localized light areas in correspondence of some superficial stone inclusions. After three year of ageing, these areas are still visible and also the bricks layouts appeared recognizable thanks to the different behaviours towards sonic signal of the header bricks respect to the positions characterized by two bricks with a mortar layer in between.

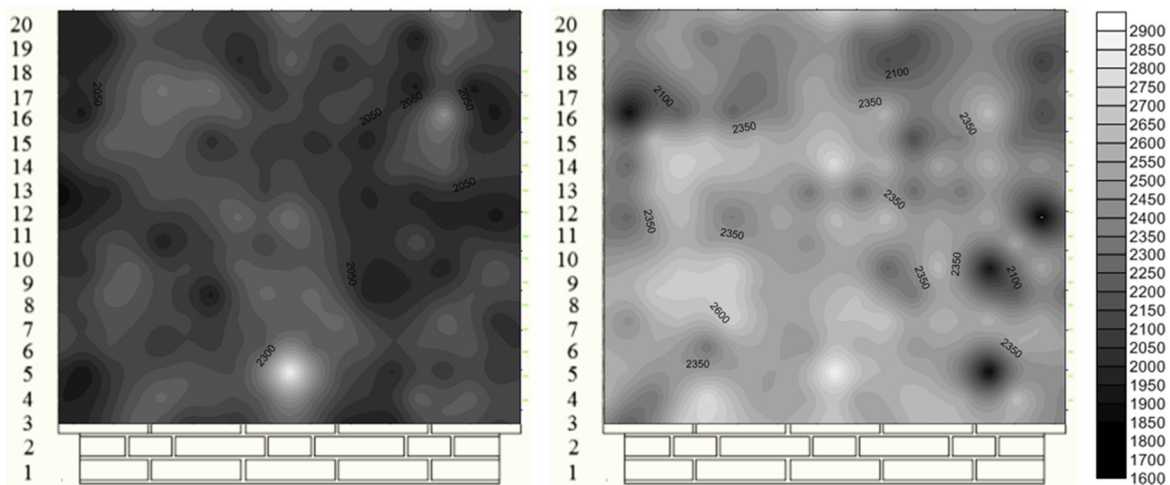


Figure 6.29: PNDAs, grey-scale maps of sonic velocities isoclines superimposed to the wall layout, front side in undamaged conditions of the wall (left) and after three years of ageing (right)

For brevity, for the following walls, only some results are shown with reference to the sonic measurements carried out in the two more different damaged conditions of the wall: as-built conditions and after 3 years of ageing.

PNDB

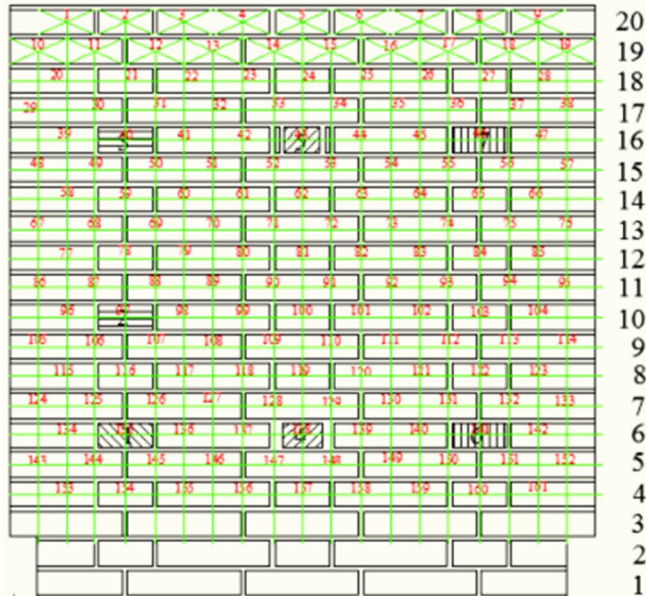


Figure 6.30: PNDB, front side, measurement grid for sonic tests in direct transmission

The average value of sonic velocity obtained in the wall in its as-built conditions approx. 2100 m/s is quite similar to the value obtained for PNDA, indicating also in this case a good quality of the masonry. The peak values are, also here, detected in correspondence of the stations located on the 9 superficial stone inclusions. The up and down movements are connected to the masonry layouts: greater values on the stations corresponding to headers bricks (Figure 6.31). The values of signal attenuations were quite uniformly distributed, indicating the absence of defects inside the wall.

After three years of ageing, the average value of the velocity increased (2360 m/s) but it was lower than that measured after two years of ageing. In this case, the signal velocities varied quite a lot around the average value (CoV=12% vs. 7% measured in the first year) and it is noticed an increase tendency in the bottom part of the wall (Figure 6.32). Moreover, as seen for the previous wall, the signal attenuation obtained after three years of ageing, increased, comparing with the values obtained in the as-built conditions of the wall, reaching an average value of 37 dB. The attenuation was not uniformly distributed all over the wall, indicating some differences, probably due to the presence of moisture and salt decay, inside the wall. In detail, it seemed that the masonry course 19 and 20 in the upper part of the wall were in completely different conditions, healthier, respect to the other courses (Figure 6.33).

The bi-dimensional maps obtained for the values of velocity for the wall in undamaged conditions and after three years of ageing are reported in Figure 6.34.

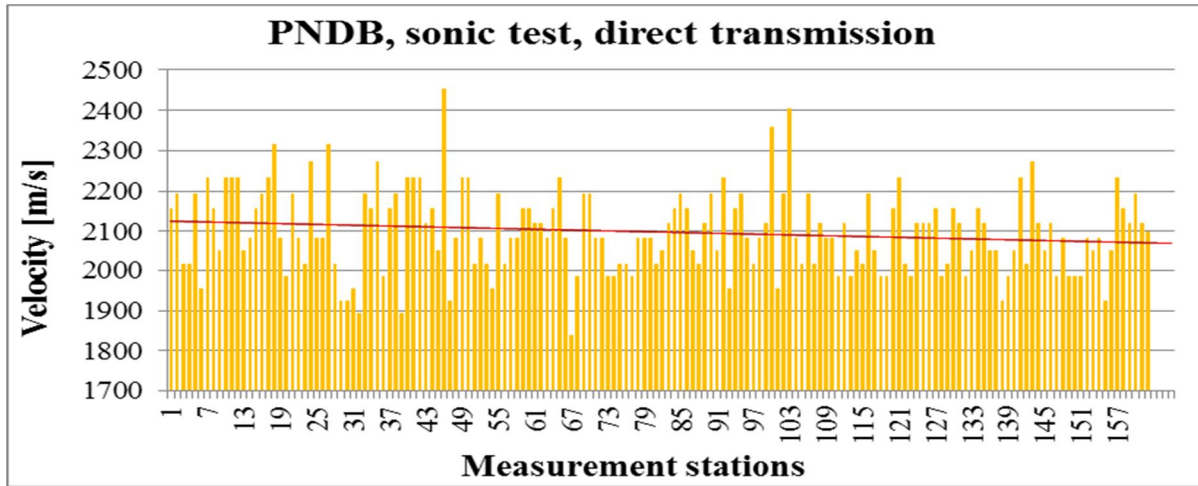


Figure 6.31: PNDB in as-built conditions, sonic tests in direct transmission, values of signal velocity. The red line represents the average velocity (2097 m/s).

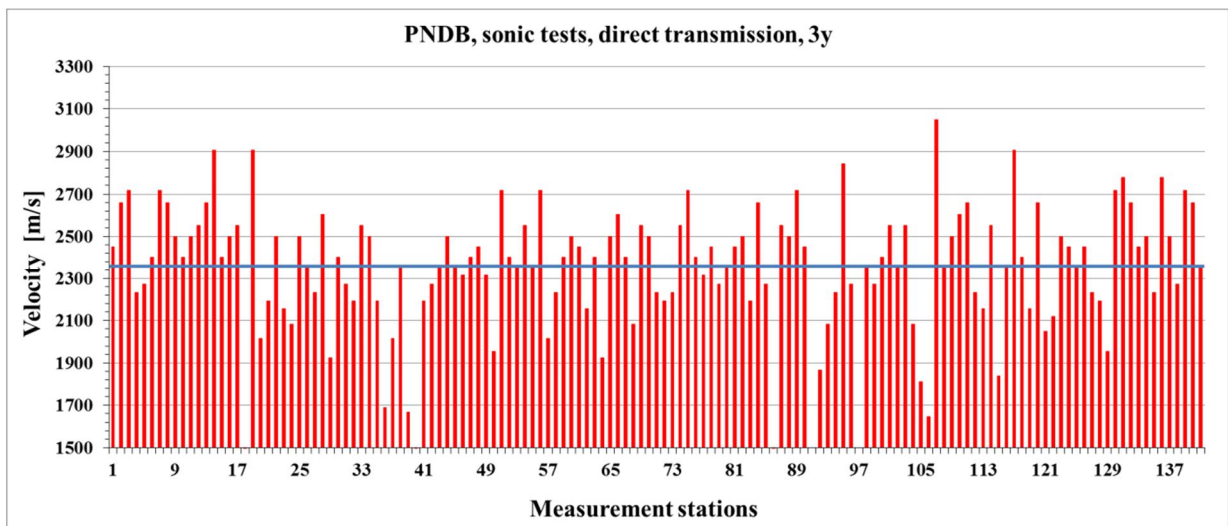


Figure 6.32: PNDB, sonic tests in direct transmission after 3 years of natural ageing, signal velocity. The blue line represents the average velocity (2360 m/s).

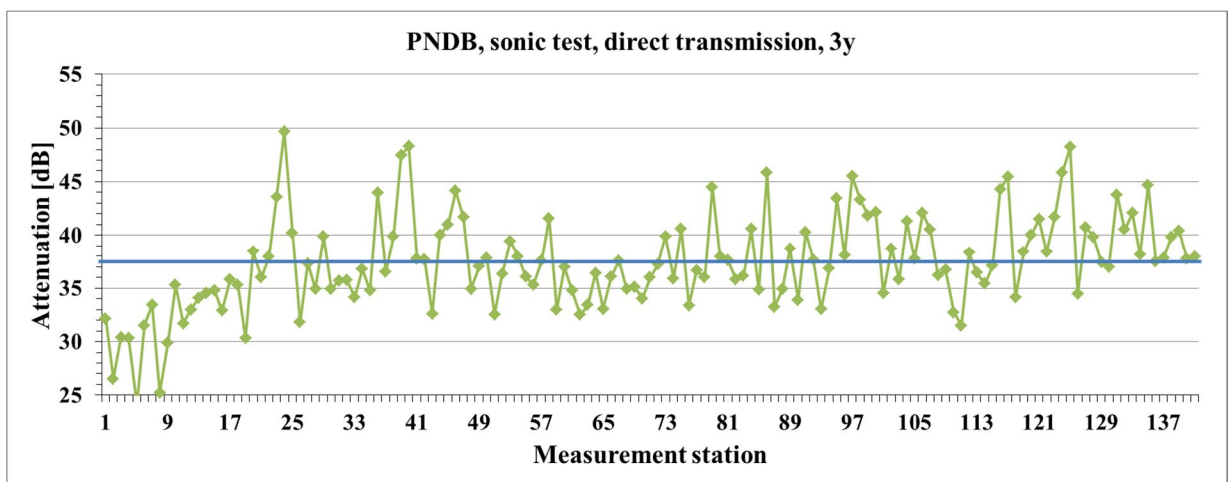


Figure 6.33 PNDB, sonic tests in direct transmission after 3 years of natural ageing, signal attenuation. The blue line represents the average value (37 dB).

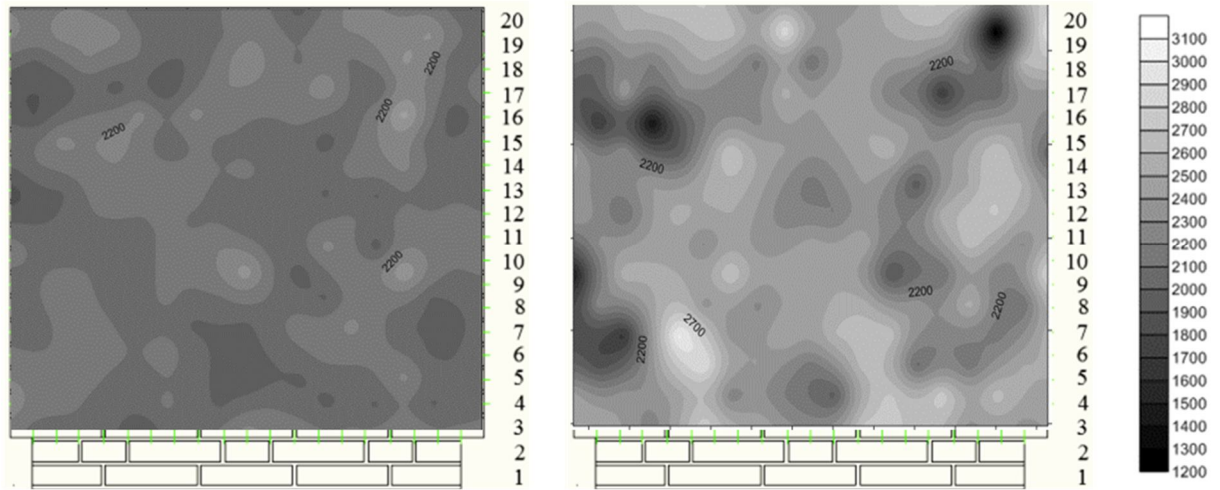


Figure 6.34: PND, sonic test: maps of direct velocities superimposed to the wall geometry, in undamaged conditions of the wall (left) and after three years of ageing (right)

PNDC

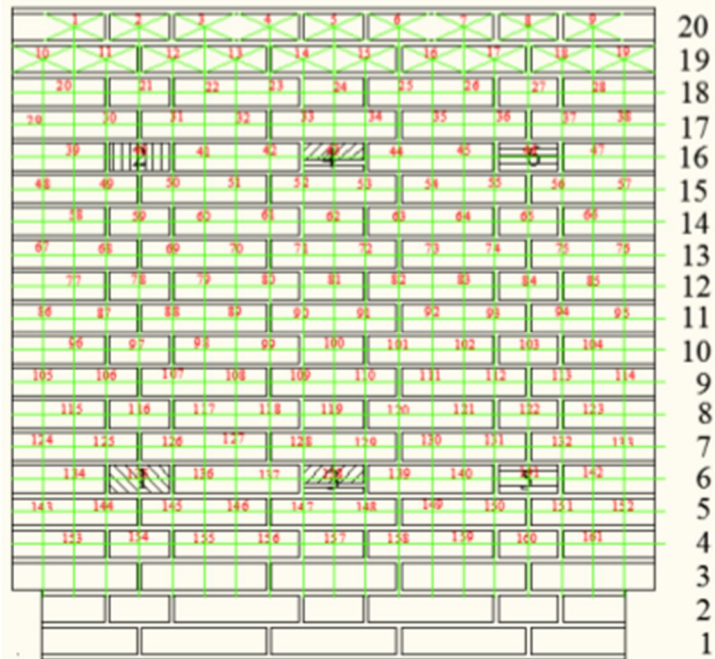


Figure 6.35: PNDC, measurement grid for sonic tests in direct transmission

Similarly to what has been reported for wall PNDB, after the visualization of the measurement grid, the reference values of velocity measured in the as-built conditions of the wall were reported together with those measured after three years of ageing, although, in this case, the natural ageing consisted only in the outdoors exposure also to rain water, without any brine addition into the tub (Figure 6.36, Figure 6.37).

The average value of velocity increased from 2132 m/s (similar to the values recorded for the other two 25cm thick walls in undamaged conditions) to 2441 m/s, greater than in the previous cases. While almost no variations were recorded in the velocities measured in the first campaign, with the exception of the stations located on the stone inclusions, sparse values (CoV=9%) are visible after three ageing seasons. Lower values near the bottom of the wall and greater value near the top.

After three years of ageing 36 dB of average attenuation was measured. The distribution of the signal attenuation is quite different along the wall: low values in the top masonry courses 19 and 20 (avg. 27 dB), uniformly distributed values in the centre part of the wall very close to the average one and high values below masonry course 9 (Figure 6.38).

By comparing the 2D maps of sonic velocities, also in this case an overall increase in the measured values is visible together with a more disperse velocities distribution (Figure 6.39).

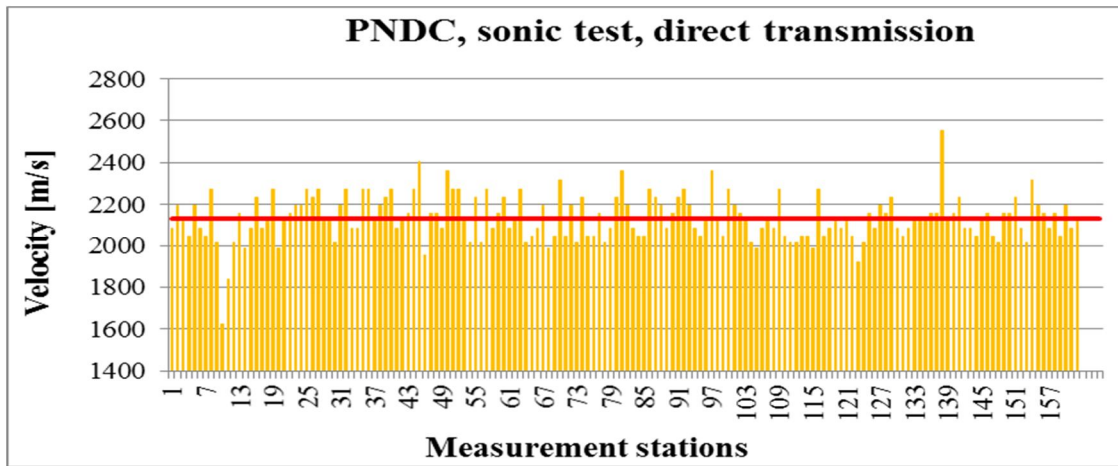


Figure 6.36: PNDC in as-built conditions, sonic tests in direct transmission, values of signal velocity. The red line represents the average velocity (2132 m/s).

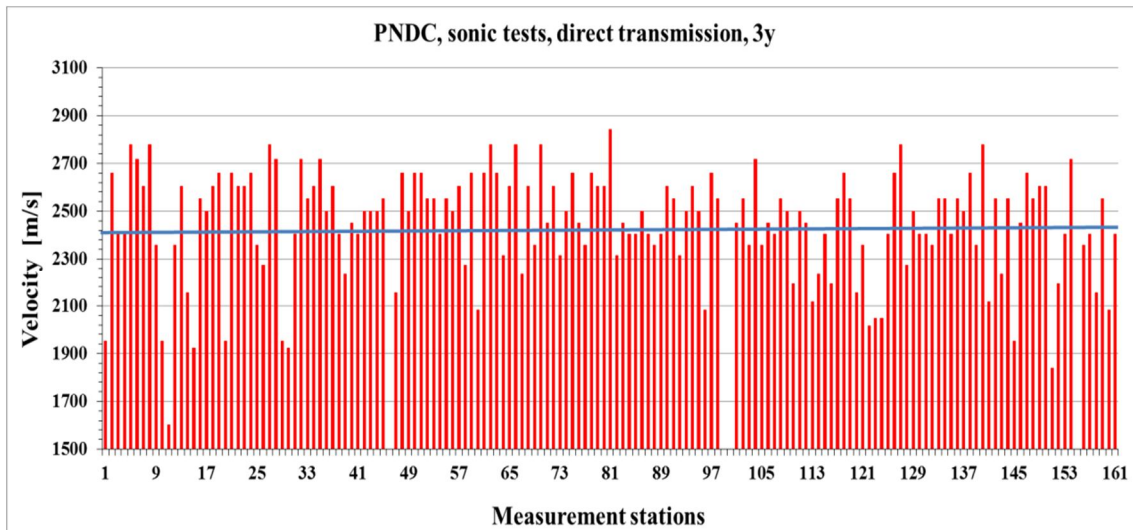


Figure 6.37: PNDC, sonic tests in direct transmission after 3 years of natural ageing, signal velocity. The blue line represents the average velocity (2441.35 m/s).

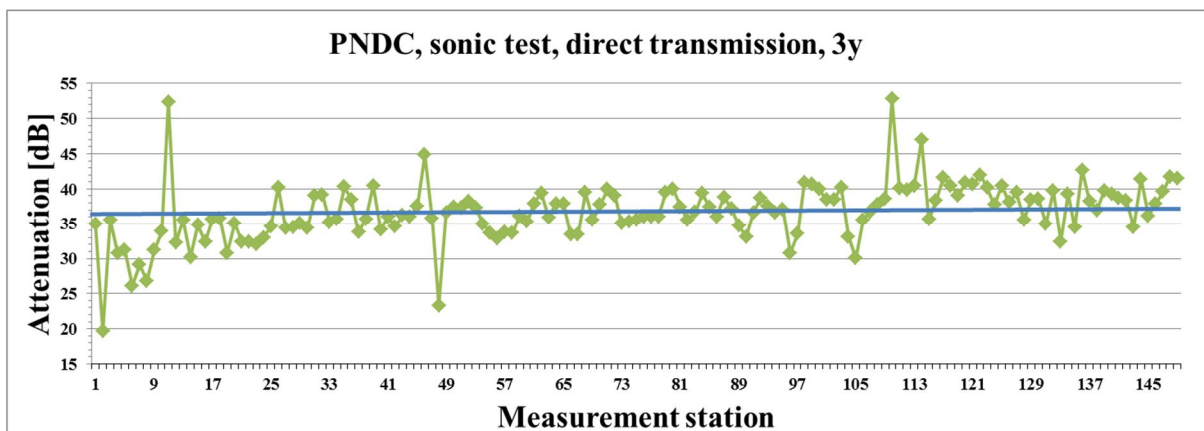


Figure 6.38 PNDC, sonic tests in direct transmission after 3 years of natural ageing, signal attenuation. The blue line represents the average value (36 dB).

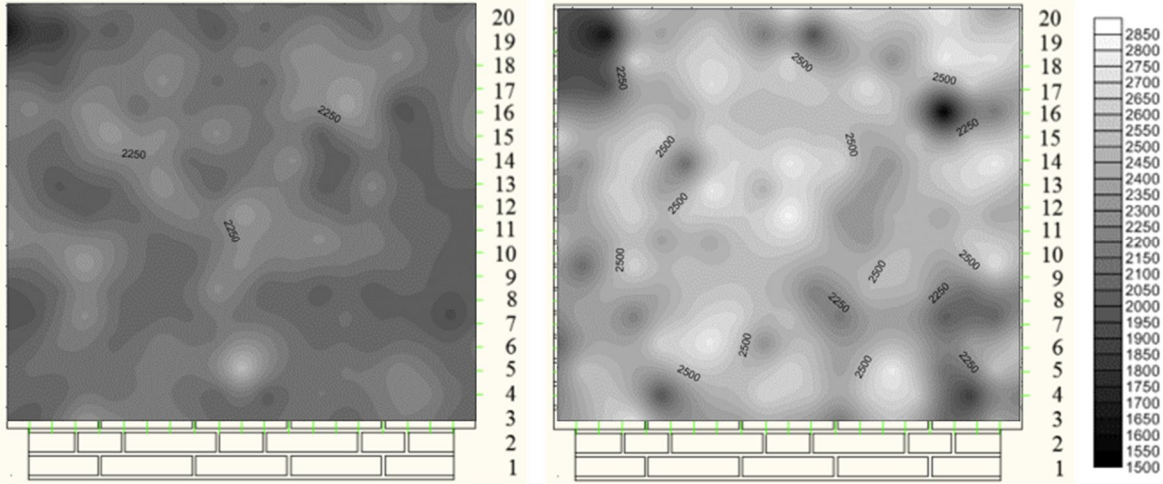


Figure 6.39: PNDC, grey-scale maps of sonic velocities isoclines superimposed to the wall layout, front side in undamaged conditions of the wall (left) and after three years of ageing only by rain water (right)

PNDD

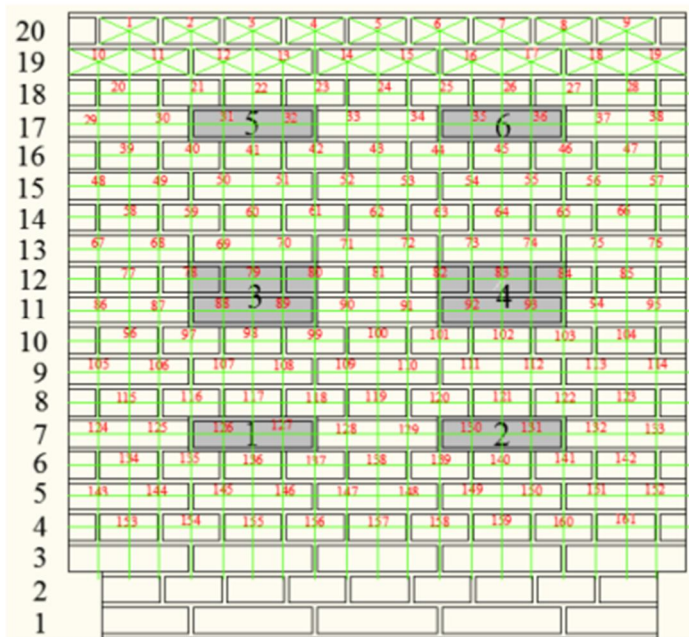


Figure 6.40: PNDD, measurement grid for sonic tests in direct transmission superimposed to the front wall layout, where the positions of internal simulated voids are highlighted

Prior to start the natural ageing procedure, the average value of sonic velocity measured for this 3-headers wall was approx. 2427 m/s. The non-uniform distribution of the velocity values are due to the presence of internal defects, simulated voids, causing a sudden drop down of the velocities in that positions (Figure 6.41).

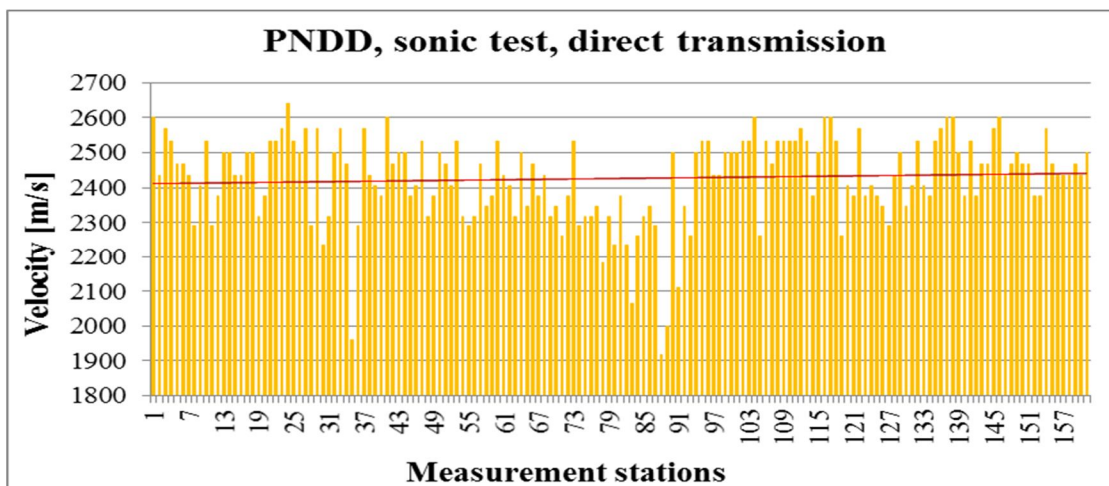


Figure 6.41: PNDD in as-built conditions, sonic tests in direct transmission, values of signal velocity. The red line represents the average velocity (2427 m/s).

Differently from what seen until now, after three years of ageing, a decreasing in average of the sonic velocity was measured obtaining a value of approx. 2300 m/s (Figure 6.42).. This lowering and the more sparse distribution of velocity values indicated the occurrence of

decay, i.e. due to the salt crystallization/hydration cycles, which are expected having seen the visible degradation of the wall front and rear surfaces (6.1). These variations on the sonic velocity values were associated to an incredibly increase in the signal attenuation in the lower part of the wall, the moist and damaged one, with values between 45 and 70 dB (Figure 6.43), confirming the presence of some decayed areas.

In the 2D maps, the level of the moist areas is visible, together with some delimited areas characterized by low velocity (Figure 6.44).

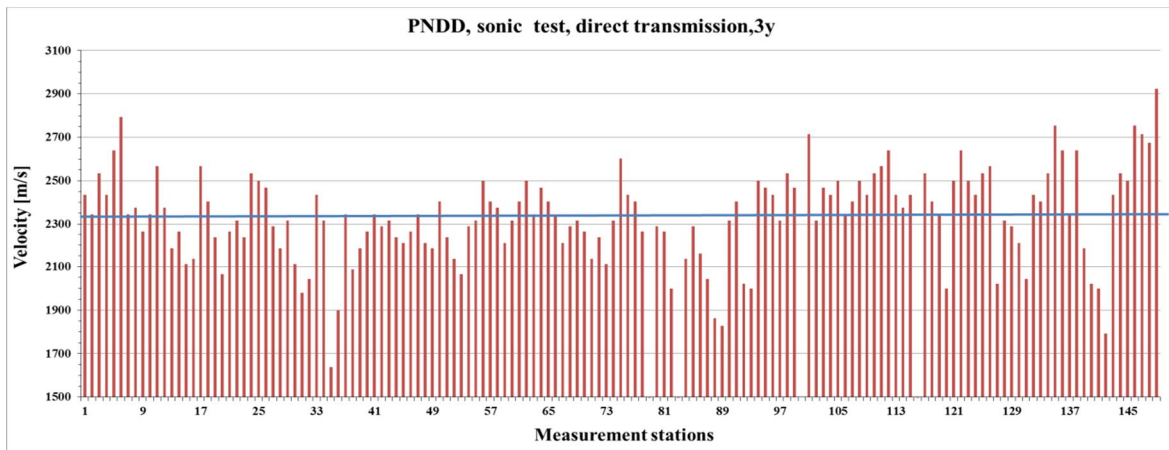


Figure 6.42: PNDD, sonic tests in direct transmission after 3 years of natural ageing, signal velocity. The blue line represents the average velocity (2328 m/s).

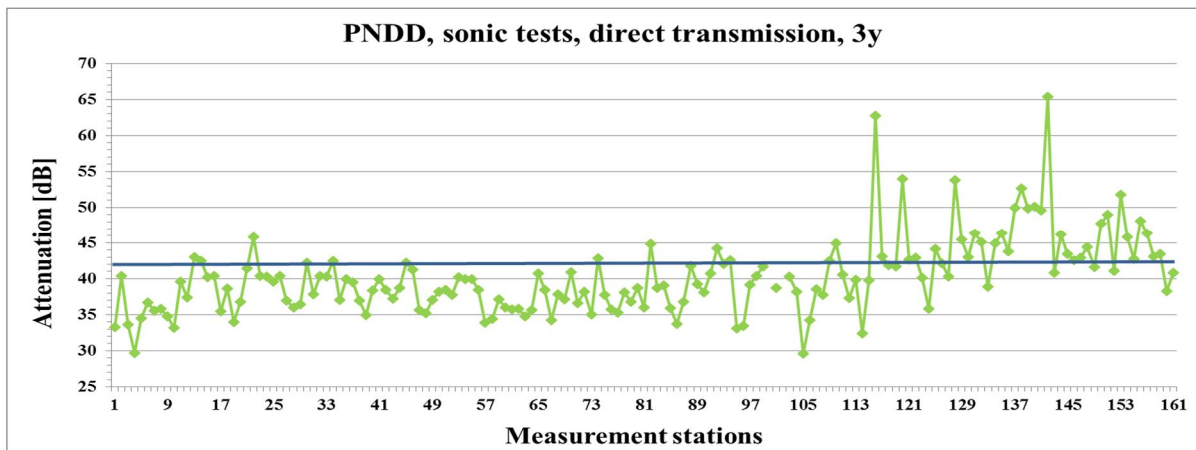


Figure 6.43 PNDD, sonic tests in direct transmission after 3 years of natural ageing, signal attenuation. The blue line represents the average value (42 dB).

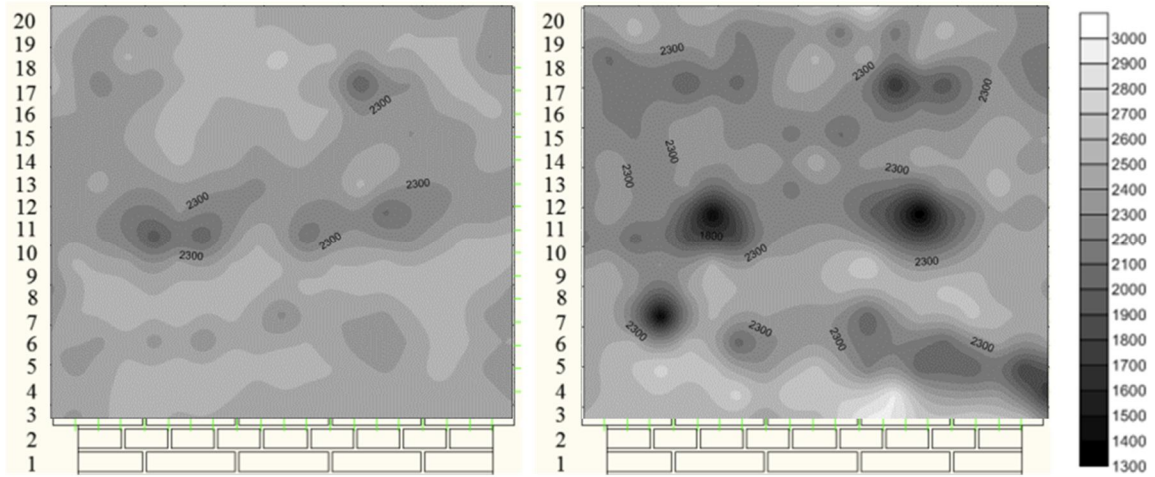


Figure 6.44: PNDD, grey-scale maps of sonic velocities superimposed to the wall layout, front side in undamaged conditions of the wall (left) and after three years of ageing (right)

PNDE

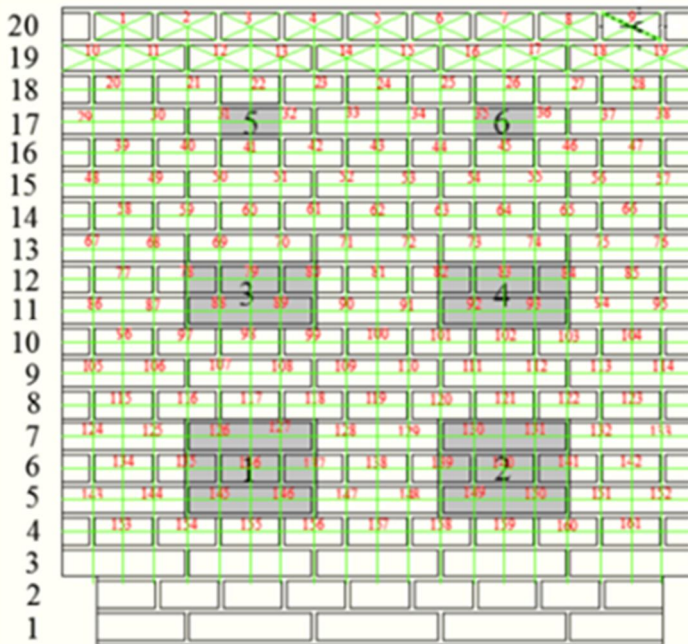


Figure 6.45: PNDE, measurement grid for sonic tests in direct transmission superimposed to the front wall layout, where the positions of internal simulated voids are highlighted

The average value of sonic velocity obtained in this wall in as-built conditions is equal to 2422 m/s, quite similar to that obtained in wall PNDD. The velocities are almost uniformly distributed with the exception of the values recorded in correspondence of the artificially simulated internal voids and visualized in blue (Figure 6.46).

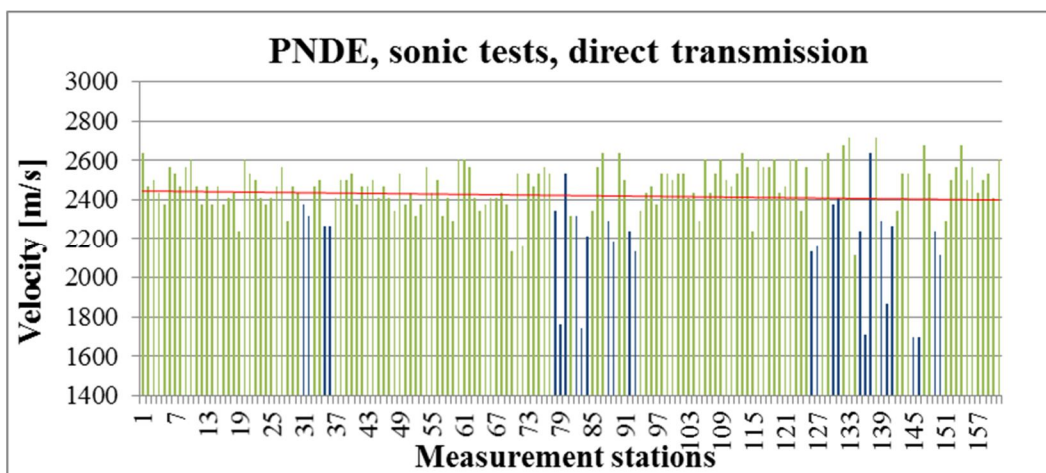


Figure 6.46: PNDE in as-built conditions, sonic tests in direct transmission, values of signal velocity. The red line represents the average velocity (2422 m/s).

After three years of natural ageing, the values of velocity were fairly regular in all masonry courses, with the exception of some measurement stations in the lower part of the wall (masonry course 4 to 9) on the areas interested by visible salt efflorescences on the surface and, in some cases, corresponding to the positions of internal defects (Figure 6.47). The average attenuation measured at this time period was equal to 40.3 dB and it presented an increasing tendency at lowering masonry course, rising from 32.94 dB recorded in the top course, 20, until a maximum average value of 46.4 dB recorded in the masonry course 4, characterized by the presence of salt crystallizations on the surface (Figure 6.48).

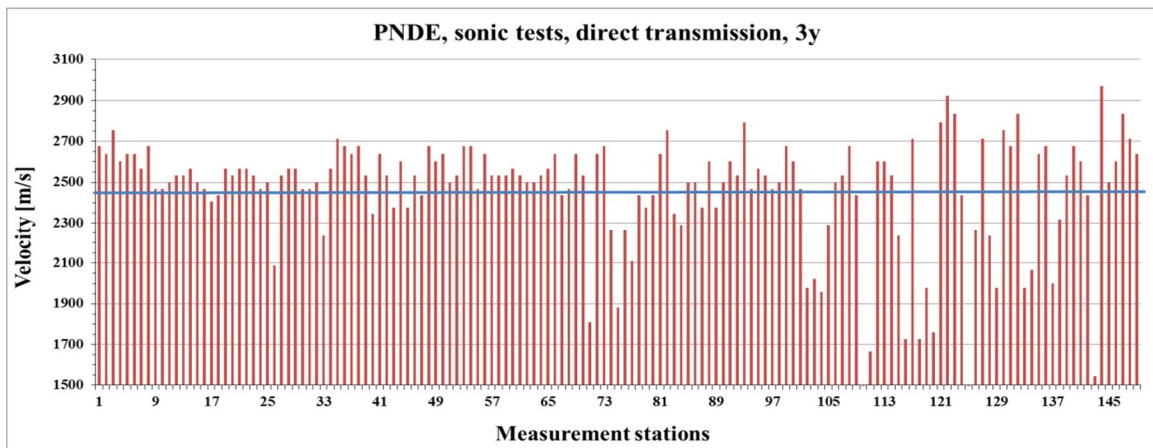


Figure 6.47: PNDE, sonic tests in direct transmission after 3 years of natural ageing, signal velocity. The blue line represents the average velocity (2450 m/s).

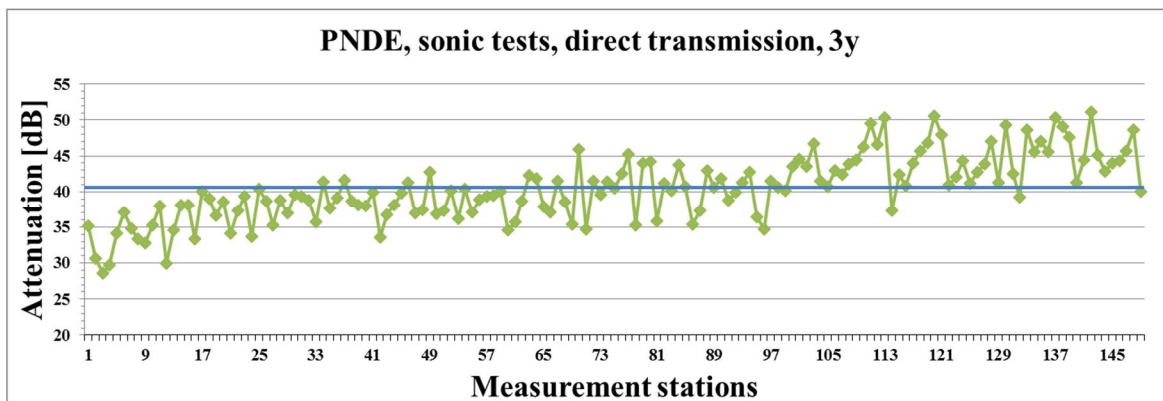


Figure 6.48 PNDE, sonic tests in direct transmission after 3 years of natural ageing, signal attenuation. The blue line represents the average value (40.30 dB).

The grey-scale maps of apparent velocities are reported for the two different measurement periods, prior to the beginning of the ageing and after three years of ageing (Figure 6.49). While in the image referred to the as-built conditions of the wall, the distribution was uniform with the exception of the areas, darker, characterized by defects, which are quite well identifiable, a more non-homogeneous distribution was recorded after three ageing seasons.

Here, the differences between the lower and upper part of the wall are evident and the positions of defects, somehow hidden by the occurrence of weathering decay effects, i.e. salt efflorescences.

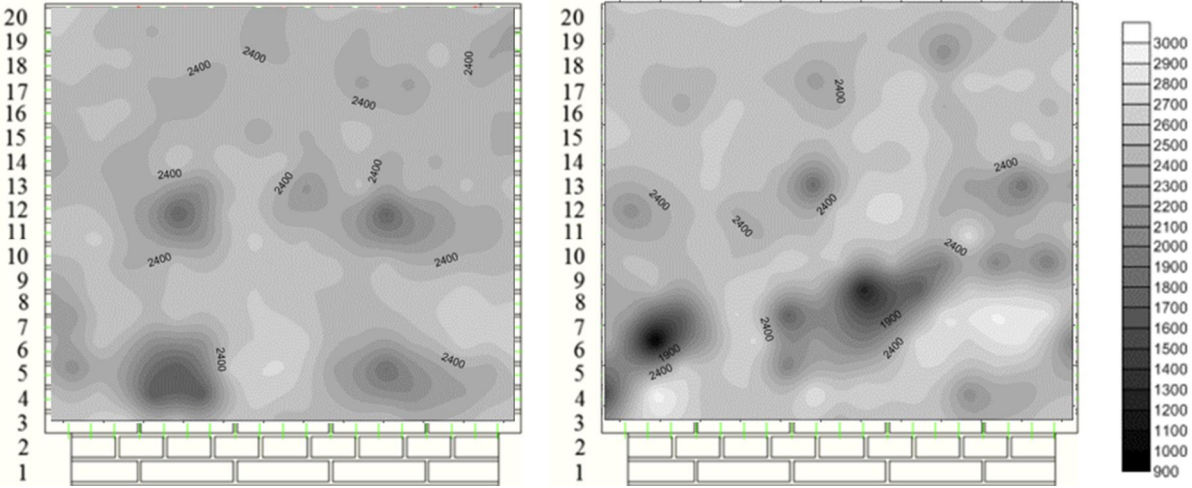


Figure 6.49: PNDE, grey-scale maps of sonic velocities superimposed to the wall layout, front side in undamaged conditions of the wall (left) and after three years of ageing (right)

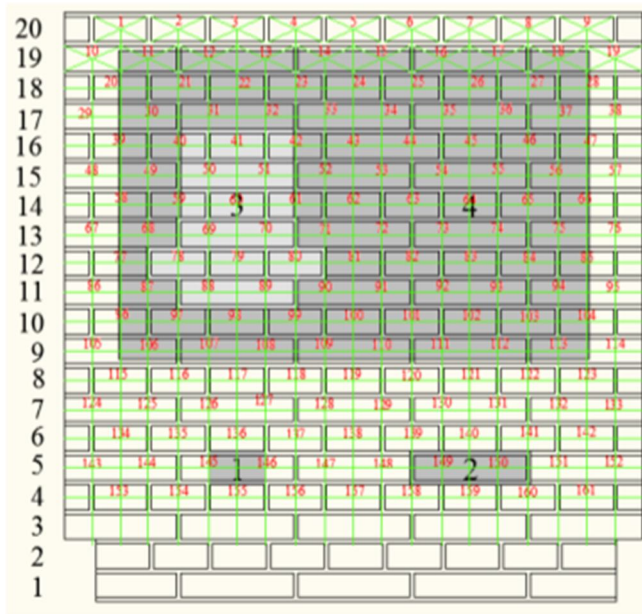
PNDF

Figure 6.50: PNDF measurement grid for sonic tests in direct transmission superimposed to the front wall layout

The average sonic velocity measured prior to the beginning of the weathering procedure was a little lower than in the other two three-header walls and approx. equal to 2350 m/s due to the fact that this wall is partly a rubble masonry wall (from masonry courses 9 to 19). Indeed, this portion, made of less consistent portions of bricks and mortar, presented on average the lowest velocity values measured, which were comparable to those measured in correspondence of the two simulated voids positioned at the masonry course 5 (Figure 6.51).

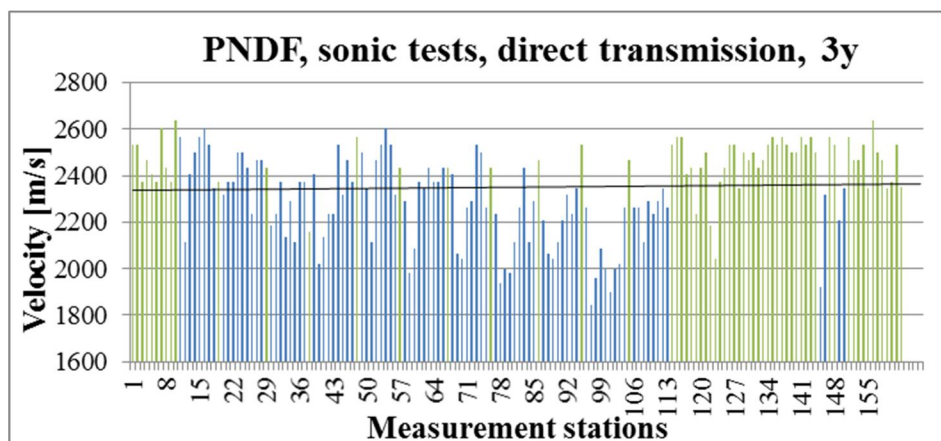


Figure 6.51: PNDF in as-built conditions, sonic tests in direct transmission, values of signal velocity. The black line represents the average velocity (2351 m/s). In blue the values recorded in correspondence of the rubble masonry and simulated defects

To evaluate the feasibility of the sonic technique in identifying the presence and spread of decay due to aggressive environmental agents, the same tests were carried out also at the end of the 2nd and 3rd seasons. The velocity values recorded in this last measurement campaign are on average lower than those recorded in undamaged conditions (2203 m/s) and presented an increasing tendency in the lower part of the wall (masonry courses 4 to 9) reaching the maximum values in masonry course 8, which corresponded to the evaporation band (Figure 6.52). The same increasing tendency moving from the top to the bottom parts of the wall is recorded in the values of signal attenuation, indicating the presence of degradation which worsened the transmission of the signal, by deadening it (Figure 6.53).

The differences between the top part of the wall, above masonry course 10 and the lower part, below the same masonry course, are clearly highlighted in the two-dimensional velocity maps for both considered periods. Although, after three years of ageing the separation between the two areas is more evident and the evaporation band appeared as a dark strip (lowest velocities) (Figure 6.54).

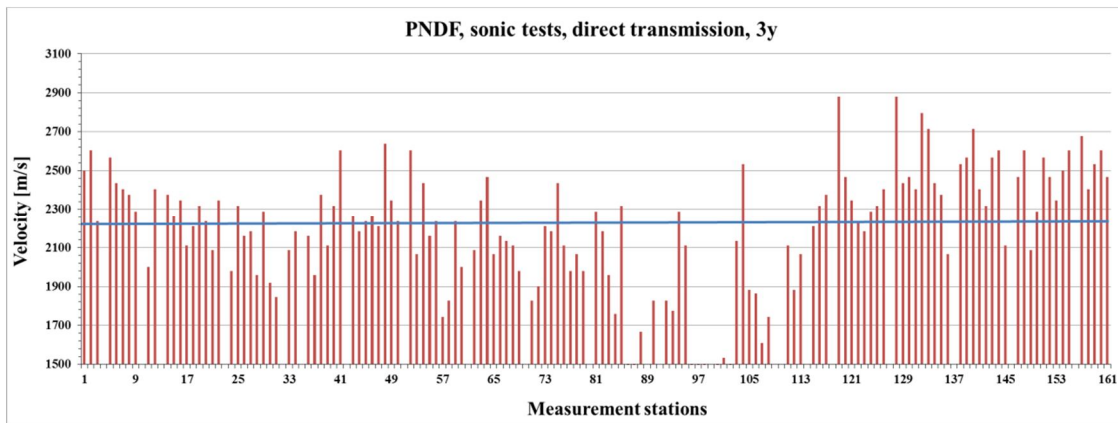


Figure 6.52: PNDF, sonic tests in direct transmission after 3 years of natural ageing, signal velocity. The blue line represents the average velocity (2203 m/s).

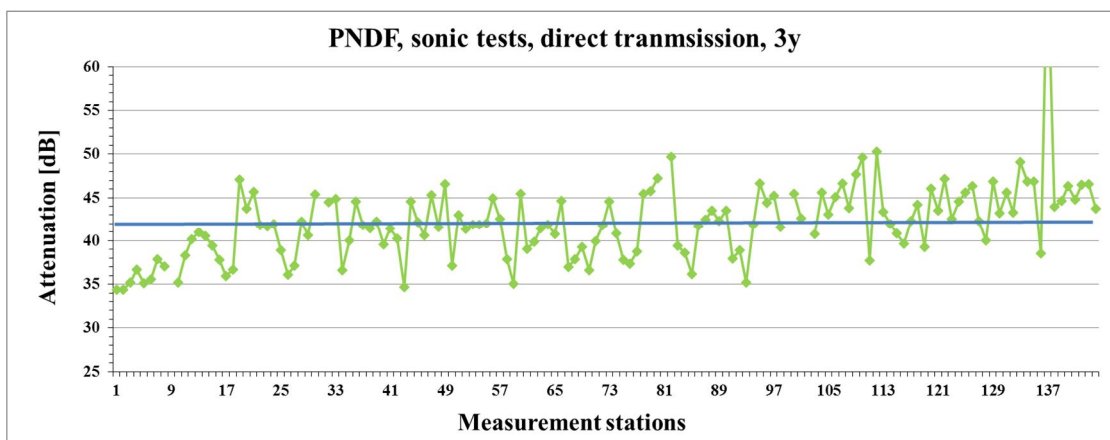


Figure 6.53 PNDF, sonic tests in direct transmission after 3 years of natural ageing, signal attenuation. The blue line represents the average value (42.05 dB).

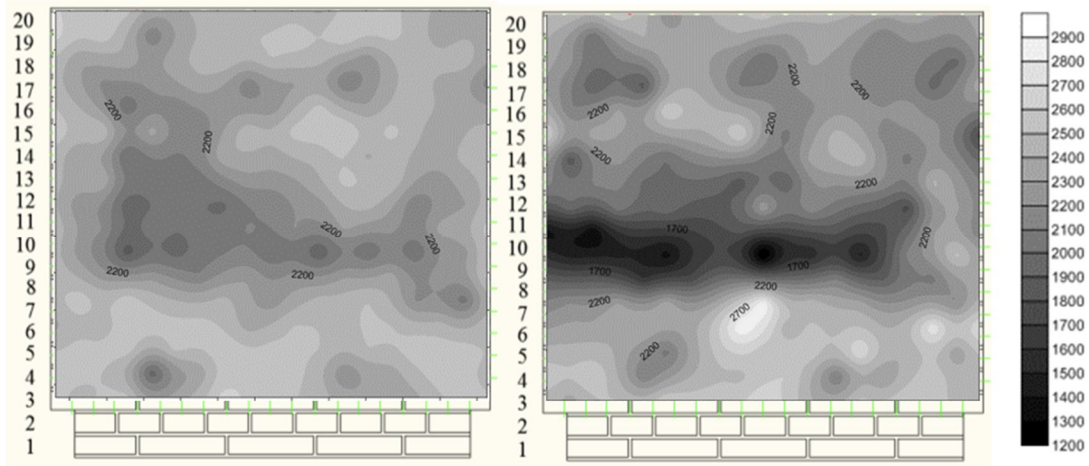


Figure 6.54: PPDF, grey-scale maps of sonic velocities superimposed to the wall layout, front side in undamaged conditions of the wall (left), after three years of ageing (right)

6.2.2. Sonic tests in surface transmission

In addition to the direct sonic tests (6.2.1) which allowed an in-depth evaluation of the health-state conditions of the investigated masonry walls, a superficial monitoring was carried out by means of sonic tests in surface transmission, employing an innovative procedure (report Smoohs). Usual measurement grids for these types of data acquisition are square or rectangular meshes on which the data are collected along vertical or horizontal paths. Instead, herein an innovative circular measurement grid for data collection was used, already proved to be effective (Colla 2007). The stations were positioned at the intersection between 8 concentric circumferences of radius varying from 0.1 m to 0.8 m and 16 diameters with different angles (i.e. Figure 6.55). Thus, both the hammer and the receiver (micro-accelerometer) were placed on the same wall surface that is the front. Also in this case, data were analysed in terms of time of flight (time difference between the starting instant of the hammer signal and the receiving time of the 1st wavefront) and sonic signal velocities (considering ideal path lengths). Results were visualized in such a manner to obtain a map distribution of the measured parameters.

The measurements were carried out only on the front sides of the walls, with the exception of wall PNDA in which also the rear side, plastered was studied.

As for the sonic tests in direct transmission, in order to evaluate if the technique was able to detect the damaging effects caused by a natural ageing procedure, since their beginning, the tests were carried out at three different time periods for each brick masonry wall: prior to the beginning of the ageing procedure that is in the undamaged conditions of the wall, after two ageing and after three ageing seasons. The data acquired for the as-built walls, were used as references.

Herein, by way of example, only some results are reported, with reference to one two-header and one three-header full-scale wall.

PNDC

The sonic measurements grid for superficial transmission test in 25 cm thick walls, and thus, for wall PNDC, contained 212 measurement stations. The results reported here refers to two different surveying periods: March 2010, before the beginning of the ageing procedure, and July 2011, during the 2nd ageing season. Note that, at the time period of the first campaign two of the six stone inclusions were still missing and that the weathering procedure consisted, in this case, only to the exposure to sun radiation and rain water.

The test grid used for sonic data acquisition is shown superimposed to the wall layout and indicating with numbers the consecutive positions of the hammer. The receiver, indeed, was fixed in the centre of the grid (Figure 6.55 left).

The results obtained for all the circumferences, in terms of time of flights, ToF, in the two measurement campaigns, are visualized in the same chart. The values measured in the as-built conditions of the wall are reported in black, while those referred to the damaged conditions in red. The circumferences are indicated in the legend by their radius (from 0.1m to 0.8m) followed by a letter representing the state of ageing of the wall (U=undamaged, D=damaged) (Figure 6.55 right).

This 2D data visualization for the reference period, immediately points out the areas of homogeneous brick masonry, where the values of ToF are aligned on the circles and identifies the positions of the stone inclusions. The comparison of data acquired in the two different periods highlights a good repeatability of measures, i.e. in line with expectation as no material degradation was detected in this wall.

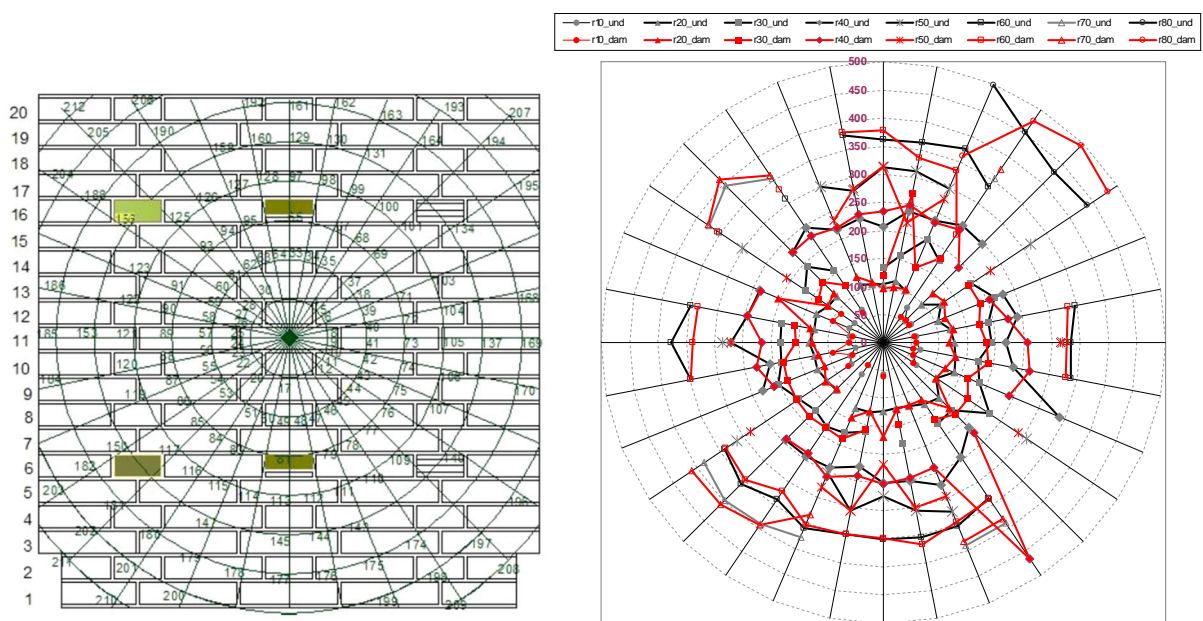


Figure 6.55: PNDC, front side: measurement grid overlapped onto the wall layout (left) and time of flight values collected in two different periods

PNDE

The same testing procedure was applied to evaluate the decay evolution also in this three-header wall, presenting internal simulated voids, and which was subjected to 0.05% -wt. Na₂SO₄ capillary rise during the outdoor exposure.

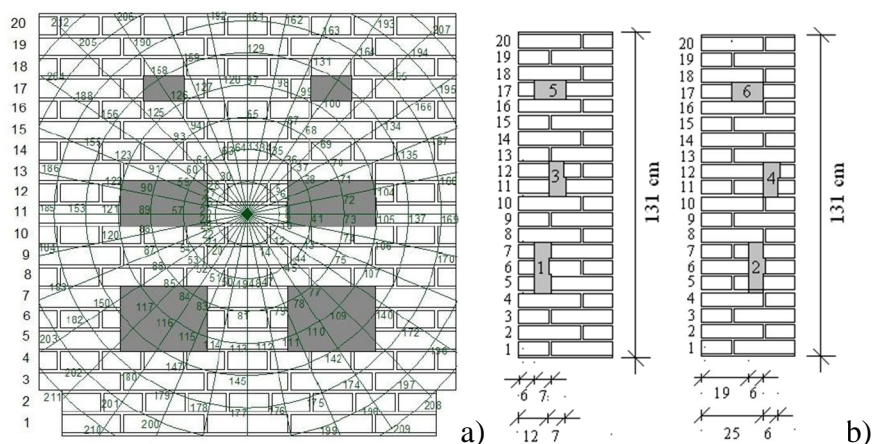


Figure 6.56: PNDE front: a) measurement grid of sonic superficial transmission tests overlapped to wall layout (numbers refer to the stations of the hammer), b) position of the defects within the wall thickness

The results reported herein, are referred to two measurement campaigns, one prior to the beginning of the ageing procedure (July 2010), and one after two ageing seasons (November 2011).

As for wall PNDC, time of flights (TOF) charts reporting with the same colour the stations belonging to the same circumference are used to present the sonic test results (Figure 6.57). Blue tones are used to represent the data acquired in as-built conditions while pink tones for the 2nd measurement campaign. Again, the circumferences are indicated in the legend by their radius followed by a letter representing the wall ageing state.

In as-built conditions, the arrival times of the individual signals gradually increase from the smallest circle, characterized by the shortest measurement paths to the increasing circles. Some anomalies in this behaviour are detected for the values from measurement paths crossing the defects, especially for those located on the wall's left side. The average velocity, calculated considering all the measurement paths, was of about 1720 m/s.

Instead, in the 2nd measurement campaign the arrival times do not gradually increase with increasing length of the paths except for the first 3 circumferences, where no changes occurred. The average signal velocity obtained was slightly lower than the one measured in 2010 and it was about 1695 m/s, index of a worsening of the masonry quality, but some stations placed in the lowest masonry courses, presented higher values of velocity than in 2010.

This effect was confirmed when the average sonic velocities at each semi-circle were plotted (Figure 6.58) as, below the horizontal diameter there is an increasing tendency of velocities from the 6th until the 8th circumference.

An apparent increase in velocity was detected in the wall masonry courses which were in saturated conditions at the time of data acquisition when the pores of the bricks and mortar joints were filled by the brine but it was associated with greater signal attenuation, index of the presence of a certain decay. Thus, the proposed procedure was able to discriminate areas at different moisture content but seemed not so sensitive in detecting the presence of i.e. salt efflorescences and further investigations are still required (A1.8).

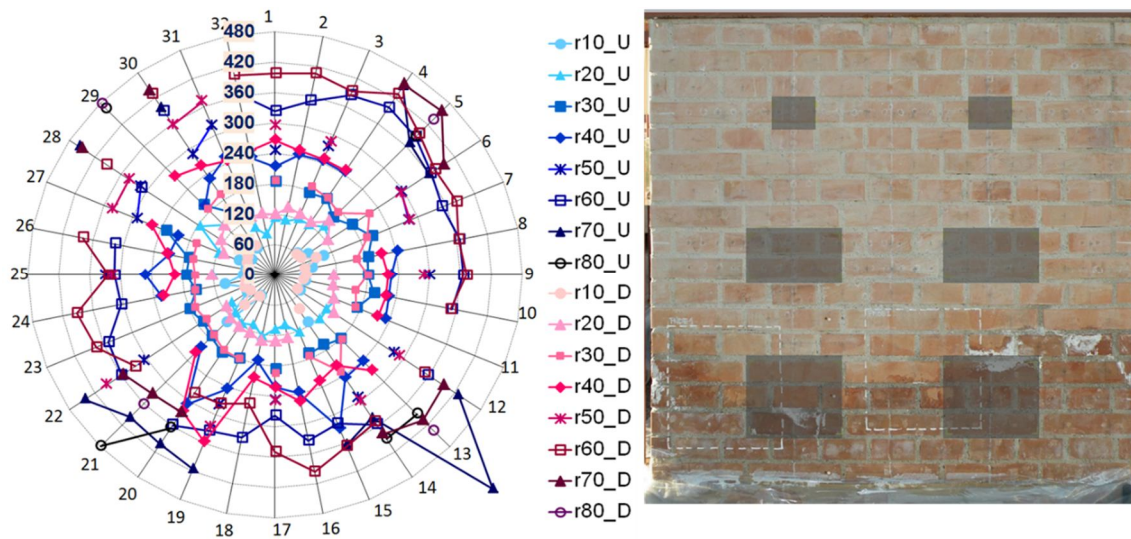


Figure 6.57: PNDE front: a) measurement grid of sonic superficial transmission tests overlapped to wall layout (numbers refer to the stations of the hammer), b) position of the defects within the wall thickness

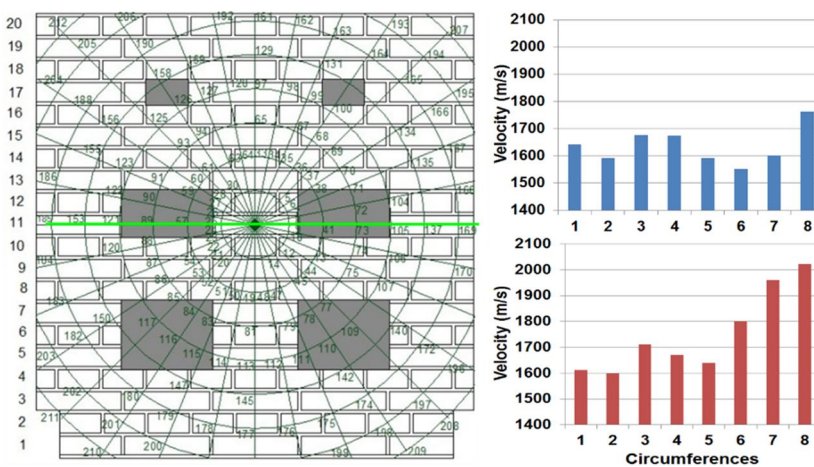


Figure 6.58: PNDE, sonic velocities at the end of the 2nd ageing season of stations above (top right) and below (bottom, right) the horizontal diameter of the test grid (left, in green)

6.3. Infrared thermography

The reliability of the infrared thermography technique in monitoring temperature and moisture evolution as well as material deterioration in unplastered and plastered brick walls' surfaces was tested in addition to its accuracy in identifying the wall texture behind plaster or detecting the presence of defects such as stone inclusions or simulated voids.

Repeated IR investigations were carried out also in collaboration with the researchers of the CETMA laboratory of Brindisi, during the different ageing seasons in order to monitor the evolution over time of the natural weathering effects and brine capillary rise.

A passive IR approach was considered but, on each measurement campaign, the IR surveys were repeated at different hours of the day (i.e. early morning, late morning, afternoon) that is both during heating or cooling transient phases, in order to obtain the best performances of the this approach by exploiting the effects of sun expositions, being the brick walls outdoors exposed.

Each monitoring survey consisted in acquiring simultaneously images both in the visible and infrared field. The data acquired were qualitatively analysed (chap. 3.2) in order to identify the positions of stone inclusions and defects, and correlate aspects such as the effects of weathering visible on wall surfaces with those identified by IRT.

Some exemplary results of this monitoring are reported below.

Since the first IR investigations carried out after 2 months of ageing, in the early morning, the reliability of the technique, although applied in passive mode, in detecting material discontinuities, as for example inclusions of stones of different origins, was demonstrated (Figure 6.59). The identification of defects within the masonry thickness, taking IR images of the front sides of the walls exposed to South was also easier in the early morning. Instead, the same identification, looking at the rear sides of the wall was easier at noon, during the cooling phase of the surfaces. Due to the scarce penetration power of the technique, which is a superficial technique, only the most superficial defects were detectable (i.e. Figure 6.60, Figure 6.61).

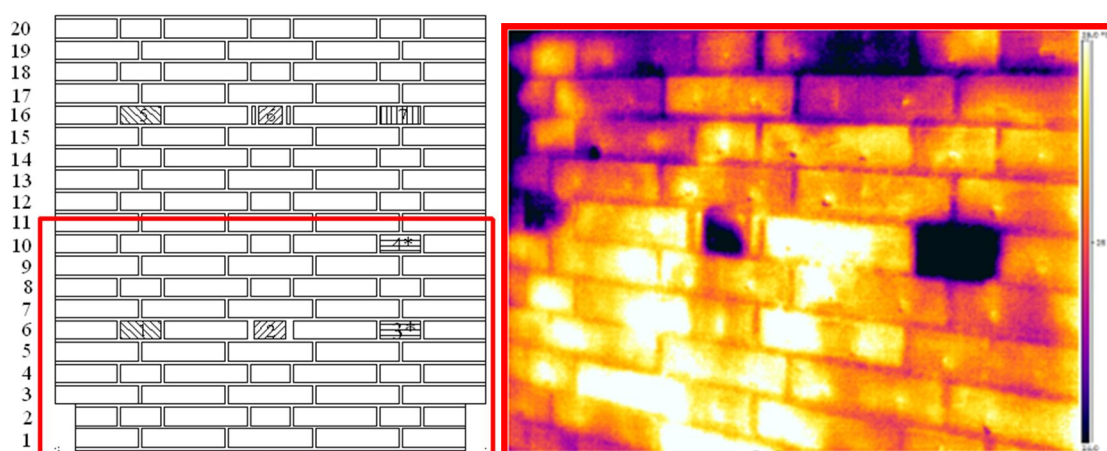


Figure 6.59: PNDA, front side, September 2010, early morning: material discontinuities visible as cold spots

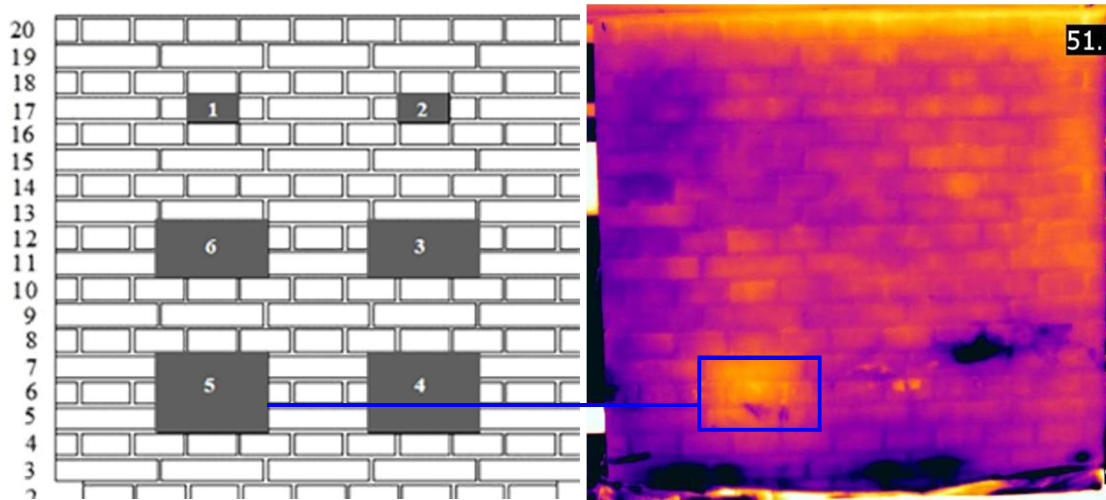


Figure 6.60: PNDD rear side, October 2011, noon: identification of position and extension of a hidden void



Figure 6.61: PNDE, front side, September 2011, early morning: clear detection of a simulated void within the wall thickness

For the purposes of this thesis, however, it was most important to assure the feasibility of the technique in monitoring moist areas and salt decay effects.

Qualitatively, the IR thermography allowed identify the level of capillary rise, detect surface areas with white salt efflorescences, which appeared colder in the IR field, as well as delamination on bricks since their first appearance (Figure 6.62). However, because of logistic laboratory constrains which, for the majority of full-scale walls studied, allowed acquiring thermograms only on little portion of the walls, the determination of the height of the moist level was not so easy i.e. for wall PNDA (Figure 6.63).

Instead, for walls PNDD and PNDE which presented at least one surface free to be entirely monitored via IRT, the exact distribution of moisture from brine capillary rise could be determined by looking at the temperature variations along vertical profiles. Some examples referring to different ageing period are reported (Figure 6.64, Figure 6.65, Figure 6.66).

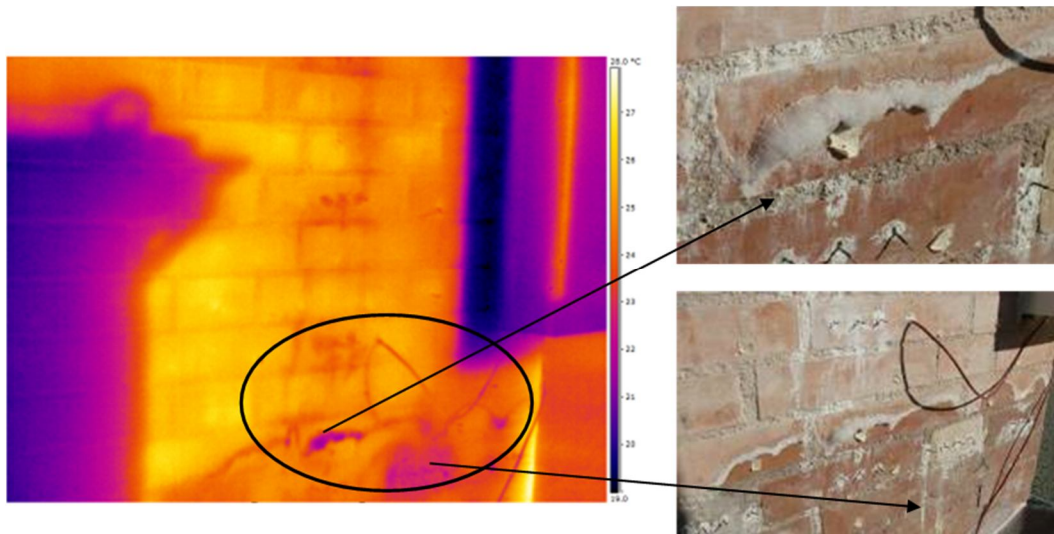


Figure 6.62: PNDB, front side, early morning: salt efflorescences and bricks with different thermal properties were detected

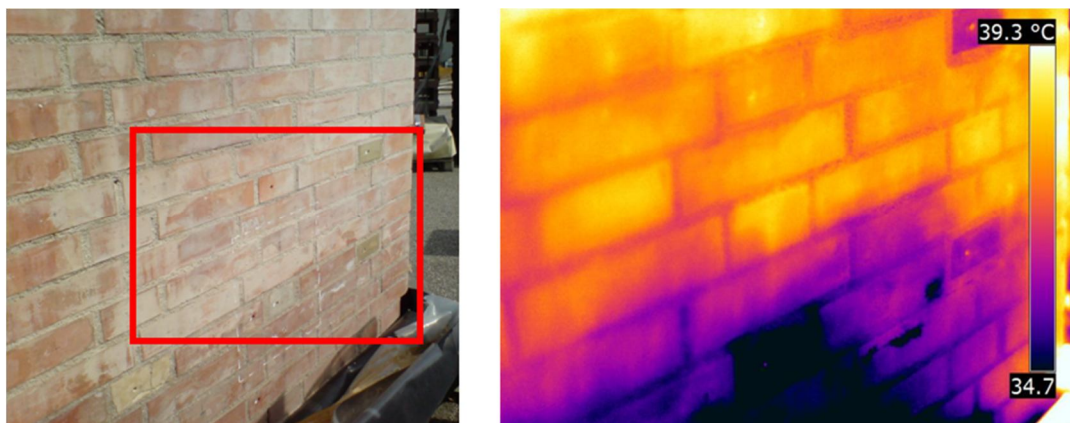


Figure 6.63: PNDA, front side, September 2011, early morning:

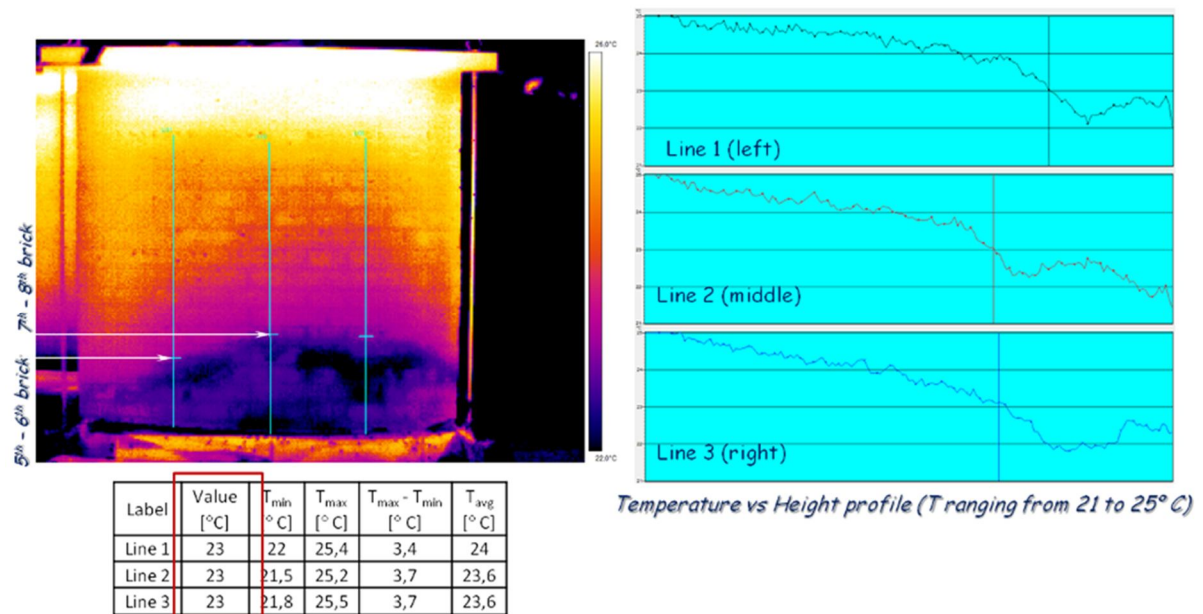


Figure 6.64: PNDD, rear side, September 2011, afternoon. Evaluation of moisture content [Largo]

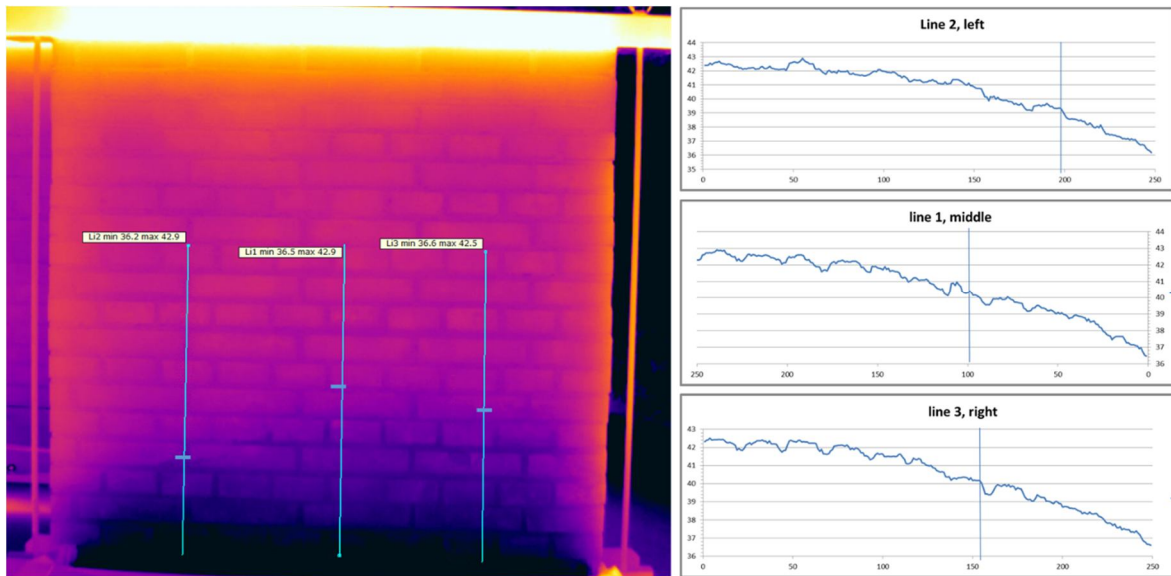


Figure 6.65: PNDD, rear side, September 2012, afternoon. Evaluation of moisture content trough vertical profiles of temperature

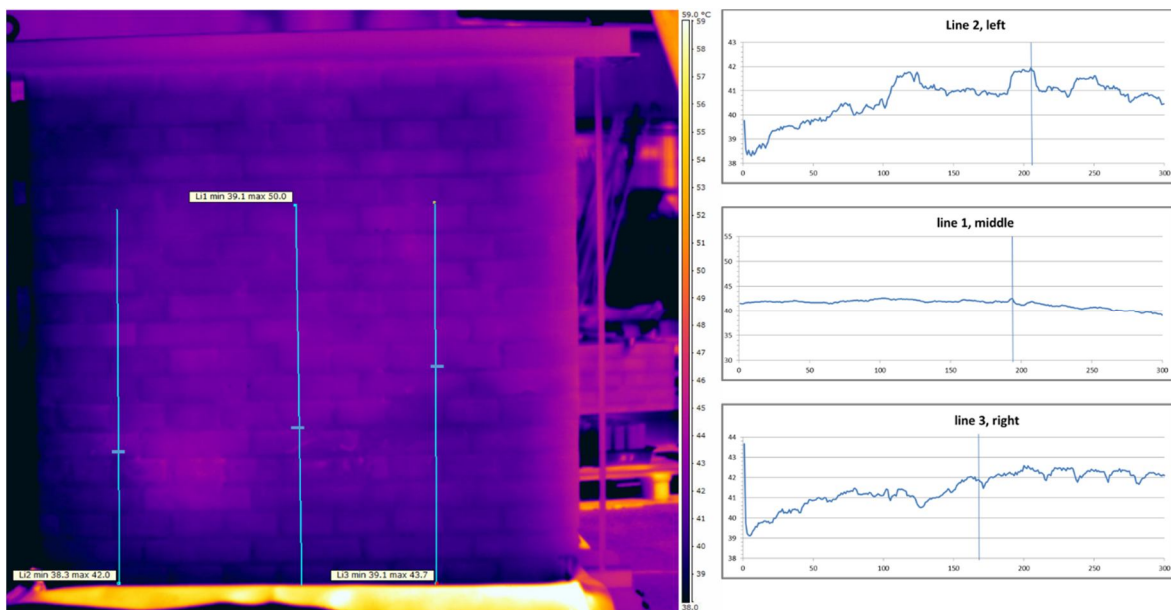


Figure 6.66: PNDE, front side, September 2012, afternoon. Evaluation of moisture content trough vertical profiles of temperature

6.4. GPR radar

With the aim of obtaining an in-depth monitoring, repeated GPR radar surveys were also carried out on the outdoors exposed brick walls, at different time periods, corresponding to the different ageing levels.

The purpose of these investigations was to evaluate the moisture content and distribution within the masonry walls and its variations over time as well as the presence of salt contaminations due to weathering in addition to brine capillary rise from the base.

A GSSI system and medium to high frequency antennas were employed (3.4). Vertical and horizontal survey lines were considered on both surfaces of the walls in order to obtain data on vertical or horizontal sections of the same walls.

Herein, only some examples of the results obtained almost at the beginning of the ageing process are reported. They are visualized as 2D images in grey colours, radargrams, and are aimed at showing the potentiality of this fast and accurate non-destructive technique for the considered investigation purposes.

First of all, some results obtained for wall PNDC at the beginning of the ageing period are visualized. The conditions of masonry were: no solution on the bottom, but high moisture content on the lower masonry courses due to rainwater. The acquisitions were carried out in July 2010, with a Palm 2 GHz antenna, along several vertical and horizontal survey lines (Figure 6.67).

These tests were aimed at investigating the high moisture content due to rainwater, which was visible as a darker areas, without any deliberate salt contaminations of the masonry, with the exception of the amount of soluble salts within the porous materials. Two representative raw radargrams collected along two vertical survey lines are reported in Figure 6.68. Although these data were not post-processed, they showed clear information. Near the vertical black straight line corresponding to the reflection of the surface, some little hyperboles are visible, indicating the positions of the horizontal lime mortar joints separating the brick courses. The vertical mortar joints in the middle of the wall section are also visible as hyperboles vertically aligned, in the middle part of the radargram. The back surface reflection is visible, allowing determining i.e. the wall thickness. This reflection was not constant along the wall height. Indeed, in the lower part of the radargram, the reflection from the rear side is curved and the wall appeared thicker (red arrows in Figure 6.68). Actually, this is only due to the presence of moisture areas which affects the GPR data. Thus, from these files, the height of the moist level is clearly measurable; moreover looking at the changes in the curvature of the rear side reflection, it is possible to discriminate also saturated area from moist and dry ones.

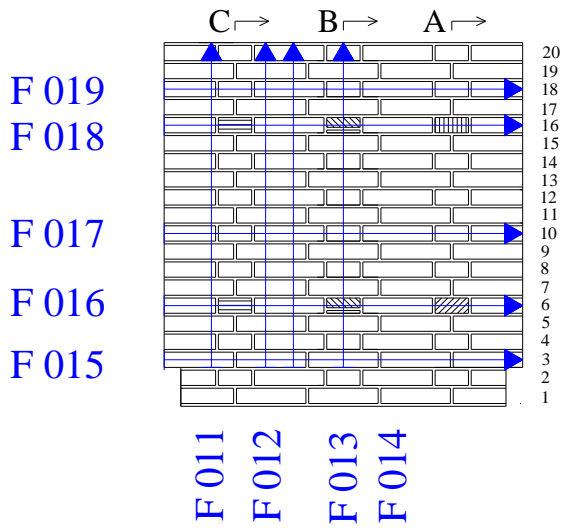


Figure 6.67: PNDC, GPR survey lines as numbered blue lines superimposed to the wall layout (front side)

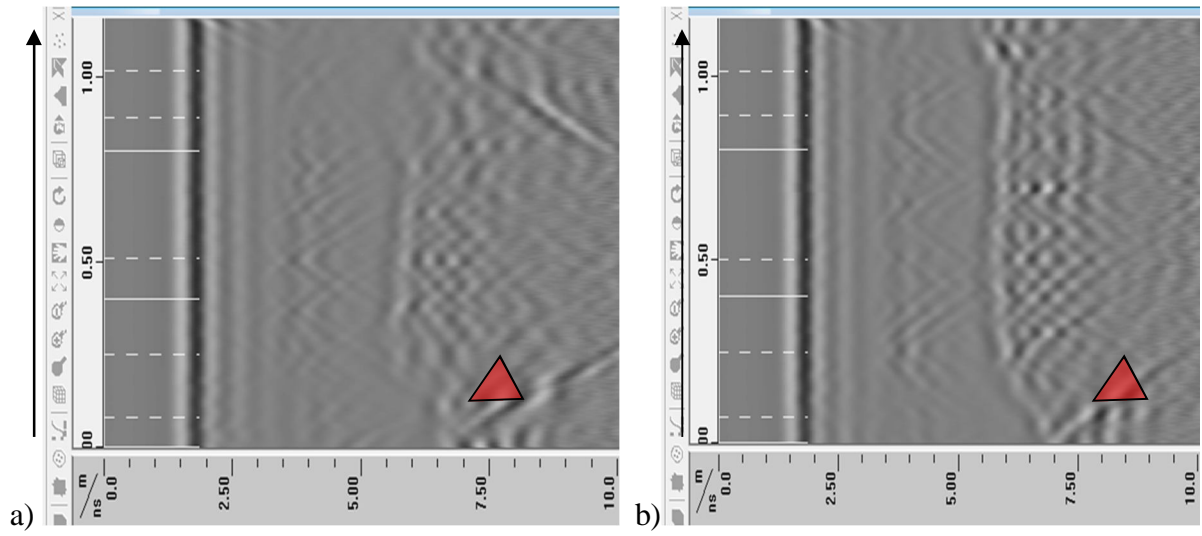


Figure 6.68: a) GPR survey along vertical line 11; b) GPR survey along vertical alignment 14.

Similar results were obtained for wall PNDA, at the end of the 2nd ageing season (October 2011). This wall was subjected to NaCl (0.1%wt) capillary rise from the base. The weathering effects were visible on the wall surfaces both in terms of moist areas and salt efflorescences and clearly detected by means of GPR radar.

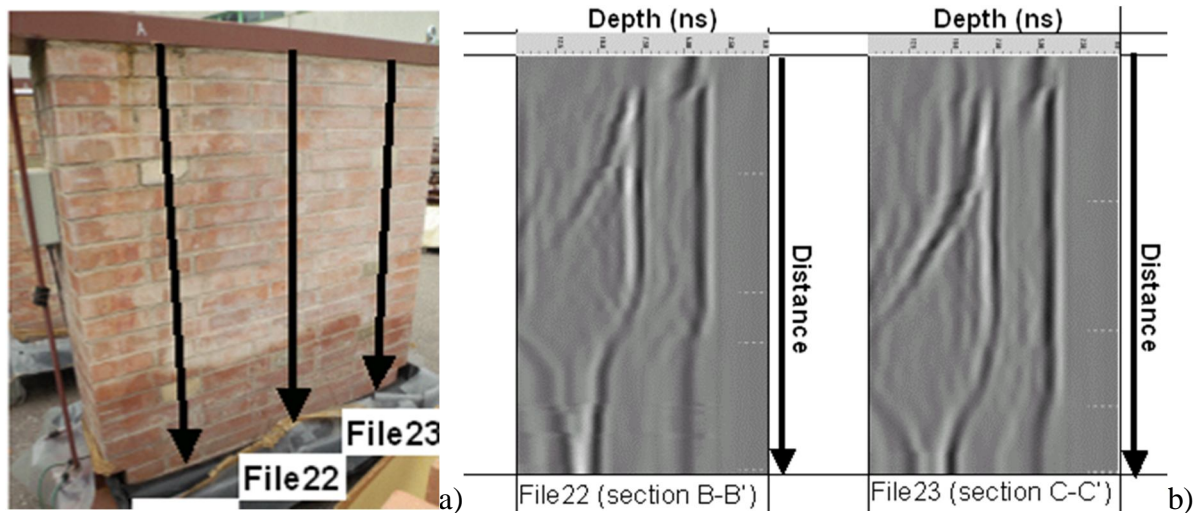


Figure 6.69: a) status of wall PND and superimposed GPR survey alignments; b) modification of wave reflection at the bottom as a function of rising damp height. See the greater modification on file 22 respect to file 23 due to the higher rising damp level in correspondence of the first survey alignment

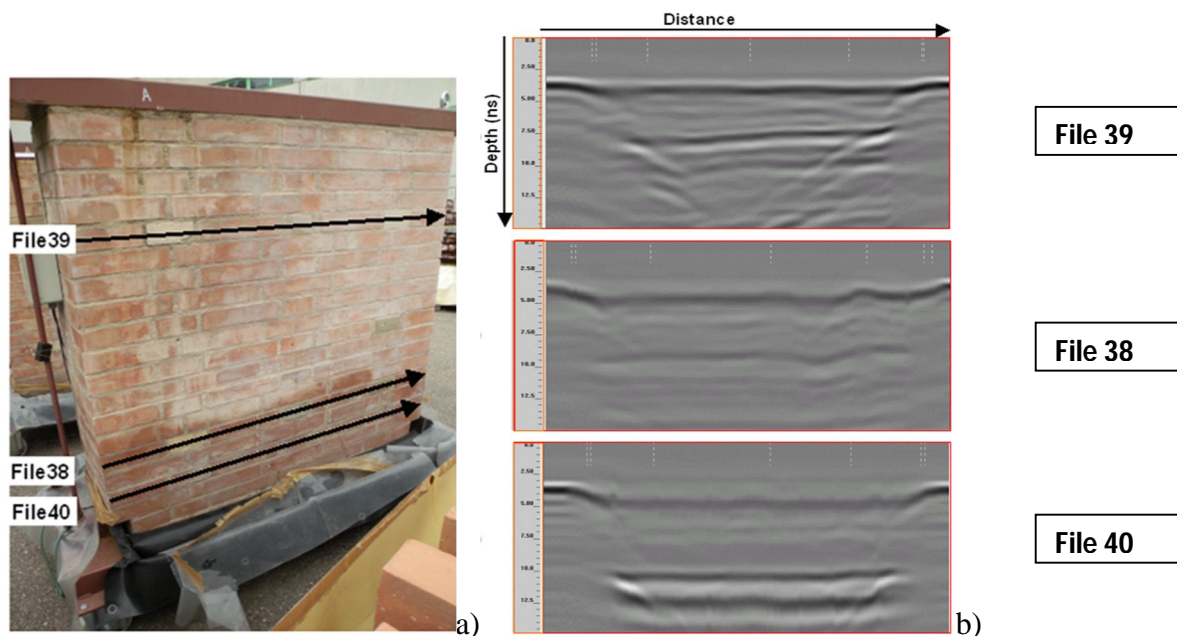


Figure 6.70: PDNA, a) photo of the wall at the time of data acquisition with superimposed GPR survey alignments for the identification of salts contamination; b) modification of wave reflection with faint reflection of the back as a function of salt contamination. See the greater modification on file 38 with respect to files 39 and 40 due to the greater contamination on the course along the evaporation front

6.4.1. Data fusion: GPR radar and IR thermography

GPR survey investigations were also carried out in view of further combinations of techniques, or data fusion, which could help at improving the amount and accuracy of information recovered.

Herein an example of data fusion by using GPR and IR thermography data is reported, with reference to a plastered stone wall.

During the same day of investigation, GRP grid survey and IRT were performed on the same area; hence 3D radar image and IR image were obtained. Through data post-processing the size of the images obtained using GPR and IRT has been equalized. This allows to put directly in comparison the surface temperature map and the slice obtained from the GRP 3D image at 0.6ns; in fact, ideally dividing into two equal portions the investigated area it is possible to create an image of the same obtained by the two techniques, see Fig. 60. The portion of wall that can be considered in dry situation is perfectly identified by the two techniques; the thermogram adds more information on the variation of moisture in the area subject to capillary rise that are not appreciable through a 3D GPR slice performed on a single depth level. Thanks to 3D GPR slice it is possible to detect the presence of the mortar joints not identified by ITR, then information about the wall layout is added. Superimposing the complete 3D GPR slice to the thermogram the respective information were resumed by the same image obtaining a resuming sketch of moisture trend and wall layout; see results in Fig. 61.

Fig. 60: comparison of results obtained for rising damp investigation by means of IRT and GPR grid; the coloured map is the thermogram and the greyscale map is a slice of the 3D GPR image performed at 0.6ns from the wall surface

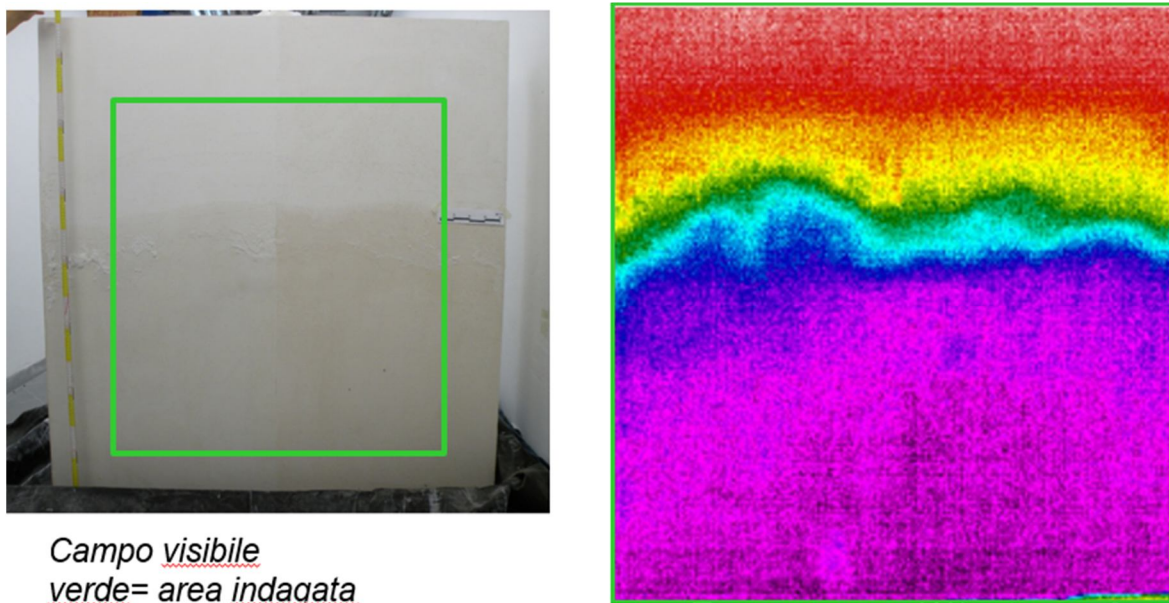


Figure 6.71: comparison of results obtained for rising damp investigation by means of IRT and GPR

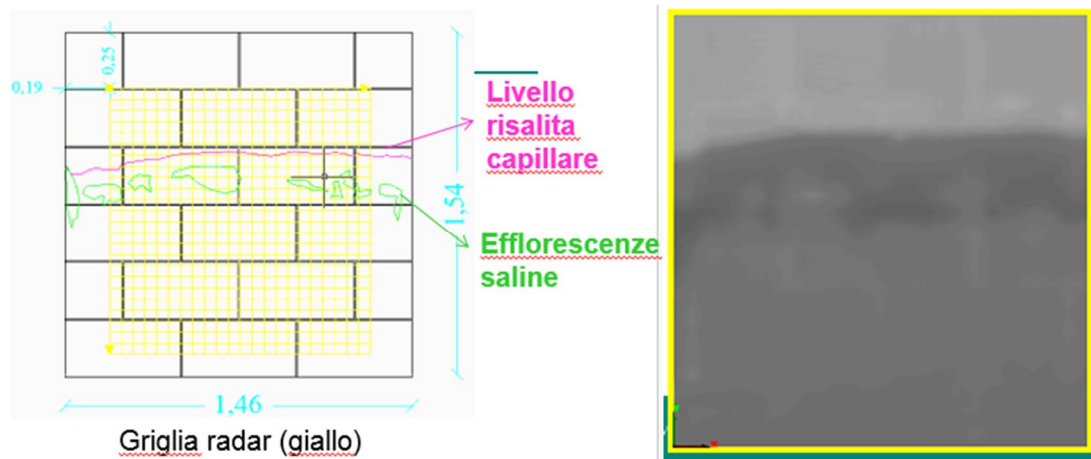


Figure 6.72: Grid for GPR data and results

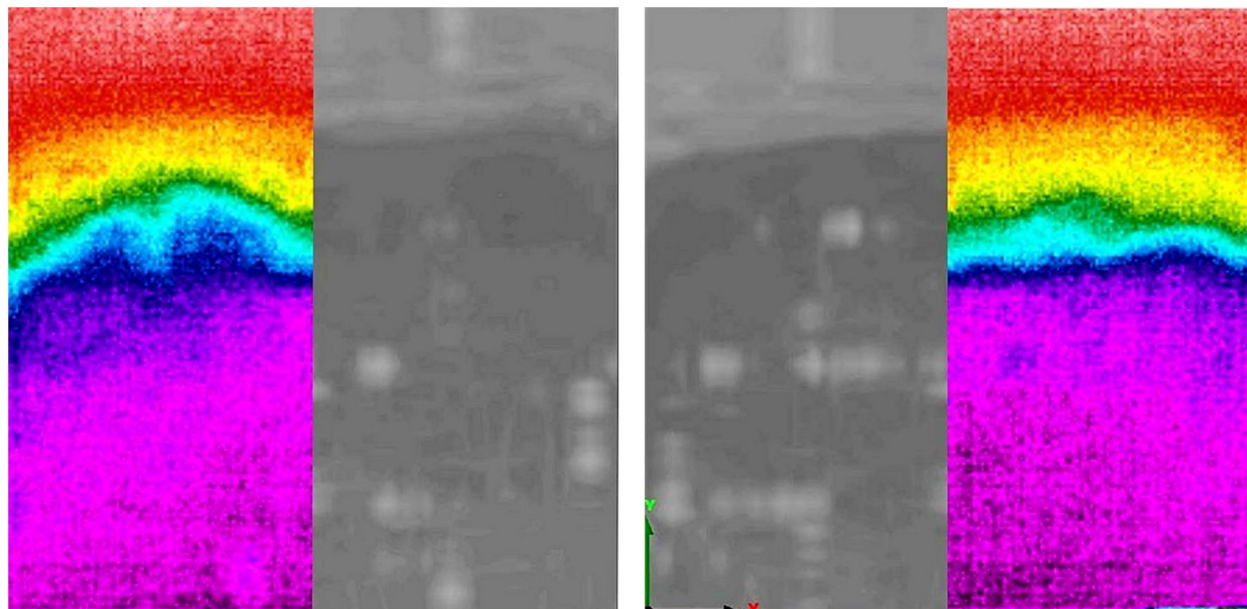


Figure 6.73: comparison of results obtained for rising damp investigation by means of IRT and GPR

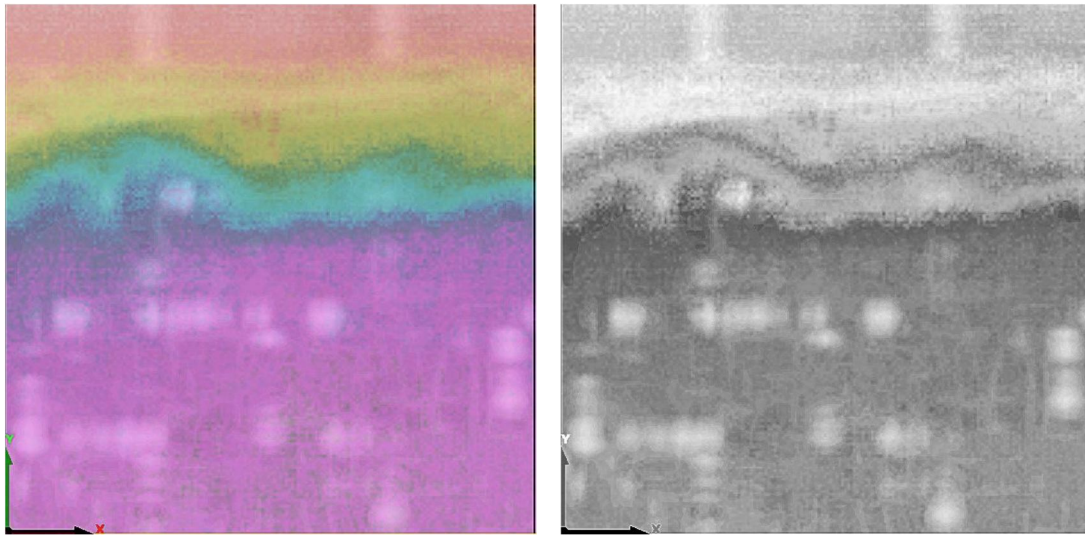


Figure 6.74: examples of IRT and GPR data fusion as a coloured map (left) and as a greyscale map (right)

6.5. Wireless electric potential monitoring & ion-chromatography analyses

From July 2010, the wall PNDB was subjected to capillary rise of NaCl solution from the base using a solution at low concentration (0.05% by weight, almost equal to 0.0086 mol/l). The phenomena of contaminated water migration in the wall was studied using different wireless monitoring systems:

- a device for the measurement of environmental parameters (relative air humidity, air temperature and internal wall temperature),
- a device for the determination of the moisture content.
- a potential-measuring device for salt concentration survey,

In this way the phenomenon of salt contamination and crystallization was investigated accurately providing information related to key parameters as: the evolution in salt concentration, the availability of water within the wall and the effects induced by the environmental boundary conditions.



Figure 6.75: Wall PNDB, front side with monitoring sensors, 3rd May 2011

Sensors for moisture content monitoring coupled with climate condition monitoring

At the end of November 2010, three sensors for the moisture content monitoring, connected to a Smartbrick device, were inserted in the front side of the wall, at 10 cm depth in the masonry course 7 (this corresponds to a sensor height of about 39.5 cm). The environmental data were recorded with a Smartmote device, already installed on the right face of the same wall (East side).

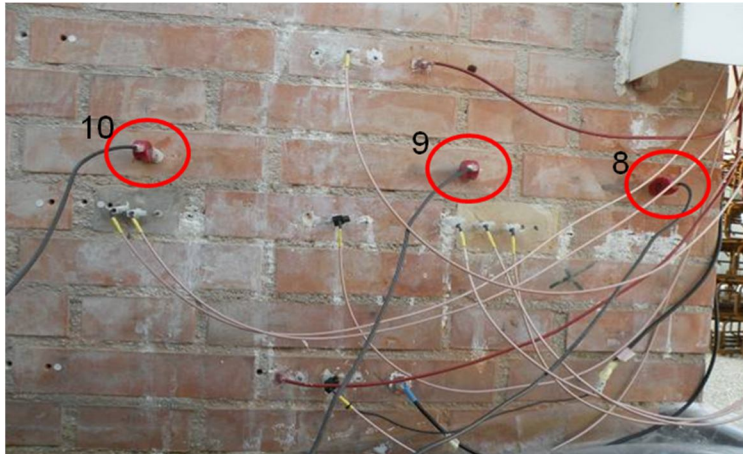


Figure 6.76: Wall PNDB, detail of the front side with position of moisture content sensors

Herein the collected data of air temperature, relative humidity and inner moisture content for the entire period of monitoring are reported together with the amount of rainfall, measured by a rain gauge installed in the roof of the laboratory.

The climatic parameters have not been measured continuously as the dedicated wireless unit was removed from the wall in some time periods and it was used inside the laboratory to monitor the ageing tests carried out on single units of building's materials or on simple masonry assemblies.

For brevity, the graphs reported below were not analysed in details but, by way of example some reflections can be done considering the values registered in May 2011 (Figure 6.77:). Here, the daily variations of the environmental parameters can be evaluated; in detail, the air temperature ranged from 10°C to 40°C and the relative humidity from 20% until 90% in rainy days. The moisture content inside the wall followed the daily variations of relative humidity but with a certain delay.

In addition, the moisture content varied along the horizontal profile (masonry course 7) and the minimum values (ranging from 42% to 50%) were recorded from sensor n°10, positioned in the middle of the wall. The maximum values of moisture content were registered by sensor n°9 (55%-62%) while intermediate values are collected by the outer sensor, n°8 (from 50% to 55%).

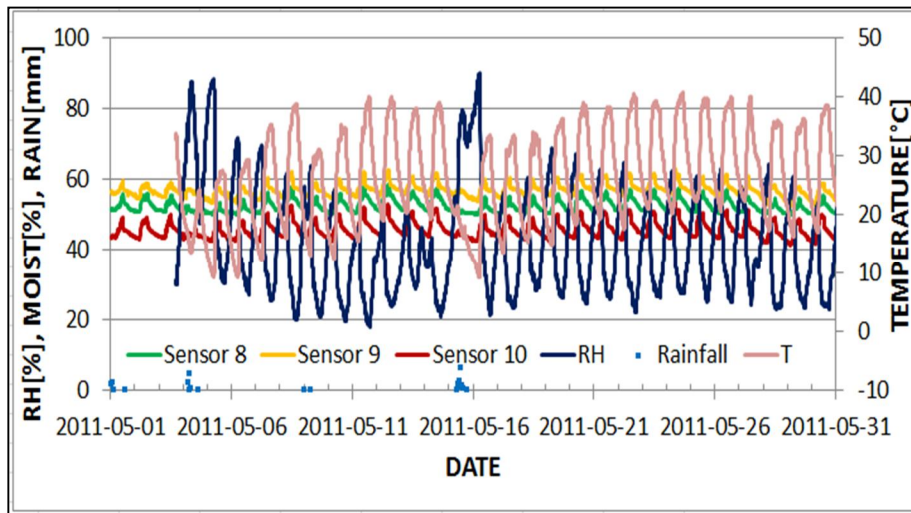


Figure 6.77: Wall PNDB, recorded values of air temperature, relative humidity and amount of rainfall together with values from 3 moisture sensors (May 2011)

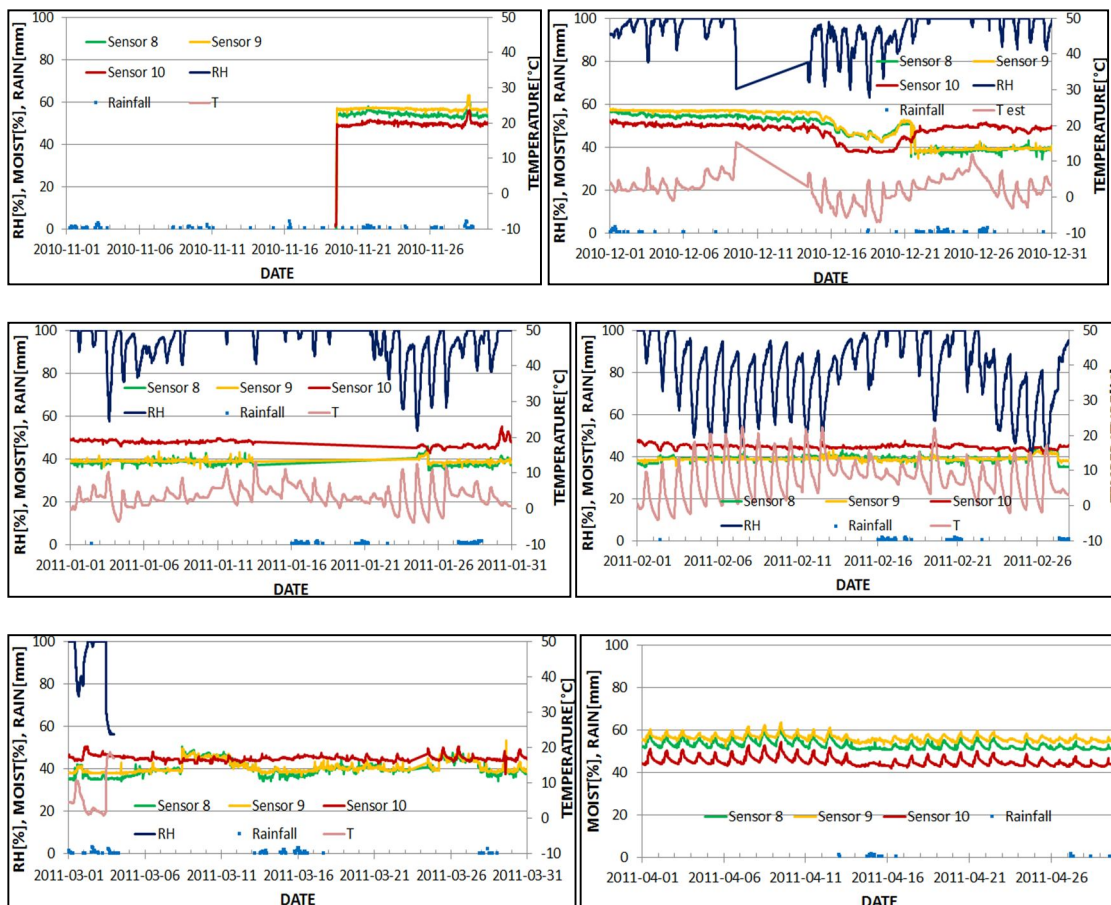


Figure 6.78: Wall PNDB, recorded values of air temperature, relative humidity and amount of rainfall together with values from 3 moisture sensors (November 2010 - April 2011)

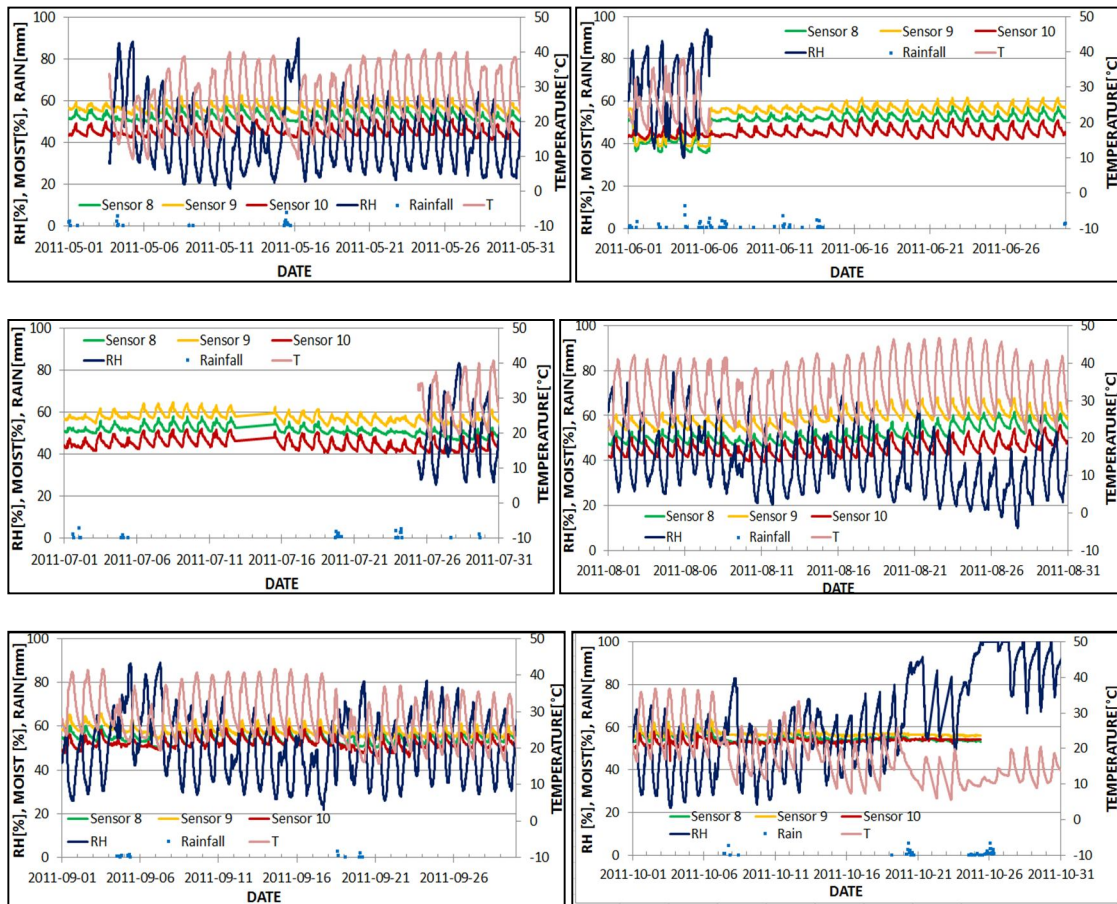


Figure 6.79: Wall PNDB, recorded values of air temperature, relative humidity and amount of rainfall together with values from 3 moisture sensors (May - October 2011)

Sensors for salt transport monitoring coupled with climate condition monitoring

After the laboratory calibration tests on single masonry materials, the Ag/AgCl sensors, connected to a Smartmote device, were applied to monitor the salt transport and content in the masonry wall PNDB. The potential sensors were distributed on the wall following both a horizontal semi-profile on the sixth masonry course from the base (this corresponds to a sensor height of 36 cm above the wall base), and a vertical profile along a section at 18 cm from the wall centreline, at six heights, from course 3 to 18 (that is from about 16.5 cm to 114 cm above the wall base). Potential sensors were inserted in the different masonry components of the wall: bricks, mortar joints and two different natural stones, the Varignana sandstone in the centre of wall, and a porous limestone from Palestine, on the right-hand side of the wall. In order to evaluate in a complete manner the salt distribution through the wall transversal section, in each test position the potential sensors were inserted to three different depths: 2 cm, 6 cm and 10 cm (**Errore. L'origine riferimento non è stata trovata.** bottom). Intervals of data acquisition were set at 10 minutes. The reference electrode was incorporated on the rear of the wall near the base (10 cm depth, second masonry course).

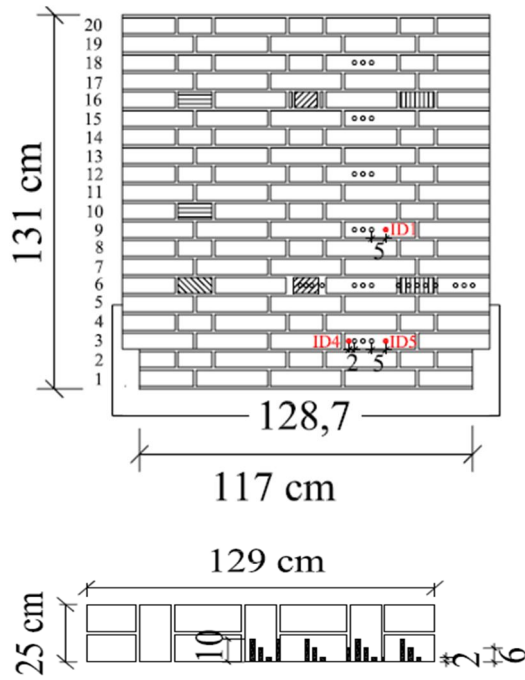


Figure 6.80: Masonry wall PNDB, distribution of potential (in black) and inner temperature sensors: a) front view, b) horizontal section at course 6

The potential sensor stations were defined with a code:

- The first letter indicates the profile direction, vertical or horizontal (V o H)
- The 2nd letter indicates the material (A= Bolognese sandstone, B= brick, J=mortar joint, L=stone from Lecce, P=stone from Palestine e S=sandstone from quarry near Schwabish Gmund)
- The number that follows the first two letters indicates the masonry course, starting from the bottom of the wall
- Then there is the letter “d” with a number that indicates the depth of the sensors (2, 6 and 10 cm)

Potential data were acquired, not continuously, from June 2010 until November 2011 as in some time period the wireless system was removed from the wall and used for calibration tests inside the laboratory. Herein, as an example, only some data collected along vertical profiles were reported with reference to a summer period (May 2011) and a winter period (November 2011).

Tab. 1: Overview of sensors distribution on front surface of wall

				VB18d10	VB18d6	VB18d2								
				VB15d10	VB15d6	VB15d2								
				VB12d10	VB12d6	VB12d2								
				VB9d10	VB9d6	VB9d2								
HA6d10	HA6d6	HA6d2	HJ6d10	VB6d10	VB6d6	VB6d2	HJ6d6	HP6d10	HP6d6	HP6d2	HJ6d2	HB6d10	HB6d6	HB6d2
				VB3d10	VB3d6	VB3d2								

1st example:

Potential-difference measurements collected during a sunny period in May 2011 along the vertical profile of the wall, from sensors placed in bricks, at different depths, are plotted together for comparison (**Errore. L'origine riferimento non è stata trovata.**). The strong periodic phase shifts are correlated to daily variations of T and RH. The height of the maximum salt content (potential minimum in the graph) moves towards lower positions with increasing depth into the wall section

The mean values of potential differences for the vertical profile during sunny periods in May 2011 are visualized (**Errore. L'origine riferimento non è stata trovata.**); here, the standard deviation is given as error bars. The lowest potential, which proportionally corresponds to higher salt content, is recorded by near-surface electrodes in brick-rows 12 and 9. Below these rows, the standard deviation is significantly higher than above. Especially near-surface electrodes show high deviation values. In addition, by observing in detail the single curves in **Errore. L'origine riferimento non è stata trovata.**, it is interesting to note that the height of the maximum salt content (potential minimum in the graph) moves towards lower positions with increasing depth into the wall section.

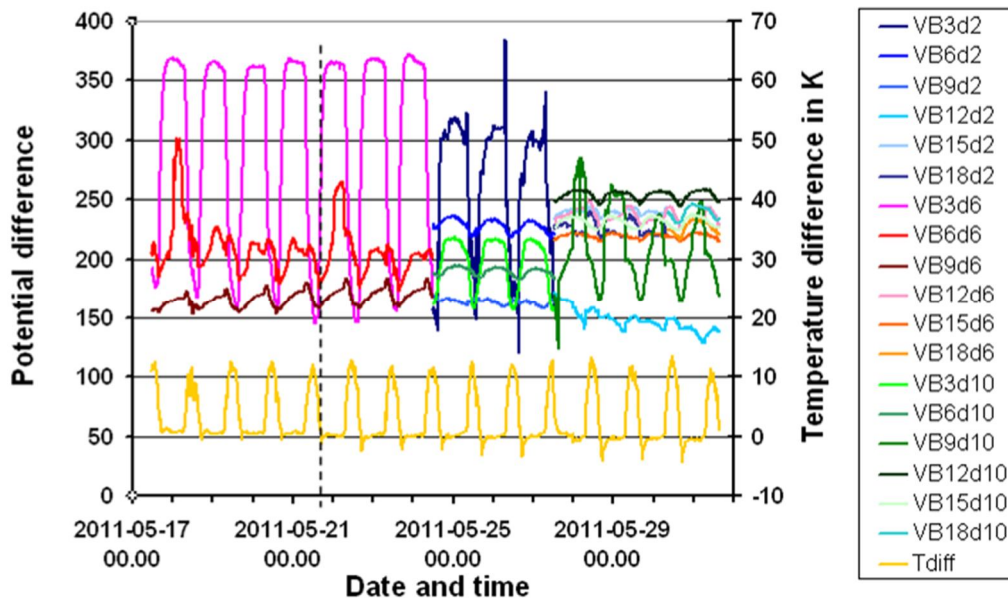


Figure 6.81: Wall PNDB, potential data along the vertical profile and temperature difference between front surface (2 cm depth) and near reference electrode (depth 10 cm) on backside in May 2011

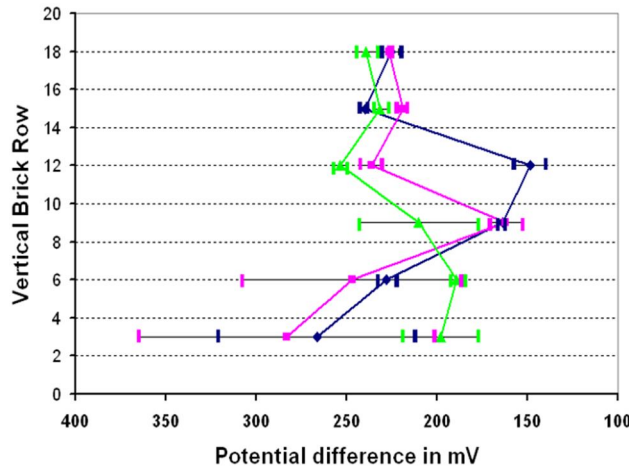


Figure 6.82: Mean values of potential differences along the vertical profile in sunny periods in May 2011

2nd example:

Monitoring campaign November 2011, winter time (two days on each vertical profile).

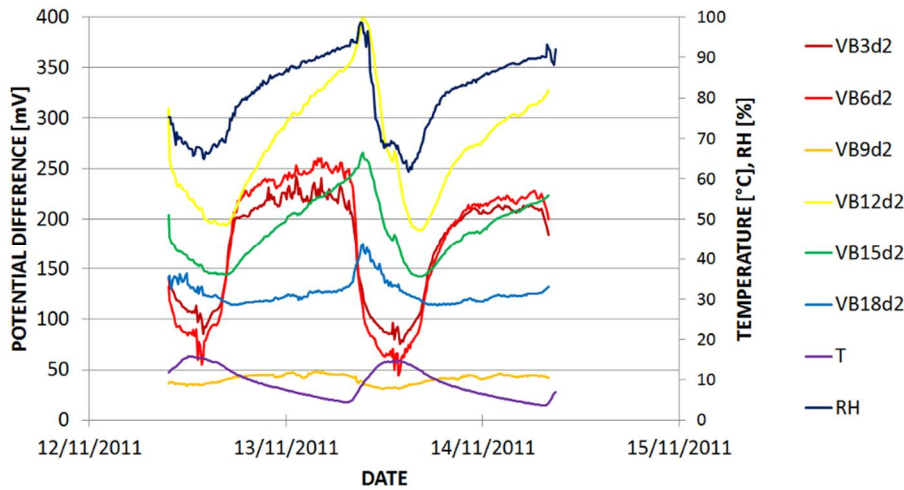


Figure 6.83: _Wall PNDB, potential data along the vertical profile at 2 cm depth together with air temperature and relative humidity (2 days in November 2011)

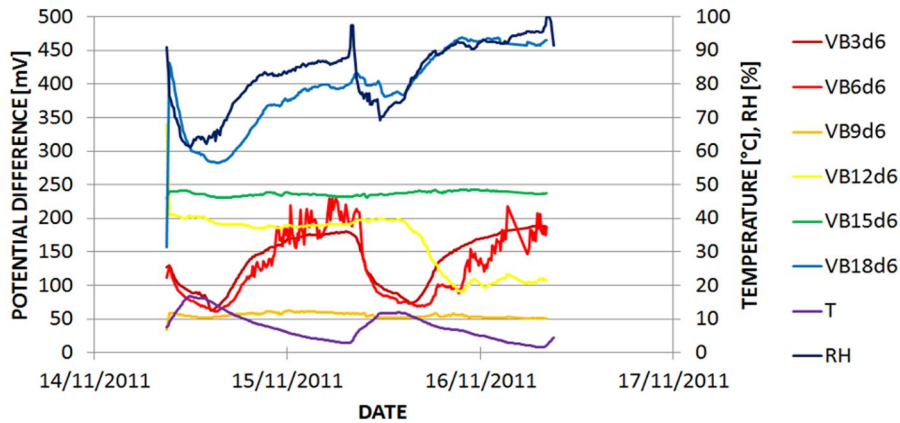


Figure 6.84: Wall PNDB, potential data along the vertical profile at 6 cm depth together with air temperature and relative humidity (2 days in November 2011)

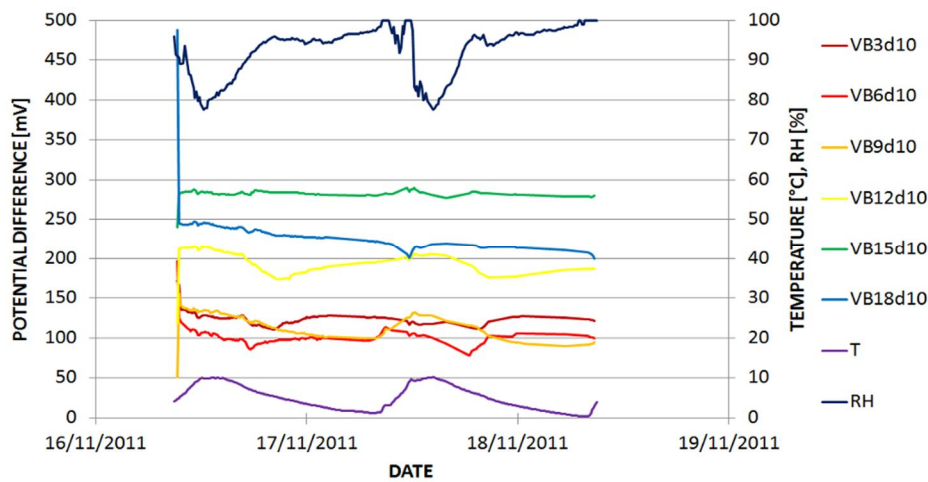


Figure 6.85: Wall PNDB, potential data along the vertical profile at 10 cm depth together with air temperature and relative humidity (2 days in November 2011)

From the monitoring campaign carried out in November 2011, it's possible to note that the sensors at 2 cm depth are more influenced by the variations of relative humidity than the deeper ones; in detail, they followed the trend of the relative humidity especially in the lower masonry courses. These variations are almost not visible at 10 cm depth.

The maximum values of potential difference (meaning lower salt content) were recorded at 6 and 10 cm depths, at the higher masonry course (15 and 18), not interest by damp rise.

The sensors positioned at masonry courses 3 and 6 registered almost the same values thus, the salt content in the lower part of the wall is almost the same.

In this case, as already reported for the summer time campaign, no activation peaks were noted.

Ion-chromatography analysis on mortar and brick powder samples

Report D5.2 part 4 + EWCHP 2011/2012

In order to quantify the amount of salt content within the full-scale walls subjected to natural ageing in addition to brine capillary rise from the base, ion-chromatography evaluations were performed on powder samples of both porous construction materials.

Two full-scale walls were analysed, wall PNDB and PNDE, at two different time periods: at the end of the 1st ageing season (March 2011) and during the 4th ageing season (September 2013), in order to evaluate and quantify the salt movements within the masonry and changes

These dust samples were collected by drilling small holes (5 mm in diameter) at different positions in the front faces of both walls (the one facing South), following a vertical and a horizontal profile. This micro-destructive testing procedure was performed by means of a standard drill with masonry drill bits and the resulting dust samples were collected with the help of a funnel in separate plastic bags for every centimetre of depth drilled, up to a certain, variable depth (5-8 cm) (Figure 5).

The samplings were repeated twice, at two different levels of decay in order to evaluate also the movements and variation over time of such contents. The analyses were intended to measure mainly two types of salt: sodium chloride and sodium sulphate. These salts, on one hand, were used to simulate the brine rise on wall PNDB and PNDE respectively, and on the other hand were detected into the masonry construction materials since their

These laboratory analyses were performed at the MPA laboratory of the University of Stuttgart thanks to the collaboration of Dr. F. Gruener.



Figure 6.86: Salt analyses on mortar joints: Mortar dust sampled after 4 ageing summers (sept. 2013);

PNDB (brine: NaCl 0.05 wt.-%)

In this study only chloride concentrations are taken into account. Compared with chloride input by preloading with diluted NaCl solution, the chloride contamination of the raw materials can be neglected.

The powder samples collected at different heights and depth profiles on the front side of the masonry wall PNDB after about 10 months of outdoor exposure (from June to March) in natural ageing conditions, including 4 months (mid July to mid November) of ageing by brine capillary rise from the base (NaCl, 0.05% wt.) were prepared and analysed by ion-chromatography. In the following, only the results obtained on masonry courses 3, 6 and 9 (these correspond respectively to heights of 16.5, 36 and 55.5 cm) at positions close to the vertical profile of potential measurements are shown (Table 2 and Figure 9). Plotted values correspond to detailed investigations at increasing depth, up to 5cm in total, with resolution of 1 cm.

In the data, generally a greater salt content is visible up to depths of 1 cm. This may depend on the salt-transport mechanism due to evaporation. This process tends to move the pore solution in the wall from the inner section to the outer surface, where subsequent salt deposition appears occurs.

In addition, the chemical data show that the salt concentration increases with increasing height from the wall base, for all depths. The highest amount is found at row 9 with a maximum near the surface. This is in good agreement with potential value curves (see Figure 8) from data measured between masonry courses 3 and 9. For this purpose, Figure 10 visualizes the two sets of data as maps over the vertical cross-section of the wall. In Figure 10 the potential values are inverted by multiplying by minus one, because the potential difference decreases with increasing salt content.

This characteristic is related to the capillary rise of the brine level. At the end of March 2011 when sampling was performed, the efflorescence level, which contains several salts, was visible at masonry course 6 (36 cm height) on the left-hand side of wall and around course 12 (75cm height) on the right-hand side of the wall (Figure 4).

Table 2 Values of chloride concentration in bricks at masonry course 3, 6 and 9 along the vertical profile

Brick row	Depth (cm)				
	0 – 1	1 – 2	2 – 3	3 – 4	4 – 5
3	0.0109	0.0036	0.0037	0.0059	0.0041
6	0.0566	0.0162	0.0141	0.0203	0.0185
9	0.0907	0.0264	0.0294	0.0428	0.0385

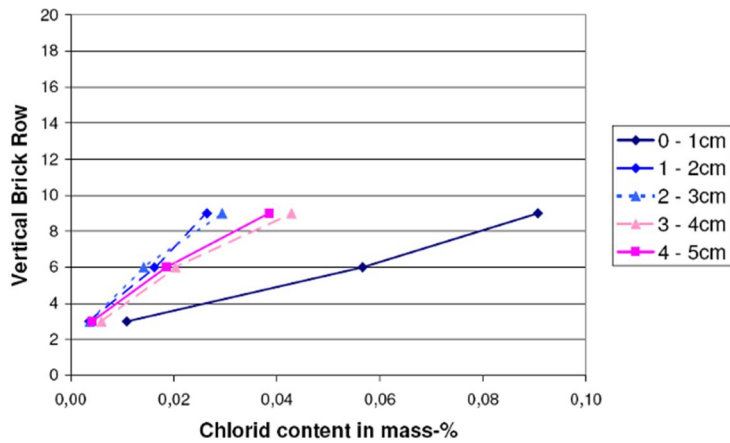


Figure 6.87: Wall PNDB, chloride concentration distribution on brick powder samples from the wall's south side

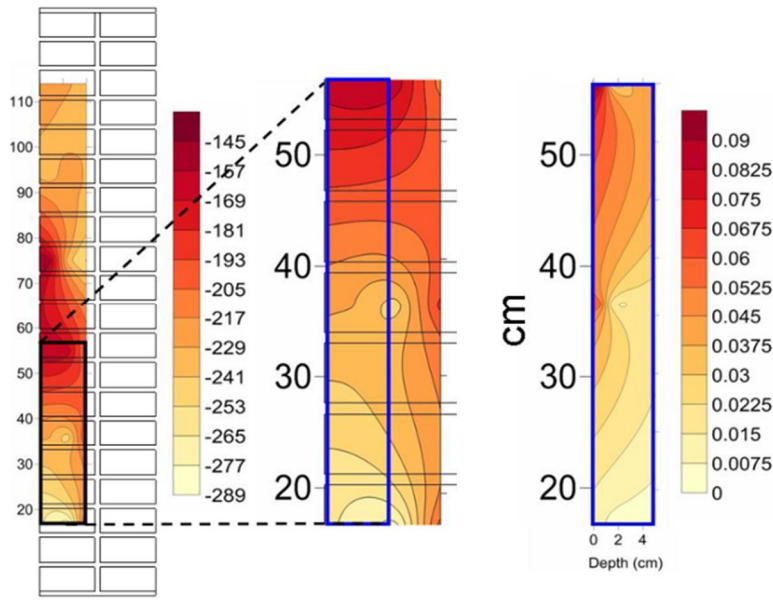


Figure 6.88: Compared visualization of potential data (inverted) (in mV, left-hand side and centre) and chloride concentrations from salt analysis (weight %, right-hand side) as maps through the vertical wall cross-section

From these data we can affirm a rising moisture level in the past during the suction test as far as masonry course 9 (this equals 54 cm from the wall base). On the other hand, secondary dissolution, mobilization and transport of highly soluble chlorides by long-standing rain events and high atmospheric relative humidity can account for redistribution of the salt enrichment zone (even at higher levels). At relative humidity above 75.5%, sodium chloride present in building materials dissolves and can be transported in the pore system until the surrounding conditions change and NaCl crystallizes again. This could explain the uneven distribution of efflorescence on the wall if the front surface is observed.

Although by chemical analysis a much higher information resolution is obtained at depths of up to 5 cm, the comparison of the potential measurements (Figure 10) with the salt analysis shows good agreement. (A1.6)

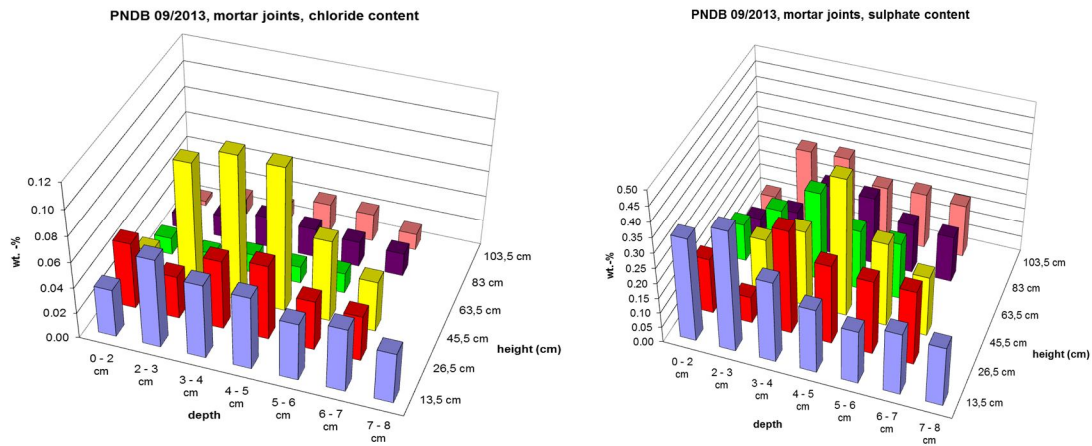


Figure 6.89: Full-scale wall PNDB, salt content on mortar joints at different heights from the wall base and different depth from the surface measured

PNDB comparison of salt content measured at the end of two different periods

Chloride content:

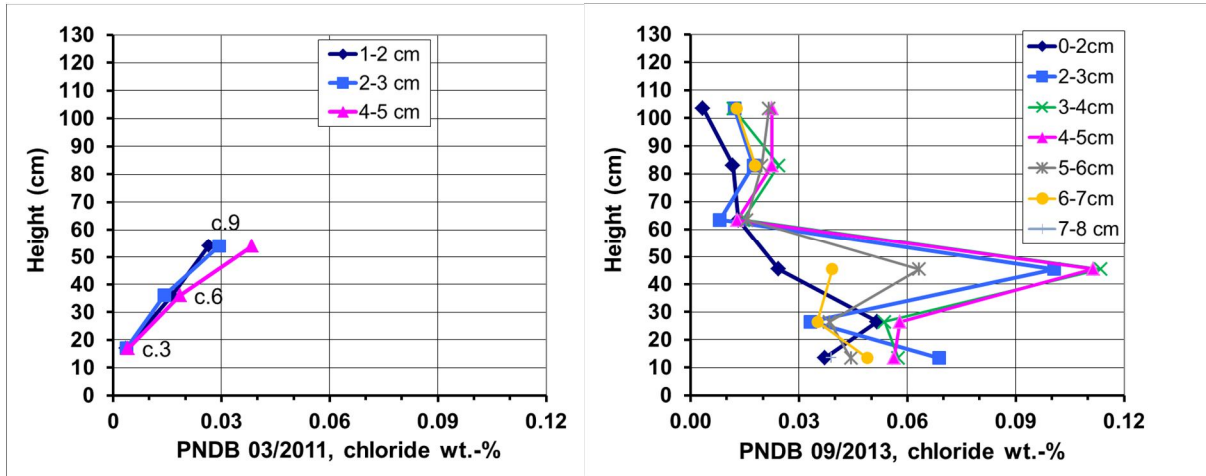


Figure 6.90: Full-scale wall PNDB, sodium chloride content measured along vertical profiles at different depths from the masonry surface at two different ageing periods: after 1 ageing summer (March 2011) and during the 4th ageing summer (September 2013)

Sulphate content:

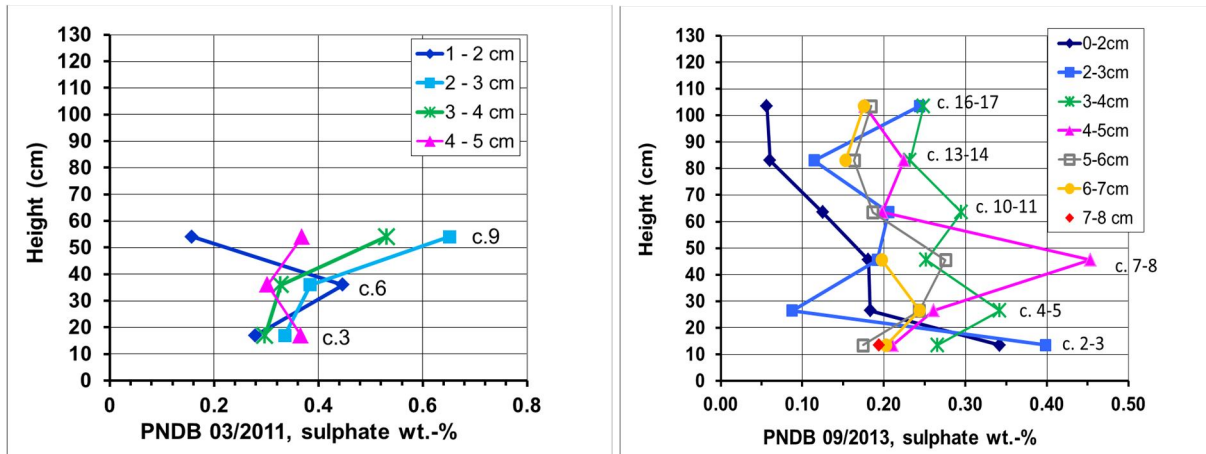


Figure 6.91: Calibration images are recorded by DICiod 1st period! July 2013

After 3 years of ageing and weathering outside there is a remarkable enrichment of NaCl in a height of 40 – 50 cm and in a depth of about 2-5 cm. During wetting by rain water the walls will be drenched to a certain depth. Afterwards during drying process in a first stage there is capillary transport of moisture and salts back to the surface. In a second stage when the pores close to the surface are not filled with enough moisture for a persistent moisture film, drying takes place inside the mortar and moisture is transported by diffusion of water vapour. The crystallization of NaCl in the pore solution will concentrate inside the mortar in a zone between the maximum wetting depth and the outer drying zone (in average over frequent occurrences), where the pores are drying very quickly. As a result this zone gets friable with time and is the enrichment zone of soluble salts. The depth of this zone is dependent on the

type of salt, the pore structure of the material and the climate conditions (frequency of wetting – drying cycles by rain, relative humidity). In the case of gypsum the enrichment zone is very often at the surface (gypsum crusts) or close to the surface in materials (mortar, sandstones) with fine porosity (small pore - diameters). Salts with higher solubility than gypsum can penetrate deeper and in higher concentration into the material at the same time (than gypsum).

Is there a loss of the surface due to blistering , delamination or sanding visible?

The sulphate content in this wall only comes from the materials (mainly from the bricks). In this case it was only affected by weathering and nearly no influence from an initial capillary suction. I think that the distribution of sulphate may be controlled by weathering and by local effects from the brick rows, because the initial sulphate concentrations of the bricks may fluctuate random or nonsystematic.

PNDE (brine: Na₂SO₄ 0.05 wt.-%)

Mortar dust sampled after 4 ageing summers (sept. 2013).

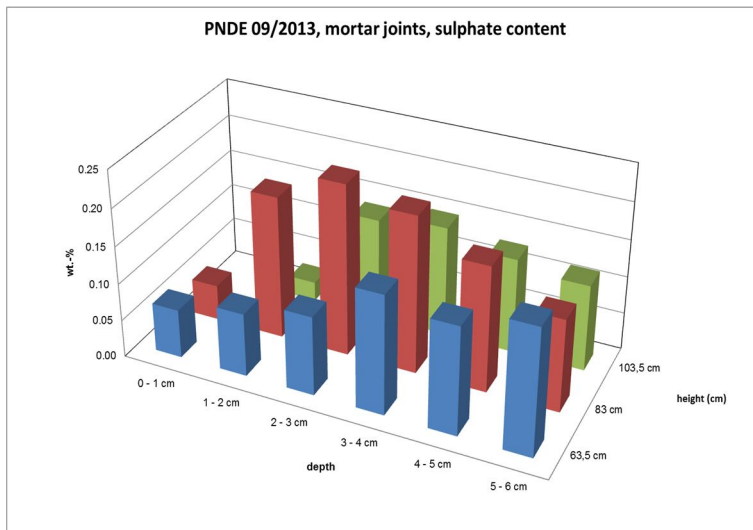


Figure 6.92: Results of salt analyses on mortar joints

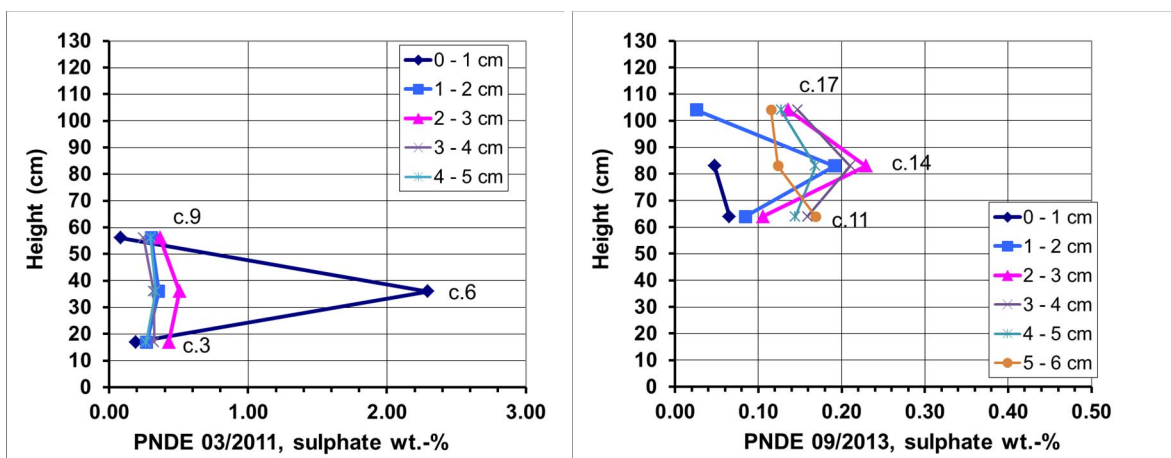


Figure 6.93: Comparison between sulphate content measured in March 2011 (after 1 ageing season) and in Sept. 2013 (after 4 ageing seasons)

The sodium sulphate spreads to a higher zone. After one season there was a high concentration level close to the surface in a height of app. 35 cm. After 4 seasons the zone of higher concentrations is now at a level of about 80 to 90 cm in height. The highest enrichments are now in a depth between 1 to 3 cm. That's not unusual for a salt enrichment zone caused by weathering. In the beginning the sodium sulphate was brought into the wall by capillary suction (+ some amounts from the material itself). As a result the highest concentrations were found in the bottom zone and close to the surface, because enough moisture was available for a first enrichment close to the surface (evaporation zone). Later on the salt movement and enrichment process was controlled by relative humidity (sorption process in the pores) and wetting during rain events. In both cases during the following drying process there are always two stages (capillary transport in the first stage of drying and mainly diffusion of water vapour in the second stage). And the (vertical) capillary transport between mortar and bricks is also influenced by boundary effects. Its not the same whether you have a composite of two different materials (mortar and brick) or only a monolithic material. This may be also a cause for "jumps" in concentrations

6.6. Laser scanner

The aim was to favour solution evaporation and salt crystallization and to provoke material damage. The degradation process was monitored based on a contactless, rapid and accurate image diagnostic technique. In particular, high-resolution laser scanning by triangulation technique was adopted. 3D data acquisition was repeated at the end of both seasons.

The proposed procedure successfully extracted quantitative information about areas of material spalling and detachment even in the initial phases of decay.

All the measurements have been performed keeping the laser scanner perpendicular to the wall surface to be monitored, at a distance of about 40 cm. A tripod has been used to change the relative height of the instrument. It was necessary to avoid excessive brightness, acquire multiple scans. Data at the end of two ageing seasons (Ott 2010, Nov 2011).

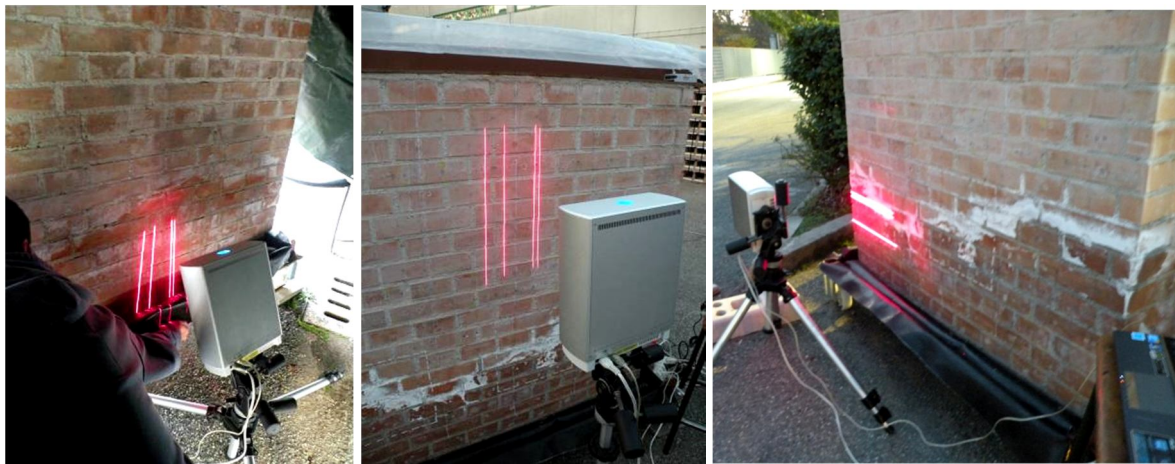


Figure 6.94: *example of Laser Scanner survey along: a) vertical alignments and b) horizontal alignment, Dark testing area below a plastic sheet*

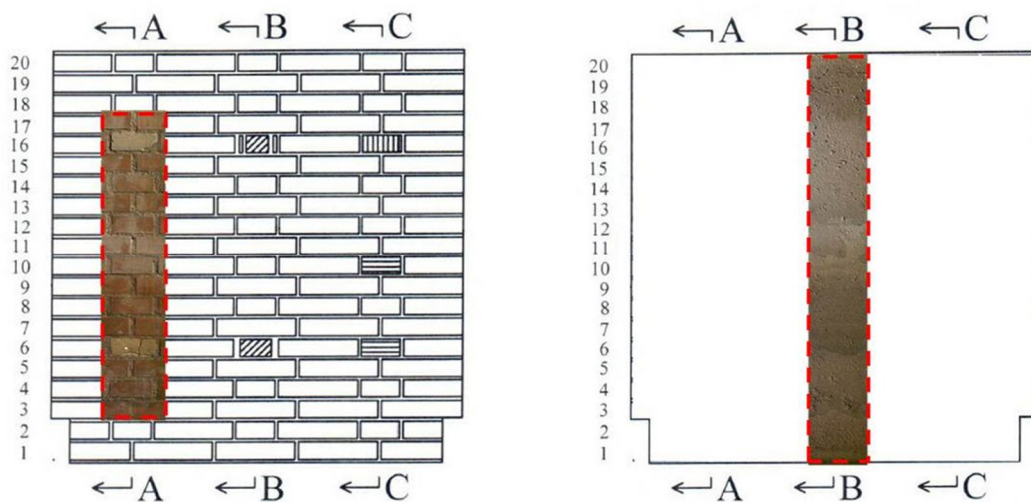


Figure 6.95: Wall PNDA: monitored surfaces in the front-side (left) and back plastered side (right).

As already mentioned, multiple scans have been collected at each measurement position in order to capture at least a section of the masonry surface; then, to visualize and analyze the whole set of data collected in each position, the scan images have to be combined together. First of all, as each mesh is oriented with its own scanner reference system, a relative repositioning was performed, aimed at reconstructing the original object geometry and thus at visualizing correctly the data.

In the preliminary phase of this process, the approximate 3D rototranslation matrix has been calculated by measuring at least 3 tie-points in 2 contiguous scans which are manually selected. The procedure has then continued involving an algorithm able to minimize the difference between two clouds of points: the Iterative Closest Point (ICP). This algorithm is conceptually simple; it iteratively estimates the transformation parameters necessary to minimize the distance between the points of two raw scans and then it transforms the coordinates using such values. Thus, a fine alignment of each scan can be obtained. Once all the meshes are aligned in the same reference system, they have been merged together in order to create an only surface.

This process has been followed for each of the two measurement campaigns thus obtaining surfaces consisting of 3D merged models that can be compared between each other (Fig. 5, Fig. 6).

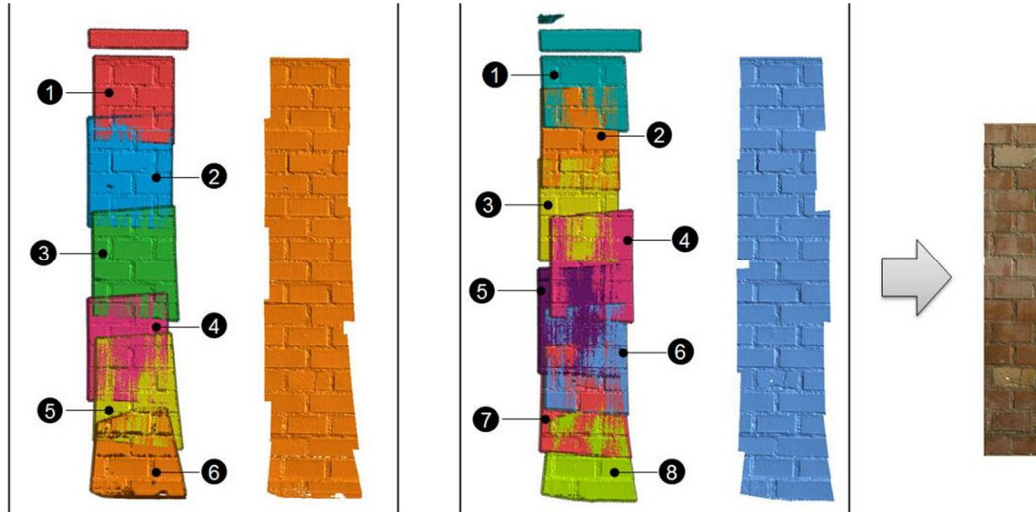


Figure 6.96: PNDA Front, footprints of the scan-positions and 3D merged models of 2010 (left) and 2011 (center), texturized sub-area (right)

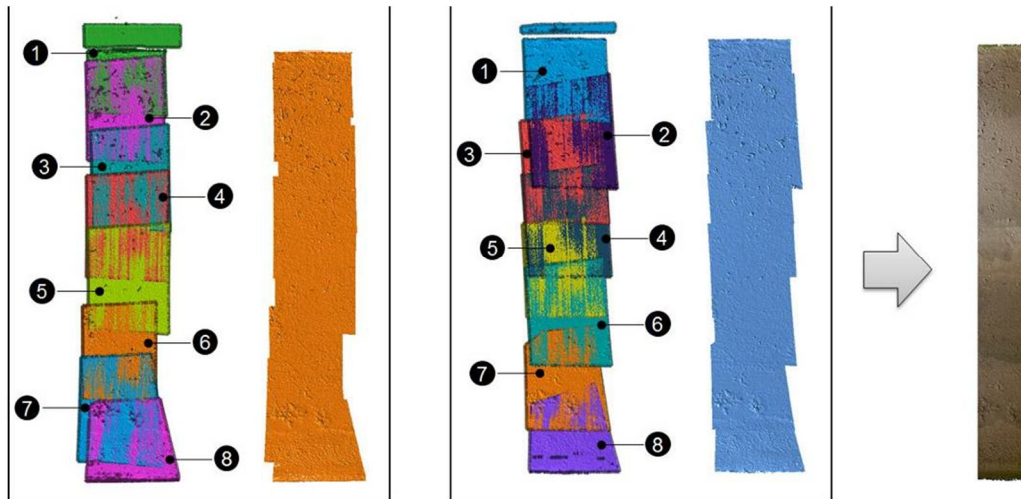


Figure 6.97: PNDAs Back: footprints of the scan-positions and 3D merged models of 2010 (left) and 2011 (center), texturized sub-area (right)

During this “merging” procedure, problems that may occur in this kind of test have been encountered. It is known, that with elongated and plane objects where the scans are essentially positioned along one direction, problems may arise with their alignment. If the central scans are strongly connected to each other, the scans at the extremes present only one side constrained and the residuals are usually larger in this area. This occurs in our case, and thus, not to affect the data quality a sub-area has been chosen for each monitored position.

The meshes derived from the point clouds measured at the end of each ageing period have been used separately, first of all, to perform a visual inspection. This is possible, with 3D model, especially when a photographic texture is superimposed to the mesh. In detail, some detachment areas and areas with material losses have been identified in both measuring campaigns. Thus, it was possible to detect the appearance of superficial decay also at the very beginning phases of natural weathering.

In order to make considerations over the variations over time in the 3D geometry of the object caused by material spalling, or to salt crystallization cycles, the surface “2010” was subtracted to the “2011” one, generating a displacement map. In Fig. 7, the 2011-2010 difference displacements maps for both sides of the wall are presented.

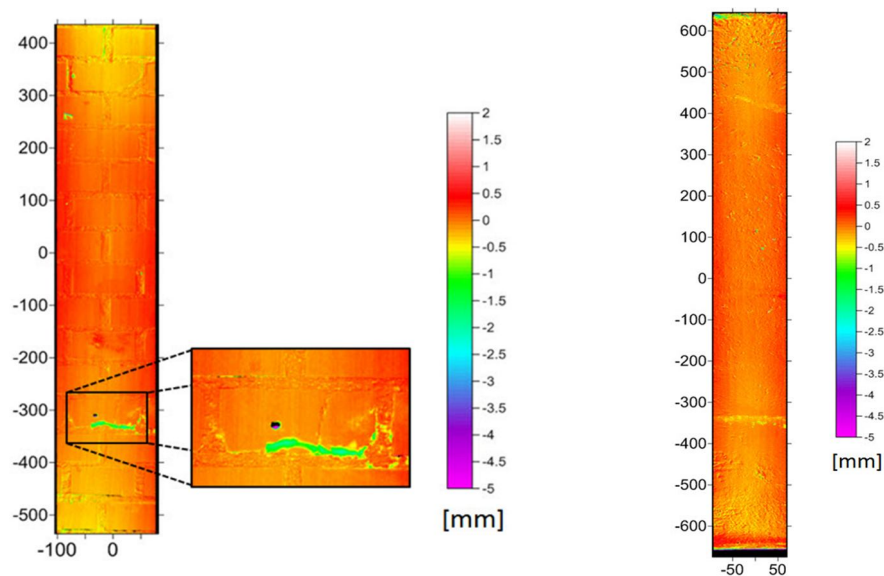


Figure 6.98: Difference displacement map (mm): 2011-2010: front side(left); rear side (right)

The highest and lowest values correspond to a major change of the surface occurred in time are reported in Fig. 7. In the front side, not plastered, the greater area of negative displacements is visible at masonry course 6 (from the base) in the natural stone inclusion. Thus, it seems that this material was more sensitive to the natural environmental ageing than the bricks or the mortar layers.

In the rear side, the greater negative displacements are concentrated along a straight horizontal line that is located at about the same height from the wall base that in the front side, which approximately corresponds to the level of moisture rise. In addition, some sparse pitting phenomena can be identified in the entire plastered surface.

For a more thorough study of the surface it is possible to split the changes affecting each constituent material. Thus, in this case two classes have been created: one concerning the bricks and one for the mortar layers, considering the stones as part of the “brick” class. In addition, it has been created a third class concerning the outliers: outliers are errors that have been easily recognized by the operator. In detail, in this specific case some displacements were caused by the presence of labels sparse in the surface. These labels were present only in one of the two years, and their presence, when the surface comparison is performed, could be incorrectly interpreted as a material variation.

By examining the three classes, called respectively Bricks, Mortar and Outliers, the percentage of material that can be considered acquired (positive values) or lost (negative values) are represented with cake diagrams (Fig. 8). The material belongs to one class instead of the other according to the threshold used. The threshold value correspond to the instrumental accuracy in the Wide mode ($\sigma = \pm 0.381$ mm). Thus, the areas with displacements contained in this range can be considered without surface variations.

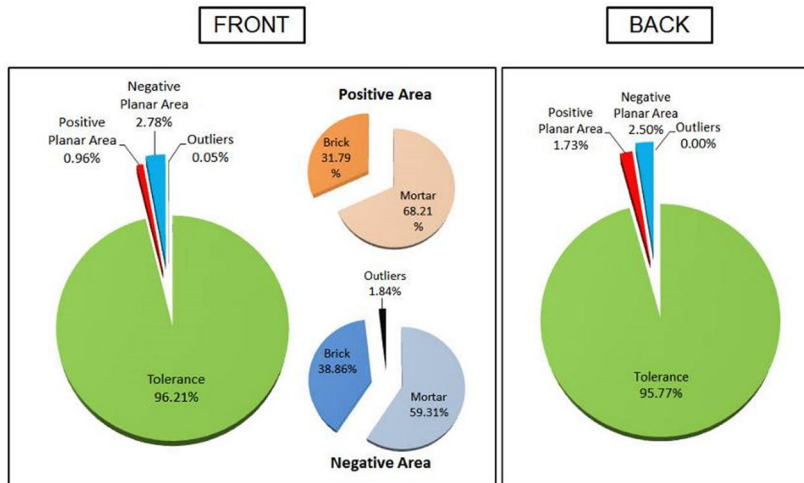


Figure 6.99: PND-A diagrams.

Table 2. Analysis of the comparison between the 2011 and 2010 3D model.

PND-A Front	Class	Positive Z >	Negative Z <	In tolerance
Area (mm ²)	Mortar	1115.97	2819.30	
	Brick	520.13	1847.07	
	Outliers	0.00	87.26	
	Tot	1636.10	4753.63	164381.35
Volume (mm ³)	Mortar	113.60	463.71	
	Brick	41.48	609.40	
	Tot	155.08	1073.12	
PND-A Back		Positive Z >	Negative Z <	In tolerance
Area (mm ²)	Tot	3603.04	5221.12	199848.47
Volume (mm ³)	Tot	834.65	3105.20	

From these data, it is possible to note that both surfaces of the wall have suffered some damages, despite of the different orientation and the presence of plaster. In both surfaces, the negative areas are almost two times greater than the positive, acquired areas (in percentage).

However, the rear side, although it is exposed to the North, presents more changes than the surface without plaster.

In the latter, it seems that the moisture and salt movements have affected greater the mortar than the brick surfaces. The decay of the mortar appears almost in the same percentage as swelling or salt crystallizations (positive areas) and material losses (negative areas). In the bricks, the negative areas are also due to material losses; instead, the positive areas are only apparent because the volume increase is mainly due to some flakes that are separating at this time point (material losses).

6.7. Digital image correlation

Finally, an additional investigation was carried out with the purpose of evaluating and quantifying the amount and spread of the simulated decay process in outdoor exposed solid brick walls considering the digital image correlation technique, thanks to the collaboration with the researchers of the department of Mathematics of the University of Bologna.

In this first experience, primarily aimed at testing the feasibility and the accuracy of a simplified DIC procedure, implemented in view of further application on-site, also in historical masonry, only one surface of wall PNDD, the rear side, was studied. A VIC 3D testing equipment which has been recently become available at the CIRI-EC lab. was employed (§3.6.1) (SchTecn DIC [4]) to monitor the selected brick surface at two different time instants, that is at two different levels of decay: almost at the beginning of the 4th ageing season (beginning of July 2013) and at the end of the same season (end of October 2013).

This proposed diagnostic methodology presents several innovative intrinsic aspects. Indeed, up to now, by the knowledge of the author, in the field of civil engineering, only indoors applications of the 3D DIC method have been studied, always to monitor specimens during the application of an external mechanical or thermal force which causes a stress-strain state in the investigated specimen' surface and without changing the relative positions between the DIC cameras and the investigated element. Moreover, the monitored surfaces were usually properly treated (i.e. by painting, coating, spray, etc.) prior to start the tests, in order to have at disposal a random pattern of dots, non-repetitive, isotropic and with high-contrast chromatic areas, which represents a pre-requisite of the DIC technique (5 -di LabExpFlood). Herein, however, it was chosen to use the same masonry texture with this purpose, after having tested its reliability during mechanical tests in smaller wall assemblies, as explained in the following chapters (§8 and 9 (8, 22)). The only precaution adopted was to mark some points in known positions with the aim of having at disposal "fixed" reference points to register the second period's images on the ones of the first period (white crosses in Figure 6.100 left).

The DIC cameras were positioned at a height from the ground of approx. 1 m and at about 4 m distance from rear side of wall PNDD with a relative distance between them of approx. 70 cm (Figure 6.100). After the adjustment of the exposure time, focus and aperture range of the lens of both cameras (§3.6.2), the calibration was carried out.

In the first measurement campaign a big target with 12 x 9 black dots and a space grid of 84 mm was considered, while, in the second campaign was employed a different big pattern, with 12 x 8 dots, spacing 90 mm (Figure 6.101). The calibration phase was quite complex for both periods due to the sudden and repeated light/brightness changes which characterize natural outdoors conditions and the calibration score obtained was not really good (between 0.07 and 0.09 pixels), index of a not-really high accuracy, although acceptable and accepted by the commercial software (appeared "green").

After the calibration, for both testing periods, a series of images, up to 150, was manually recorded in few seconds. Note that the wall surface appeared different in the two periods both in terms of moist areas and amount and distribution of salt efflorescences as visible from the single DIC images recorded (Figure 6.102, Figure 6.103).



Figure 6.100: Wall PNDD, rear side, October 2013 and testing set-up

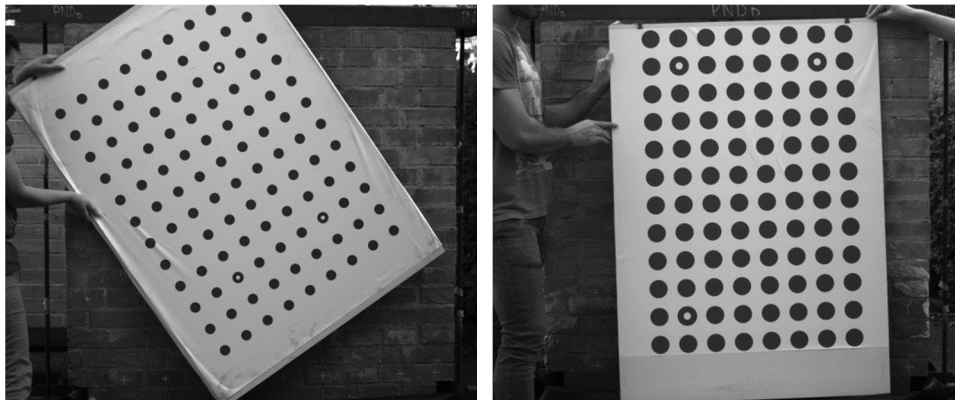


Figure 6.101: Calibration targets used in July 2013 (left) and October 2013 (right); images recorded by DIC



Figure 6.102: PNDD, rear side, July 2013, DIC images acquired at the same time instant by the left (a) and right (b) camera



Figure 6.103: PNDD, rear side, end of October 2013, DIC images acquired at the same time instant by means of the left (a) and right (b) camera

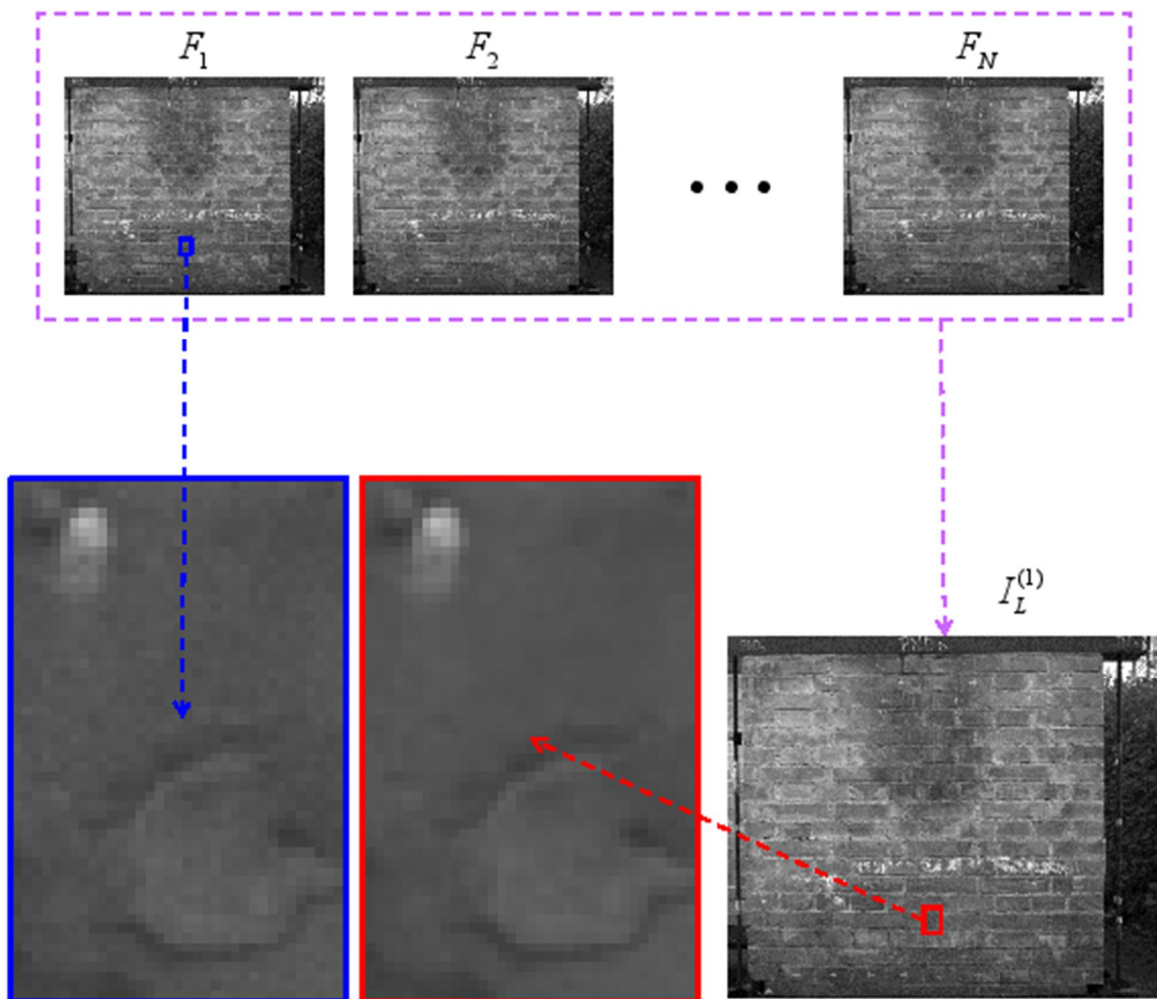


Figure 6.104: Wall PNDD, averaging procedure of the series of DIC images acquired in the first period (July 2013). In blue and red, a detail of a not-averaged image and the average one to highlight the lower noise level obtained.

The data analysis has foreseen, for each measurement period and for both cameras, the averaging of the series of acquired images in order to obtain a pair of representative images, characterized by a lower noise level (Figure 6.104).

Then, both pairs of images were separately analysed in order to obtain, for the two periods, the beginning and the end of the 4th ageing summer, 3D maps with the three coordinates of each pixel along the three main directions. Thus, also the out-of-plane coordinates, z, which are difficult to measure with usual instruments, could be measured everywhere and i.e., visualized as coloured maps (legend: -3 to +3 mm) superimposed to the corresponding visible image (Figure 6.105, Figure 6.106).

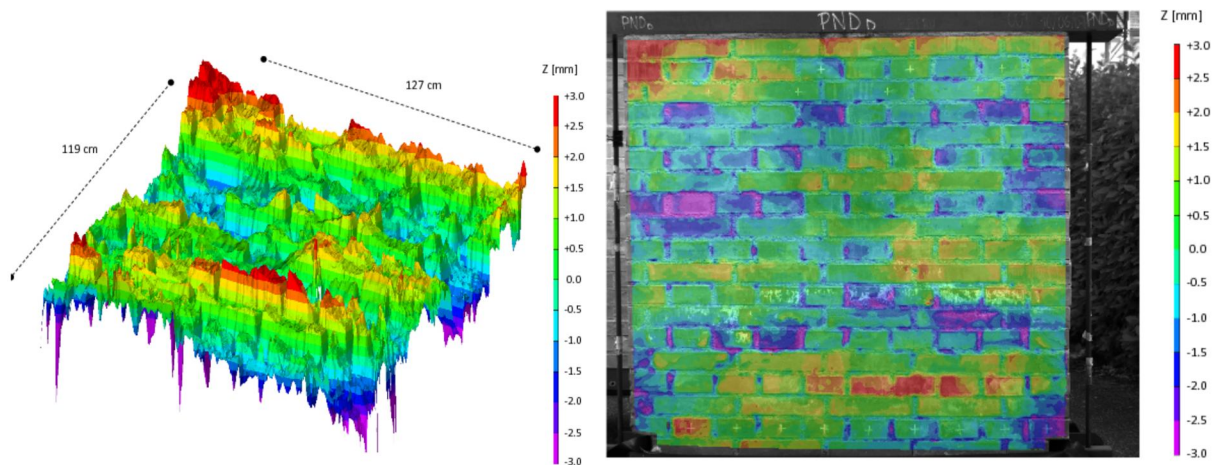


Figure 6.105: PNDD, 3D maps of Z-coordinates obtained from the analysis of the averaged images taken in July 2013 (left), also visualized as 2D semi-transparent coloured maps superimposed to the visible image (right)

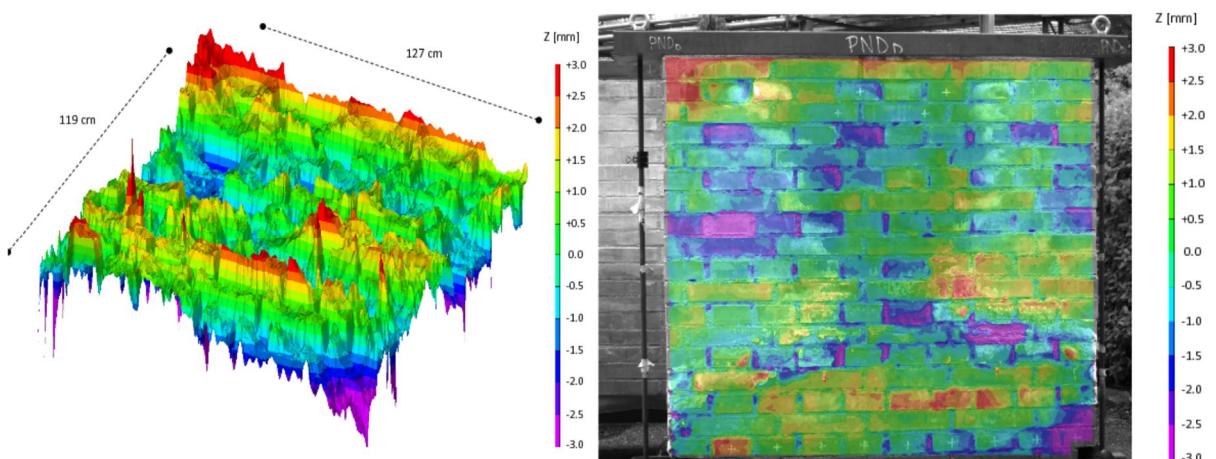


Figure 6.106: PNDD, 3D maps of Z-coordinates obtained from the analysis of the averaged images taken in October 2013 (left), also visualized as 2D semi-transparent coloured maps superimposed to the visible image (right)

In order to compare the images acquired in the two different periods, for the two sets of averaged data, the coordinates of each pixel were extracted in a .csv file. These files were used to perform the registration of the images acquired in the second period on the images acquired in the first period and to overlap them in the same 3D reference metric system in order to obtain comparable images, by operating a mathematical translation. This operation was carried out with a Matlab routine which was on-purpose developed at the Department of Mathematics (Figure 6.107).

Finally, by subtracting each pixel of the 2nd period averaged image to those of the 1st one, a map of differences was determined in order to detect the presence of changed areas which are caused by material losses (i.e. detachment of brick flakes) or material “acquisition” corresponding to i.e. salt efflorescences. This first calculation shows that the procedure is promising and seems to be effective, at least qualitatively, opening a new perspective in the field of imaging diagnostic (Figure 6.108).

A further analysis step, still on-going, would be the quantification of the areas varied between the two tested periods, by calculating the volumes of “acquired” or loss materials, possibly also distinguishing between bricks and mortar joints.

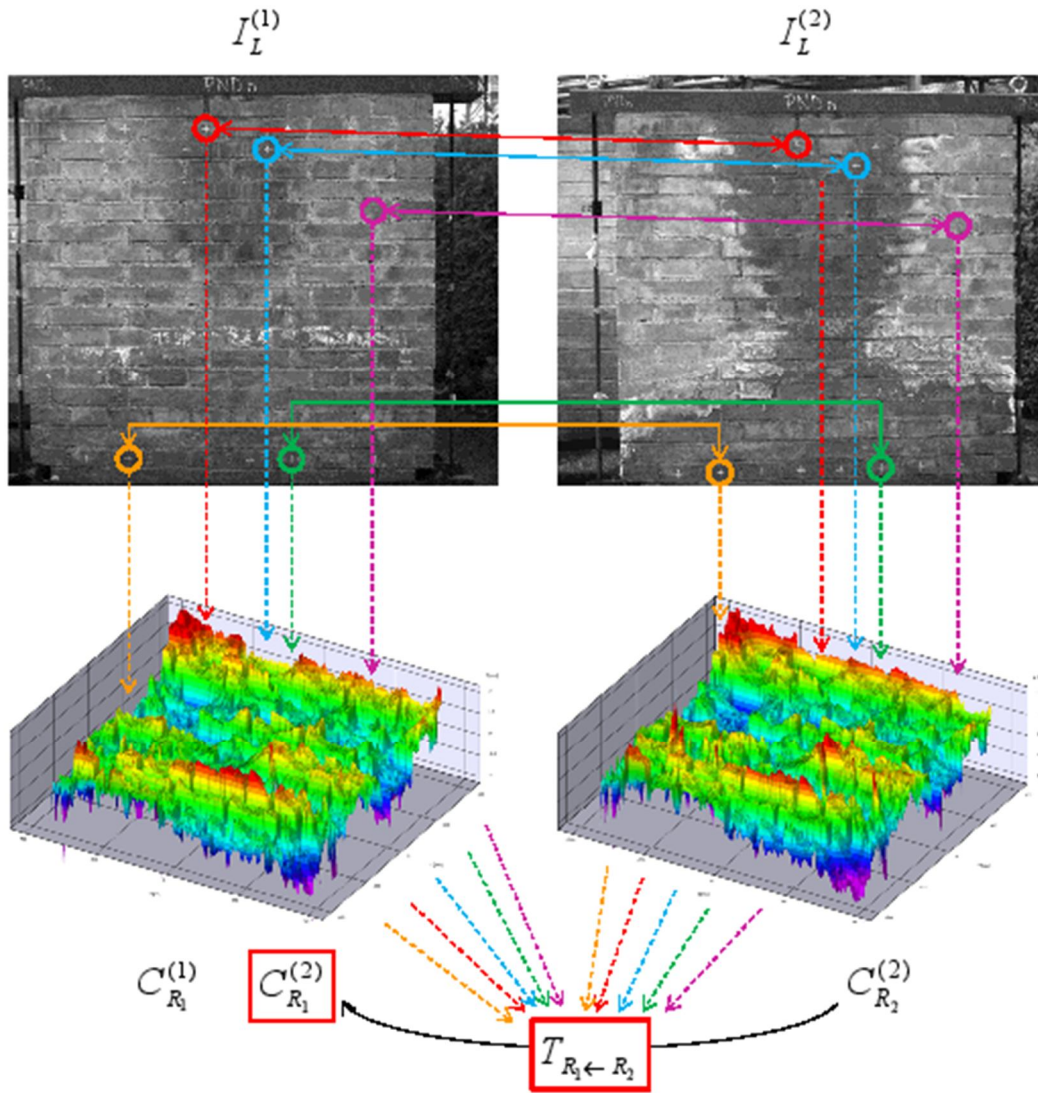


Figure 6.107: Registration procedure of the DIC images acquired in two different periods

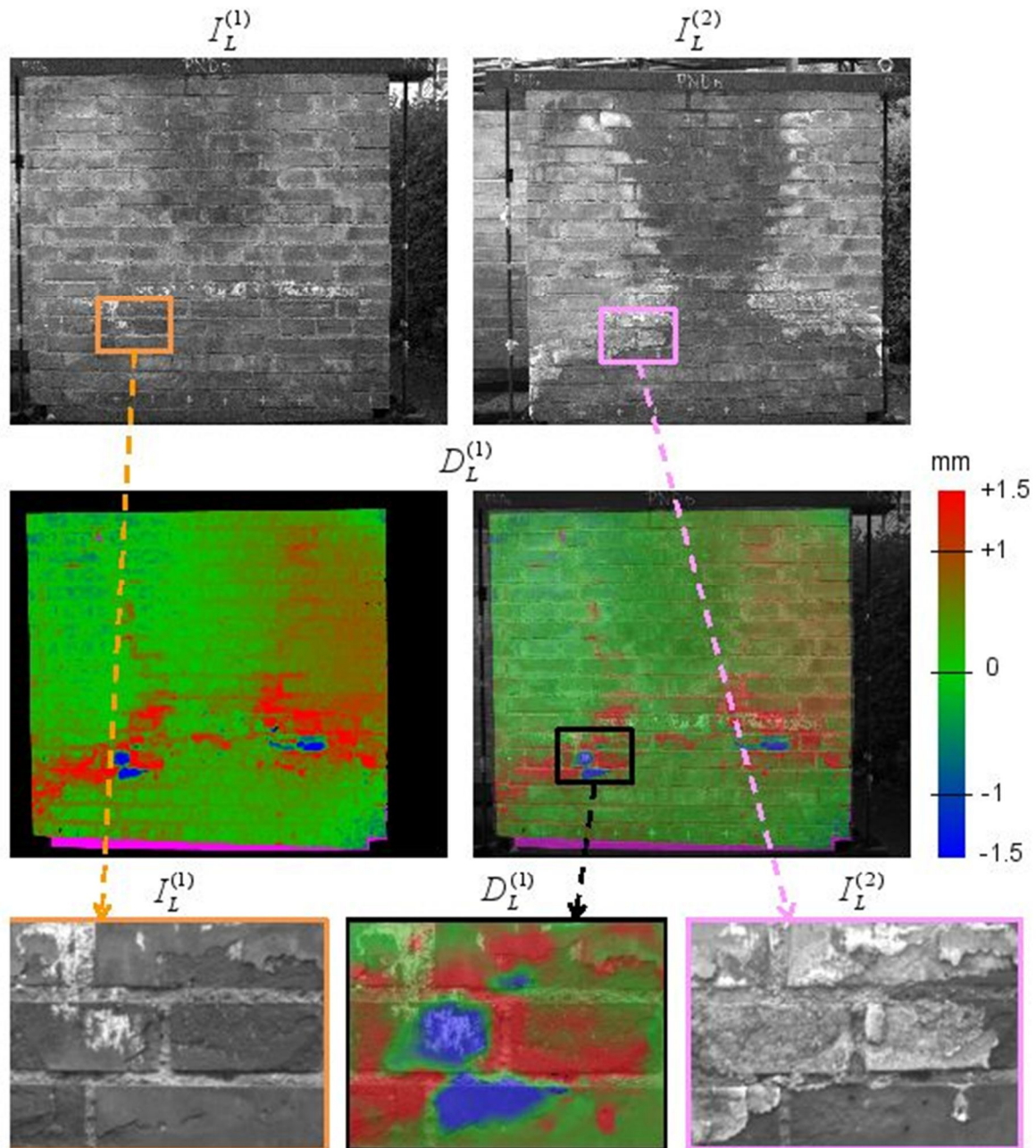


Figure 6.108: Results presented in terms of differences maps (in the centre of the image) and a detail of this “difference” image compared with the same detail as visible in the first (bottom left) and second (bottom, right) measurement campaign

7. Non-destructive sonic evaluation of masonry specimens subjected to natural or accelerated ageing

In this chapter the results of the non-destructive evaluation of degradation effects due to natural or accelerated ageing treatments on the small walls and six-brick columns (§4.4) are reported, after a brief description of the testing set-up and procedures.

Sonic tests in direct transmission mode were first of all carried out on 3 small brick walls and 9 columns in as-built conditions, to non-destructively characterize the health-state of the masonry and record reference values of sonic velocity, signal attenuation and elastic modulus of elasticity to be later used for comparisons.

Then, the same tests were repeated on several natural and artificial weathered masonry assemblies at the end of the specific ageing periods.

Comparison between the obtained parameters were carried out with the aim of assessing possible variations on the elastic properties caused by the replicated decay processes.

Moreover, additional direct sonic tests, were carried out on 5 small walls in cracked conditions, after the mechanical compression tests (§4.4)

7.1. Sonic evaluation: data acquisition and analysis procedure

For each specimen, prior to start the measurements, a geometric survey was performed in order to measure the lengths of the ideal straight paths of the signals in the different stations. Then, the chosen measurements points, were traced on the specimens' faces, after a rough cleaning of the surfaces, if necessary (i.e. to eliminate the layer of salt efflorescences present on the surfaces at the end of the accelerated ageing treatments).

For the small walls, direct sonic test in the plane of the wall (horizontally) were carried out. The data acquisition stations were positioned on the right and left faces of the specimen (looking at the front) in the centre of each brick head. They were numbered from 1 to 7 (and corresponding 1'-7'), starting from the bottom of the small wall. The sonic measurements were carried out, positioning the hammer in the wall's right face and the receiver in the left face on each masonry course and vice versa, acquiring data starting from the bottom (Figure 7.1 left). The emitted signals were not amplified (1x) while the received signals were amplified (10x).

On the six-brick columns, direct sonic tests were carried out in two directions: in the plane of the wall (horizontally) and vertically, crossing the entire height of the specimen. Thus, 6 measurement stations were positioned on the lateral faces of the column, in the centre of each brick head, numbering them, on the right face, progressively from 1 to 6' from the bottom upwards (and 1'-6' respectively) on the left side. The data were acquired on each brick,

starting from the bottom, placing once the hammer in the right face and the receiver in the opposite face and once vice versa (Figure 7.1 centre). Other 2 stations were positioned (7 and 7'), respectively, in the centre of the top and bottom face of the masonry specimen. Only one measure was performed between these stations, by positioning the hammer on the top and receiving the signal at the bottom (Figure 7.1 right). Also in these cases, emitted signals were not amplified (1x) while the received signals were 10-times amplified (10x).

During the data acquisition, attention was drawn on the presence of visible defects, cracks, or salt efflorescences in order to be able to explain possible variations on the measured values.

The sonic data were analysed in terms of time of flight, sonic signals velocity and signals attenuation.

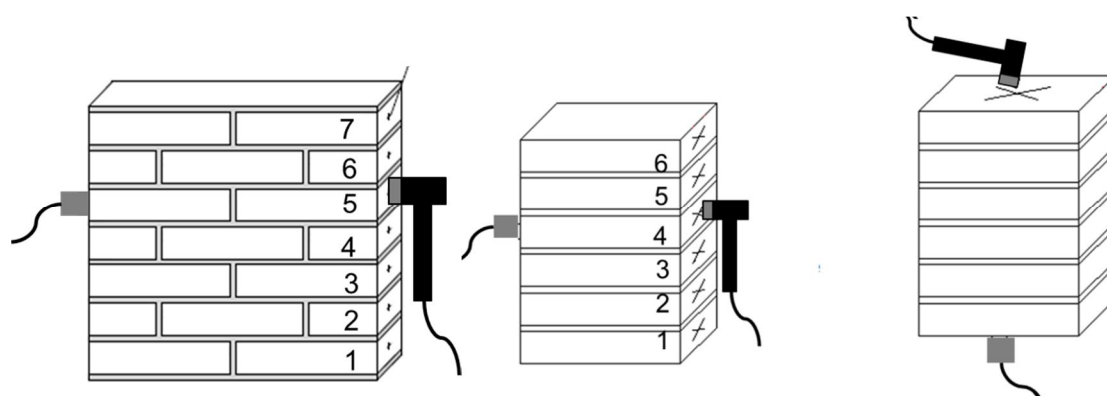


Figure 7.1: Sonic tests: measurement stations on small wall (left) and six-brick column (centre and right)

7.2. Small walls

Direct sonic tests along the plane of the wall were carried out on three as-built small walls, 3 walls subjected to a different number of accelerated ageing cycles and 6 walls naturally aged, after 1 year of weathering (Table 7.1).

Table 7.1: Characteristics of the small walls evaluated by sonic tests in direct transmission

Specimen code	Ageing treatment	Salt solution	N° of cycles / year
A, B, C	None, as-built	/	/
VI	acc. ageing	10%-wt. Na ₂ SO ₄	18 cycles
V	acc. ageing	10%-wt. Na ₂ SO ₄	26 cycles
II	acc. ageing	10%-wt. Na ₂ SO ₄	38 cycles
VII	natural ageing	water	1 season
VIII	natural ageing	water	1 season
IX	natural ageing	0.05%-wt. NaCl	1 season (65*)
X	natural ageing	0.05%-wt. NaCl	1 season (65*)
XI	natural ageing	0.05%-wt. Na ₂ SO ₄	1 season (37*)
XII	natural ageing	0.05%-wt. Na ₂ SO ₄	1 season (37*)

*estimated number of salt phase changes during the considered ageing summer

7.2.1. As-built walls

First of all, 3 small brick walls (A, B, C) in as-built, undamaged conditions were considered.

The values of sonic velocity varied from 2100 m/s to 2800 m/s, which indicated a properly constructed masonry, nominally characterized by high values of compressive strength and high value of modulus of elasticity. The signal attenuation presented low values, varying from 4 to 18 dB, pointing out the absence of defects or voids (Gabielli et al, 2011).

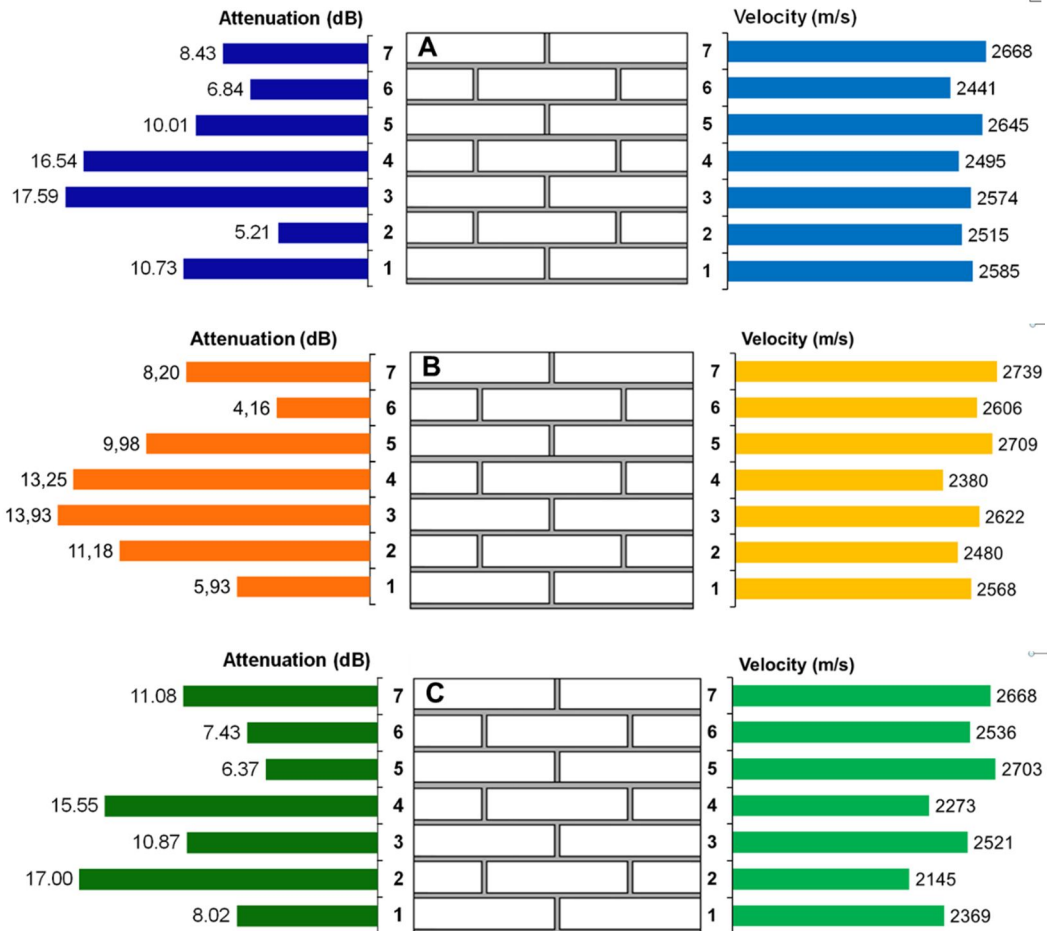


Figure 7.2: Small walls, as-built: values of sonic signal attenuation (left) and direct velocity (right) on each masonry course

The graphs reporting the calculated velocities for each masonry course on the 3 undamaged specimens showed an interesting “zigzag” behaviour (Figure 7.2 right). Higher values of velocities were measured on the masonry courses which presented only 1 vertical mortar joint (odd courses) while lower values were recorded when the sonic wave signals crossed two vertical mortar joints (even courses). Thus, these variations are useful to obtain information on the brick masonry layouts or on the design details.

In order to obtain more reliable reference values for the measured parameters to be later used for comparison, by discarding or at least limiting the dispersions due to intrinsic materials’ inhomogeneities, the values of velocity and attenuation measured on each masonry course of

the three small walls were averaged, obtaining approx. 2535 m/s and 10.40 dB. The simplified value of velocity is quite accurate (CoV=5%) while the averaged attenuation values are more dispersed (CoV= 31%) (Table 7.2). By plotting these values course by course it is noted that the averaged velocities are still able to show the sort of zigzag behaviour (Figure 7.3 right) and, anyhow, the resulting averaged values of attenuation are less dispersed.

From the averaged measured velocities, the values of the dynamic modulus of elasticity were calculated on each masonry course according to Eq. 3.7. From these values, by applying a reduction of 30% (Pascale, 2008), the values of static modulus of elasticity were estimated (Table 7.2)

Table 7.2: Small walls, as-built, direct sonic tests: average values of measured parameters

Masonry course	Time of flight [μ s]	Velocity [m/s]	Attenuation [dB]	E dyn [MPa]	E [MPa]
1	195.33	2507.25	8.23	10660.64	7462.45
2	207.33	2380.07	11.13	9639.10	6747.37
3	190.67	2572.21	14.13	11206.04	7844.23
4	207.33	2382.64	15.11	9626.46	6738.52
5	183.33	2685.75	8.79	12215.34	8550.74
6	194.67	2527.69	6.14	10826.42	7578.49
7	182.67	2691.95	9.24	12272.25	8590.57
	Avg	2535.36	10.40	10920.89	7644.63
	CoV [%]	5.01	31	9.88	9.88

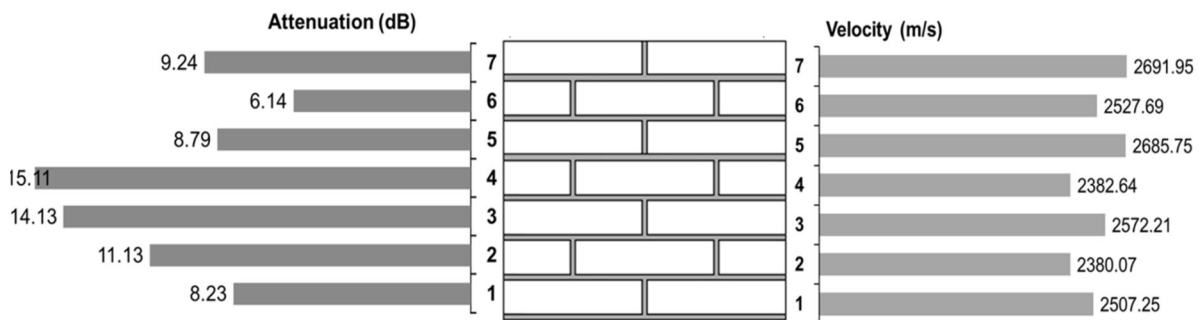


Figure 7.3: Averaged values of direct sonic velocity and attenuation for the three as-build small walls

7.2.2. Naturally aged small walls

Later, a similar testing procedure was conducted on the 6 small masonry walls naturally aged.

The tests were performed after 1 season of ageing in order to evaluate the effects of this initial environmental degradation. It is worth to remind that, in addition to outdoors exposure, these small walls were subjected to capillary rise from the base using water (VII and VIII), sodium

chloride solution (IX and X) or 0.05% -wt. sodium sulphate solution (XI and XII) (Figure 7.4).

In these cases, sonic tests in direct transmission mode were carried out starting from masonry course 2 or 3 due to the presence of the tub.



Figure 7.4: Arrangement of the small walls naturally aged

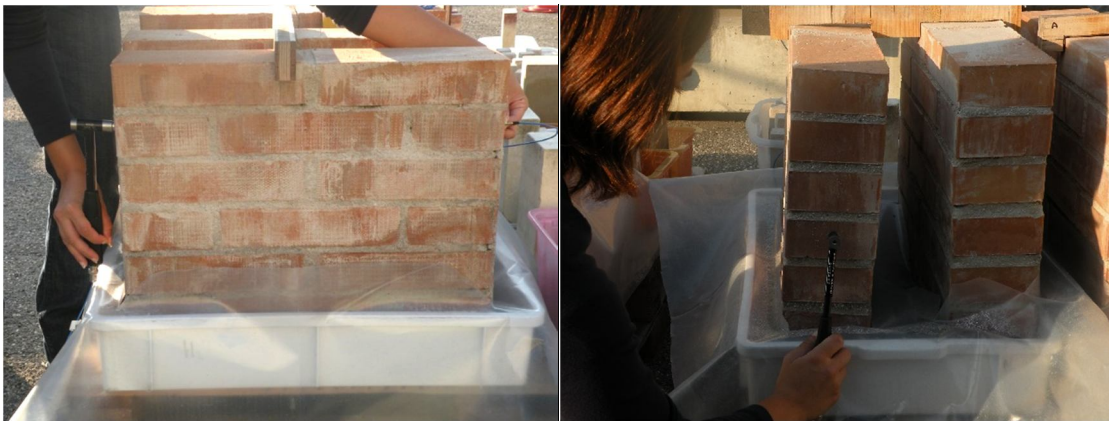


Figure 7.5: Small walls, direct sonic tests: phases of data acquisition

First of all, by way of example, the results obtained for 3 small walls, 1 for each pairs in terms of direct sonic velocity are reported (Figure 7.6, Figure 7.7, Figure 7.8).

Overall, the values of velocity increased up to a certain height and then decreased, according to the different visible height of the capillary rise level and the presence of salt efflorescences. Moreover, the variations due to the masonry layouts which were very clear on the as-built walls, are no more visible after 1 season of ageing, independently to the types of solution used to simulate the capillary rise. This is probably caused by the presence of water and salts into the materials pores, both of brick and mortar. Thus, the ability of the technique in distinguishing between different materials is masked by the effects of the weathering processes (see Figure 7.10).

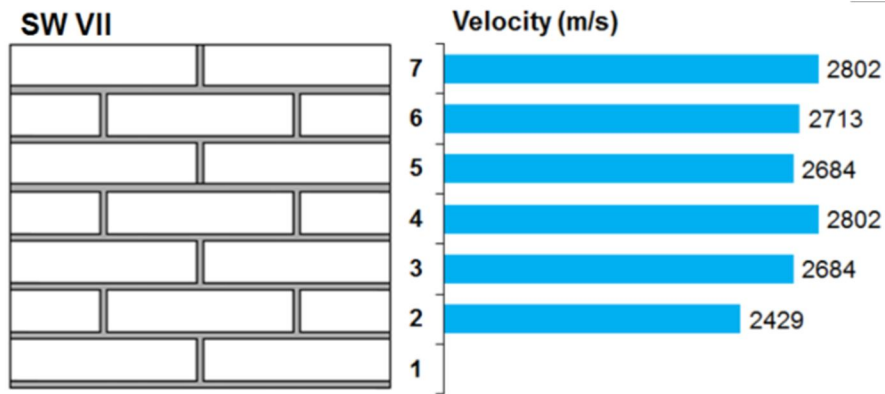


Figure 7.6: Small wall VII (tap water), direct sonic tests: attenuation (left) and velocities (right)

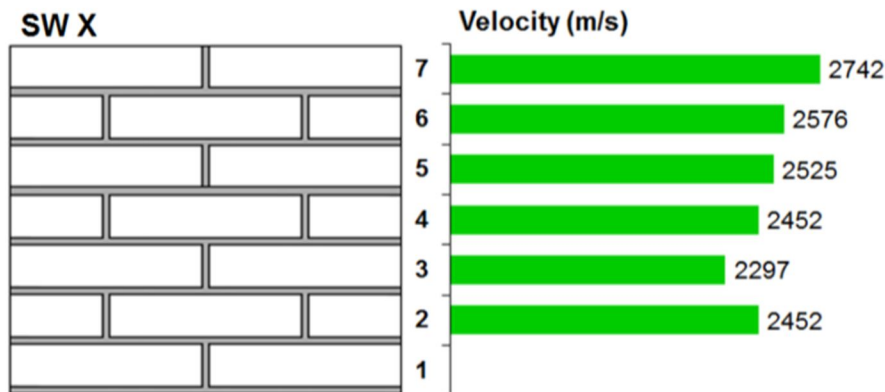


Figure 7.7: Small wall X (0.05% -wt. NaCl), direct sonic tests: attenuation (left) and velocities (right)

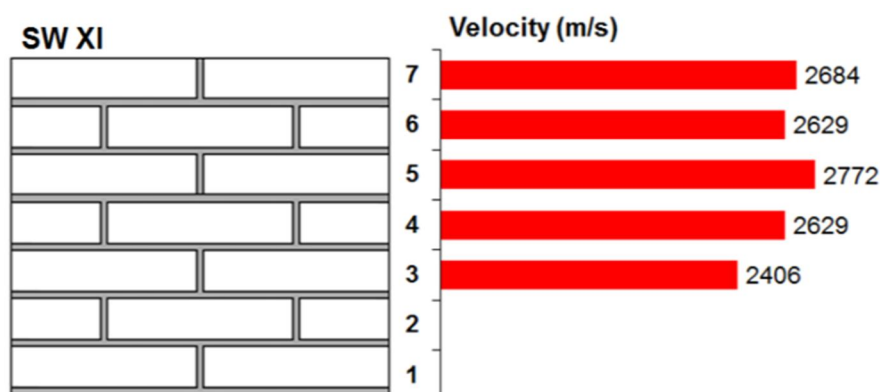


Figure 7.8: Small wall XI (0.05% -wt. Na₂S₀₄), direct sonic tests: attenuation (left) and velocities (right)

The highest values of velocity were measured on small wall VII, subjected to water capillary rise while the lowest ones were measured for the specimen subjected to sodium chloride rise, small wall X (Table 7.3). It was expected to collect lowest values for the small wall subjected

to sodium sulphate, but, this behaviour is explainable taking into account that the considered ageing season had favoured the sodium chloride hydration/crystallization cycles almost twice as for the sodium sulphate (4.4).

Anyhow, a specific evaluation was carried out in order to better understand the behaviour of small wall X. Thus, for each masonry course, the signal attenuation measured were visualized together with the velocity (Figure 7.9 left). The two parameters are not really in agreement, as the lowest value of velocity was measured at masonry course 3 while the highest signal attenuation was determined at masonry course 5. In addition, the courses 6 and 7 showed values very similar to the ones measured on the walls in undamaged conditions. This result was confirmed by the experimental evidence, as, the visible level of capillary rise was at masonry course 5. In addition, in this position, some blistering of the brick surface was detected (Figure 7.9 right). Thus, the signal attenuation seems to be a parameter more sensible to the localized initial environmental decay than the signal velocity (Figure 7.10).

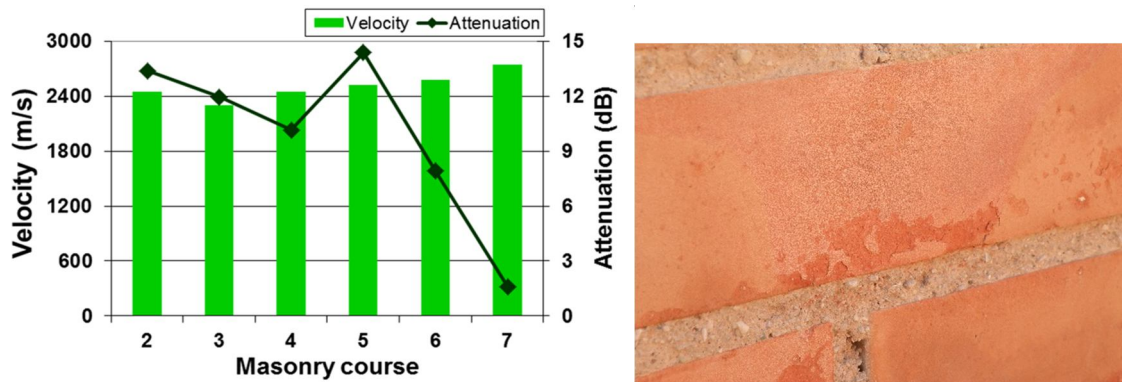


Figure 7.9: Small wall X (0.05%-wt. NaCl): sonic velocities and signal attenuation (left), visible superficial decay (right) (Gabrielli et al., 2009)

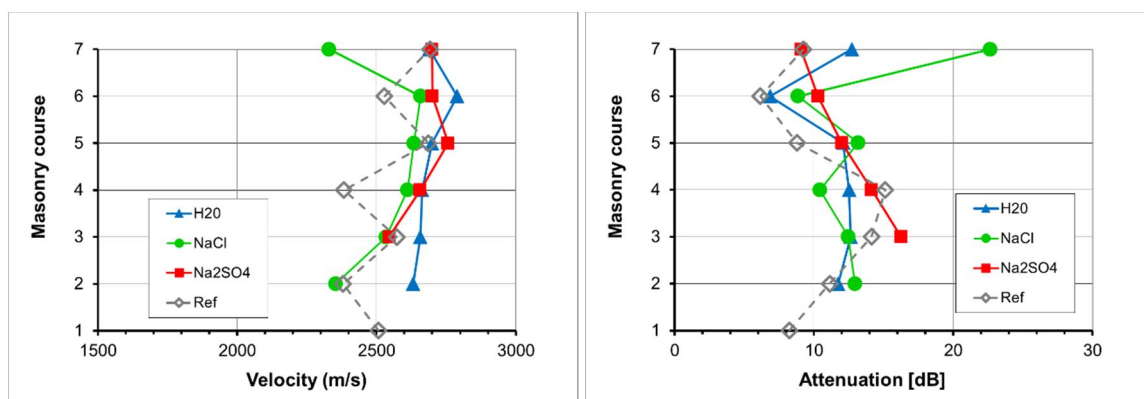


Figure 7.10: Average values of direct sonic velocity (left) and attenuation (right) measured for the pairs of naturally aged small walls. In grey, the reference profiles.

Finally, from the average values of velocity, the values of the elastic dynamic modulus were determined, as well as the “hypothetical” static ones (Table 7.3). A reduction in these values is recorded for the small walls subjected to salt capillary rise, compared to the specimens in

contact with tap water. Anyhow, these values also indicated that the environmental decay already occurred on the small walls had only slightly affected the mechanical properties of the masonry.

Table 7.3: Small walls naturally aged, direct sonic tests: average values of measured parameters

Small wall	Velocity [m/s]	Attenuation [dB]	E dyn. [MPa]	E [MPa]
VII	2685.69	11.53	12239.94	7343.97
VIII	2690.11	11.02	12280.65	7368.39
Avg	2687.90	11.28	12260,30	7356,18
CoV [%]	2.05	20.14	4.02	4.69
IX	2533.55	16.95	11054.17	6632.50
X	2507.26	9.91	10675.62	6405.37
Avg	2520.41	13.43	10864.89	6518.94
CoV [%]	5.74	35.96	10.63	12.40
XI	2623.87	9.83	9735.31	5841.18
XII	2718.97	14.87	10433.28	6259.97
Avg	2671.42	12.35	10084.29	6050.57
CoV [%]	2.96	23.50	6.91	8.06

7.2.3. Artificially aged small walls

The same procedure described before was used to perform sonic tests in direct transmission mode on the three small walls at the end of the artificial ageing treatments. In these cases, a rough cleaning of the surfaces before starting the tests was necessary as the surfaces were completely covered by salts (Figure 7.11).

The results in terms of signal velocity and attenuation are visualized for each masonry course (Figure 7.12, Figure 7.13, Figure 7.14). The values of the dynamic modulus of elasticity and the estimated values of the static modulus were also calculated (Table 7.4 - Table 7.6).



Figure 7.11: Small wall II at the end of artificial ageing treatment (38 cycles) (left) and detail of data acquisition (right)

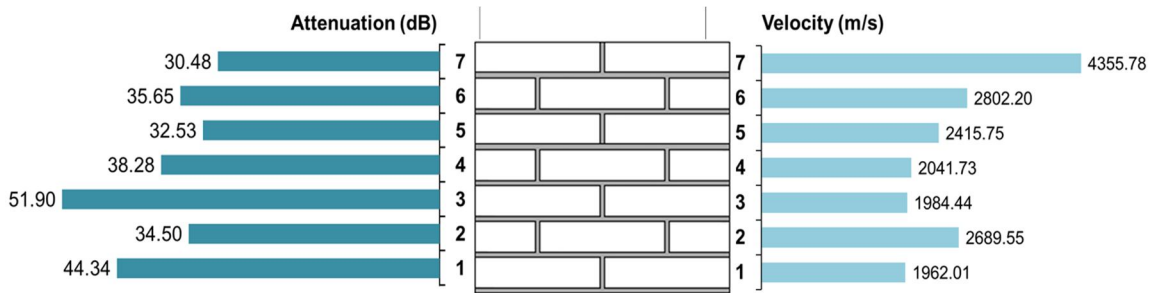


Figure 7.12: Small wall VI, after 18 ageing cycles: values of sonic signal attenuation (left) and direct velocity (right) on each masonry course

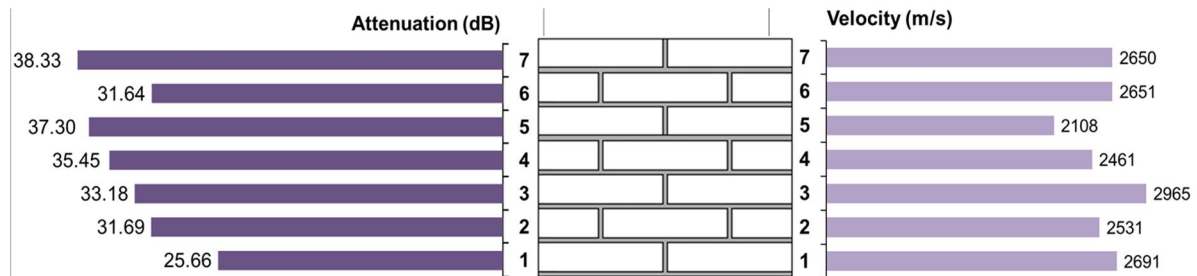


Figure 7.13: Small wall V, after 26 ageing cycles: values of sonic signal attenuation (left) and direct velocity (right) on each masonry course

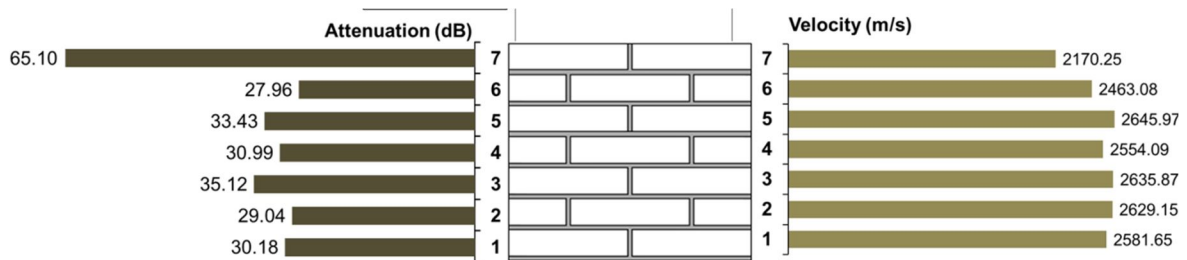


Figure 7.14: Small wall II, after 38 ageing cycles: values of sonic signal attenuation (left) and direct velocity (right) on each masonry course

The graphs reporting the calculated velocities for each masonry course on the 3 artificially aged small walls do not show the “zigzag” behaviour noted for the small walls in as-built conditions. Thus, as for the specimens naturally aged, it is not possible to discriminate between the different layout compositions of the masonry courses. The weathering treatments affecting both brick and mortar joints seemed to return them no longer differentiable (Figure 7.15).

These profiles, at the increasing number of ageing cycles, became less dispersed, and in the case of the most damaged small wall, II, it was almost vertical (values around 2600 m/s), with the exception of the top masonry course which presented the lowest velocity (2100 m/s).

The values of attenuation are almost constant, around 35dB for all the masonry courses of the three small walls. Higher values were measured at masonry course 3 of specimen VI and course 7 of small wall II, both presenting brick delaminations and cracks in correspondence of

the measurement stations. Thus, the attenuation seems to be a reliable parameter to evaluate localized decay effects.

Table 7.4: Small wall VI, after 18 cycles of accelerated ageing, direct sonic tests: average values of measured parameters

Masonry course	Time of flight [μ s]	Velocity [m/s]	Attenuation [dB]	E dyn [MPa]	E [MPa]
1	270,00	1962,01	44,34	6518,18	4562,73
2	191,00	2689,55	34,50	12248,52	8573,96
3	267,00	1984,44	51,90	6668,07	4667,65
4	253,00	2041,73	38,28	7058,68	4941,07
5	212,00	2415,75	32,53	9881,65	6917,15
6	182,00	2802,20	35,65	13296,04	9307,23
7	133,00	4355,78	30,48	32126,05	22488,23
	Avg	2607,35	38,24	12542,45	8779,72
	<i>CoV [%]</i>	<i>32.3</i>	<i>19.61</i>	<i>72.2</i>	<i>72.2</i>

Table 7.5: Small wall V, after 26 cycles of accelerated ageing, direct sonic tests: average values of measured parameters

Masonry course	Time of flight [μ s]	Velocity [m/s]	Attenuation [dB]	E dyn [MPa]	E [MPa]
1	188	2691	25,66	12262,13	8583,49
2	200	2531	31,69	10849,80	7594,86
3	171	2965	33,18	14890,76	10423,53
4	205	2461	35,45	10258,68	7181,07
5	245	2108	37,30	7526,67	5268,67
6	191	2651	31,64	11900,20	8330,14
7	192	2650	38,33	11894,85	8326,39
	Avg	2580	33,32	11369,01	7958,31
	<i>CoV [%]</i>	<i>10.13</i>	<i>12.83</i>	<i>19.67</i>	<i>19.67</i>

Table 7.6: Small wall II, after 38 cycles of accelerated ageing, direct sonic tests: average values of measured parameters

Masonry course	Time of flight [μ s]	Velocity [m/s]	Attenuation [dB]	E dyn [MPa]	E [MPa]
1	199,00	2581,65	30,18	11285,50	7899,85
2	194,00	2629,15	29,04	11704,53	8193,17
3	194,00	2635,87	35,12	11764,47	8235,13
4	200,00	2554,09	30,99	11045,77	7732,04
5	193,00	2645,97	33,43	11854,79	8298,35
6	208,00	2463,08	27,96	10272,64	7190,85
7	235,00	2170,25	65,10	7975,26	5582,68
	Avg	2525,72	35,98	10843,28	7590,30
	<i>CoV [%]</i>	<i>6.69</i>	<i>36.35</i>	<i>12.71</i>	<i>12.71</i>

Overall, although the small differences, it seems that the values of velocity decrease at increasing number of ageing cycles (Table 7.7). These values, however, for small wall VI and V are greater than the reference value (2535 m/s). Instead, the velocity measured on small wall II, which underwent 38 artificial ageing cycles was a little lower (10 m/s of difference). The average values of attenuation, instead, for these three aged walls are three times higher than the reference values. Thus, sonic tests seems to be able to distinguish between damaged and undamaged masonry but not so accurate to quantitatively differentiate the different levels of decay.

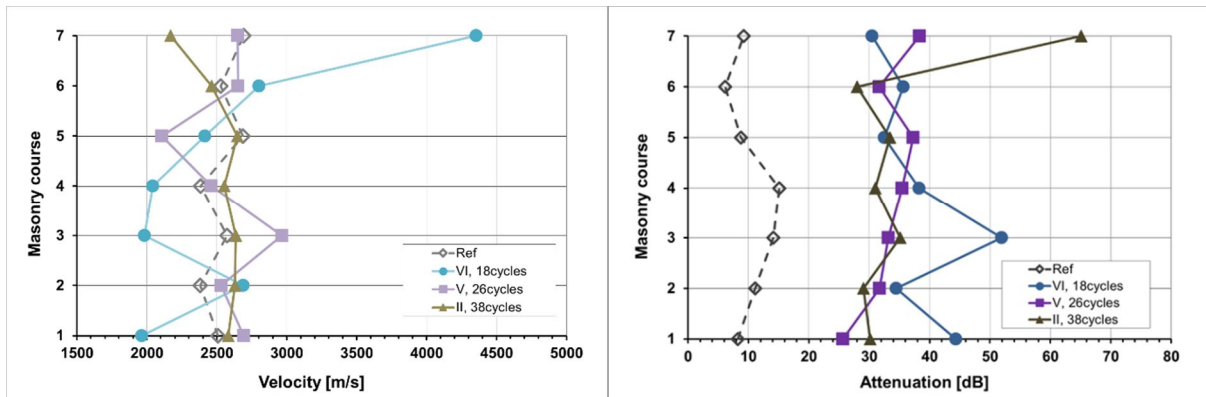


Figure 7.15: Average values of direct sonic velocity (left) and attenuation (right) measured for the three artificially aged small walls. In grey, the reference profiles.

Table 7.7: Small walls artificially aged, direct sonic tests: average values of measured parameters

Small wall	Velocity [m/s]	Attenuation [dB]	E dyn. [MPa]	E [MPa]
VI	2607,35	38,24	12542,45	8779,72
V	2580	33,32	11369,01	7958,31
II	2525,72	35,98	10843,28	7590,30

7.2.4. Sonic tests, small walls mechanically damaged

Direct sonic tests following the same procedure were carried out also after the execution of mechanical tests (§ 8), in order to evaluate the accuracy of this non-destructive technique in detecting mechanical damages such as cracks and loss of materials.

Three small walls were considered. Small wall I was not subjected to weathering treatment and thus, the damages were only caused by the mechanical tests. Instead, the other two, VI and V underwent to artificial ageing treatment, respectively 18 and 26 cycles, prior to be subjected to compression tests.

For all the walls, the values of velocity and attenuation presented almost an opposite trend, by they gave complementary information. Indeed, while the lowest values of velocity are measured in correspondence of the greater cracks, greater attenuation were measured in presence of diffused cracks and exfoliations. Thus, a better knowledge on the health-state of masonry can be achieved by evaluating both parameters.



Figure 7.16: Small wall I, after mechanical compression test: values of sonic signal attenuation (left) and direct velocity (right) on each masonry course

Table 7.8: Small wall I, cracked, direct sonic tests: average values of measured parameters

Masonry course	Time of flight [μ s]	Velocity [m/s]	Attenuation [dB]	E dyn [MPa]	E [MPa]
1	264	1924	18.40	6269.66	4388.76
2	336	1524	24.97	3931.75	2752.23
3	362	1406	27.85	3347.67	2343.37
4	704	723	42.09	885.15	619.60
5	896	564	47.85	537.89	376.52
6	476	1074	59.22	1951.43	1366.00
7	468	1090	45.49	2010.82	1407.57
	Avg	1186	37.98	2704.91	1893.44

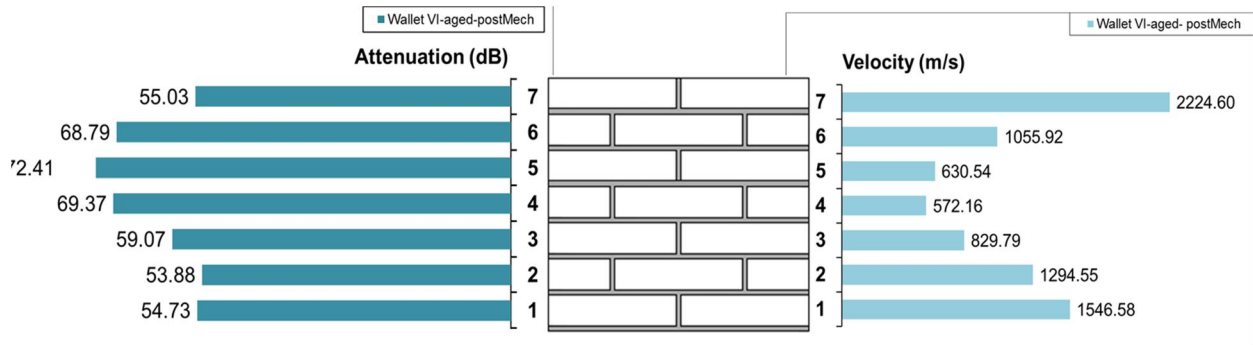


Figure 7.17: Small wall VI, aged, after mechanical compression test: values of sonic signal attenuation (left) and direct velocity (right) on each masonry course

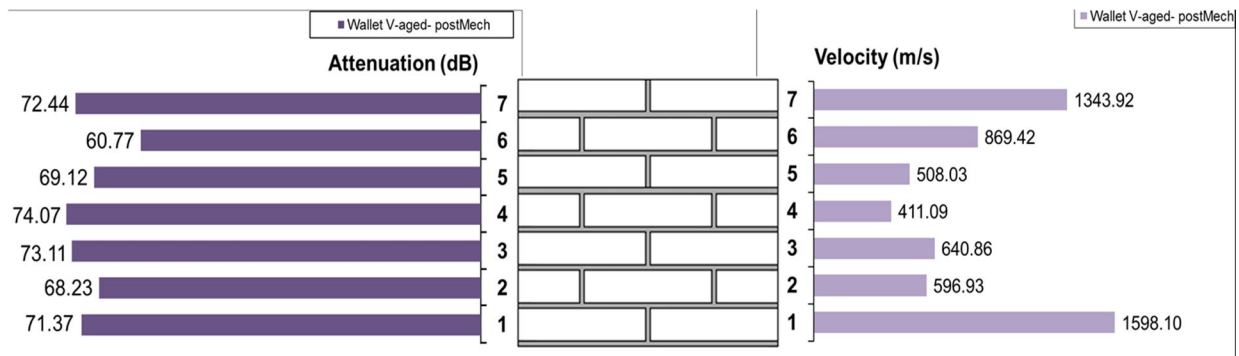


Figure 7.18: Small wall V, aged, after mechanical compression test: values of sonic signal attenuation (left) and direct velocity (right) on each masonry course

7.3. Six-bricks columns

Direct sonic tests were then carried out on three series of six-brick columns, 0S, 3S and 4S. The columns of series 0 were in undamaged conditions at the moment of the test, and they were considered to obtain reference values of sonic velocity, signal attenuation and dynamic modulus of elasticity. The specimens of series 3S and 4S were tested after, respectively, 26 and 38 cycles of artificial ageing with high-concentrated sodium sulphate solution.

7.3.1. Undamaged six-brick columns (series 0S)

These masonry columns were tested following the procedure reported in §7.1. Thus, for each specimen, 12 horizontal (2 for each brick row) and 1 vertical measurements were recorded.

The obtained values of velocity and signal attenuation were displayed.

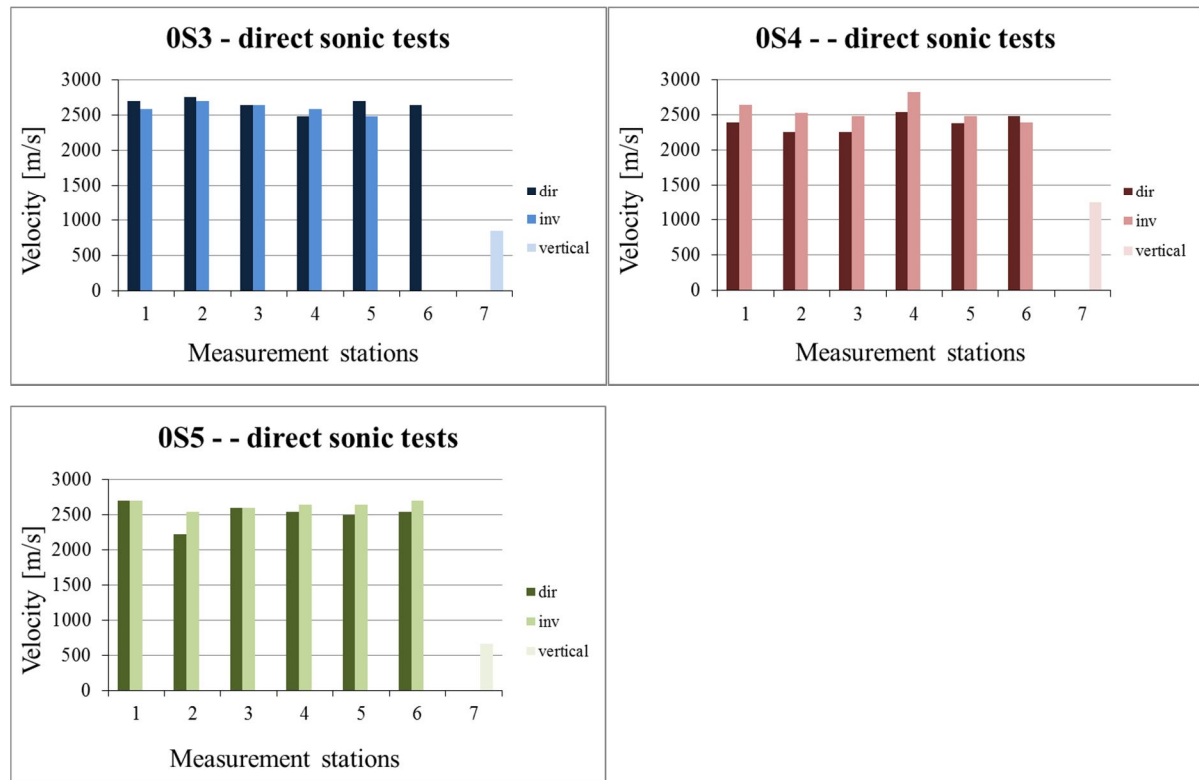


Figure 7.19: Values of direct velocity

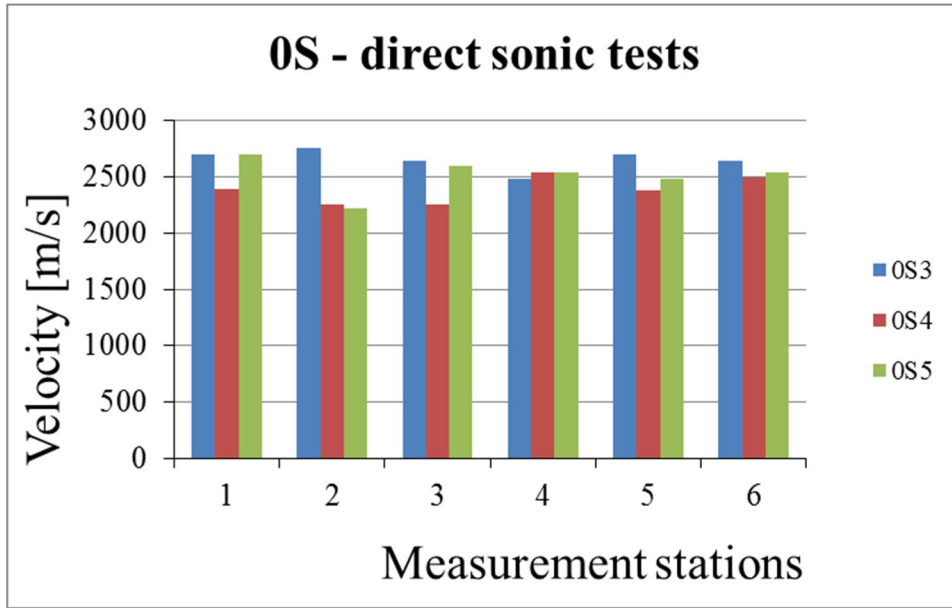


Figure 7.20: Direct velocity on each masonry course

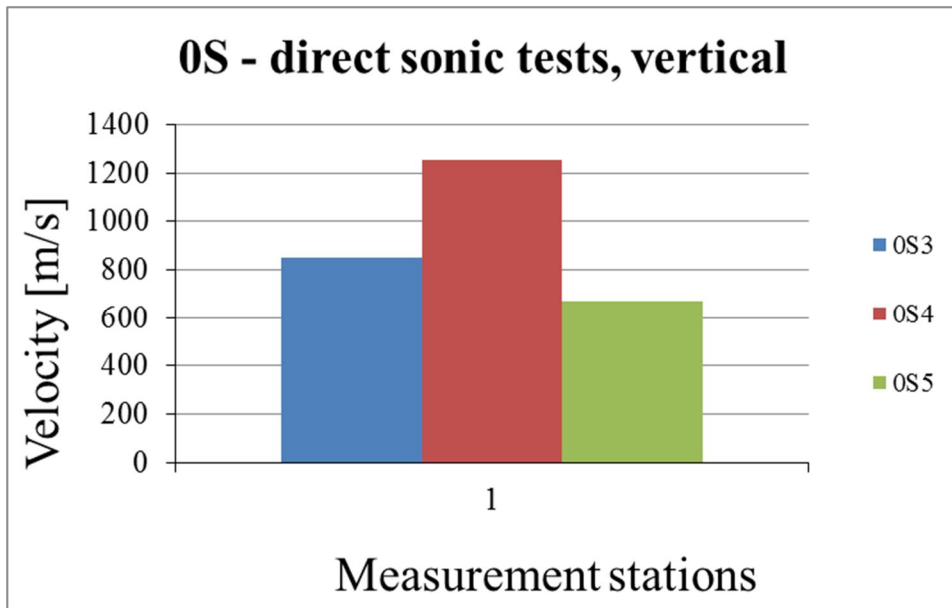


Figure 7.21: Direct velocity, vertical directions

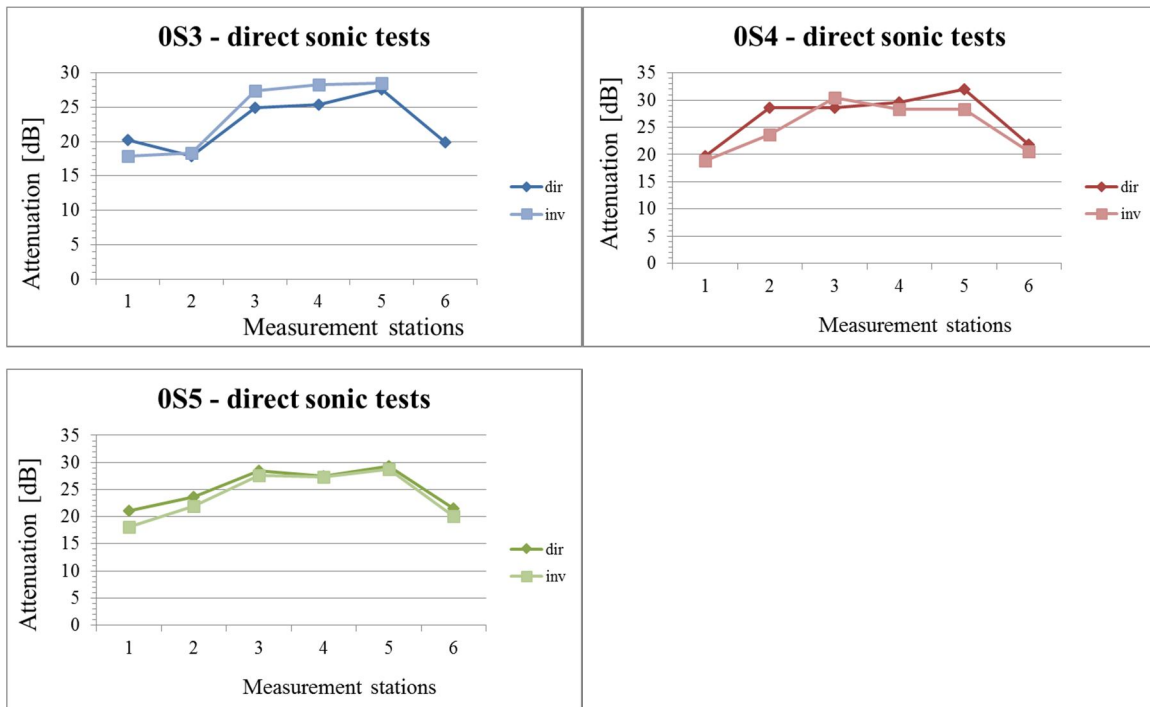


Figure 7.22: Attenuation values on each masonry course

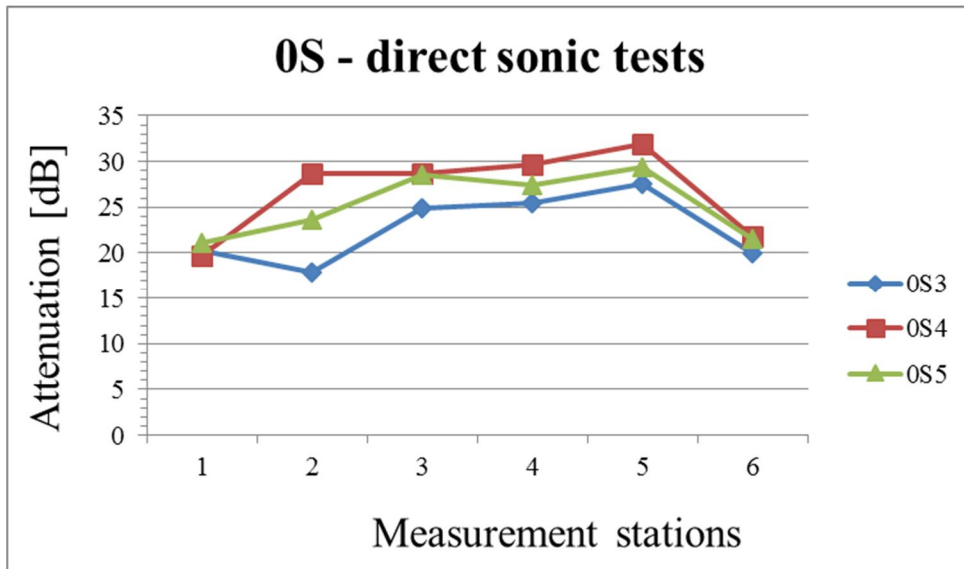


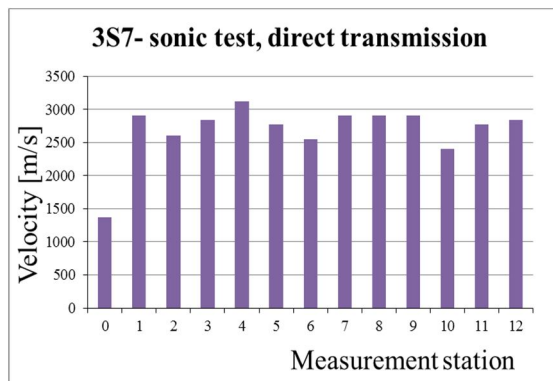
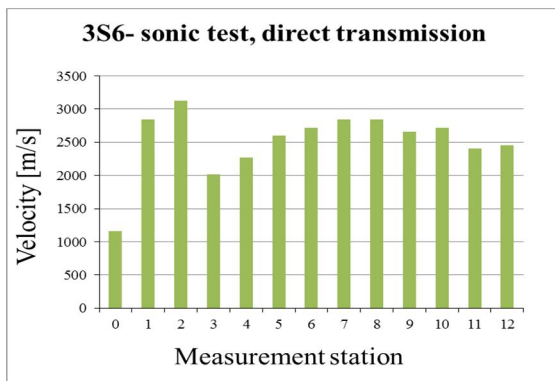
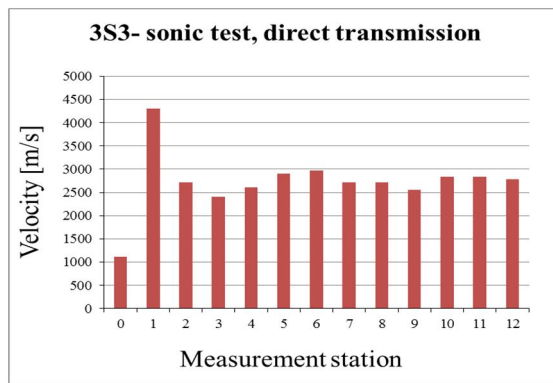
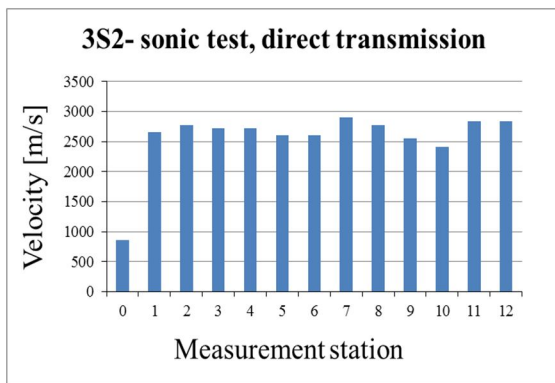
Figure 7.23 Average values of attenuations

7.3.2. Six-brick columns, artificially aged (26 ageing cycles)

The same procedure



Figure 7.24: Data acquisition



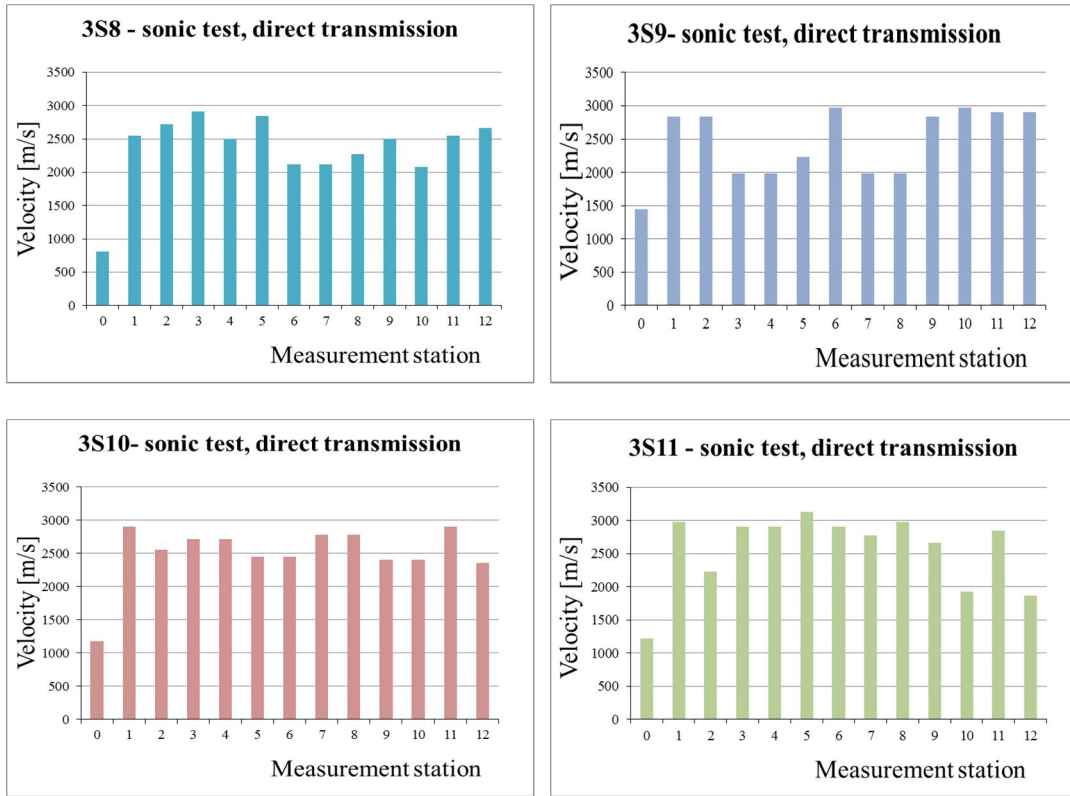


Figure 7.25 Values of direct velocities

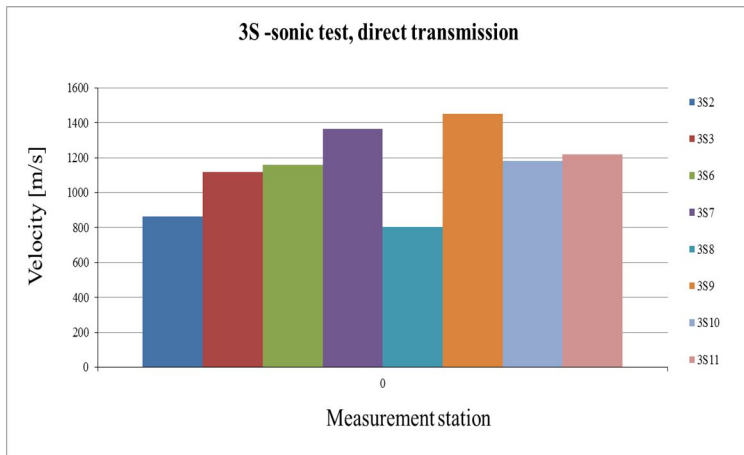


Figure 7.26: Direct velocity vertical station

7.3.3. Six-brick columns, artificially aged (38 ageing cycles)

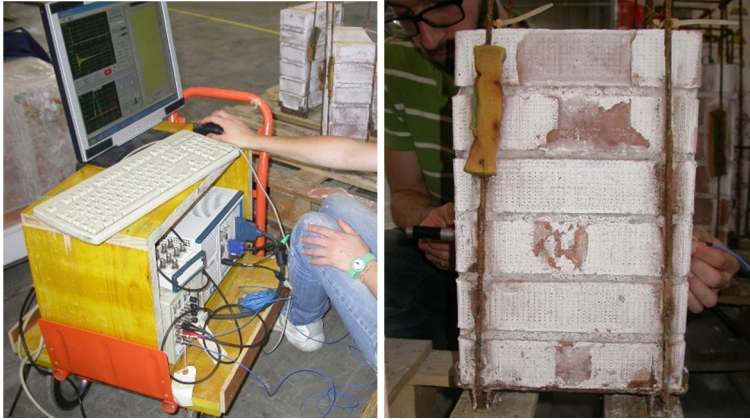
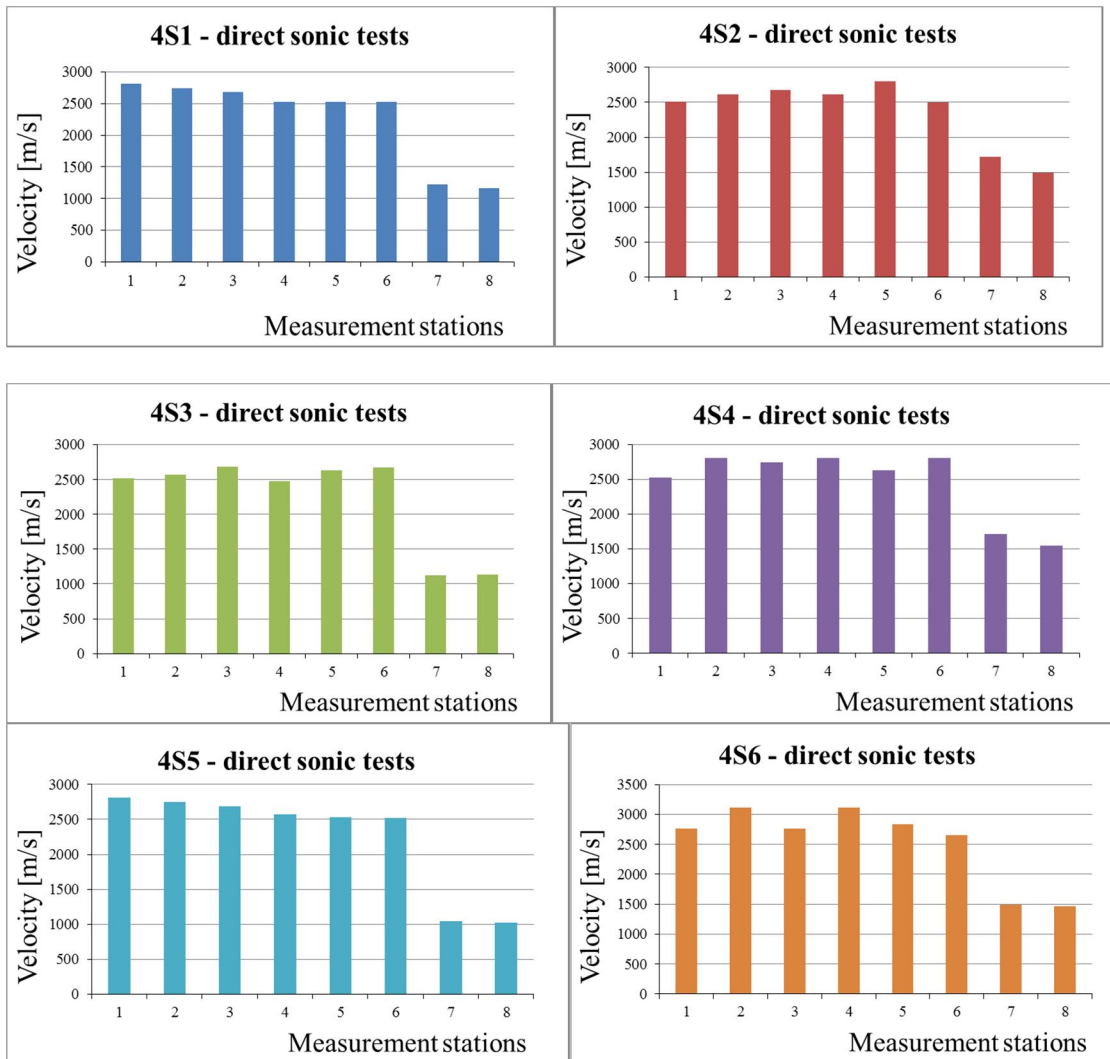


Figure 7.27:) Phases of data acquisition



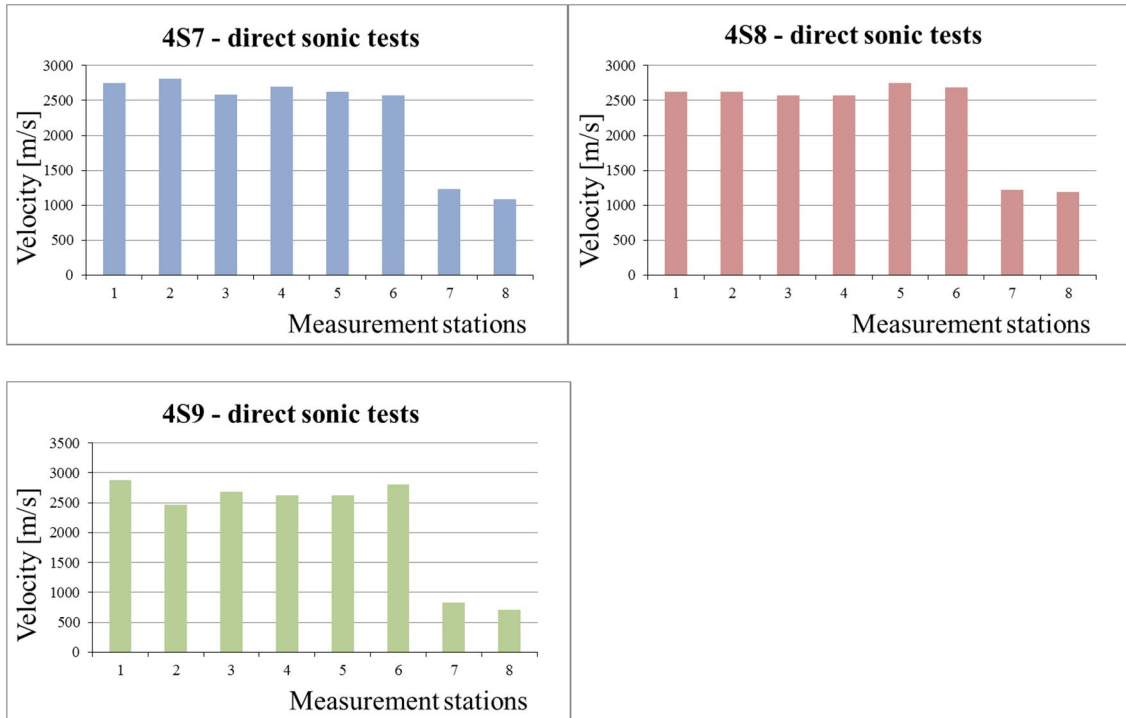


Figure 7.28: and direct velocity (right) on each masonry course

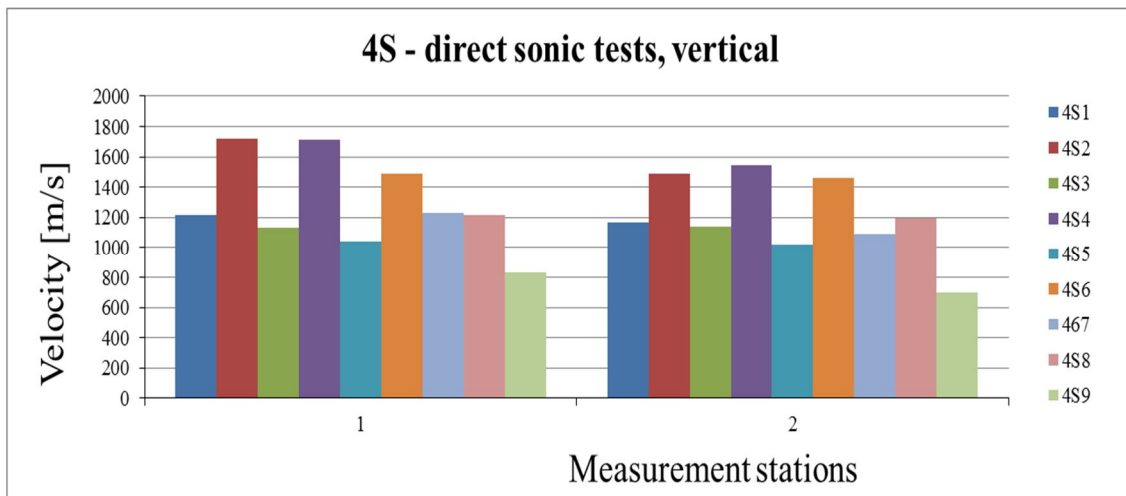


Figure 7.29: and direct velocity (right) on each masonry course

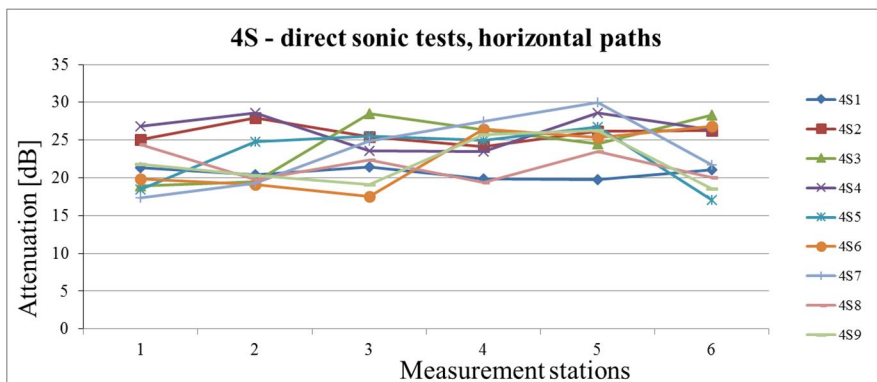


Figure 7.30:) and direct velocity (right) on each masonry course

Table 7.9: OS, comparison of results

	Avg velocity [m/s]		Attenuation [dB]		Ed [MPa]
	horizontal	vertical	horizontal	vertical	
OS3	2628	850	23,05	49,62	1301
OS4	2475	1252	25,89	37,33	2822
OS5	2576	667	24,64	41,18	801
Avg	2560	923	24,53	42,71	1641
<i>CoV [%]</i>	<i>3,05</i>	<i>32,39</i>	<i>7,73</i>	<i>14,71</i>	<i>64,00</i>

Table 7.10: 3S, comparison of results

	Avg velocity [m/s]		E [MPa]
	horizontal	vertical	
3S2	2700	864	2115,11
3S3	2864	1118	2272,71
3S6	2624	1159	3163,75
3S7	2796	1367	1097,51
3S8	2485	805	3561,96
3S9	2538	1450	2361,11
3S10	2619	1181	2511,79
3S11	2675	1218	997,69
Avg	2663	1145	2260
<i>CoV [%]</i>	<i>4,71</i>	<i>19,38</i>	<i>39,40</i>

Table 7.11: 4S, comparison of results

	Avg velocity [m/s]		Attenuation [dB]		E [MPa]
	horizontal	vertical	horizontal	vertical	
4S1	2635	1192	20,65	36,04	2557
4S2	2619	1604	25,82	35,59	4632
4S3	2592	1133	24,35	45,07	2310
4S4	2719	1628	26,25	39,84	4772
4S5	2643	1030	22,93	45,30	1910
4S6	2873	1476	22,54	37,27	3924
4S7	2672	1161	23,45	33,46	2425
4S8	2638	1206	21,59	38,74	2617
4S9	2682	768	21,97	43,53	1061
Avg	2675	1244	23,28	39,43	2912
<i>CoV [%]</i>	<i>3,10</i>	<i>22,50</i>	<i>8,10</i>	<i>11,00</i>	<i>43,20</i>

7.4. Conclusions

Sonic tests in direct transmission mode were carried out on different sets of small walls and six-brick columns naturally or artificially aged in order to evaluate the reliability of this non-destructive testing technique in assessing the decay effects caused by simulated weathering procedure as well as their evolution over time. Comparisons with the same tests carried out in undamaged specimens were carried out.

First of all, the values of direct sonic velocity and signal attenuation on the as-built small walls stated the homogeneity and good quality of masonry as well as the absence of voids or defects. At the same time, velocity differences measured between odd and even masonry courses, characterized respectively by one or two vertical lime mortar joints, indicated the reliability of the technique in distinguishing between the two materials, identifying the masonry layout.

The tests carried out on small walls outdoors exposed in addition to capillary rise from the base of tap water, 0.05%-wt. sodium chloride or sodium sulphate solution at the end of the 1st ageing season, has shown the potentiality of the method in assessing decay effects since the beginning throughout variations on both values of velocity and attenuation. Differences due to the geometry are no longer visible, as hidden by the environmental effects. Moreover, from these tests the specimens subjected to NaCl rise resulted the more damaged. This is in line with the appearance of the walls at the moment of the tests and explainable by the greater number of sodium chloride hydration/crystallization cycles possibly occurred in function of the microclimatic conditions.

The tests on small walls subjected to a different number of accelerated ageing cycles, confirm the potentiality of this non-destructive technique in evaluating the presence of water and salt related damages within the masonry materials. The attenuation seems a more sensible parameter than velocity to assess the presence of localized decay phenomenon; thus, it is important to study both values. Instead, a scarce accuracy in distinguishing the different levels of decay was detected because of a large dispersion of the data, although a decreasing in the values of velocity at increasing number of ageing cycles was measured.

The results on the six-brick columns confirmed the previous considerations. On each six-brick column, undamaged or decayed, along the horizontal paths, that is along single bricks, the values of velocity and attenuations were very similar. Instead, along the vertical paths, more disperse values were obtained, with coefficient of variations up to 33%, due to the different materials crossed by the waves. By comparing the data obtained for the as-built six-columns with the values measured for the two environmentally damaged series, an increase on the velocity values at increasing number of ageing cycles, both along the horizontal and vertical paths was measured, due to the presence of moisture and salts within the materials' pores. This results also on increasing values of estimated dynamic moduli, index of a greater stiffness of the damaged specimens. At the same time, lowering values of attenuation were recorded, probably because the damages are localized near the surfaces while the centre of the bricks, where the measurements were carried out, were still not affected by decay.

8. Mechanical evaluation of wallets subjected to natural or accelerated ageing

This chapter reports the procedure and results of the mechanical tests, uniaxial compression tests, carried out on the series of 0.5 x 0.5 x 0.12 m³ masonry wallets, described in §4.4. Actually only 5 of the 12 wallets prepared were tested. They presented different starting conditions: 1 wallet was in sound conditions (I) whilst 4 wallets were already damaged. These latter specimens were tested after being subjected to different ageing treatments: 3 wallets (VI, V and II) undergone to a different number of accelerated ageing cycles while 1 specimen (XII) was naturally aged (**Errore. L'origine riferimento non è stata trovata.**). The remaining masonry specimens were not tested because they were left to continue the weathering process.

The first part of the chapter describes the testing equipment and procedure followed for the mechanical tests as well as those employed for the non-destructive monitoring of the same which was performed by means of acoustic emission or digital image correlation. In the second part, the data analysis procedures were explained and the main mechanical and non-destructive results were visualized for each wallet. Finally, a comparison and critical discussion of the outcomes is presented.

Table 8.1: Characteristics of the masonry wallets subjected to mechanical test

Specimen code	Ageing treatment	Salt solution	N° of cycles / year
I	None, as-built	/	/
VI	Accelerated ageing	Na ₂ SO ₄ 10%-wt.	18
V	Accelerated ageing	Na ₂ SO ₄ 10%-wt.	26
II	Accelerated ageing	Na ₂ SO ₄ 10%-wt.	38
XII	Natural ageing	Na ₂ SO ₄ 0.05%-wt.	end of 3°year (157*)

*estimated number of salt phase changes during three summers

Each wallet was subjected to uniaxial compression tests according to [1]. The main aim of these destructive tests was to evaluate the effects of the decay due to environmental agents on the principal mechanical properties of masonry, such as compressive strength and modulus of elasticity.

For this purpose a series of wallets which differs only for the initial health state was subjected to the same test. In addition to the traditional monitoring devices, two non-destructive diagnostic techniques were employed to monitor the tests. The reliability of these techniques in assessing the mechanical damage and in following its evolution since the beginning of the test was evaluated. In detail, the acoustic emission (AE) and the digital image correlation (DIC) technique were considered. Actually, the AE method was employed only once, to monitor the compression test of the undamaged specimen, wallet I. Some specific adjustments were carried out in order to verify the applicability of AE in non-destructively detect the time instants corresponding to the formation of cracks as well as the crack opening evolution over

time in inhomogeneous material [1a]. On the other hand, the DIC method was used to monitor the 4 remaining compression tests and it was chosen in order to obtain a more complete knowledge on the behaviour of masonry and of its constituent materials under compression as it potentially allows recovering full-field displacement and strain maps of the investigated surface. Indeed, there was also an intrinsic aim connected to this monitoring because a simplified DIC procedure was adopted in view of further application on-site and to historical masonry structures. This procedure consisted in not applying any pattern to the investigated surface, as the same masonry texture was used with this purpose avoiding coating [1b, 22]. Thus, these laboratory investigations were also used to evaluate the accuracy and reliability of such streamlined DIC testing procedure in quantifying the behaviour of masonry wallets under mechanical compression.

In addition, the values of modulus of elasticity obtained from the compression tests herein reported were compared with the values of the dynamic moduli estimated from the velocities measured via non-destructive sonic tests performed before and after each mechanical test (§7), in order to assess the accuracy of this latter technique.

8.1. Preparation of the wallets

Before performing the mechanical tests, the 5 one-header brick wallets were measured, visually inspected and properly prepared.

First of all, a geometric survey was carried out by measuring the three main dimensions - length, width and height - of the wallets, in order to calculate their actual average resistant areas. Indeed, these may differ from the design areas because of minor adjustments occurred during construction but, above all, because of the ageing treatments which had underwent the specimens (Table 8.2). After that, the main masonry faces were cleaned. This practise consisted in a rough scrub of the surfaces by a metal brush and it was performed in order to remove dust, salt deposits and brick flakes possibly present. The cleaning procedure, more demanding but absolutely necessary for the three wallets subjected to accelerated ageing tests which presented surfaces completely covered by salts, had had different aims. Indeed, it was performed to ease the crack pattern survey, to obtain an adequate, stable and clean surface on which install the traditional wired monitoring devices and to achieve a not-homogeneous coloured texture to be used as reference pattern from the DIC system during the mechanical test monitoring [1b].

Table 8.2: Geometric dimensions of the wallets

Wallet	Length [mm]	Width [mm]	Height [mm]	Base area [mm ²]
I	507	120	442	60840
VI	513	120	456	61560
V	506	120	460	60720
II	510	118	460	60180
XII	514	121	470	62194

After that, a crack pattern survey was performed. It was aimed at qualitatively evaluate the initial health-state of the wallets and it consisted in recording in hand-made drawings to be later reported in cad, the position and extension of existing cracks as well as areas with lack of materials, both on the mortar joints and on the brick surfaces, or the presence of brick

scales/detachments. This initial decay is due in a minor amount to some initial defects of the construction materials but almost always it is caused by the ageing treatments (**Errore. L'origine riferimento non è stata trovata.**). The knowledge of such damages was useful to isolate them from those that will appear during the application of compression load. This was done because the existing damages could potentially represent weak points of the masonry and/or act as crack's starting points during the mechanical tests.

Figure 8.1: Crack pattern survey: wallet

Then, two thin metallic plates were rigidly coupled to the upper and lower faces of each wallet by means of a layer of cement mortar in order to guarantee the mutual planarity and parallelism of these faces and to assure a uniform distribution of the compression loads.

Furthermore, the traditional measuring instruments were installed. Indeed, to measure the global movements of the masonry specimens under compression [1], 5 inductive linear transducers, LVDTs, able to record displacements between 0 and 10 mm, with an accuracy of $\pm 1\%$ were employed. For each wallet, these instruments were fixed on the two main faces, at known positions and distances, by means of glued supports. Later, they were connected to a data acquisition control unit. More in detail, four LVDTs were placed with a vertical alignment, near the edges of the specimen, at about 6 cm from the corresponding external border, to measure the axial displacements, which are the displacements along the direction of load application (Figure 8.2, red numbers). The fifth transducer was employed to measure the transversal displacements, along the horizontal direction, x and it was placed roughly in the middle section of the wallet: front face, 4th brick course (Figure 8.2, in blue).

Finally, the so-prepared masonry wallets were positioned and centred under the plate of the testing machine chosen for the load application.

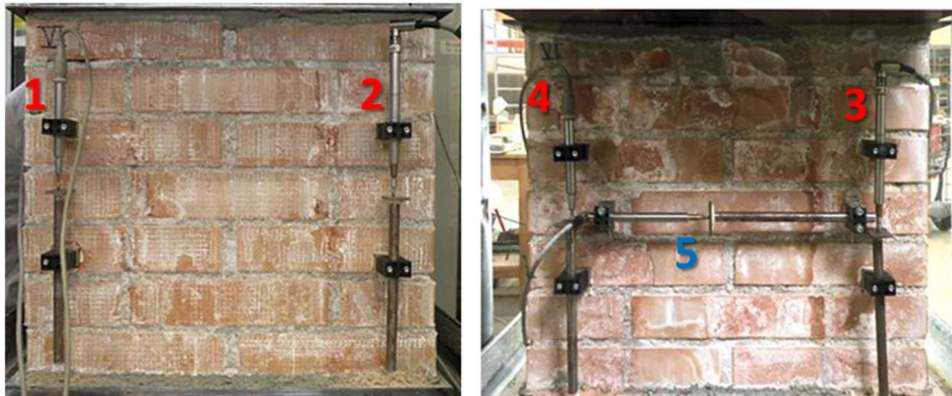


Figure 8.2: Set-up example, wallet VI: position of the LVDTs on the rear (left) and front face (right). In red the vertical transducer and in blue the horizontal one.

8.2. Mechanical tests: equipment, set-up and testing procedure

The mechanical tests were carried with a universal load control testing machine, Metrocom 400t, by increasing the uniaxial compression load until the failure of the masonry specimen. The 200t load scale of the testing machine was selected taking into account the expected value of the maximum strength of this type of masonry when it is in sound condition, which was estimated from the mechanical properties of the single building constituent materials (§4.1). A

low load application velocity, approximately equal to $0.2 \text{ N/mm}^2 \cdot \text{min}$, was chosen in order to gradually increase the compression and avoid drastic load changes which may affect or invalidate the results. In average, a mechanical test lasted approximately 1 hour and a half (Table 8.3).

For all the wallets, during the first part of the compression test, when the specimens were already in their elastic field, three pauses at constant load of 2 minutes each were performed (Figure 8.3). These load-breaks were aimed at allowing the proper settling of the wallets under the load plates and compensating any possible rotation between the specimen's surfaces and the testing machine frame, although the planarity and parallelism should have been guaranteed by the two metallic plates coupled to the bottom and top masonry faces. These steps were carried out at different load levels which were properly chosen according to the behaviour showed by the single masonry wallet throughout the test. In particular, during the compression of wallet I, the load was paused at lower levels compared with the tests of the other specimens, in order to gather acoustic emission events which may have occurred also at such low load values. Anyhow, after the pauses, the application of compression load was monotonically continued up to the collapse of the specimen. This was not identified by the peak of maximum load but by the complete failure of the wallet, thus, each test was continued also over the load peak value. This latter part of the test was aimed at collecting the descending branch of the load-displacement graph which could give additional information on the behaviour of masonry under compression, such as the values of residual strength usually defined in correspondence of a certain, fixed value of strain, i.e. 1.5% [2].

However, as the testing machine used was not a displacement control machine and due to the brittle and explosive crushing failure of the wallets, it was possible to collect only few data after the peak, except for one specimen, wallet XII. Thus, due to this limitations, the ultimate values of strength and strain – corresponding to the masonry complete collapse - were measured to define a sort of residual values, considering that these could anyway be useful to differentiate between the behaviour of the different aged wallets.

Table 8.3: Set-up parameters and characteristics of each mechanical test

Masonry wallet	Uniaxial compression test		
	Data acq. frequency	Load pauses [2 min]	Test duration
I	0.5 data/sec	40, 78, 117 kN	1h 40min
IV	1 data/sec	80, 160, 240 kN	1h 10min
V	2 data/sec	165, 330, 495 kN	1h 20min
VI	2 data/sec	165, 330, 495 kN	1h 10min
XII	2 data/sec	165, 330, 495 kN	1h 40min

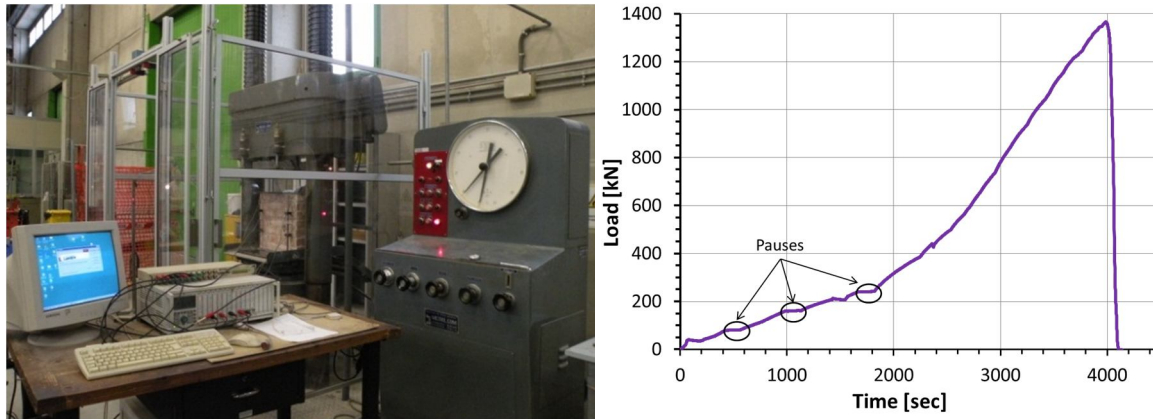


Figure 8.3: Example of testing set-up (left), time-history of a compression test (right).

8.3.1 Data acquisition and analysis

During the test, the values of load and displacements were collected by means of an acquisition unit with a dedicated Labview software and visualized in terms of load-displacement graphs. Then, the axial displacements measured via the 4 vertical LVDTs, were used to recover the stress-strain diagram and thus to determine the principal parameters characterizing the behaviour of the brick wallets under compression [1]. In detail, the evolution of the axial stress, f_m , was calculated by dividing at each time instant the applied loads, P , for the effective area of the resistant section of the wallet, A , whilst the values of axial strain, ε_m , were determined dividing the displacements measured by each vertical LVDT by the respective gauge length. Their average value was also calculated and used to obtain the stress-strain graph. For each wallet, the peak and ultimate values of compressive strength, f'_m and f_{mr} and the corresponding strains, ε'_m and ε_{mu} were recorded. Then, assuming an elastic behaviour of masonry up to the load peak point (§8.4) the allowable strain ductility $\mu_\varepsilon = \varepsilon_{mu}/\varepsilon'_m$ was estimated [2, 3].

In addition, from the stress-strain diagram the secant modulus of elasticity or Young's modulus, E , was determined as the slope of the curve between the ordinates corresponding to $0.1 \cdot f'_m$ and $0.4 \cdot f'_m$.

Similarly, the displacements in the transversal direction, parallel to the bed joints and measured by the horizontal LVDT were used to recover the values of the transversal strain that were reported in the stress-deformation graph. Again, the transversal strains ε'_{mt} and ε_{mtu} , corresponding to the maximum and ultimate compressive strength were evaluated.

Moreover, simplifying the behaviour of masonry and considering it as an isotropic elastic material, the Poisson ratio, ν , was then estimated considering the transversal and axial strains measured at $0.1 \cdot f'_m$ and $0.4 \cdot f'_m$ as:

$$\nu = \Delta\varepsilon_{mt} / \Delta\varepsilon_m, \quad (8.1)$$

Finally, the shear modulus of elasticity, G , was calculated according to the Lamè equation:

$$G = \frac{E}{2 \cdot (1 + \nu)}. \quad (8.2)$$

During each compression test, a visual monitoring was also performed, paying serious attention to the subsequent opening of cracks, writing down the load level at which they occurred as well as their position and extension. At the end of the mechanical test, a visual observation was repeated to reproduce in drawings the resulting crack pattern to be used, for example, as comparison with the maps acquired via DIC (Figure 8.4).



Figure 8.4: Visual observation and crack pattern survey of masonry wallet II (a) and VI (b)

8.3. NDT monitoring of the mechanical tests: equipment and testing procedure

In addition to the traditional measuring tools installed on the wallets' main surfaces, the monotonic compression tests were monitored by means of two non-destructive techniques: acoustic emission and digital image correlation. In the following paragraphs, the testing equipment and procedure are described for both methods.

8.4.1 AE monitoring

The acoustic emission method (§3.7) was used to monitor the behaviour of one of the reference masonry specimen, wallet I, when subjected to compression. This monitoring was performed in collaboration with the researchers of the Polish Academy of Science.

In order to check the reliability of different AE sensors in monitoring anisotropic and inhomogeneous materials such as masonry, four acoustic emission sensors (Physical Acoustic Corporation) with different sensitivity and characterized by a response in a different frequency range were used in this compression test: three broadband piezoelectric sensors (V103-RM “flat”, FD25 and FD27 multi-resonant) and one multi-resonant narrowband sensor (D9241A). Three of these sensors (V103-RM, FD25 and D9241A) were glued to one main face of the specimen (rear side) along one principal diagonal, while an additional sensor, FD27, was glued to the centreline of the lower plate of the testing machine with the function of guard sensor to the background noise (Figure 8.5).

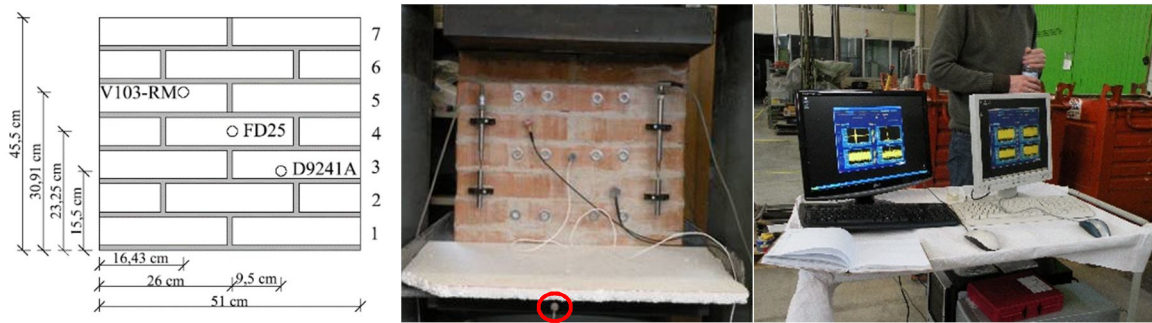


Figure 8.5: Wallet I: geometry of the specimen with the position of three AE sensor (left), rear face of the specimen during the test with AE sensors and LVDTs (center), AE testing equipment (right)

Besides the sensors, the AE equipment was composed by an acoustic amplifier (EA System) with variable gain which allows selecting the more suitable high-pass filter frequency (20 kHz and 100 kHz); an acquisition board PCI-9812 (Adlink Tech. Inc.) to sample and digitalize the data, and a personal computer to record, display the data in real time and store them for later analysis.

The data obtained from this active tests, in terms of number of AE events, cumulative energy and cumulative hit-rate calculated from AE events were used to identify the time instants of crack opening and to non-destructively assess the evolution of the mechanical damage [1a].

8.4.2 DIC monitoring: set-up, equipment and testing procedure

The compression tests carried out on the other 4 masonry wallets were monitored via a 3D, non-destructive, contactless, imaging technique: the digital image correlation technique (§3.6). This technique was used to perform a continuous monitoring of each mechanical test, since its beginning, with the purpose of enriching the information achievable with conventional measuring transducers and obtaining an overall and local picture of the deformation state of the wallets.

The DIC monitoring was performed by means of a commercial VIC 3D system, recently became available at the CIRI-EC lab of the University of Bologna. This is composed by 2 digital cameras, 5 megapixel each, with 23 mm Schneider lenses, a data acquisition and synchronization unit with 8 channels and a laptop with dedicated software. It can determine with accuracy up to 50 $\mu\epsilon$, deformations in a range varying from 0.005% to over 2000% (Figure 8.6). These two cameras, in order to obtain a stereoscopic vision of one main surface of the tested wallet, were fixed at the same steel frame and rigid tripod with a relative angle of 25° [4]. The cameras were placed in this configuration also to avoid vibrations and small relative movements during the mechanical tests, which can affect the data accuracy.

For all the tests, the set-up of the DIC equipment was realized prior to the application of load, just after positioning the wallet under the plate of the testing machine. The rigid tripod supporting the digital cameras was positioned at a defined and stable distance from the investigated surface (approx. 1.70 m). This parameter, together with the cameras' height from the ground, approx. 1.20 m, and the distance between the two optic sensors (about 0.3 m) was

chosen so that the investigated surface could be frontally captured and it could roughly fill the field of view of the cameras throughout the test duration.

A lamp with diffused white light was placed between the cameras and the tested masonry surfaces in order to minimize the non-uniform brightness field caused by the scarce ambient illumination of the laboratory and worsened by the fact of having carried out the compression tests in different days and at different hours of the day (Figure 8.7). Anyhow, during the load application, it was required to balance the brightness in order to obtain comparable data within all the mechanical tests and, above all, to improve the quality of the recorded digital images.

The set-up procedure has then foreseen the adjusting of the exposure time, focus and aperture range of the lens for the two cameras and finally the calibration. This latter aspect was carefully carried out as, as reported in §8.1, one of the purposes of this laboratory experience was to evaluate the reliability of the DIC in monitoring masonry materials without preparing their surfaces, that is in absence of the artificial coating of homogeneous colour with random pattern of dots in a high contrast colour which is usually painted on the investigated area, instead considering the natural texture of the masonry surface as reference pattern. This texture is used to determine and follow over time the changes in the geometry of the single pixel in which is divided the investigated surface during the mechanical test. Thus, it was very important to estimate the accuracy of the specific DIC configuration adopted.

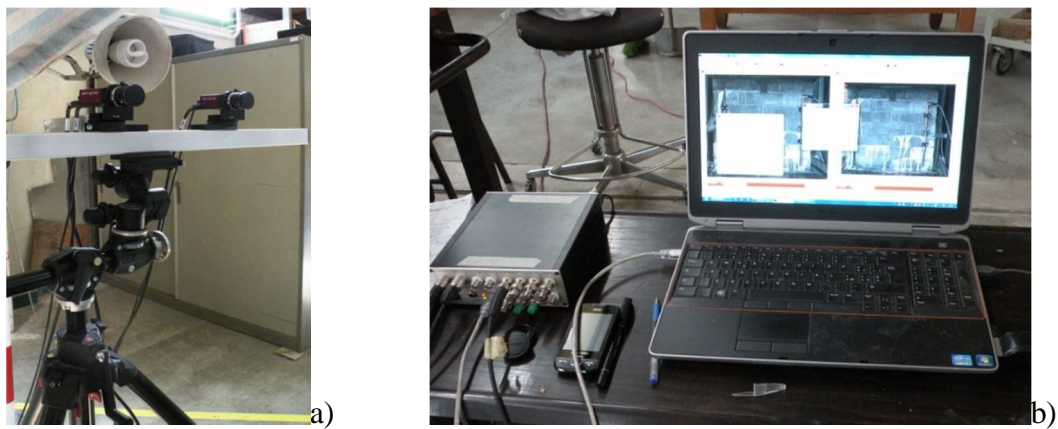


Figure 8.6: DIC testing equipment: a) digital cameras, b) laptop and data acquisition unit

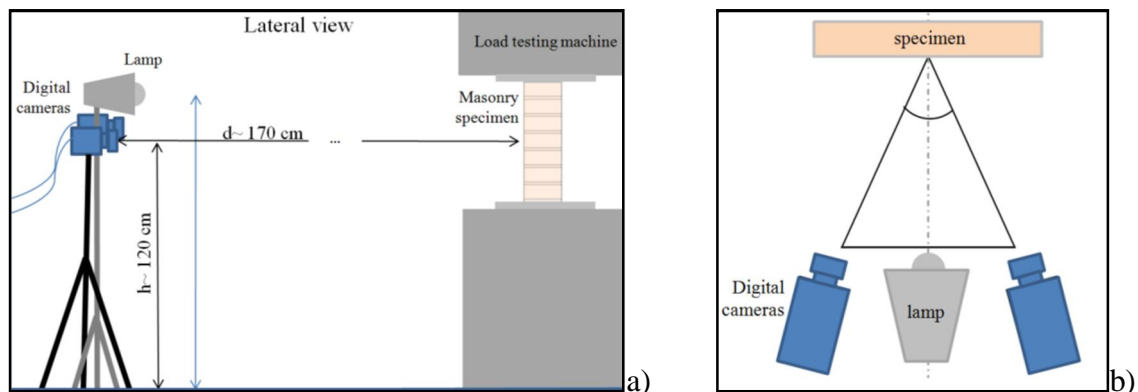


Figure 8.7: Set-up of the testing equipment: a) lateral view, b) plan view

The calibration procedure of the stereo cameras (§3.6) was performed in all the 4 tests, prior to the application of the load, with a commercially available target, which is a rigid white panel characterized by a grid of 12 x 9 black dots, spacing 15 mm. In average, an error value of approx. 0.04 pixels was obtained from the single calibrations which indicates a good accuracy of the used configuration despite the adopted simplification. Further, some reference points were applied in specific, selected positions of the surface facing the DIC cameras, at known relative distances, i.e. on the brick edges just over the mortar joints (Figure 8.8). These markers are simple black and white circle of paper with a diameter of 4 mm and were employed during the data post-processing phase as reference points where to calculate the displacements to be later compared with those measured by the traditional wired transducers (§8.5).

Finally, just before the beginning of the mechanical test, the DIC system was synchronized with the analogue data. Thus, the universal compression machine and two LVDTs were connected also to the DIC control unit; these represented reference values, respectively, for the load and for the displacements. This step was necessary in order to accurately relate, in the subsequent post-processing phase, each taken digital image with the specific state of the masonry specimen at that time, in terms of applied load and displacement showed.



Figure 8.8: Position of the glued additional markers in two different wallets

The first couple of DIC images to be used by the software as reference images, were taken in the un-deformed configuration of the wallets, at a zero load. To perform a continuous monitoring of each mechanical test, the frequency of DIC data acquisition was set to 1 image every 5 seconds. This frequency was kept constant until the formation of the first visible and audible crack. At that time instant, different for each masonry wallet, the frequency was decreased to 2 images per second with the aim of adequately capture the subsequent openings of the cracks and their quick movements or any detachment of brick flakes or portion of mortar joints that could occur. The monitoring was not interrupted at reaching the maximum compression load but it was continued over this value, up to the complete failure of each specimen. Thus, a large amount of images was recorded: approx. 2400 during each uniaxial compression test.

8.4. Data analysis and visualization of results

This paragraph is divided into 5 subsections, one for each masonry wallet and it reports the results obtained from the mechanical tests and from the correspondent non-destructive monitoring, after a brief explication of the data analysis procedure.

The mechanical results were the applied load and the global displacements of the masonry which were measured and stored in the data acquisition unit during the test. The variation of these values over time were available at the end of each compression test for post-processing, as a .csv file made of 6 columns: 1 column for the load values, 4 columns for the displacements collected by the 4 vertical LVDTs and 1 column for the horizontal displacements. The data post-processing in excel, consisted, firstly in correcting the different parameters by applying the values of the constants which are characteristics of the testing machine and measurement devices employed. Then, the load values were used to determine the variations of stress and the recorded displacements to estimate the strains, parallel and perpendicular to the direction of load application according to §8.3.1.

8.4.3 Wallet I

Mechanical results

The compression test of the undamaged wallet consisted in increasing monotonically the axial load until the collapse of the specimen, with the exception of three pauses, at the beginning of the test, in which the load was kept constant for almost two minutes (Table 8.4). This compression test lasted almost 1hour and 40 minutes (Figure 8.9).

The global behaviour of the wallet under compression can be completely evaluated from the load-displacement and corresponding stress-strain graphs (Figure 8.10).

The vertical displacements increased almost linearly with increasing load and, in average, are appreciable since the third load pause (0.03 mm). The maximum value of average vertical displacement was equal to 0.92 mm and was recorded approximately at the 94% of the maximum load reached (~994 kN). The horizontal displacements were almost null at the beginning of the test and became appreciable only at about 215 kN (-0.02 mm). From this time instant, the transversal displacements increased linearly with the increasing load although two discontinuities were appreciable in the displacement curve: one at about 400kN and one, bigger, at approx. 600kN (Figure 8.10 left). These correspond to the opening of the 1st and 2nd visible cracks. After the 2nd leap, the transversal displacements continued increasing linearly with the applied load, reaching a value of -1.24 mm at the maximum load. The maximum value, of -1.36 mm, was achieved some instants later, at the end of the test that is at the complete collapse of the wallet.

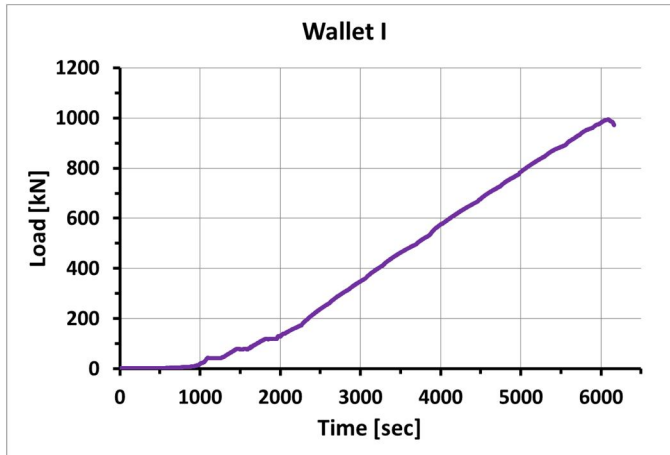


Figure 8.9: Wallet I, load-time history

Table 8.4: Wallet I, uniaxial compression test [1a]

Time from the test beginning [minutes]	Load [kN]	Load pause [minutes]	Vertical displacement [mm]	Horizontal displacement [mm]
18	40	p1=2.5	0.008	0.001
24	78	p2=2	0.016	-0.002
30	117	p3=2.5	0.029	-0.004
95*	930.29	/	0.92*	-0.928
102	993.77	/	/	-1.242

*instant at which occurs the maximum vertical displacement

The remarkable differences in the slopes of the axial displacement curves recorded by the 4 vertical transducers indicate the presence of a rotational component instead of a pure compression, probably caused by the different settlements of the mortar joints and not perfect parallelism between the top and bottom masonry surfaces. Thus, in order to obtain a more representative behaviour of the masonry as a whole, the axial strains were estimated from the averaged values of vertical displacements.

The main mechanical properties obtained from the experimental data are summarized in Table 8.5 and Table 8.6. The maximum compressive strength f'_m is a little bit greater than the value estimated from the building constituent materials and equal to 15MPa (§4.1). This value is an index of a well-constructed masonry with high compressive resistance. The measured modulus of elasticity is lower than the value suggested by [5] for the design of new masonry constructions, $E = 1000 f'_m$, instead the relation between the secant moduli suggested by the same norm, $G = 0.4 E$, was respected.

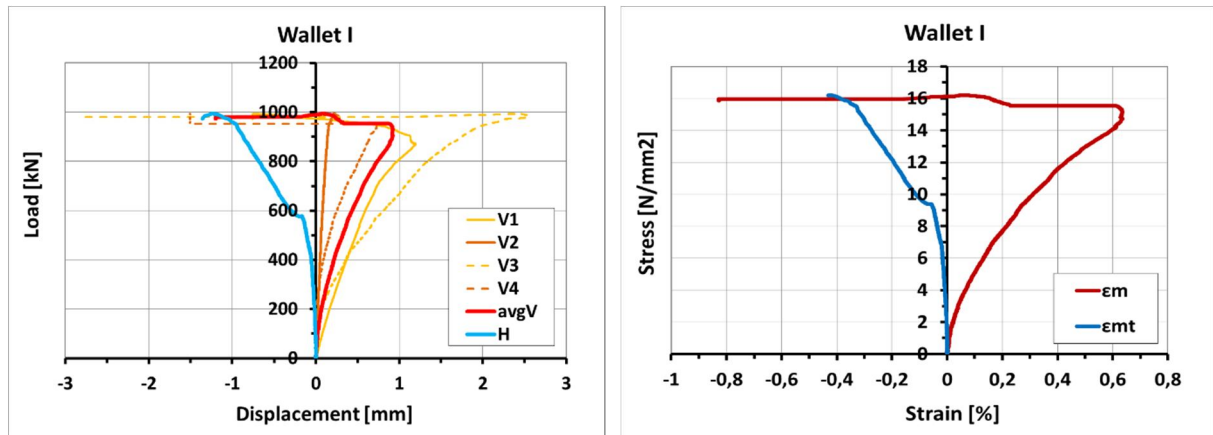


Figure 8.10: Wallet I, load-displacement and stress-strain graphs

Table 8.5: Wallet I, values of strength, strain and ductility

	f'_m [N/mm ²]	f_{mr} [N/mm ²]	f_{mr}/f'_m [%]	ϵ'_m [%]	ϵ_{mu} [%]	μ_ϵ
Wallet I	16.20	15.85	98	0.05	-0.83	-16.07

Table 8.6: Wallet I, secant moduli and Poisson's ratio

	E [N/mm ²]	v	G [N/mm ²]
Wallet I	3601.26	0.13	1600.26

AE results

In addition to the traditional displacement transducers, this compression test was monitored by AE sensors. This active test attended to evaluate the reliability of this NDT technique in following the appearance and subsequent opening of cracks in masonry [1a]. The main results, elaborated by the researchers of the Polish Academy of Science were herein briefly summarized for convenience considering two AE sensors.

With reference to the AE sensor placed in the middle of the masonry main face, the time evolution of the energy release connected to the acoustic emission events was displayed together with the transversal displacements collected by the horizontal LVDT (Figure 8.11 left). In the first 8 minutes of test no acoustic events were recorded; the first AE events were generated at a load of about 24 kN that means at a stress of 0.39 MPa (approx. 2.4% of the total stress). No AE events were recorded during the three loading pauses (corresponding to p1, p2 and p3). The same behaviour is visible in the curve of the cumulative energy where the three load breaks are identifiable as horizontal plateau.

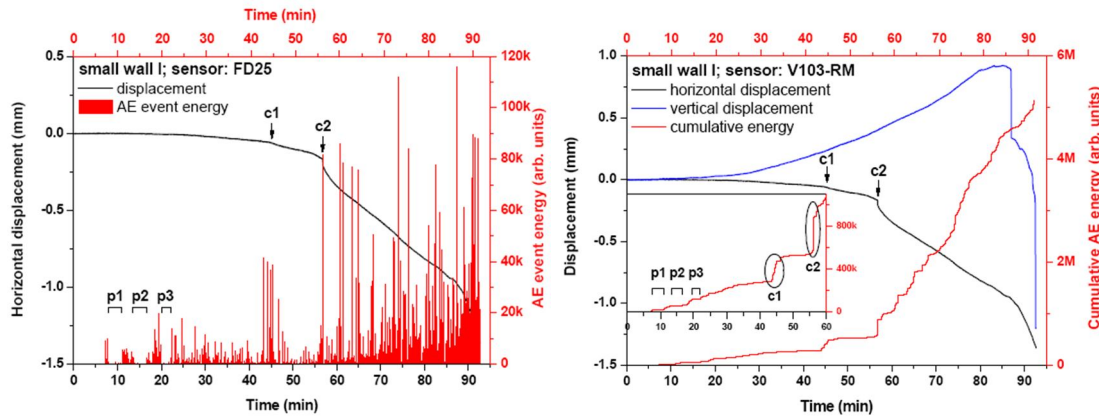


Figure 8.11: AE event energy as function of the horizontal displacements (left), cumulative AE energy as function of the axial and transversal displacements (right)

Some AE events of significant intensity were then recorded. The 1st one occurred at about 45 minutes from the beginning of the test which is at the time instant corresponding to the opening of the 1st crack, visible in the front face of the specimen, in the left brick of the 1st masonry course and identifiable in the slope of the horizontal displacements as a discontinuity (c1). This event was associated with an increase in the cumulative energy, visible by a vertical section in the curve in Figure 8.11 right. It was recorded from all the AE sensors, although it is most evident in the graph relative to the sensor V103-RM which was located above, that is on the vertical line corresponding to the fractured area (Figure 8.5 left). A 2nd rapid increase in acoustic emission corresponding to the opening of the 2nd crack was also visible (“c2”, Figure 8.11 right). After that, several events were recorded in sequence, indicating the subsequent openings of new or existing cracks during the load application. The exponential rise on the number and intensity of AE events identified the approach of the material to failure, which occurred at 993 kN. This behaviour was already detected by other authors for different structural materials, also innovative [6, 7] and for natural rocks of volcanic origin [8] if loaded up to the collapse. Thus, this simple experimental work proved the reliability and effectiveness of the AE method in detecting the beginning of the mechanical damage and its seriousness evolution over time also for inhomogeneous materials such as masonry.

8.4.4 Wallet VI

Mechanical results

The brick wallet VI was mechanically tested after being subjected to 18° cycles of accelerated ageing; among the three artificially aged wallet, this was the less decayed one.

The same testing procedure followed for wallet I was used here, but the three pauses at constant load were performed at slightly greater load levels. This compression test lasted approximately 1 hour and 10 minutes (Figure 8.12). The displacement responses at different load levels are summarized in Table 8.7. In this test, both the maximum values of axial (0.82 mm) and transversal (-0.96mm) displacements were recorded before the load peak but at two different time instants. The maximum load recorded was of about 1366 kN.

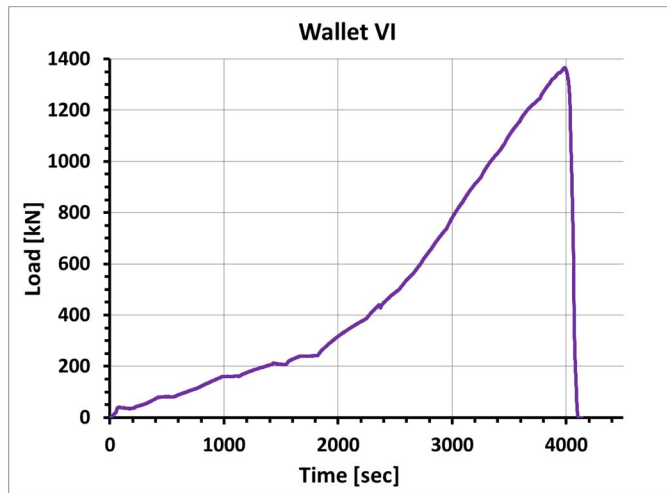


Figure 8.12: Wallet VI, load-time history

Table 8.7: Wallet VI, uniaxial compression test

Time from the test beginning [minutes]	Load [kN]	Load pause [minutes]	Vertical displacement [mm]	Horizontal displacement [mm]
8	80	2	0.16	-0.036
19	160	2,5	0.20	-0.062
30	240	2	0.24	-0.081
65*	1330.61	/	0.82*	-0.89
66**	1359.83		0.65	-0.96**
66,5	1366.14	/	0.57	-0.94

*time instant corresponding to the maximum axial displacement, **time instant corresponding to the maximum transversal displacement

As for the previous compression test, the load-displacement and stress-strain diagram were determined (Figure 8.13) and the main mechanical parameters measured (Table 8.8, Table 8.9).

In the first part of tests, no visible cracks were recorded although a certain assessment of the masonry wallet was visible in the load-displacement curves as a parabolic branch. After the 2nd load break all the displacement curves increased linearly, although at about 340 kN, it was noticed a slight change in the horizontal displacement slope and in the vertical displacements recorded by LVDT 2. This corresponds to the opening of the 1st vertical crack, visible at the 2nd masonry course. Only at 900 kN other vertical cracks occurred which were visible on masonry courses 6 and 7 although they were not associated to changes in the slopes recorded by the wired transducers. A significant change in the slope of all the devices happened later at about 1200 kN together with the openings of a vertical crack in the middle of the specimen, at masonry course 4. After the peak of the maximum load, we tried to record the descending branch but it was not possible due to the fragile and explosive collapse of the wallet which occurred just few instants later.

The crack pattern at the end of the mechanical test was also recorded (**Errore. L'origine riferimento non è stata trovata.**).

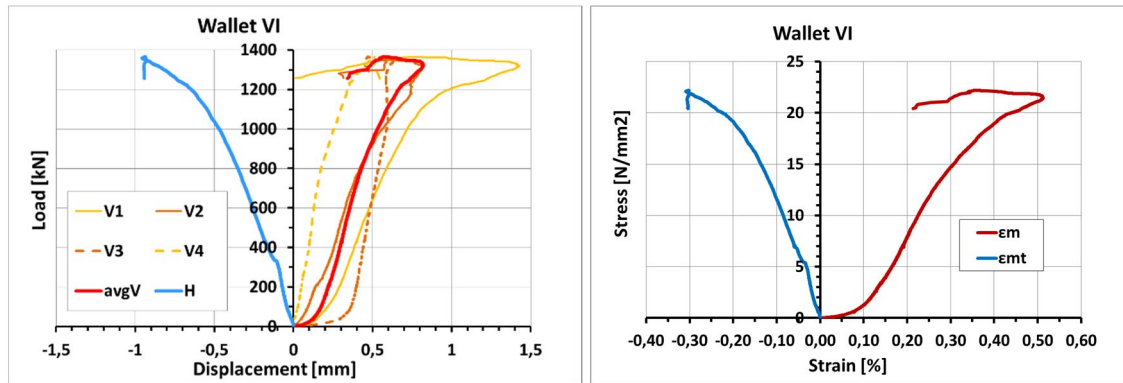


Figure 8.13: Wallet VI, load-displacement and stress-strain graphs

Table 8.8: Wallet VI, values of strength, strain and ductility

Wallet	f'_m [N/mm ²]	f_{mr} [N/mm ²]	f_{mr}/f'_m [%]	ϵ'_m [%]	ϵ_{mu} [%]	μ_ϵ
VI	22.19	20.41	92	0.36	0.51	1.43

Table 8.9: Wallet VI, secant moduli and Poisson's ratio

Wallet	E [N/mm ²]	ν	G [N/mm ²]
VI	7323.23	0.64	2237.19

DIC: data analysis procedure and results

In this section the DIC data analysis procedure was reported prior to show the results of the monitoring of the wallet VI during compression. The same procedure was repeated also for the remaining 3 tests.

The DIC data post-processing was performed by means of dedicated software at the end of the mechanical test. First of all, it has foreseen the identification of the area of interest (AoI) within one of the two reference images collected by the left or right cameras and it represents the area to be analysed. Then, in order to obtain a more precise data computation without losing any interesting data during this process, some additional analysis starting points were positioned on the AoI and placed in strategic positions, i.e. near the edges of the AoI or in proximity of obstacles (such as the two vertical LVDTs, which are outside the mid-plan of the masonry surface). To ensure the efficiency of these start points in the process of image comparison, the initial guesses proposed by the software were checked; this issue was performed by looking at the suggested points' positions in highly zoomed images, identifying them in the series of un-deformed and deformed images (zoomed at the pixel level) and changing manually such positions if and where necessary (Figure 8.14).

After that, the grid for tracking the displacement between the subsequent images was selected by choosing the adequate values of two parameters: the subset size and the step size. The

subset size, indeed, controls the area used for the image correlation while the step size defines the spacing of the points to be analysed. In our experiences, taking into account the dimensions of the studied masonry wallets, the set-up characteristics and the calculation time, it was selected a grid with a subset of 29 pixels x 29 pixels and a step size of 7, which approximately led to an average uncertainty value of 0.039 pixels that means 0.01 mm (Figure 8.15).

Then, after recalling the calibration parameter, the data analysis began with the comparison of subsequent images. The correlation of each couple of images with the following ones has required from 1.7 to 2 iterations and the calculated projection errors was on average equal to 0.040. These parameters usually served to verify the acceptability of the DIC analysis and they confirmed the good quality of the collected data [9, 10].

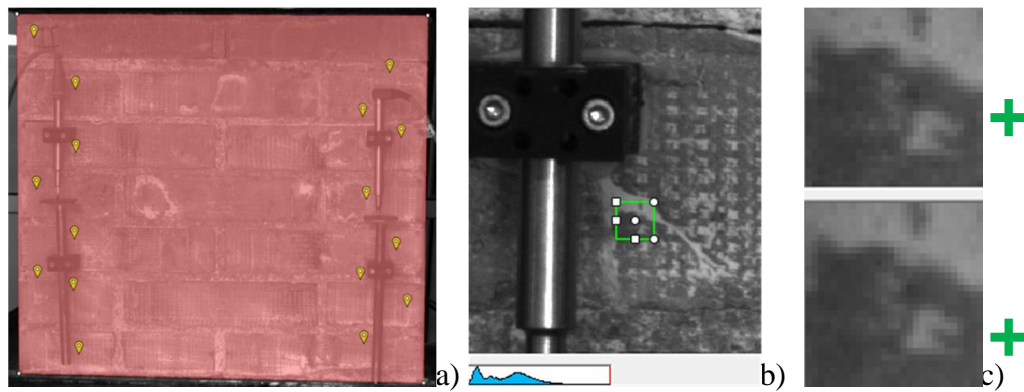


Figure 8.14: Example of: a) selection of the area of interest (in red) and positioning of the starting points (in yellow), b) detailed position of one start point (in green), c) zoomed-in images at pixel level: reference (top) and deformed image (bottom)

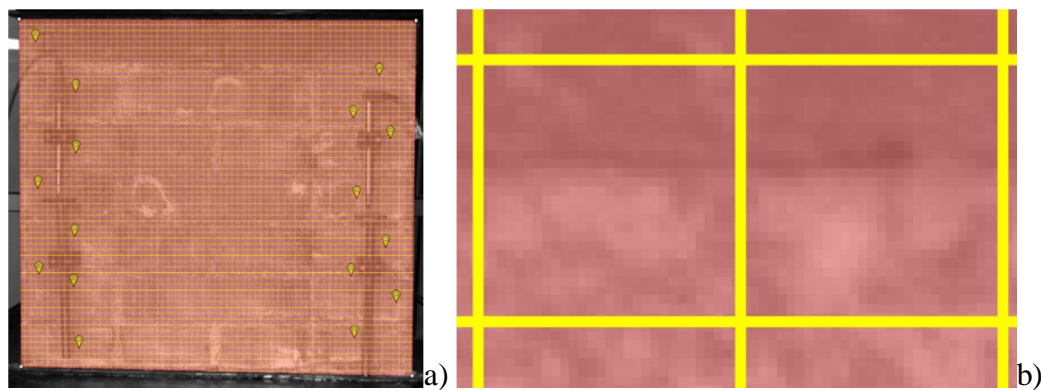


Figure 8.15: View of the assigned grid for the data analysis (in yellow) superimposed to the AoI (a), zoom at pixel level showing the dimensions of grid subsets (b)

After the first data analysis process, the obtained results, prior to be visualized, were additionally elaborated by means of a DIC software tool which is aimed at removing or at least reducing any rigid motion which could have occur during the mechanical test. Thus, at the end of the DIC data analysis, the coordinates of each pixel of the scanned area, their

displacements (u , v , w) along the three directions (x , y , z) and their corresponding strains (ϵ_{xx} , ϵ_{yy} , ϵ_{xy}) and stresses (σ_{xx} , σ_{yy} , σ_{zz}), during the application of load were available.

Note that the reference system was automatically chosen at the beginning of the analysis by the DIC software which positioned the origin of the axis in the centre of the analysed image that is approximately the centre of the masonry wallet (Figure 8.16).

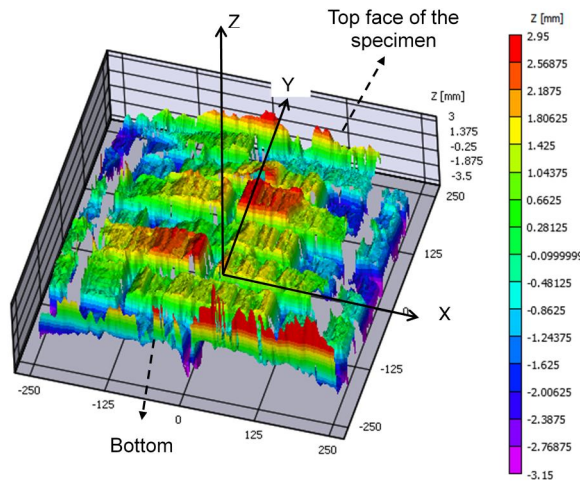


Figure 8.16: Example of map with the geometric position of each pixel of the surface at a certain time instant, with the position of the 3D reference system

At the end of the data analysis process, the outputs can be visualized in terms of 3D full-field coloured maps of one of the parameters mentioned before, i.e. displacements, at each time instant and load level. Herein, the different maps are visualized as coloured plots superimposed to the corresponding deformed image to allow seeing exactly and in a simple way the positions where changes or damages occurred. However, the results are not only qualitative as it is possible to export quantitative data for each pixel of the image from these maps.

By way of example, with reference to wallet VI, the transversal, axial and out-of-plane displacement maps recorded at the maximum load are reported in Figure 8.17. From these maps, important information may be extracted to quantitatively evaluate the behaviour of the masonry as a whole and of its constituent materials under compression.

A particular innovative aspect is represented by the possibility of determining the out-of-plane displacements, which are not recordable with traditional measuring tools although they can give important information to understand the 3-dimensional masonry response under a certain compression load. To better measure the variations of the displacements along the three main direction throughout the mechanical test, quantitative data can be extracted also along lines. As an example, the out-of-plane displacements along a vertical line positioned almost in the middle section of the wallet are reported for three different loads; the variations of displacements are clearly visible and measurable. In this case, the maximum value of about 4 mm was recorded at the maximum load, in the 4th horizontal mortar joint from the bottom (Figure 8.18).

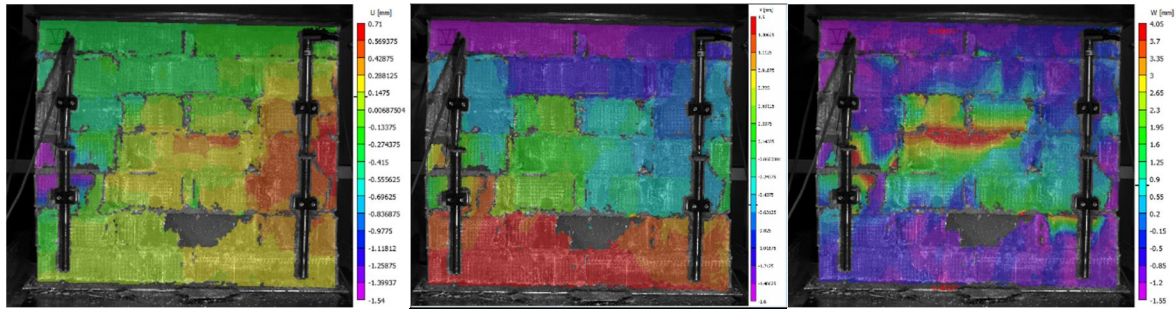


Figure 8.17: Wallet VI, maps of horizontal (left), vertical (centre) and out-of-plane displacements (right) at the peak load

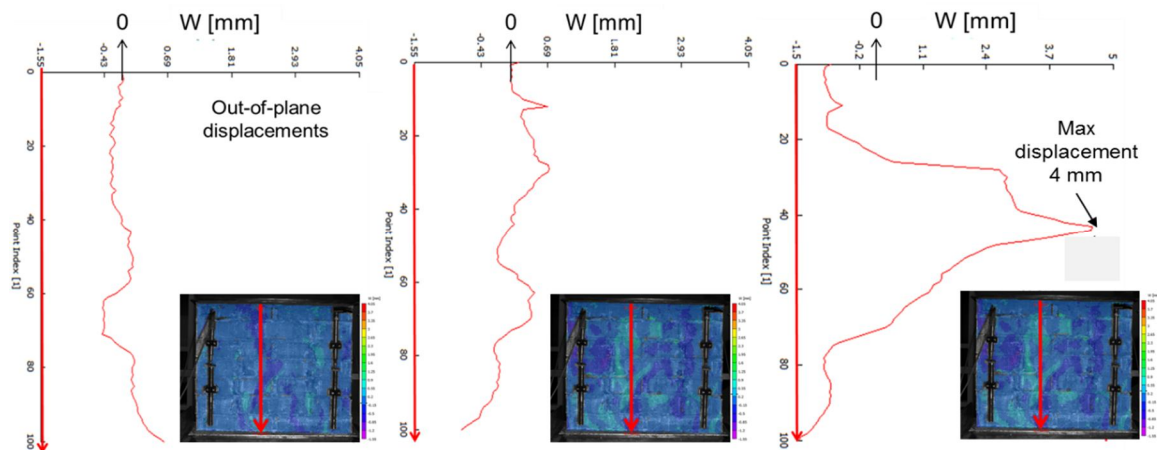


Figure 8.18: Wallet VI, evolution of the out-of-plane displacements along a vertical line: at 0kN, 900kN and 1366kN, from left to right

Being the mechanical test a uniaxial compression test, particular attention has to be made to the displacement and corresponding strain along the vertical direction, y in order to calculate the mechanical characteristics properties of the brick wallet.

Thus, the 3D maps of axial strains ε_{yy} were determined for the all test duration in order to evaluate their variations at increasing loads (or stresses). These maps easily showed the strain changes throughout the compression test. At the beginning of the test, at 0kN, the strains are overall constant and equal to zero while at 80 kN a slight compressive state on the mortar joints was noted. From this time instant, the axial strains increased almost linearly with increasing load and they were always greater on the mortar joints, most deformable, than on the brick units. In correspondence to the 3rd load break, at 240 kN, they are greater than 0.01%. Nevertheless, these deformations are not symmetrical nor uniformly distributed among all the mortar joints (Figure 8.19).

More severe strains were measured at higher load levels, starting from 900kN where the different behaviour of the mortar ($\varepsilon \sim 0.02\%$) and the bricks ($\varepsilon \sim 0.0015\%$) was even more evident. At the maximum load, of 1366 kN, compressive strains of approx. 0.025% were estimated together with a local tensile strain state, caused by the opening of cracks which led to the expulsion of material flakes (Figure 8.20). In this latter image as well as in the subsequent images recorded until the end of the test, some areas of the surface appeared grey,

that means that these areas were no longer analysed, due to the falling down of brick portions [1b].

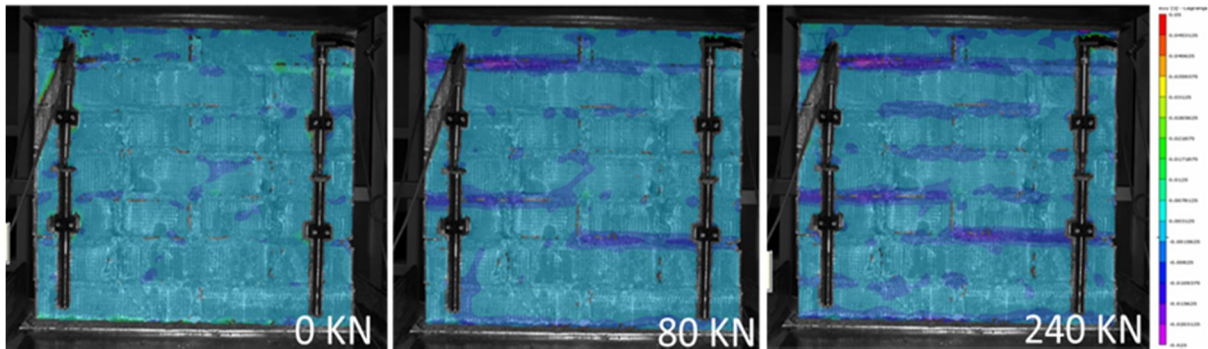


Figure 8.19: Wallet VI, trend of full-field maps of ε_{yy} strains at increasing loads: from 0kN to 240kN

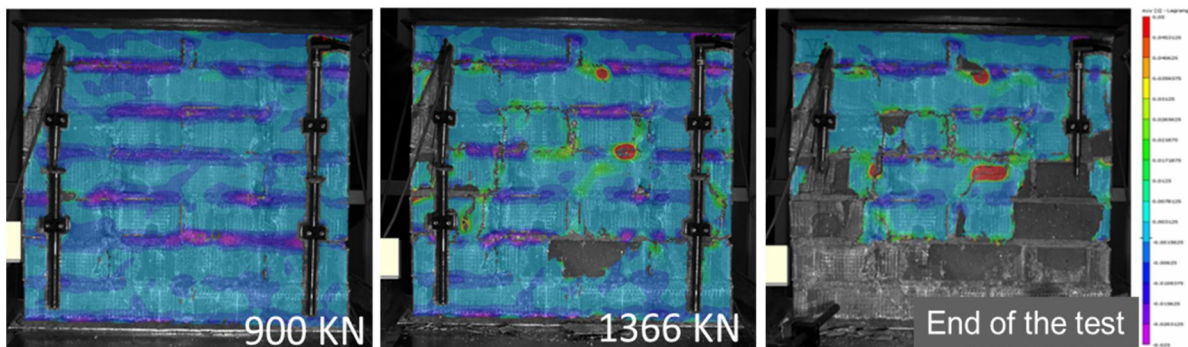


Figure 8.20: Wallet VI, trend of full-field maps of ε_{yy} strains at greater increasing loads, from 900kN until the end of the test which corresponds to the fragile collapse of the wallet

As for the vertical displacements, from the axial and out-of-plane displacements the corresponding variations of strains at different time instants were also determined during the test. The values of ε_{xx} and ε_{xy} remained almost constant and null for the main part of the compression test. Only after the openings of the first severe cracks, at 900kN, some localized variations were detectable which were of about 0.05% at the maximum load (Figure 8.21, Figure 8.22).

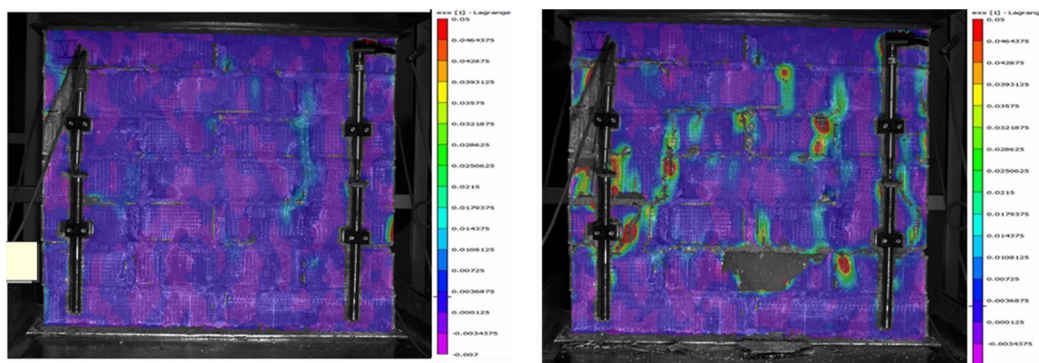


Figure 8.21: Wallet VI, maps of ε_{xx} at two different load levels: 900kN (left) and at the maximum load (right)

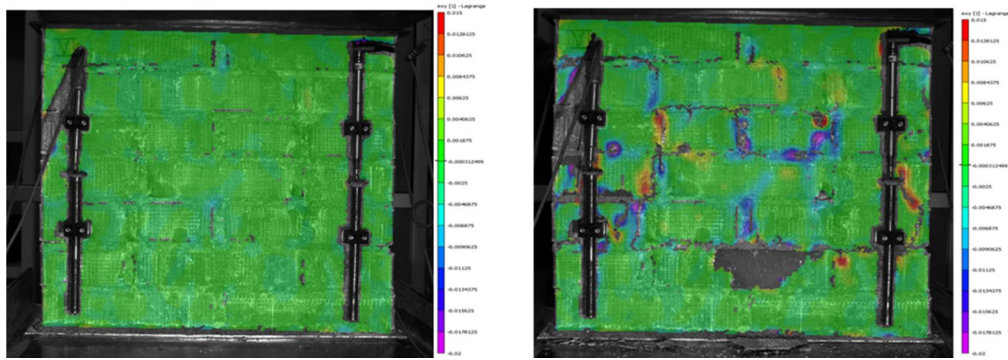


Figure 8.22: Wallet VI, maps of out-of-plane strains, ϵ_{xy} , at two different load levels: 900kN (left) and at the maximum load (right)

Moreover additional analyses were performed by means of the extensometer tool of the DIC software, because one of the main aim of this laboratory experience was to evaluate the feasibility and accuracy of the adopted simplified DIC procedure in monitoring masonry subjected to mechanical tests. Thus, virtual strain gauges were employed to compare the DIC results with those obtained through LVDTs. These virtual extensometers were placed in pre-determined positions, approximately corresponding to those of the traditional transducers. Each extensometer position was defined by means of two of the additional reference points applied to the investigated masonry surface before the beginning of the test (Figure 8.23left). Knowing the initial length of the segment between these two points, it was then possible to derive the deformations between them at increasing load levels.

The average axial strains were determined from the two virtual extensometers placed near the two vertical LVDTs on the same masonry surface, while the horizontal virtual extensometer was used to evaluate the transversal strains (Figure 8.23 right). The slopes of the stress-strain curves obtained with this technique are comparable with those recorded with the wired measuring tools (Figure 8.13 right). Here, the maximum average axial deformation measured with the virtual tools was equal to 0.50%, some point percent greater than that obtained by means of the two real LVDTs (0.41%). Instead, a perfect correspondence was found for the transversal strains. A quite good correlation was also obtained for the values of the mechanical characteristics properties calculated as, in average, a discrepancy of about 20% is recorded, demonstrating the feasibility and accuracy of the adopted simplified DIC procedure (Table 8.10).

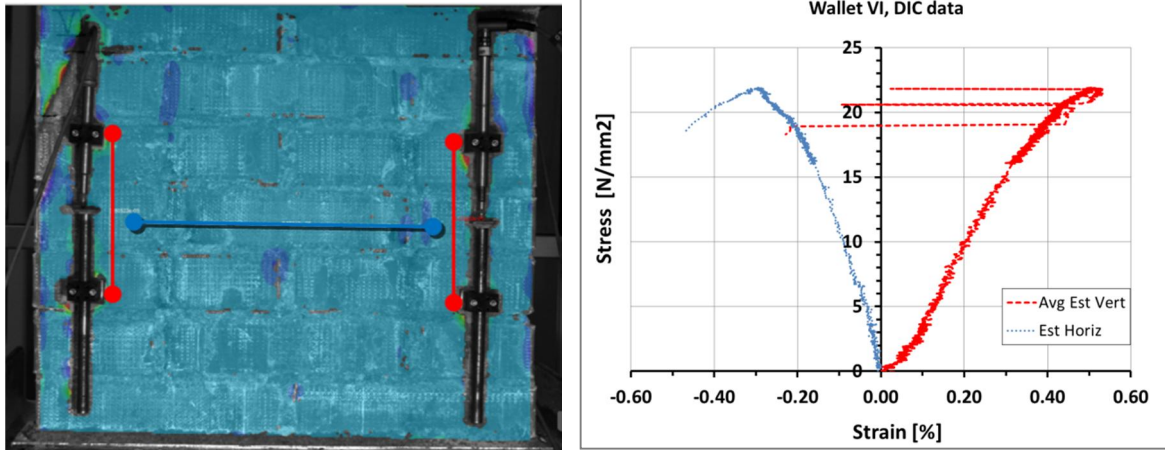


Figure 8.23: Wallet VI, position of the virtual extensometers (left) and resulting stress-strain diagram (right)

Table 8.10: Wallet VI, mechanical properties determined by traditional tools and DIC system

	ϵ'_m [%]	ϵ'_{mt} [%]	E [N/mm ²]	ν	G [N/mm ²]
LVDT	0.36 (0.41*)	-0.30	7323	0.64	2237
DIC	0.50	-0.29	5633	0.50	1872

*considering only LVDT 1 and 2

8.4.5 Wallet V

Mechanical results

This masonry wallet was subjected to 26 cycles of accelerated ageing prior to undergone to uniaxial compression test. As for the previous wallets, the load-time history (Figure 8.24) and the principal characteristics of the mechanical compression test are reported (Table 8.11). This test lasted, similarly to wallet VI, approx. 1h and 20min but the three load pauses were performed at greater load levels: 165kN, 330kN and 495kN. The maximum value of axial displacement, equal to 0.58mm, was measured before the load peak whilst the maximum horizontal displacement (-1.84mm) just after that, some instants before the complete collapse of the wallet.

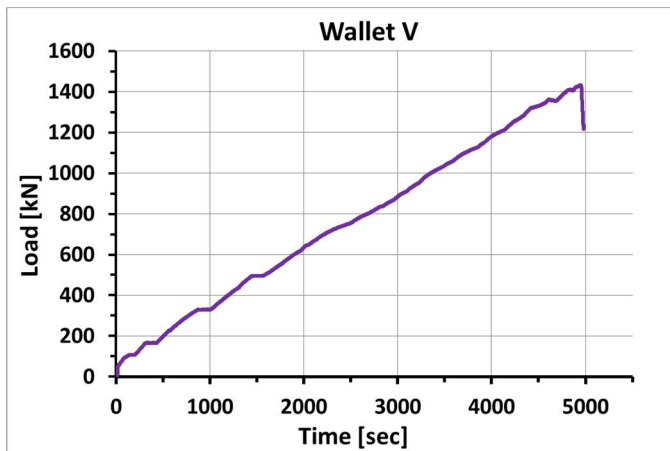


Figure 8.24: Wallet V, load-time history

Table 8.11: Wallet V, uniaxial compression test

Time from the test beginning [minutes]	Load [kN]	Load pause [minutes]	Vertical displacement [mm]	Horizontal displacement [mm]
6	165	1	0.07	-0.021
15	330	2	0.11	-0.14
26	495	2	0.13	-0.22
79*	1395,36	/	0.58*	-1.26
82,5	1432,99	/	0.57	-1.56
83**	882,38	/	/	-1.84**

*time instant corresponding to the maximum axial displacement, **time instant corresponding to the maximum transversal displacement

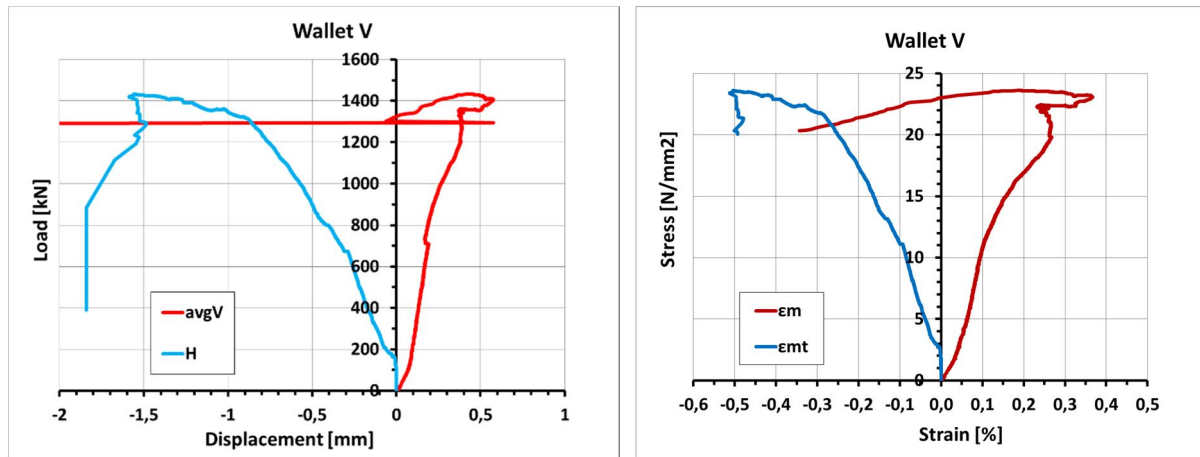


Figure 8.25: Wallet V, load-displacement and stress-strain graphs

In this case, the vertical displacement's data were affected by some rigid movements of the wired measuring transducers caused by an accidental relative contact between the horizontal transducers and the two vertical ones which were on the same face. This occurred at the beginning of the test and after the maximum load, in the descending branch of the test. These data were neglected in the data analysis visualization and elaboration.

After a first part corresponding to the masonry assessment, the load-horizontal displacement curve is almost linear until approximately 1300 kN, while the load-vertical displacement one presents a linear branch followed by a parabolic one which starts at about 700 kN (Figure 8.25). Actually, at this load level a discontinuity is visible also in the displacements recorded by the horizontal transducer. At 700 kN, indeed, two vertical cracks appeared on masonry course 6 and 7. However, the first crack opening (visible on masonry course 4) occurred at a lower load level, approx. at 500 kN but it seems to not have affected the data. Also the subsequent openings of new cracks at loads greater than 700 kN were not directly identifiable in the graph. The unexpected and explosive collapse of wallet V occurred some instants after the load peak at 1433 kN.

The estimated values of the main mechanical parameters are summarized in Table 8.12, Table 8.13.

Table 8.12: Maximum and residual values of stress and strain from the compression tests

Wallet	f'_m [N/mm ²]	f_{mr} [N/mm ²]	f_{mr}/f'_m [%]	ϵ'_m [%]	ϵ_{mu} [%]	μ_ϵ
V	23.60	20.38	86	-0.14	-0.34	2.45

Table 8.13: Results of the compression tests in terms of elastic moduli

Wallet	E [N/mm ²]	ν	G [N/mm ²]
V	9903.72	1.09	2361.74

DIC results

Similarly to what has been previously reported for the wallet VI, herein, some exemplary results obtained from the digital image correlation monitoring of the destructive compression test are summarized.

First of all, 3D maps of the displacements along the three main directions are visualized at the maximum load (Figure 8.26). These maps, that in this case are also more important as at this time instant two of the 4 vertical LVDTs were already fallen down, show localized points with high values of horizontal displacements (about 2mm) as well as of vertical displacements (approx. 6 mm).

Then, the variations of strains were also visualized as coloured maps superimposed to the deformed images, using for each parameter the same colour scale. As an example, herein the axial, transversal and out-of-plane strains were reported with reference to three different load levels corresponding to three important steps of the mechanical tests: the opening of severe cracks (700 kN), the maximum load (1433 kN) and the end of the test, that is the complete failure of the specimen (Figure 8.27, Figure 8.28, Figure 8.29). These maps shown axial deformations, ε_{yy} , ranging from -0.023 to 0.4% and smaller transversal deformations, ε_{xx} , between -0.044 to 0.14 %.

In addition, from them, the differences in the behaviour of the two masonry constituent materials are clearly evident, especially on the maps of the axial strains where the mortar joints appeared more compressed than the bricks since the beginning of the test. At the maximum load, this difference is of about one order of magnitude.



Figure 8.26: Wallet V, horizontal (left), vertical (centre) and out-of-plane displacements (right) at the peak load (1433 kN)

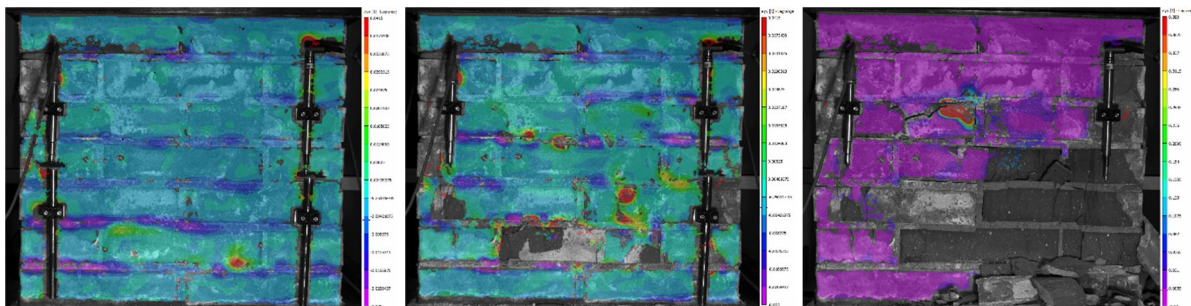


Figure 8.27: Wallet V, trend of full-field maps of ε_{yy} strains at different, increasing load levels: 700 kN (left), 1433 kN (centre) and at the end of the test (right)

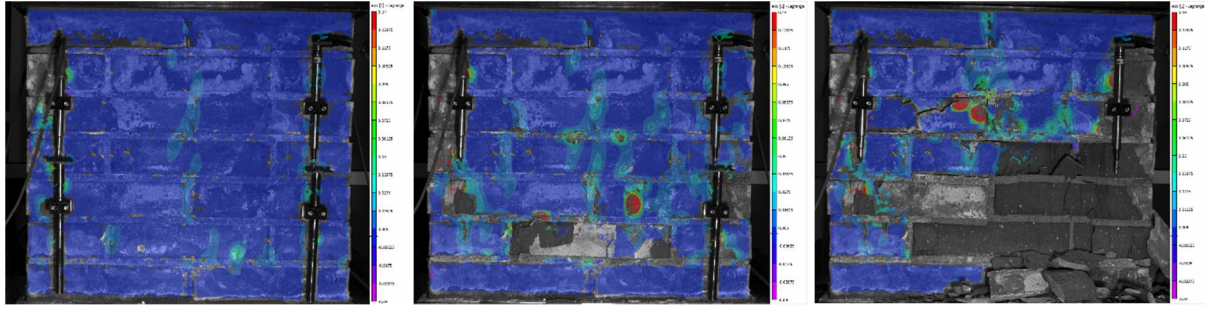


Figure 8.28: Wallet V, maps of ϵ_{xx} at three different load levels: 700 kN (left), 1433 kN (centre) and at the end of the test (right)

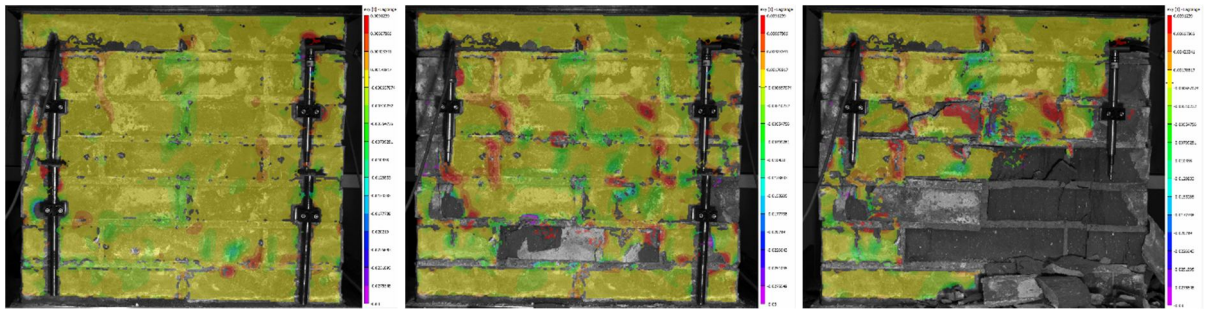


Figure 8.29: Wallet V, maps of out-of-plane strains, ϵ_{xy} , at three different load levels: 700 kN (left), 1433 kN (centre) and at the end of the test (right)

With the aim of evaluating the accuracy of the DIC technique in monitoring the mechanical behaviour of masonry subjected to compression, also in this case, 3 virtual extensometers (2 vertical and 1 horizontal) were used. These were employed to extract DIC data on specific positions, comparable to those of the LVDTs, to recover the stress-strain diagram and estimate the mechanical characteristics properties of the brick masonry specimen considered (Figure 8.30). Thus, these data were compared with those collected by the wired traditional transducers (Table 8.14). From this comparison, it is noted a quite good correlation between the mechanical properties (elastic moduli and Poisson's coefficient) measured from traditional devices and those obtained from the unconventional, non-destructive system, although a quite big difference was recorded on the maximum values of axial and transversal deformations.

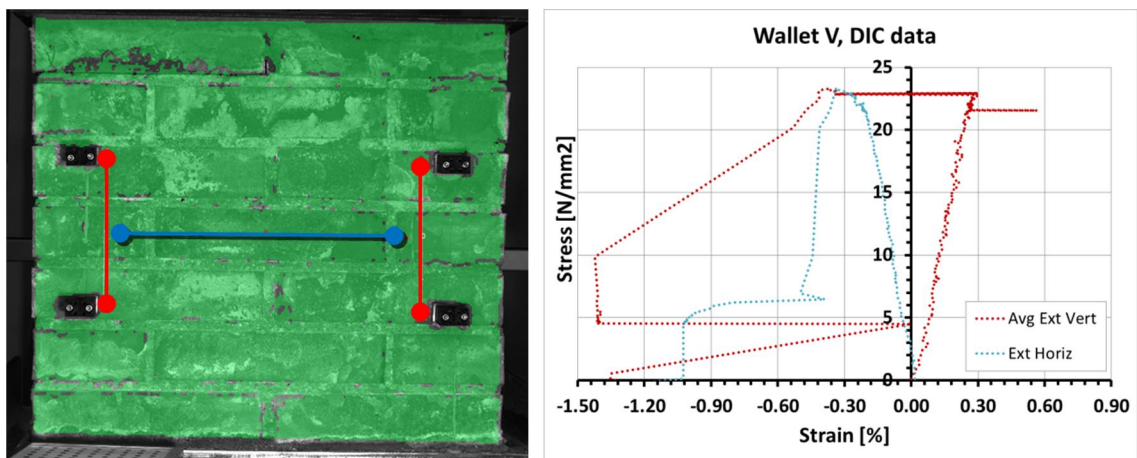


Figure 8.30: Wallet V, position of the virtual extensometers (left) and resulting stress-strain diagram (right)

Table 8.14: Wallet V, mechanical properties determined by traditional tools and DIC system

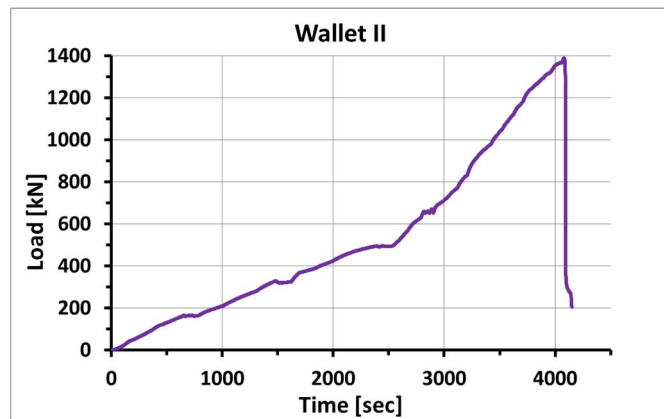
	ε'_m [%]	ε'_{mt} [%]	E [N/mm ²]	ν	G [N/mm ²]
LVDT	-0.14	-0.50	9904	1.09	2362
DIC	-0.39	-0.35	10567	1.19	2408

8.4.6 Wallet II

Mechanical results

This masonry specimen, which was subjected to the greatest number of accelerated ageing cycles, equal to 38, was mechanically tested few weeks after the ending of the treatment.

The same testing procedure followed for the previous masonry assemblies was used. This compression test lasted approximately 1 hour and 10 minutes (Figure 8.31, Table 8.15). The displacement responses at different load levels are summarized in Table 8.7. In this case, both the maximum values of axial (0.84 mm) and transversal displacements (-1.09 mm) were recorded after the load peak corresponding to 1390 kN.

**Figure 8.31:** Wallet II, load-time history**Table 8.15:** Wallet II, uniaxial compression test

Time from the test beginning [minutes]	Load [kN]	Load pause [minutes]	Vertical displacement [mm]	Horizontal displacement [mm]
10	165	2.5	0.31	-0.031
25	330	3	0.37	-0.038
40	495	3	0.042	-0.057
68	1390	/	0.79	-0.96
68.2	1252	/	0.84	-1.09

As in the previous tests, the load-displacement and stress-strain diagrams were determined (Figure 8.32) and the main mechanical parameters measured (Table 8.16, Table 8.17).

In the first part of the compression, until the 1st load pause, numerous audible assessment noises were detected; these slight movements were visible also in the load-displacement function as a parabolic branch. This portion of the curve was then followed, both for the horizontal and vertical displacements, by a linear branch until approx. 600 kN. At that point, the first visible crack occurred. It was a vertical crack, located in the middle section of the central brick of the 6^o masonry course. Actually, some exfoliations and delamination of the brick surfaces had already happened at lower levels of load, but they are much localized and they do not affect the global masonry behaviour nor the recorded data (Figure 8.33).

A second important crack appeared at about 1200 kN which corresponded to a change in the slope of the transversal displacements. After reaching the maximum load, we tried to record the descending branch but, again, it was not possible due to the fragile and explosive collapse of the wallet itself (Figure 8.33).

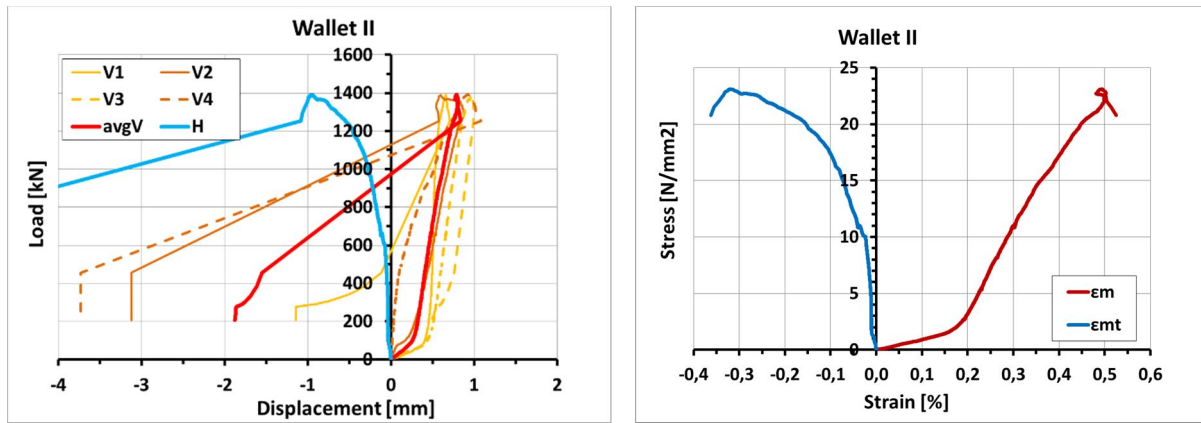


Figure 8.32: Wallet II, load-displacement and stress-strain graphs

Table 8.16: Wallet II, values of strength, strain and ductility

	f'_m [N/mm ²]	f_{mr} [N/mm ²]	f_{mr}/f'_m [%]	ϵ'_m [%]	ϵ_{mu} [%]	μ_ϵ
Wallet II	23.11	20.80	90	0.49	0.52	1.06

Table 8.17: Wallet II, secant moduli and Poisson's ratio

	E [N/mm ²]	v	G [N/mm ²]
Wallet II	7363.18	0.12	3296.04



Figure 8.33: Wallet II: exfoliations and cracks visible at ...kN (left); crack pattern at the end of the mechanical test (right)

DIC results

Similarly to what has been shown for the other two accelerated aged masonry wallets, the DIC post-processed data were visualized both as full-field 3D displacement and strain maps at different load/stress levels (Figure 8.33 - Figure 8.37). The strain maps shown comparable axial and transversal deformations, ϵ_{yy} and ϵ_{xx} , ranging from -0.03 to 0.04%, with increasing values at increasing loads. Also in this case, it's possible to determine the global mechanical response of masonry via DIC as well as to differentiate the behaviour of the two building constituent materials.

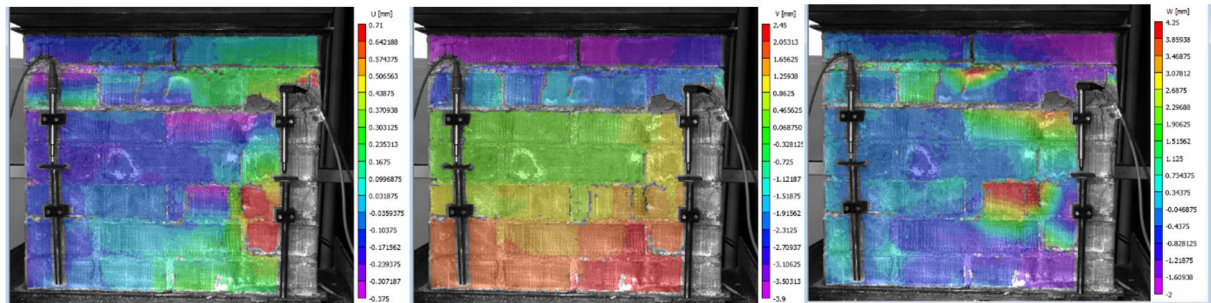


Figure 8.34: Wallet II, horizontal (left), vertical (centre) and out-of-plane displacements (right) at the peak load

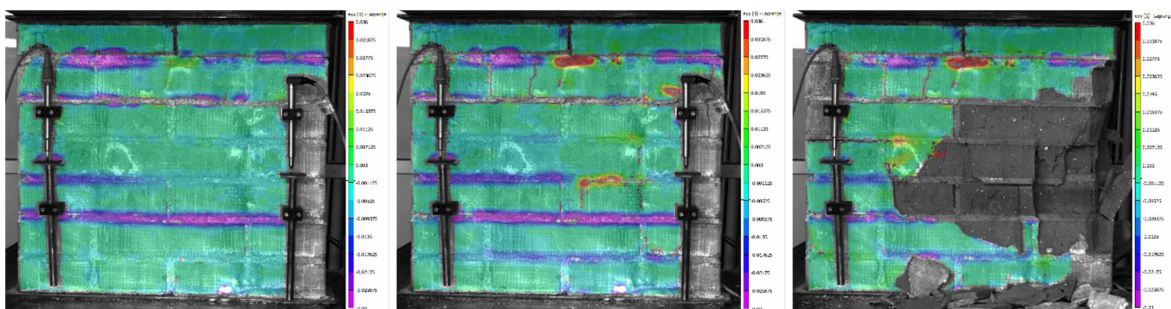


Figure 8.35: Wallet II, trend of full-field maps of ϵ_{yy} strains at increasing loading: 600kN (left), at the maximum load (centre) and at the end of the test (right)

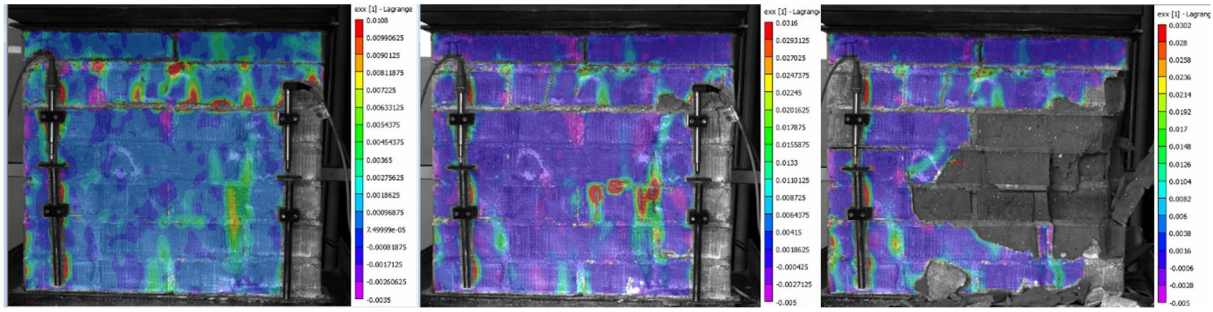


Figure 8.36: Wallet II, maps of ε_{xx} strains at increasing loading: 600kN (left), at the maximum load (centre) and at the end of the test (right)

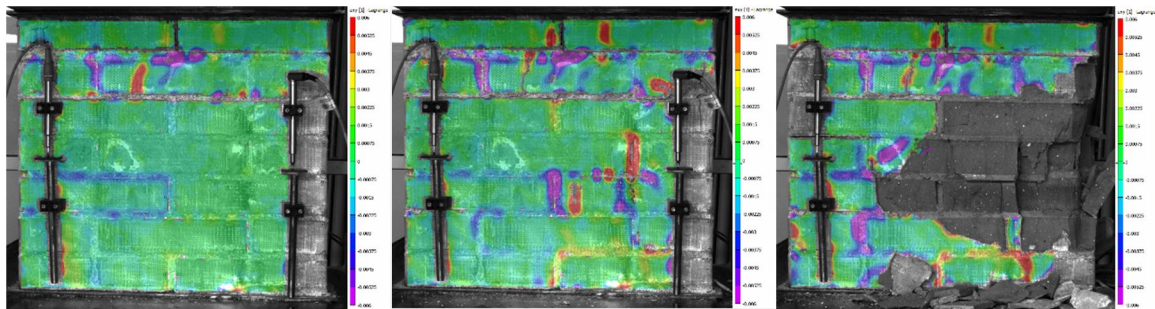


Figure 8.37: Wallet II maps of out-of-plane strains, ε_{xy} strains at increasing loading: 600kN (left), at the maximum load (centre) and at the end of the test (right)

Again, two virtual vertical (in red) and one virtual horizontal extensometers (in black) were positioned respectively near the two vertical LVDTs placed on the same face of the masonry specimen and in correspondence to the horizontal LVDT placed in the opposite face (Figure 8.38 left). These were employed to calculate the strain evolution during the mechanical test (Figure 8.38 right) and the main mechanical properties of masonry. In this case, the correlation between the DIC data and the analogic ones is worse than in the previous tests as from DIC, the wallet appeared more rigid (Table 8.18).

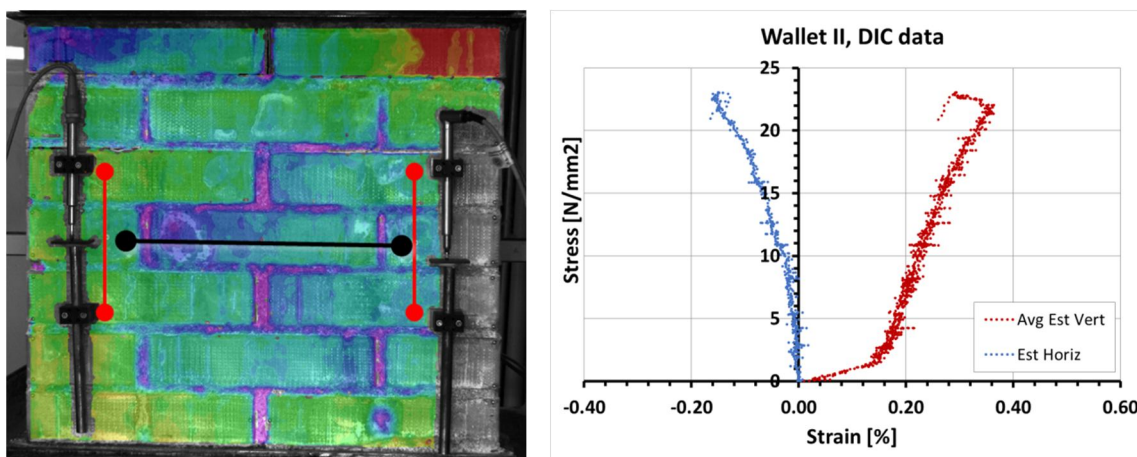


Figure 8.38: Wallet II, position of the virtual extensometers (left) and resulting stress-strain diagram (right)

Table 8.18: Wallet II, mechanical properties determined by traditional tools and DIC system

	ε'_m [%]	ε'_{mt} [%]	E [N/mm ²]	ν	G [N/mm ²]
LVDT	0.49 (0.39)*	0.32	7363	0.12	3296
DIC	0.29	0.15	9977	0.31	3781

*considering only LVDT 1 and 2

8.4.7 Wallet XII

Mechanical results

This masonry wallet was exposed outdoors and subjected to low-concentrated sodium sulphate capillary rise over three summers prior to undergone to compression test.

The set-up as well as the testing procedure of the mechanical test was analogous at those used in the other 4 tests, described in the previous paragraphs. The three load pauses were performed at 165kN, 330kN and 495kN, as in the case of wallet II (Table 8.19). After the last load break, the compression load was increased monotonically up to the maximum masonry resistance. In addition, in this case, it was possible to continue the test after the peak corresponding to the maximum load and two cycles of unloading-loading were carried out prior to reach the fragile collapse of the wallet. This compression test lasted approximately 1h and 40min (Figure 8.39).

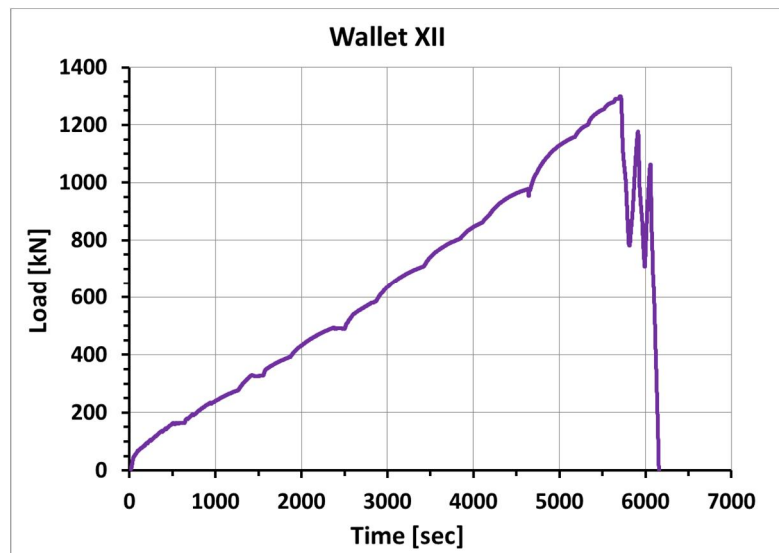


Figure 8.39: Wallet XII, load-time history

Table 8.19: Wallet XII, uniaxial compression test

Time from the test beginning [minutes]	Load [kN]	Load pause [minutes]	Vertical displacement [mm]	Horizontal displacement [mm]

10	165	2	0.14	-0.012
25	330	2.5	0.19	-0.142
40	495	2.5	0.25	-0.26
95.15	1299	/	1.12	-1.07
101.64*	619.99	/	2.48*	-2.32

*time instant corresponding to the maximum vertical displacement

This wallet react to the load application differently from the previous masonry specimens. The first part of the test was characterized by a greater assessment phase and some cracks (vertical cracks, on the 3rd and 4th masonry course) appeared just after the first pause at constant load. Other cracks were recorded at about 550 kN. However, vertical and horizontal displacements of very small entities were measured until approx. 600kN. Big cracks appeared later at 1000 kN and at the end of the test, a diffuse crack pattern was detected but the collapse was not as explosive and brittle as the other 4 masonry specimens, thus it was possible to partially record the descending branch of the load-displacement curves. So, in this test, the maximum values of both axial and transversal displacements were measured after the load peak, during the last post-compression cycle (Figure 8.40).

The principal mechanical parameters evaluated are summarized in Table 8.20 and Table 8.21

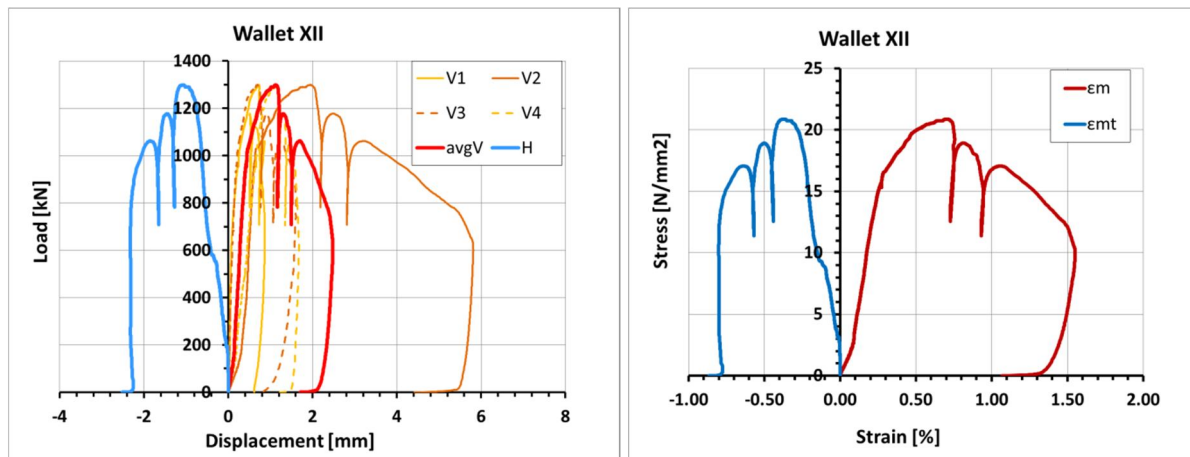


Figure 8.40: Wallet XII, load-displacement and stress-strain graphs

Table 8.20: Maximum and residual values of stress and strain from the compression tests

Wallet	f'_m [N/mm ²]	f_{mr} [N/mm ²]	f_{mr}/f'_m [%]	ϵ'_m [%]	ϵ_{mu} [%]	μ_ϵ
XII	20.89	12.01	58	0.71	1.50	2.13

Table 8.21: Results of the compression tests in terms of elastic moduli

Wallet	E [N/mm ²]	ν	G [N/mm ²]
XII	7946.90	1.28	1742.55

DIC results

As for the other tests on aged wallets, the results of the digital image monitoring were displayed first of all as coloured maps of displacements along the three principal directions (Figure 8.41). From the values of the displacements, the corresponding strains were determined and 3D maps of each parameter, at different load levels, were visualised (Figure 8.42, Figure 8.43, Figure 8.44).

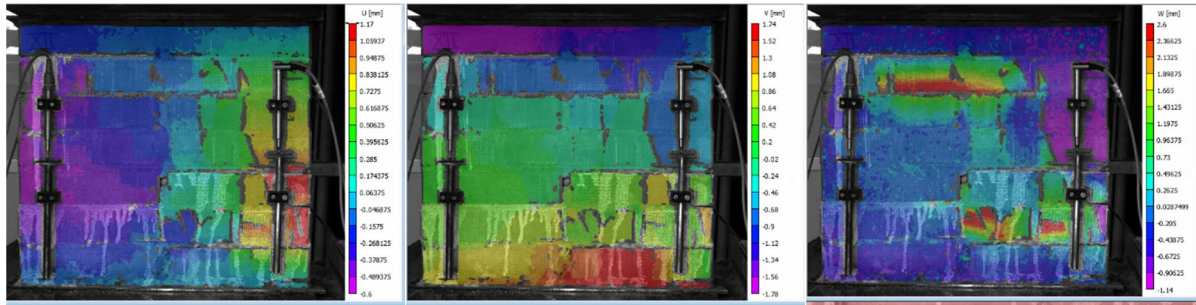


Figure 8.41: Wallet XII, horizontal (left), vertical (centre) and out-of-plane displacements (right) at the peak load

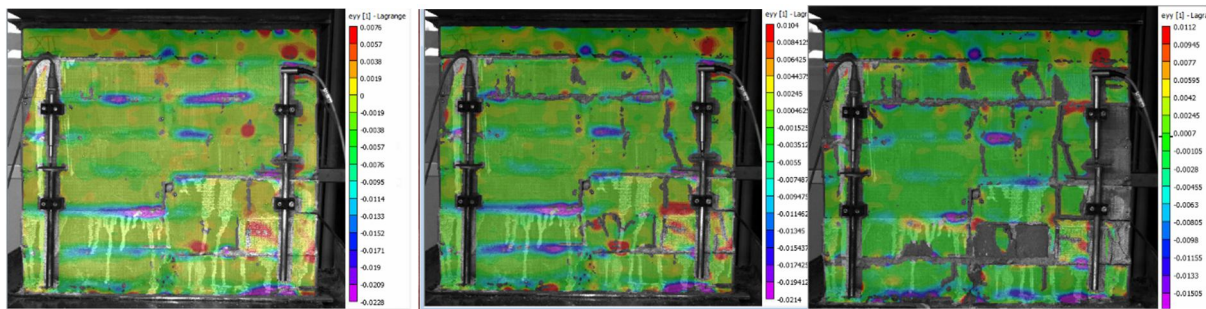


Figure 8.42: Wallet XII, trend of full-field maps of ε_{yy} strains at increasing loads: 1099kN (left), at the maximum load (centre) and at the end of the test (right)

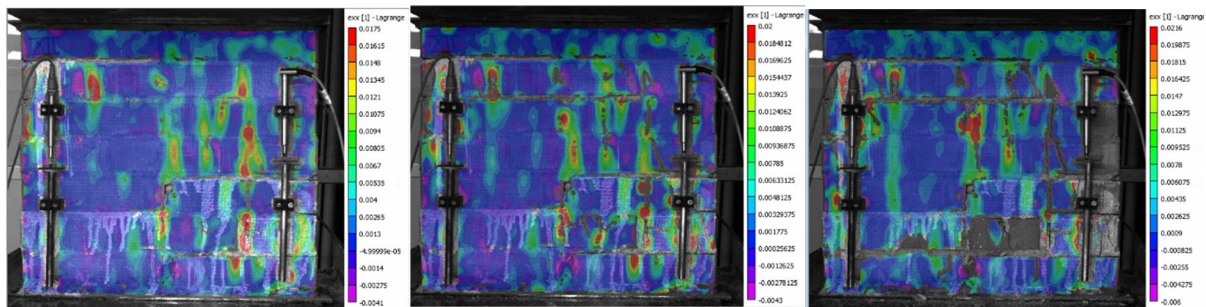


Figure 8.43: Wallet XII, maps of ε_{xx} strains at increasing loads: 1099kN (left), at the maximum load (centre) and at the end of the test (right)

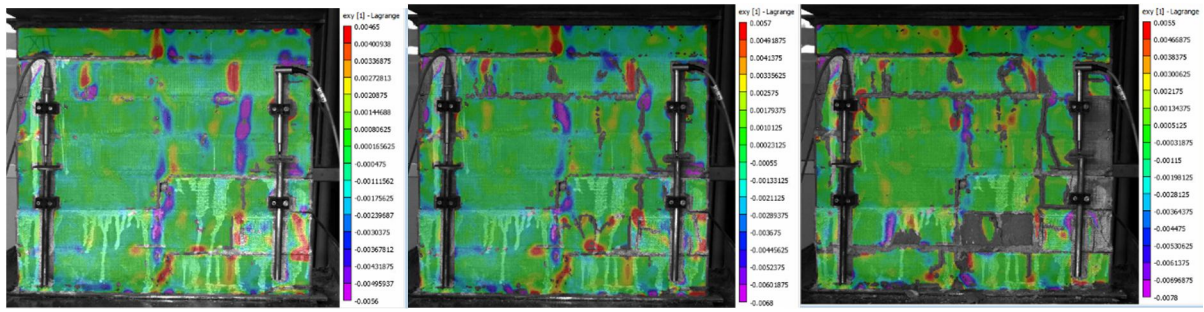


Figure 8.44: Wallet XII maps of out-of-plane strains, ε_{xy} , at increasing loads: 1099kN (left), at the maximum load (centre) and at the end of the test (right)

A very good agreement between the mechanical data obtained by traditional measuring tools and DIC data displayed by means of the virtual extensometer tool, was encountered (Figure 8.45, Table 8.22).

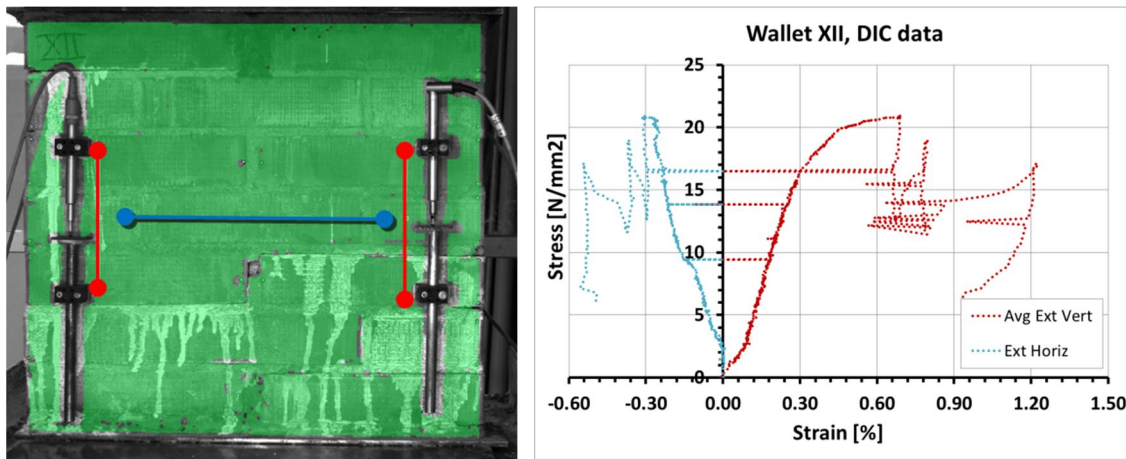


Figure 8.45: Wallet XII, position of the virtual extensometers (left) and resulting stress-strain diagram (right)

Table 8.22: Wallet XII, mechanical properties determined by traditional tools and DIC system

	ε'_m [%]	ε'_{mt} [%]	E [N/mm ²]	v	G [N/mm ²]
LVDT	0.71 (0.83)*	0.37	7947	1.28	1742
DIC	0.69	0.31	6924	1.18	1586

*considering only LVDT 1 and 2

8.5. Discussion and conclusions

In order to evaluate the effects of natural or accelerated ageing treatments on the characteristics mechanical properties of brick masonry, 5 on-purpose built masonry wallets of

nominal dimensions $0.5 \times 0.5 \text{ m}^3$, with different levels of initial decay, were subjected to uniaxial compression tests. In addition to the traditional measuring devices, these tests were continuously monitored by means of two non-destructive testing techniques, the acoustic emission and the digital image correlation technique and their reliability in assessing the mechanical damage and in following its evolution over time since the beginning of the test was evaluated.

First of all, the results of the mechanical compression tests carried out on the 5 different brick masonry walls and obtained by means of the traditional wired measure devices are herein summarized (Table 8.23, Table 8.24). The characteristic mechanical parameters obtained for the reference, undamaged wallet, I, are compared with the values determined for the other 4 specimens which were subjected to different ageing treatments prior to undergone to uniaxial compression tests.

This comparison has not to be intended as an absolute truth due to the scarce number of specimens tested and knowing that the mechanical behaviour of masonry, being a composite material, is affected by high dispersion. Nonetheless, the results are reliable in terms of relative values. Indeed, some differences between the undamaged wallet and the aged ones are clearly established.

Overall, aged masonry specimens appeared more resistant and stiff than the reference, as-built brick wallet. Indeed, they showed greater values of both peak and “residual” compressive strengths with an average increase of about 40%. A considerable increase was also measured for the values of the elastic moduli. In detail, the Young’s modulus, E , is almost twice for the aged specimens than for the undamaged one as well as G , with the exception of the naturally aged wallet which presents a value similar to that recorded for the as-built masonry specimen. The Poisson ratio, ν , which measures the Poisson’s effect that is the tendency of a material compressed in one direction to expand in the other two perpendicular directions, also increased considerably, as a consequence of the stiffness increase (Figure 8.46).

Table 8.23: Maximum and residual values of stress and strain obtained from the mechanical compression tests

Wallet	f'_m [N/mm ²]	f_{mr} [N/mm ²]	f_{mr}/f'_m [%]	ϵ'_m [%]	ϵ_{mu} [%]	μ_ϵ
I	16.20	15.85	98	0.05	-0.83	-16.07
VI	22.19	20.41	92	0.36	0.51	1.43
V	23.60	20.38	86	-0.14	-0.34	2.45
II	23.11	20.80	90	0.49	0.52	1.06
XII	20.89	12.01	58	0.71	1.50	2.13

Table 8.24: Summary of the compression test results in terms of elastic moduli

Wallet	E [N/mm ²]	ν	G [N/mm ²]
I	3601.26	0.13	1600.26
VI	7323.23	0.64	2237.19
V	9903.72	1.09	2361.74

II	7363.18	0.12	3296.04
XII	7946.90	1.28	1742.55

This increase in stiffness is apparently associated also with an increase in ductility, but this result has to be considered “carefully” due to the limitations of the test set-up which do not allow to measure a real value of ductility. In addition, the collapses of the aged specimens, were much more fragile and explosive than the failure of the undamaged one, suggesting a more brittle behaviour of the firsts.

The greater strength and stiffness of the aged brick masonry specimens compared to the as-built one are in line with the resistance increase resulting from the mechanical tests carried out on the single units of building materials (§5.5). This variation of the mechanical behaviour of masonry in compression is probably caused by the presence of water and salt crystals into the material pores, previously filled only with air that led to an increase of both density and resistance. In addition, the presence of salts created new bonds at the brick-mortar interfaces, which are apparently stronger than the usual bonds, at least when masonry is subjected to compression.

From the results obtained, it is not possible to discriminate between the different ageing treatments to which were subjected the 4 wallets considered, due to scarcity of masonry assemblies tested and the small differences recorded on the measured values.

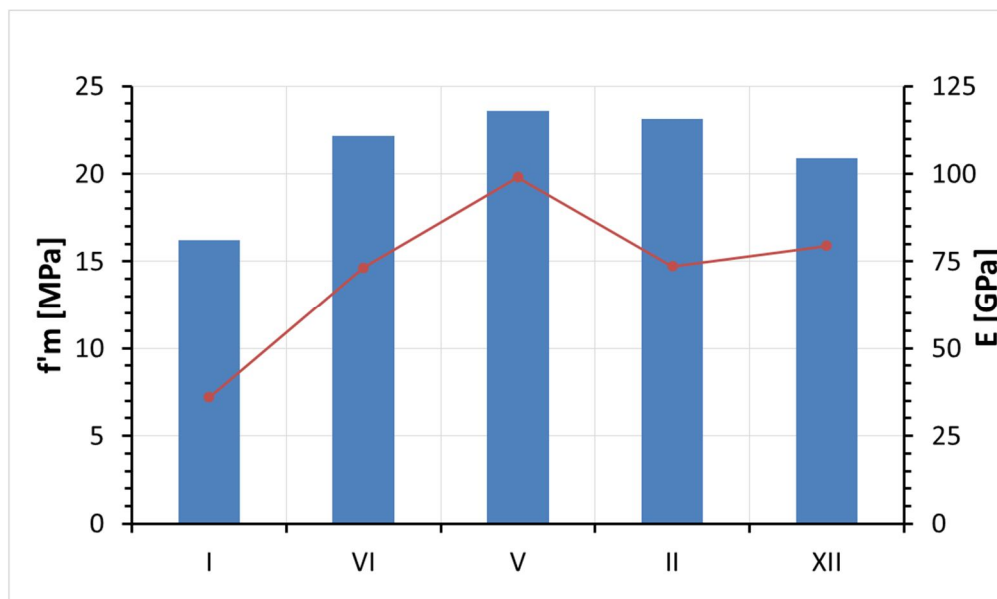


Figure 8.46: Compressive strength and modulus of elasticity for the 5 wallets

The acoustic emission technique applied to monitor one mechanical compression test, the one of the undamaged brick masonry wallet (§8.5.1), has proven to be accurate in evaluate the mechanical decay, that is in determining the time instants at which cracks occurred and in following this process since the beginning, for low levels of load.

On the other end, the digital image correlation monitoring technique, which was employed to monitor the other 4 mechanical compression tests (§8.5.2 - 5) has demonstrated to be accurate and reliable in determining 3D full-field displacement and strain maps at different load levels, and also at the beginning of the tests. From these maps, the mechanical behaviour of the whole masonry and of the single building constituent materials could be evaluated. In addition, the feasibility of the simplified DIC procedure adopted, which would serve in view of further application on-site and on historical masonry, was demonstrated by comparing the results obtained through software tools, virtual extensometers, with the values recorded by means of traditional LVDTs. However, the small differences measured on the 4 differently aged walls do not allow to discriminate between the diverse amount of initial decay. This is not to be ascribed to an inability of the non-destructive technique as it is mainly due to the few tests performed and the data dispersions which are characteristic of masonry materials.

9. Mechanical evaluation of masonry assemblies subjected to accelerated ageing

The results of the mechanical destructive tests carried out on the 3 series of decayed masonry assemblies (§4.4) are herein reported and compared with the outcomes of analogous mechanical tests carried out on the series of brick masonry specimens in as-built conditions, in order to evaluate and quantify the effects and the possible variations on the mechanical properties of masonry caused by decay processes due to weathering.

Overall, 36 brick columns, made of 6 fired-clay bricks and 5 lime mortar joints, 1 cm thick, 24 triplets and 4 one-header small walls, manufactured with the same building construction materials were considered. They belong to 4 series, divided according to the different levels of environmental decay to which they were exposed. This degradation state was artificially simulated in the laboratory, prior to start the mechanical tests, by means of a certain number of ageing cycles, different for each series (Table 1). As already explained (§4.6), each cycle consisted in immersion into high-concentrated sodium sulphate solution followed by a treatment in a climatic chamber varying the boundary conditions (air temperature and relative humidity).

Each series of masonry assemblies was composed by 9 six-brick columns, 6 triplets and one single wythe wall of limited lateral dimensions (0.5 x 0.5 m²). This chapter is complementary to the previous one, chapter 8, which reported on the mechanical tests carried out on the small walls, thus, herein only the brick columns and the triplets were considered.

Table 1: Series of masonry assemblies, ageing treatments

Series	Ageing treatment	Salt solution	N° of cycles / year
0	None, as-built	/	/
2	Acc. ageing	Na ₂ SO ₄ 10%-wt.	18
3	Ac. ageing	Na ₂ SO ₄ 10%-wt.	28
4	Acc. ageing	Na ₂ SO ₄ 10%-wt.	38

The 9 columns of each set were intended to be tested in compression, applying the load with three different eccentricities ($e=0$, $e=40$ mm, $e=80$ mm). For each load configuration, three columns were prepared. Actually, due to some drawbacks occurred during the experimental phases (i.e. unexpected rupture of masonry assemblies during ageing), the number of available specimens was slightly lower, but, anyhow, at least two columns per type were tested in order to obtain results as representative as possible. Instead, the 6 triplets of each series were intended to undergo shear tests. Also in this case, as better explained in the following paragraphs (§9.5), it was not possible to perform all the planned tests, due to the detachment of the mortar joints from the bricks which happened at the end of the ageing treatments because of the decay caused by the salt crystallization/hydration cycles occurred.

All the compression and shear tests herein described were monitored by means of traditional measurement devices (i.e. LVDTs and TML displacement transducers) in order to determine the characteristic mechanical properties of masonry: compressive strength, tensile strength, shear strength as well as the corresponding strains and the modulus of elasticity. Moreover, the concentric and eccentric compression tests carried out on the six-brick columns belonging to the two series of assemblies which were in opposite health conditions (the reference undamaged one, 0S, and the most damaged one, 4S) were also monitored via a non-destructive technique, the digital image correlation technique, DIC (§3.6), in order to obtain an overall picture of the stress-strain state of one main face of the single brick column. As the DIC method was employed by means of a simplified on-purpose developed procedure [chap 8. 1b, 22], an additional, intrinsic aim of these mechanical tests was to evaluate the reliability of the method itself and the applicability of this NDT technique as an additional or substitutive measuring device (§9.4).

Thus, in this chapter, after a brief review of the relevant related literature on the experimental mechanical characterization of brick masonry, the testing procedures and laboratory testing equipment (both mechanical and non-destructive) were described, underlining the innovative aspects of the followed procedures as well as the limitations and difficulties encountered. Then, the data analysis procedure for the three different types of compression tests is explained with reference to few representative masonry assemblies, taken as example. Later the results obtained for the three series of weathered six-brick columns are summarized, compared to the undamaged one and critically discussed. Similarly, with reference to the triplets belonging to the 4 series, the shear test procedure, equipment and test set-up are described. Then, the procedure followed for data visualization and analysis are explained and all the available results reported, compared and discussed.

9.1. Six-brick columns: mechanical compression tests

The 36 brick columns belonging to the four different series of masonry assemblies were mechanically tested in order to evaluate the variations on the masonry load carrying capacity which may have occurred due to the ageing treatments to which they underwent.

These destructive tests were primarily aimed at filling the gap existing in the researches related to the weathering effects in masonry, which are mainly focused in evaluating visual or physical-chemical variations on the single units of building materials (see §2, literature review). Very few information are known on the consequences of such decay on the same properties of brick masonry considered as a whole and less is known on the effects on their mechanical properties.

Taking into account this global aim and considering that masonry structures are mostly designed to sustain axial forces, i.e. used as load bearing walls, arches and pillars, the specific six-brick columns considered were subjected to compression loads in order to determine the characteristic values of compressive strength and modulus of elasticity. Actually, with the purpose of evaluating any possible consequences of the simulated weathering procedures also on the tensile strength of masonry, it was decided to consider three different load configurations for the compression tests (Figure 1). The three load eccentricities investigated were $e=0$, used to simulate concentric loading, $e=40$ mm, to simulate an eccentric load within

the middle third of the resistant cross-section [3] and $e=80$ mm to reproduce an applied load outside the middle third of the same cross-section, that is outside the central core of inertia [SdC].

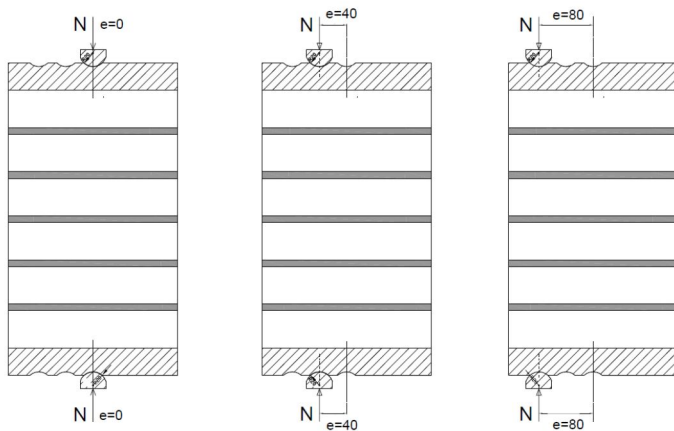


Figure 1: Types of compression tests on the six-brick columns: concentric load (left), medium eccentricity (centre) and maximum eccentricity (right)

The choice of performing compression tests with eccentric loads was made in order to study more realistic stress-strain configurations, more likely to be found in existing fired-clay brick structures. Indeed, as the majority of real masonry structures are subjected to stress concentrations deriving from load eccentricities, the common laboratory approach used to assess the mechanical properties of masonry and merely based in assuming an uniform distribution of stresses by performing concentric compressive load tests [ref. daBr] was demonstrated to be quite restrictive [3-6]. Some experimental tests and numerical models were already implemented and verified by other authors to overcome this limitation. As a results, laboratory testing procedures were proposed to evaluate the collapse mechanisms of solid brick masonry under eccentric loads and already proved to be effective [4-6].

Thus, with the aim of obtaining information complementary to those recovered from the uniaxial compression tests carried out on the one-headers wallets §8, these procedures and indications suggested by the previously mentioned researchers [3-6] were taken into account to study the behaviour of the six-brick columns.

First of all, the boundary conditions of both concentric and eccentric load tests were selected. According to [4], a theoretical configuration considering double-cylindrical hinges (Figure 2 right) instead of a cylindrical hinge and fixed base (Figure 2 left) in order to obtain, during load application, a line of thrust lying between the two hinges at a constant distance, e , from the middle vertical section of the tested specimen [3, 4].

To reproduce this load configuration in our laboratory, a metal carpentry made of several pieces was on-purpose designed and realized (Figure 3). The design phase took into account the testing aims, the indications reported in previous experimental works, the dimensions of the specimens as well as the characteristics of the laboratory universal testing machine which had to be used to perform the tests.

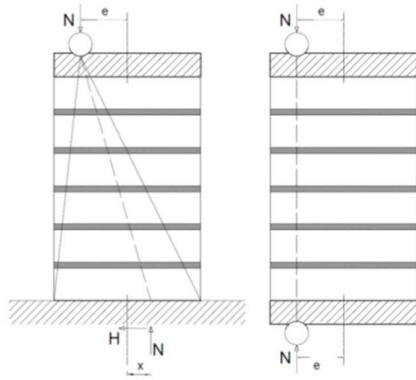


Figure 2: Eccentric load tests on brick masonry columns: top cylindrical hinge and fixed base (left), double cylindrical hinge (right) [4]

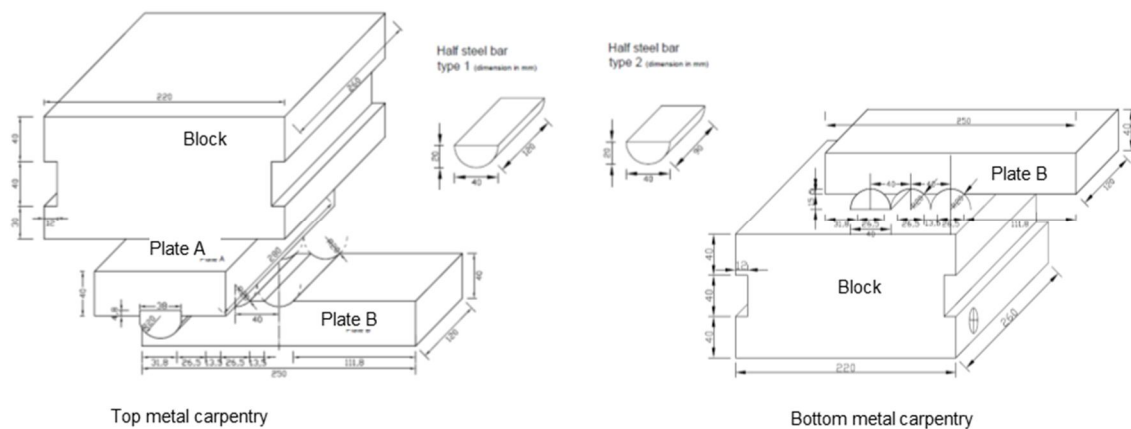


Figure 3: Metal carpentry designed and realized to perform the uniaxial and eccentric compression tests on the 6-brick columns: axonometric view of the top plates (left), axonometric view of the bottom plates (right)

The metal carpentry (Figure 3) consisted in several symmetric pieces:

- two steel plates, B, of dimensions (b x s x h) $250 \times 120 \times 40 \text{ mm}^3$ for the distribution of the compression loads. They are intended to have one main face, flat, in contact with the top or bottom brick of the masonry column; instead on the other main face they presented three cradles with semicircle shape (20 mm radius) positioned at a relative distance, between the centres, of 40 mm. The first one is located in the middle section of the plate. They are used to hold the half round bars at different positions.
- Two half round steel bar, 40 mm in diameter, 90 mm in length, to be seated in the grooves of the plate and act as load hinges, allowing also the free rotation of the plates B during the load application in one main direction.
- Two stiff steel blocks, used to adapt the universal testing machine frames and to allow the execution of such concentric and eccentric compression tests, joined to the steel plates by means of the half round bars.

In addition to these, two extra metal pieces were realized to complete the top metal carpentry: one steel plate, A, with the same dimensions of plates B but with two perpendicular grooves,

one on each main side of the plate, and one half round bar, of the same diameter of the previous but 120 mm long. These two pieces are designed to be positioned between the top rigid block and the top steel hinge, to allow the rotations in the second main direction (turned 90°).

Thus, with this carpentry it was possible to perform concentric compression tests and eccentric ones, with two different eccentricities, just moving the half round bar from one groove to the next one.

9.1.1. Preparation of the specimens and measurement devices

The six-brick columns were accurately prepared prior to start the mechanical tests.

First of all, as for the single-wythe small walls (§8.2), the current dimensions of all the columns were measured in order to evaluate possible differences with the design dimensions, which were chosen to comply with the minimum requirements of [1], as well as to know the exact area of the resistant cross-section to properly calculate the compressive stresses generated during the application of load. The heights of the horizontal mortar joints were also measured in different points in order to evaluate possible anomalies and lack of planarity and parallelism between the bricks.

A visual inspection and crack pattern survey was also performed. These surveys were aimed at highlighting existing small crack, delaminations, presence of brick flakes or lack of materials (i.e. on the mortar joints), due to original defects of the construction materials, or, more probably due to the ageing treatments because they may act as weak points during the mechanical tests. The presence of salt deposit and crystals on the main surfaces was also recorded.

These preliminary inspections are important especially for the six-brick columns belonging to the three series subjected to the artificial ageing treatments which presented several visible damages on both types of porous masonry materials.

Actually, the decayed specimens had to be cleaned before the crack pattern survey as, at the end of the accelerated ageing cycles, their surfaces were completely covered by a layer of salt depositions (Figure 4). Also in this case, as for the wallets, this operation was made by means of a rough metal brush and a vacuum cleaner to eliminate the biggest dust/salt depositions. This procedure was performed not only for ease the subsequent visual and photographic inspections but also to obtain stable and clean surfaces on which install the traditional measuring devices. They were positioned on the brick surfaces using on-purpose realized metal bases which were glued to the surfaces via a two-component fast curing adhesive, suitable to be used in porous materials [7].

Indeed, with the aim of measuring the global displacements of the column throughout the compression test, 6 inductive linear transducers, LVDTs, were employed (Figure 5 left). These had an accuracy of $\pm 1\%$ and are able to measure displacements between 0 and 10 mm [8]. The LVDTs were placed vertically, along the direction of load application in the two main faces of the specimens, in pre-established positions: 2 in the correspondence of the middle axial section of the column (below the application point of the concentric load) and 4 near the edges, at about 3.5 cm from the external borders (Figure 6). The starting length of

each of these instruments, l_0 , was measured in order to evaluate the strains from the recorded values of displacements and thus recording the stress-strain diagram and calculate the values of compressive strength, modulus of elasticity, etc.

Actually, for the tests monitored also via the non-destructive imaging method, DIC (Table 2), the six-brick columns were prepared with only 4 LVDTs, 3 on one main face (front side) and one in the centre line of the opposite face (rear side) which was the one monitored with the two DIC digital cameras. This simplification was done to not completely “cover” the surface to be non-destructively analysed with out-of-plane instruments. As for the small walls, near the bases of such instruments and/or in other pre-established positions i.e. straddling some mortar joints, some markers - black and white circle of paper of 4 mm diameter- were glued via a vinyl glue (§8.4.2). These markers were employed in the data post-processing phase as additional reference points where to calculate the global/local displacements and strains.

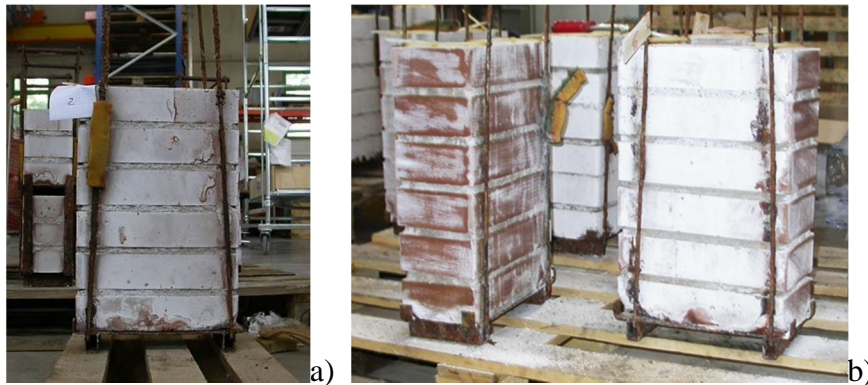


Figure 4: Appearance of: a) one six-brick column after 38 ageing cycles, b) two columns after (left) and before cleaning (right)

In addition to the “traditional” wired transducers and, in some cases, to the DIC, 6 TML displacement transducers [9], also called “omega” due to their shape (Figure 5 right) were installed. They were able to record displacements up to 5mm and usually employed not for masonry but to measure crack openings in concrete structures subjected to bending tests. For all the tests, these devices were intended to monitor the opening/closing (tension/compression) of mortar joints and, for that reason, they were positioned in the lateral faces of the brick columns, 3 for each side, above the 2nd, 3rd and 4th lime mortar joints respectively (Figure 6 right). To obtain reliable measurements which allow us to quantify and better differentiate the masonry behaviour of masonry under eccentric loads, it was very important to have a stable support for these instruments during the whole duration of the test. Despite the accurate cleaning of the surface areas (also with some alcohol) where to position the bases for the omega, prior to glue them, many difficulties have been encountered due to the presence of sodium sulphate depositions on the masonry surfaces. Indeed, the presence of these salts caused the repeated falling down of the bases supporting the instruments (i.e. see Figure 7 taken few instant before starting a mechanical test on a damaged brick column). Thus, the preparation of the six-brick columns was quite demanding as the installation of the TML devices had to be repeated several times, also changing the type of glue, and also when

the specimen was already ready to be tested, i.e. positioned beneath the load plates. Nevertheless, during some compression tests, we lost data because of the falling down of one or more of the supporting bases.

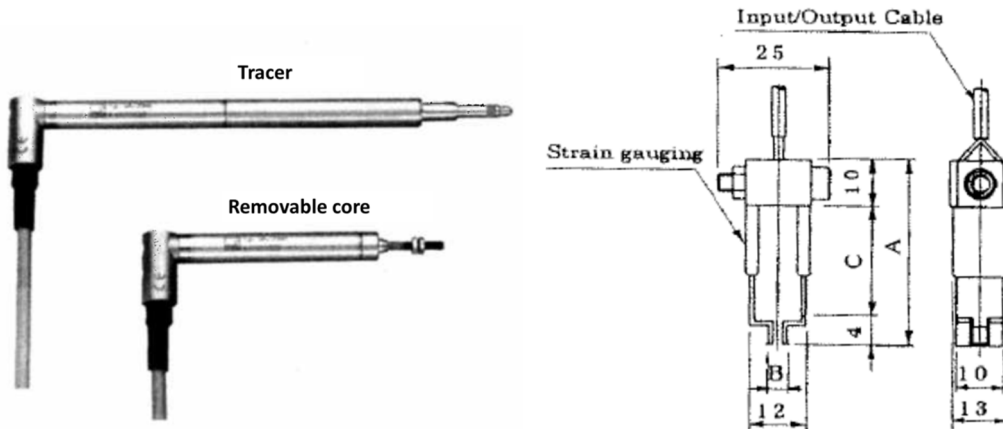


Figure 5: LVDTs [8] and TML displacement transducers [9]

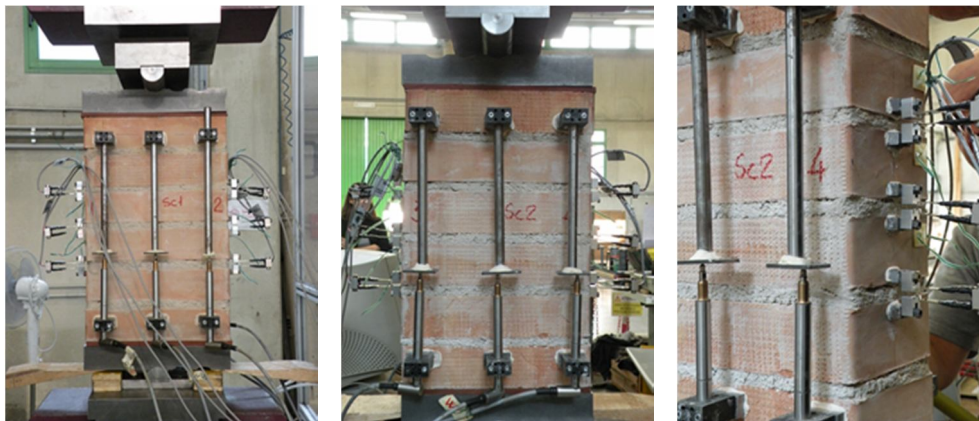


Figure 6: Concentric load test on an undamaged six-brick column, without DIC: position of LVDTs on the front side (a), rear side (b) and detail of the TML transducers installation (c)

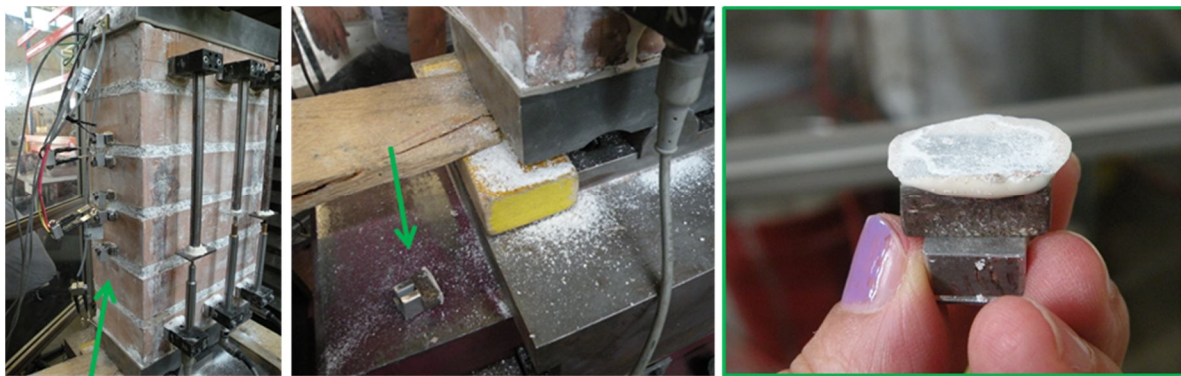


Figure 7: Example of detachment of a TML transducer base, few instant before the start of the mechanical test because of the salt depositions

Finally the so-prepared and instrumented brick-columns were positioned under the load testing machine equipped with the special metal carpentry realized; note that, a sheet of high-density cardboard, approx. 5 mm thick and a thin layer of talcum powder was interposed between the top and bottom surfaces of the brick columns and the loading plates, the so-called steel plates B, to smooth the bases of the specimen and compensate the unavoidable irregularities of the brick surfaces. Actually, in the first compression tests (i.e. Figure 6), a sheet of neoprene, approx. 8 mm thick was used but it was then discarded because too deformable.

A summary of the compression tests carried out is reported in Table 2. Herein, the six-brick columns were divided in terms of ageing treatment suffered and load configuration type. In violet are indicated the specimens monitored with the digital image correlation method during the corresponding mechanical test. Note that some six-brick columns, in italics in the table, were not tested because of their premature collapse, occurred at the end of the artificial weathering procedure or because of an abrupt movement that caused their accidental fall down prior to reach the testing machine (OS9). Moreover, the brick column 3S11 was actually a 5-brick column because the ageing cycles caused the detachment of its top brick and top mortar joint, but, anyhow, it was tested as the others.

Table 2: Series of six-brick columns, types of compression tests. In violet, the tests monitored also via DIC

Series 0	e [mm]	Series 2	e [mm]	Series 3	e [mm]	Series 4	e [mm]
OS1	0	2S3	0	3S1	0	4S1	0
OS3	0	2S4	0	3S2	0	4S5	0
OS6	0	2S8	0	3S7	0	4S6	0
OS2**	40	2S1	40	3S6	40	4S2	40
OS5	40	2S2	40	3S8	/	4S4	40
OS8	40	2S6	40	3S11*	40	4S9	40
OS4	80	2S5	80	3S3	/	4S3	80
OS7	80	2S7	80	3S9	80	4S7	80
<i>OS9</i>	/	2S9	80	3S10	80	4S8	80

*5-brick column; **monitored via photoelasticity

9.1.2. Testing equipment, set-up and procedure

All the compression tests, with concentric or eccentric load, were performed under displacement control, by means of a universal testing machine Metrocom with a carrying capacity up to 600 kN. This was connected to two acquisition units in order to have at disposal 13 channels and to a computer with a dedicated Labview software for data storage and real time data visualization (Figure 8).

The load application velocity was set to 0.5 mm/min and the data acquisition rate to 2 data/sec. The load was not uniformly distributed but applied punctually through the two

hinges (half round steel bars) in the middle section of the masonry column or with an eccentricity.

Each mechanical test consisted in several cycles of load-unload, at progressively increasing load levels (each of 100 kN), until reaching, with the last cycle, usually the fourth one, the complete collapse of the brick column (Figure 9). Actually the number of cycles varied between 3 and 6 with the load carrying capacity of each masonry specimen. Anyhow, the first cycle usually consisted in loading up to 100 kN and unloading, not to 0 kN but to 5 kN and it was aimed at allowing the assessment and settling of the column between the loading plates. The unload phases were always stopped at least at 5 kN in order to not completely discharge the specimen instead maintaining a certain load to prevent the falling down of the brick column.



Figure 8: Load testing machine (left) and control unit (right)

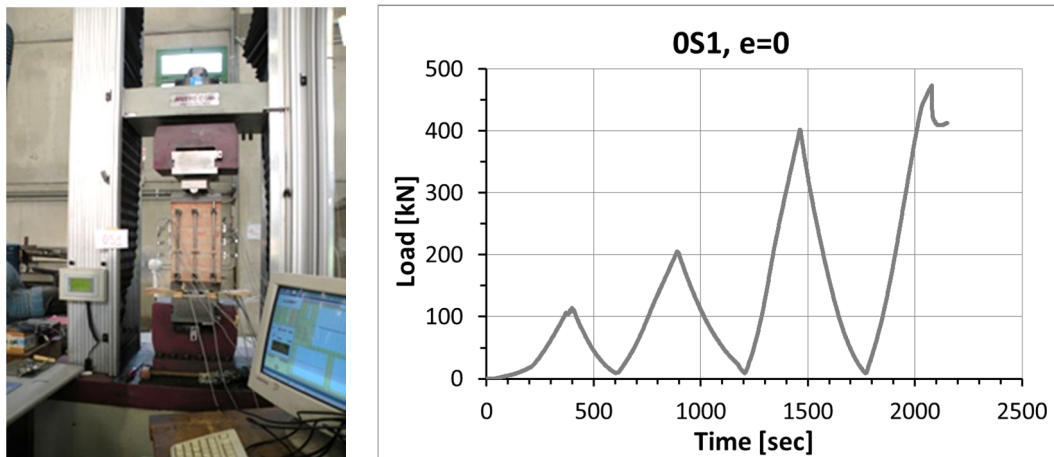


Figure 9: Example of concentric compression test on an undamaged six-brick column (left) and corresponding load-time history (right)

9.1.3. Mechanical data: acquisition and analysis

During each compression test, the values of load, global and local displacements were collected thanks to the acquisition units and the pc with dedicated Labview software. The

values of the axial displacements measured via the 6 vertical LVDTs (or 4 LVDTs when the mechanical test was monitored via DIC) were first of all plotted versus the load values. Then, the average values of displacements obtained from the two central LVDTs and the 4 (or 2) lateral LVDTs were calculated and used to recover stress-strain diagrams and thus to determine the principal parameters characterizing the behaviour of the brick columns under compression [1].

In detail, in the case of concentric load tests, considering an uniform stress distribution over the section, the values of the compression stress, f_c , in [MPa] were calculated by dividing at each time instant the applied load, N , for the effective loaded cross-section area of the six-brick column, $A=b \cdot s$, where b is the width of the section (nominally equal to the length of the brick, 250 mm) and s is the height of the section (nominally 120 mm). Thus, the maximum compressive strength, f_c' was measured in correspondence of the maximum load, N_{max} :

$$f_c' = \frac{N_{max}}{A} \quad (9.1)$$

The values of global axial strain, ε_m , were determined by dividing the displacements measured by each vertical LVDT by the respective gauge length. In detail, two average values were considered: one by averaging the strains determined from the displacements recorded with the two central LVDTs and one by averaging the strains calculated from the other 4 LVDTs (edges). The maximum value of strain under the load application point, ε_m' , in [%], was always recorded. Moreover, the values of modulus of elasticity or Young's modulus, E , in [MPa] were evaluated from the last cycle of stress-strain graph obtained considering the average strains calculated from the two central LVDTs by averaging the slopes of the descending and ascending branches between the ordinates corresponding to $0.1 \cdot f_c'$ and $0.4 \cdot f_c'$. In addition, the movements recorded at the mortar joints (positive means openings and negative closing) were displayed as load-displacement graphs but, in this case, they were only used to evaluate the masonry symmetry with respect to the central vertical axis that was the point of load application.

For the eccentric load tests, the stress distribution in the section is unknown and the assessment of the compressive strength is based on the assumption of a linear strain distribution over the section and considering a simplified perfectly brittle constitutive model (Figure 10). It is known that this model is too limitative to represent the behaviour of masonry under eccentric loads because it does not take into account the inelastic compressive response of masonry, experimentally demonstrated, and that it may led to some overestimations, i.e. apparent increase of the compressive strength due to load eccentricity [4]. Anyhow, it was assumed to be sufficiently adequate in our case as the results were not taken to assess “in absolute” the masonry behaviour but to perform a comparison between specimens in different starting decayed conditions, subjected to the same load tests.

Therefore, to evaluate the stress distribution for eccentric loading within the middle third of the cross-section (Figure 10 left), that is for $e=40$ mm, the following formulae was used:

$$f_c = \frac{N}{A} + \frac{6Ne}{b^2 s} \quad (9.2)$$

which takes into account the contribution of the moment, M , generated by the load eccentricity ($M=N \cdot e$). Also in this case, the maximum compressive strength f_c was evaluated

For load eccentricities outside the middle third of the cross-section, that is, in this thesis, for $e=80$ mm, first of all, a cracked triangular stress distribution was considered (Figure 10 centre) by performing an additional simplification and neglecting the tensile strength of masonry. Thus, the compressive strength in the external border of the section closest to the point of load application was evaluated by means of:

$$f_c = \frac{2N}{3su} \quad (9.3)$$

where u is difference between the half section width, $b/2$, and the eccentricity, e .

Then, for both types of eccentric load tests, the values of global axial strain, ε_m , were determined s , and the values of modulus of elasticity or Young's modulus, E , in [MPa] were evaluated according to the indications reported for the concentric load test. The opening/closing displacements recorded at the three central mortar joints, both on the left and right side of the six-brick columns, were displayed as load-displacement graphs, to evaluate the occurrence of tractions/compressions.

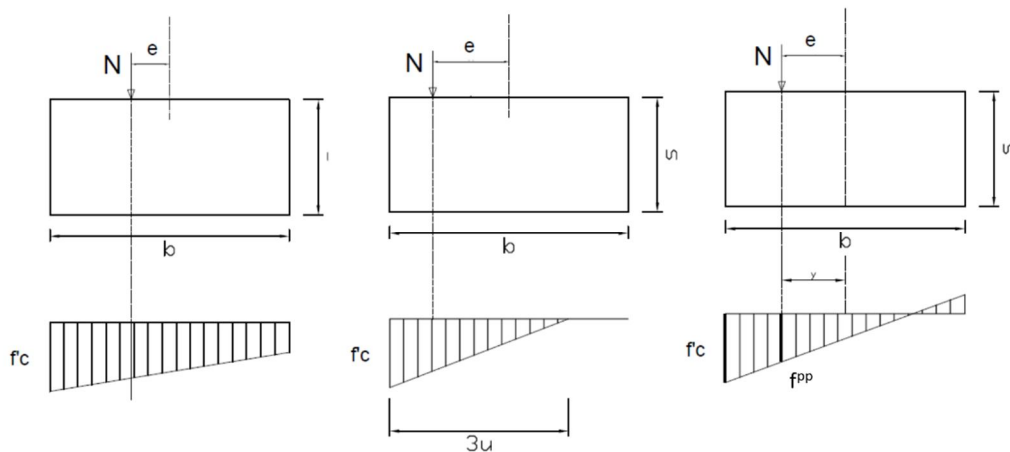


Figure 10: Linear assumed stress distribution induced by eccentric loading at increasing eccentricity (left and centre); general stress distribution under eccentric loading without neglecting the tensile strength contribution (right). f_c is the maximum strength, f_c^{pp} is the strength in correspondence of the point of load application

Actually, additional evaluations were also done as we would like to consider the contribution of the tensile strength and calculate its peak value, f_t , which may be significant to evaluate the effects of ageing treatments on the mechanical behaviour of masonry. Thus, for the eccentric load tests, we considered a partialization of the resistant cross-section area (Figure 10 right)

and by means of (9.4) we re-calculated the compressive strength in the point of load application f_c^{PP} as well as the tensile strength in the external border situated in the opposite site of the section with respect to the point of load application. The first value was thus determined according to the general, not simplified, equation:

$$f_c^{PP} = \frac{N}{A} \pm \frac{Ne}{I} y \quad (9.4)$$

which is valid for all values of e . Here, I is the moment of inertia of the section and y is the distance between the barycentre of the section and the point of load application.

Thus, the main mechanical parameters obtained for each compression test were summarized in tables (i.e. Table 3) and later discussed in function of the number of ageing cycles to which the specimens previously underwent.

Table 3: Main mechanical parameters recovered from the compression tests

	e [mm]	N_{max} [kN]	f'_c [MPa]	f_c^{PP} [MPa]	f'_t [MPa]	E [MPa]	$\varepsilon_{0.4f'_c}$ [%]	ε'_m [%]
specimen								

9.2. Six-brick columns: NDT evaluation of the mechanical test

As stated before, some compression tests (6 undamaged columns and 8 columns of the most decayed series, series 4) were also monitored by means of a non-destructive testing method, the digital image correlation technique or DIC (§3.6) thanks to the equipment which has recently become available at the CIRI-EC lab (§8.4).

This monitoring has had two aims: a) evaluate the 3D full-field stress-strain distribution of one main face of the brick columns under concentric and eccentric loads, b) study the reliability and accuracy of the simplified DIC procedure adopted in assessing the global and local strains in order to use this non-destructive method instead of the wired measuring tools. Also in these tests, indeed, as for the mechanical tests carried out on the one-header wallets (§8.4.2), the surface under investigation (the rear face of the six-brick columns) was not prepared with any coatings but the same natural texture of masonry, characterized by alternation of brick and mortar joints with their inhomogeneous surfaces was used as reference pattern for the DIC system. This allows to save time during the test preparation and, if resulted valid and usable instead of the traditional measuring tools, also to avoid the set-up problems encountered (i.e. difficulties in maintain attached the supporting bases of the instruments to the damaged masonry surfaces). Moreover in this way the surfaces were not altered and this is very important also in view of further application on-site and in historical structures or cultural heritage. The only expedient adopted during our laboratory tests, consisted in placing some little circles of paper with vinyl glue in pre-defined positions (§9.1.1) to simplify the DIC data post-processing as well as to verify the accuracy of the technique by comparing the strains calculated via DIC between these points with those resulting from the LVDTs and TLMs.

Prior to start each mechanical test, the DIC equipment was prepared by choosing the better and fixed position of the cameras, adjusting the focus and the brightness, also installing a lamp to uniformly illuminated the investigated surface with white light and, if necessary, positioning a black panel behind the specimen to avoid sudden variations of light in the background of the images or recording the passage of laboratory staff as these conditions may worsened the quality of the acquired images. Then, the cameras were calibrated and finally three channels of the mechanical control unit (load and the two central LVDTs) were connected to DIC data acquisition unit, in order to link the two types of data recorded (§8.4.2).

Finally, the frequency of data acquisition was set in 1 pair of images/5 second at the beginning of the test and 1data/2seconds later, after the appearance of the first cracks.



Figure 11: DIC testing equipment: a) digital cameras, b) laptop and data acquisition unit

9.2.1. DIC data analysis procedure

The images acquired via DIC during the mechanical tests were elaborated at the end of the compression tests by means of a dedicated software Vic 3D -2012. The steps followed for the data analysis and post-processing were the same described in §8.5.1:

- 1) calibration recall
- 2) selection of the area to be analysed (AoI) and positioning of additional starting points to not lose data around the vertical LVDT;
- 3) data analysis, which was automatically performed by the SW by comparing the pairs of reference images, acquired a 0 load to the damaged ones, recorded at regular time instants during the tests
- 4) rigid motion removal
- 5) visualization of results, in terms of 3D maps of displacements (u , v , w) along the three main directions (x , y , z) and corresponding strains. These results were visualized as coloured maps superimposed to the deformed images.
- 6) post-processing: measurement of displacements and deformations by means of lines or virtual extensometers positioned in correspondence of the added markers (near

LVDTs or TMLs); determination of the stress-strain diagrams and evaluation of the modulus of elasticity.

9.3. Example of data analysis and visualization

In the following, by way of example, the results obtained for one undamaged columns and 3 damaged specimens, also monitored by DIC are reported in detail. All the other results are then only summarized in §9.4.

9.3.1. Six-brick column OS1, concentric load ($e=0$)

Mechanical results

The six-brick column OS1 was tested in its as-built conditions, under concentric load. This mechanical tests monitored by means of 6LVDTs and 6 TMLs transducers (Figure 12), consisted in four loading/unloading cycles (Figure 13):

- 1) loading up to 100 kN (assessment cycle) and unload to approx. 5 kN,
- 2) loading up to 200 kN and unload to 5 kN,
- 3) loading up to 400 kN and unload to 5 kN,
- 4) loading until the collapse of the specimen, which occurred at approx. 470 kN and subsequent unloading.

In this last cycle the descending branch was not completely recorded due to the falling down of the LVDTs and TMLs transducers.

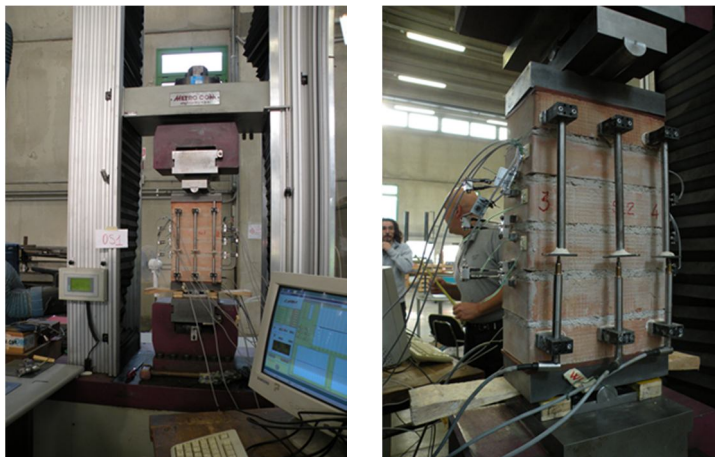


Figure 12: Six-brick column OS1, beginning of the compression test: front side (left), rear side (right)

The load-displacement graphs obtained both from the LVDTs located behind the load application point and those positioned near the edges of the specimen indicated, for all the loading/unloading cycles, a linear behaviour of masonry, until the fragile collapse of the six-brick column, denotable also from the perfect retracing of the loading branches upon the previous descending branches (Figure 14).

Visibly, no cracks appeared until approx. 400 kN. The first vertical cracks appeared in the rear side of the specimen, in the fifth brick from the bottom. Subsequent cracks, more evident, were detected on the sixth brick, again in the rear side and on the first brick of the front side (Figure 15). These denoted a certain rotational component, from the rear to the front side that intervenes during the test, probably caused by a no-proper load spreading i.e. due to the too deformable neoprene sheet positioned between the extreme brick's faces and the steel plates for the load distribution.

Thus, the brittle collapse of the six-brick column was unexpected, probably caused by the rotational component and occurred with expulsion of masonry portions on the top part of the rear side and bottom part of the front side (Figure 16).

The local displacements detected by the *omega* positioned above the 3 central mortar joints indicated a compression on both lateral masonry faces, but in different proportion: indeed, while in the left side, the mortar joints closed up to 0.3 mm, in the right side, the closing was maximum of 0.1 mm (Figure 17). This aspect confirmed the no-perfect symmetrical load distribution occurred.

Notwithstanding this, the stress-strain graphs obtained averaging the data both from the central LVDTs and the 4 lateral LVDTs, were determined (Figure 18) and the main mechanical parameters calculated (Table 4). The maximum compressive strength, evaluated according to (9.1) was probably underestimated but together with the value of the Young's modulus denoted typical behaviour of new brick masonry of good quality.

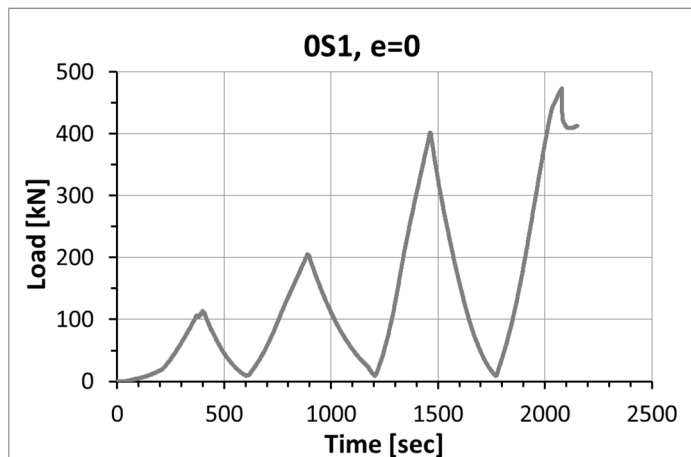


Figure 13: Six-brick column, OS1, time history graph

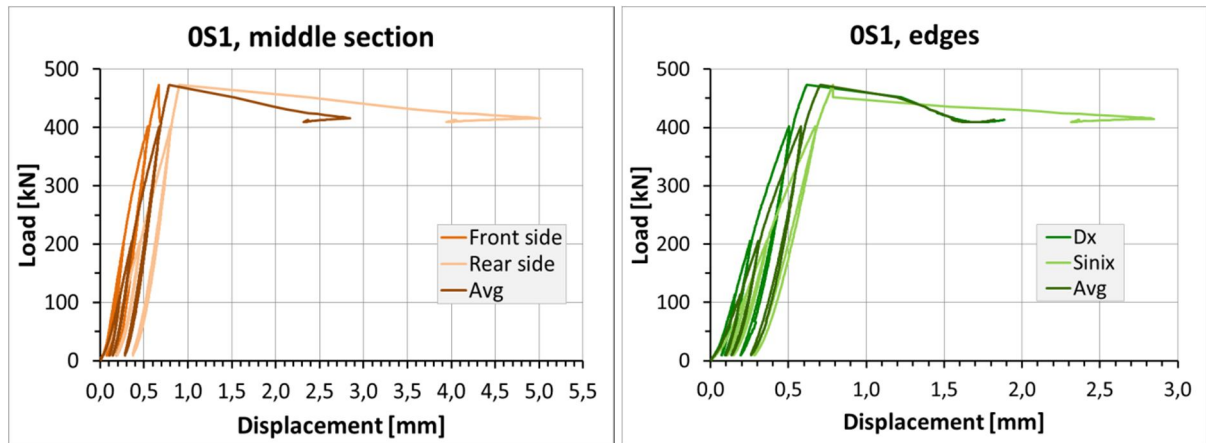


Figure 14: Six-brick column OS1, load displacement graphs recorded by the LVDTs under the point of load application (left) or near the edges (right)



Figure 15: Six-brick column OS1, visible cracks on the rear side (left) and detail of the cracks on the fifth and sixth brick (right)

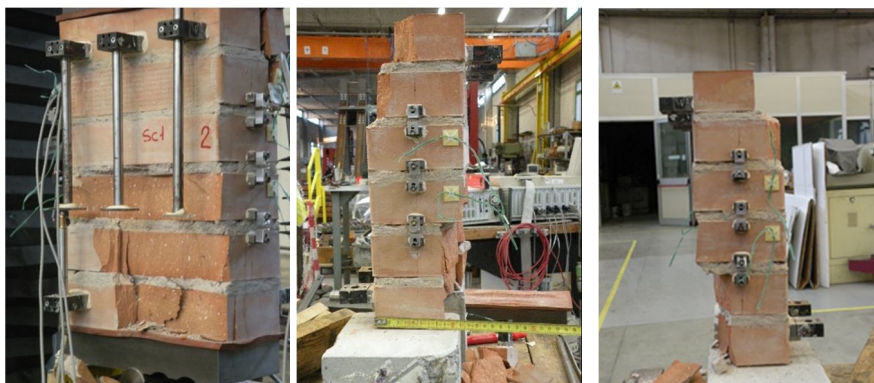


Figure 16: Six-brick column OS1 at the end of the test: a) falling down of a masonry portion on the front side, b) view of the left side, c) view of the right side

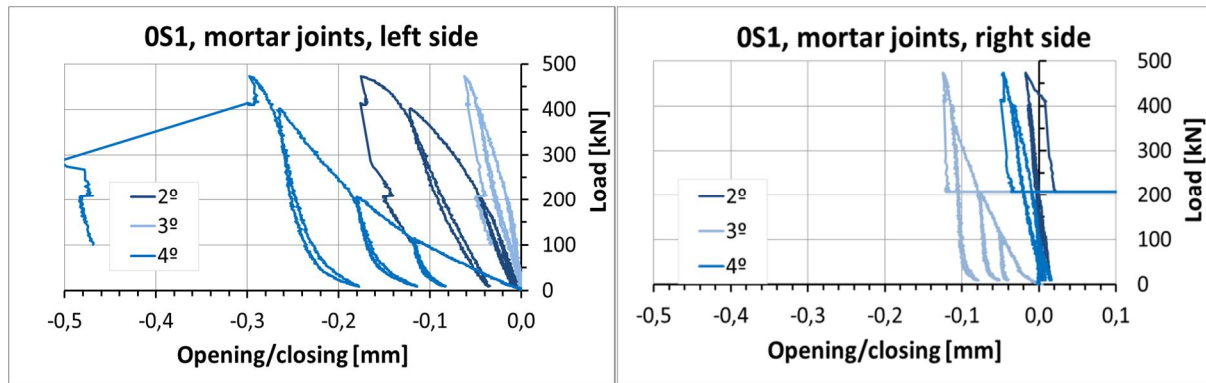


Figure 17: Six-brick column OS1, local displacements measured above the 3 central mortar joints on the left and right side

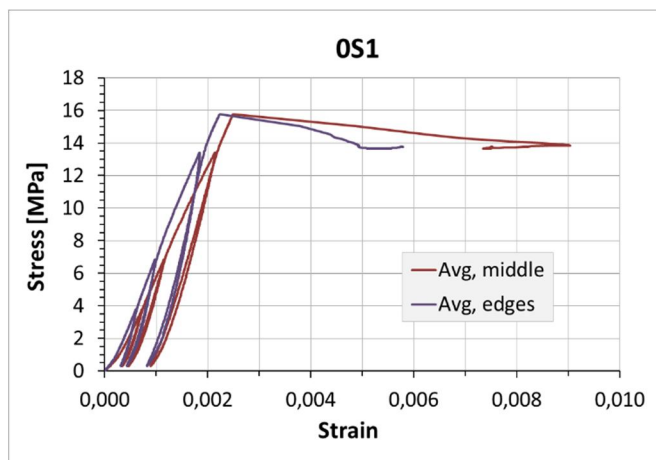


Figure 18: Six-brick column OS1, stress-strain evolution

Table 4: Six-brick column OS1, main mechanical parameters determined from the concentric compression test

	e [mm]	N_{max} [kN]	f'_c [MPa]	f_c^{PP} [MPa]	f'_t [MPa]	E [MPa]		$\epsilon_{0.4f'_c}$ [%]		ϵ'_m [%]
						LVDTs	DIC	LVDTs	DIC	LVDTs
OS1	0	473.30	15.78	/	/	9633	/	0.15	/	0.25

9.3.2. Six-brick column 4S1, concentric load ($e=0$)

Mechanical results

The six-brick column 4S1 was tested under concentric compression load, as the previous one. The only difference lied on the starting health-state condition because, in this case, the specimen underwent 38 ageing cycle before being subjected to the mechanical test. Moreover, as the test was also monitored by DIC, only 4 vertical LVDTs were employed instead of 6 (Figure 19).

The load application was performed by means of 6 load-unloading cycles, with two cycles of settlements, reaching a maximum load of approx. 603 kN, greater than what recovered for the

undamaged six-brick column 0S1 (Figure 20). Actually, in this case the full scale of the testing machine was reached, without reaching the complete collapse of the masonry column.

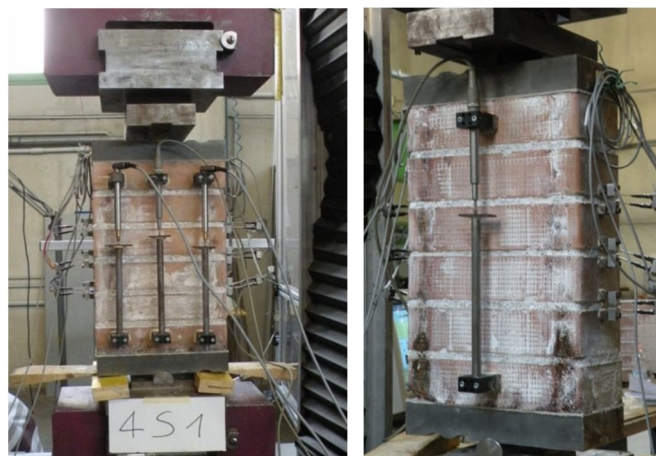


Figure 19: Six-brick column 4S1, test setup: front (left) and rear side (right)

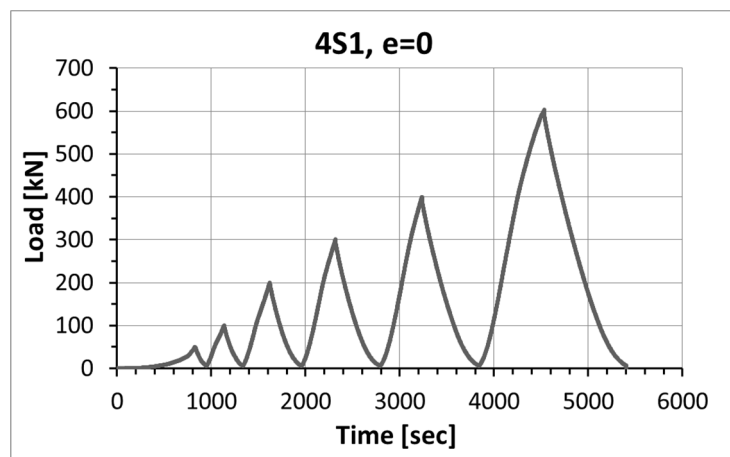


Figure 20: Six-brick column 4S1, load-time history graph

As in the previous test, the load-displacement graphs were visualized both with reference to the two central LVDTs and the two devices positioned near the edges (Figure 21). The variations of global displacement indicated a rather elastic behaviour of the masonry, almost until the collapse. While the curves obtained by the two LVDTs positioned under the load application point are almost coincident, measuring a maximum displacement of approx. 3mm, a difference is recovered between the LVDT near the left side (max. displacement 2.5 mm) and near the right side (max. displacement 3mm). Being this difference not so accentuated, it is possible to say, that overall the behaviour of this six-brick column was symmetric, as expected. This confirms that the choice to use a high-density cardboard sheet instead of the neoprene sheet was correct.

From the visual inspection performed during the test, it was found that the masonry specimen did not suffer major damages instead it remained almost intact for the first five

loading/unloading cycles. Only during the last cycle some vertical cracks appeared, both on the front and rear side of the column (Figure 22).

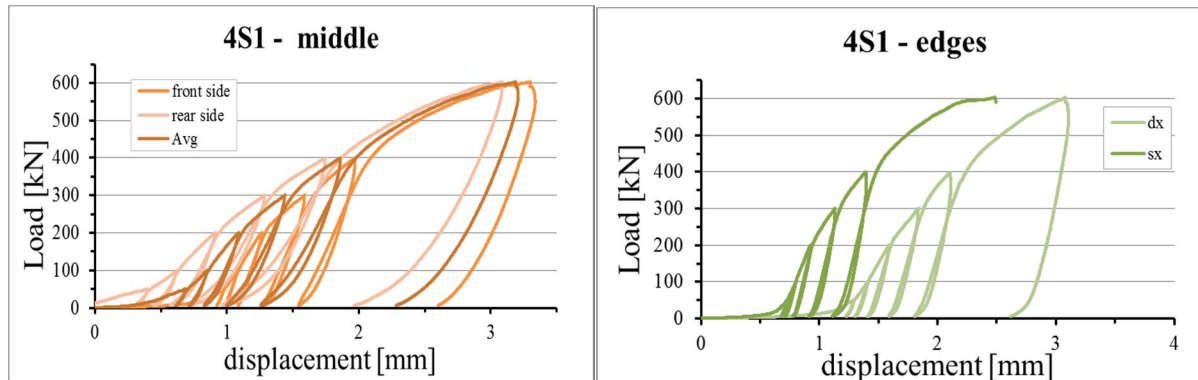


Figure 21: Six-brick column 4S1, load displacement graphs recorded by the two LVDT under the load application point (left) or near the edges (right)



Figure 22: Six-brick column 4S1: details of the crack pattern appeared on the front (left) and rear side (right)

In this case, of the 6 TMLs devices installed only 4 were reliable for all the test duration. Indeed, the supporting base of the one measuring the movement of the 2^o joint on the right side fell down few instants after the beginning of the tests and a detachment of the base of the *omega* above the 3^o joint on the same side was detected during the last loading cycle. Anyhow the data recovered by the other 4 TMLs devices, denoted a certain regularity and symmetry of the masonry behaviour as all of them were compressed and reached almost the same maximum values, between 0.4 and 0.5 mm (Figure 23).

Then, the values of stress were calculated according to eq. 9.1, the strains determined by dividing the displacements recorded by each LVDT for the correspondent initial length and the stress-strain diagrams displayed (Figure 24). The maximum compressive strength was equal to 20.34 MPa and the maximum averaged strain was about 1%.

From the last cycle of the stress-strain diagram recovered by the two central LVDTs was then calculated the modulus of elasticity, obtaining a value of approx. 6800 MPa (Figure 25).

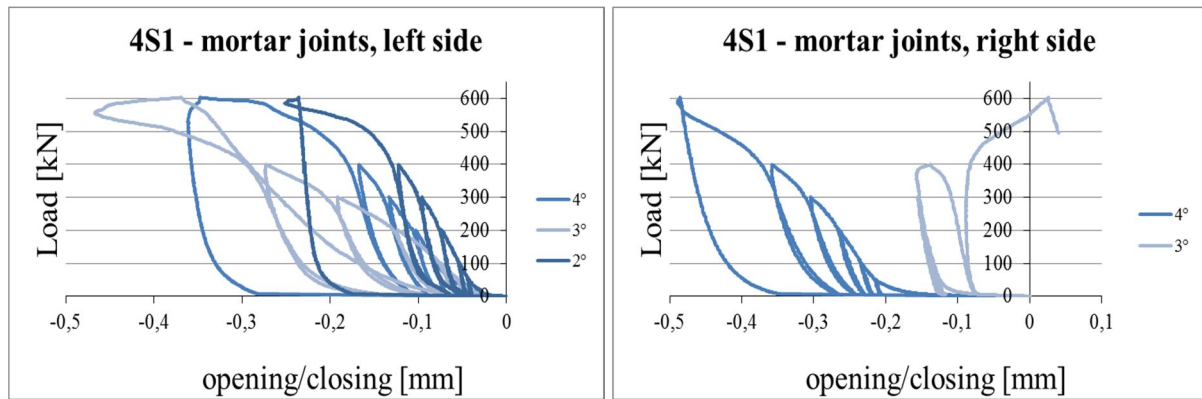


Figure 23: Six-brick column 4S1, displacements recovered on the mortar joints

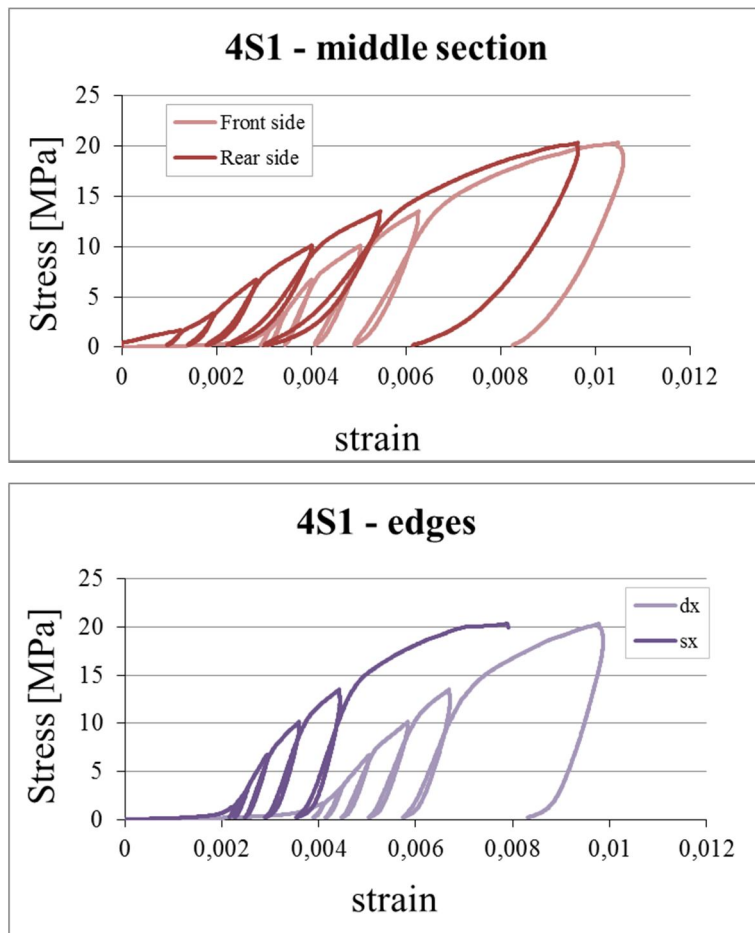


Figure 24: Six-brick column 4S1: resulting stress-strain graphs

Table 5: Six-brick column 4S1, main mechanical parameters

	e [mm]	N_{max} [kN]	f'_c [MPa]	E [MPa]	$\epsilon_{0,4f'_c}$ [%]	ϵ'_m [%]
				LVDTs	LVDTs	LVDTs
4S1	0	602	20.32	6811	0.386	1.00

DIC results: data visualization and analysis

One main face of this damaged six-brick column, the rear side, was monitored by means of the digital image correlation throughout the concentric compression test. The data analysis was performed at the end of the mechanical test, following the procedure described in 9.2.1.

Thus, first of all, the area of interest, which is the area to be analysed, was defined and some starting points added, near the obstacles (LVDT and cables covering portion of the surface under investigation) in order to not lose data during the data analysis phase (Figure 25).

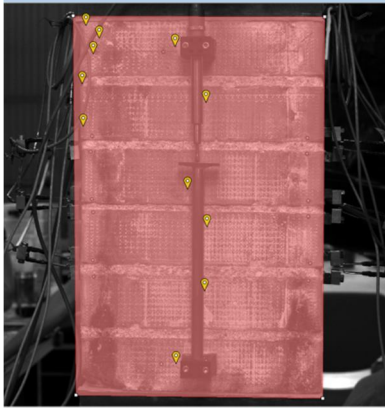


Figure 25: Six-brick column 4S1: AoI (in red) and starting point (in yellow)

As it was a concentric compression test, greater attention was paid to the deformations that occurred in the vertical direction that is in the direction of load application. The variations of the vertical strains at increasing load levels, in detail at the end of each loading/unloading cycle are reported in Figure 26, Figure 27, as coloured maps superimposed to the deformed digital images.

At the beginning of the test, before the application of the load, the strains are null everywhere whilst since the end of the 1st load cycle a certain compression state is detected. This state was greater in the mortar joints than in the brick units, since the beginning, and naturally increased with increasing loads. The deformation state appeared symmetric both with reference to the hypothetical vertical axis and the horizontal one coherently to the type of load test. Actually, not all the mortar joints behave in the same manner: until approx. 300 kN the same compression strains are recorded in all the joints while after that, the 1°, 3° and 5° joints appeared more compressed. On the other hand, the bricks appeared almost not compressed at all. Thus, this non-destructive monitoring technique was able to differentiate the behaviour of the two masonry constituent materials.

Moreover, these maps underlined a certain level of compression at the contact points that is at the interfaces between the top (or bottom) brick and corresponding load distribution plate.

The maps of the horizontal strains (in the direction perpendicular to the load application) at different load levels are also reported for completeness (Figure 28). Also in this case, the deformation state was completely null at the beginning of the test. During the application of the load, some strains in this direction were visible although of very small entity, according to

the type of test. Only during the last loading cycle, that is after the formation of the first cracks an appreciable deformation state is visible in the central part of the column.

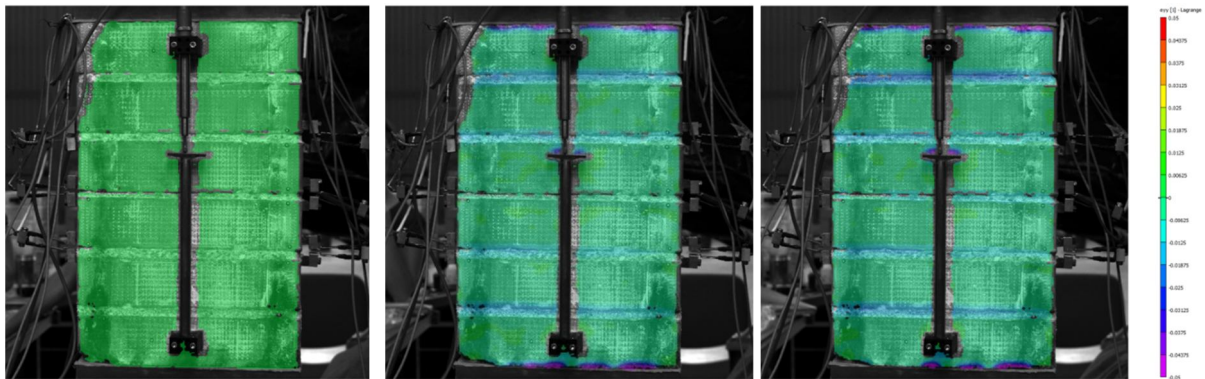


Figure 26: Six-brick column 4S1: vertical strain before the load application (left), at the end of the 2nd loading cycle (centre) and at the end of the 3rd loading cycle (right)

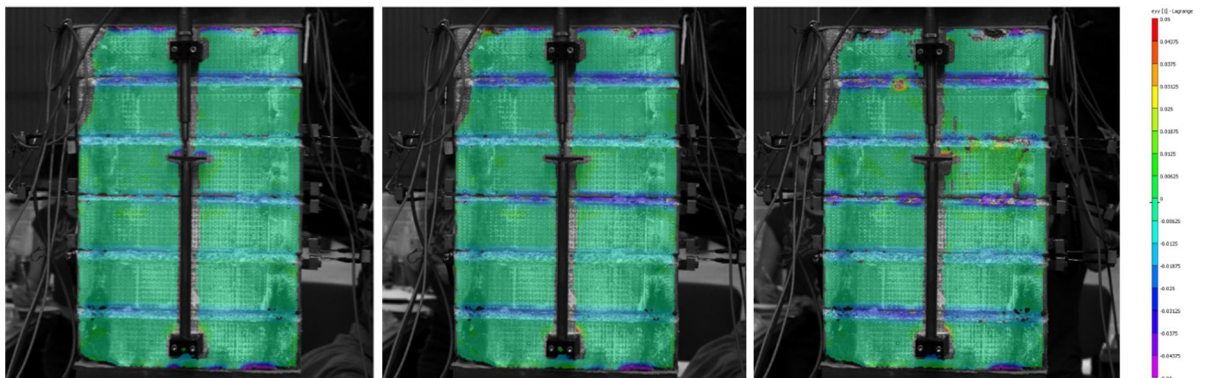


Figure 27: Six-brick column 4S1: vertical strain at the end of the 4th (left), 5th (centre) and 6th loading cycle (right)

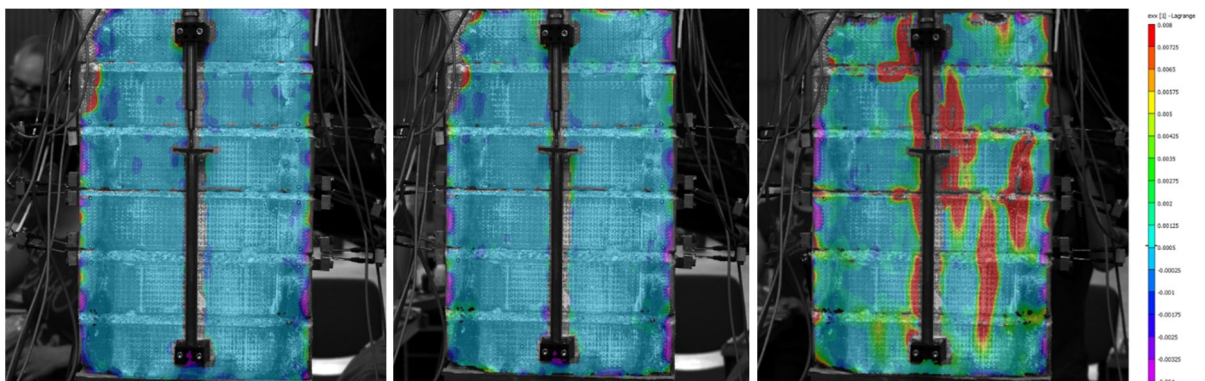


Figure 28: Six-brick column 4S1: horizontal strains at the end of the 1st, 3rd and 6th loading cycle

Finally, in the post-processing phase, in order to evaluate the accuracy of the simplified DIC procedure adopted in quantifying the behaviour of masonry under compression, a SW tool, virtual extensometer was employed. This was positioned, thanks to the additional markers, near the central LVDT and used to recover a stress-strain graph (Figure 29, Figure 30).

Qualitatively the trend of the stress-strain branches recorded with this virtual tool is similar to those recovered via the traditional wired measuring tools. Quantitatively, in terms of maximum deformations as well as modulus of elasticity, the results are comparable (Table 6). Some slight differences depended on the not exact correspondence of the position of these two devices.

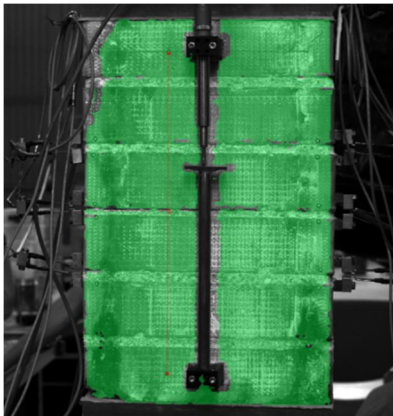


Figure 29: Six-brick column 4S1, location of the virtual extensometer, near the wired LVDT

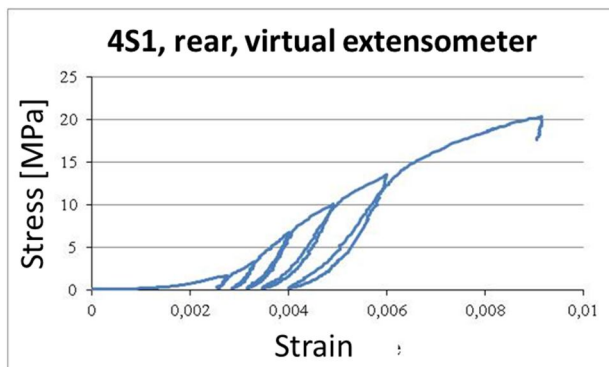


Figure 30: Six-brick column 4S1: stress-strain graph obtained from the DIC extensometer

Table 6: 4S1: main mechanical parameters, comparison between values obtained via LVDTs and DIC

	e [mm]	N _{max} [kN]	f' _c [MPa]	E [MPa]		ε _{0.4f'_c} [%]		ε' _m [%]
				LVDTs	DIC	LVDTs	DIC	LVDTs
4S1	0	602	20.32	6811	4351	0.386	0.432	1.00

9.3.3. Six-brick column 4S2, eccentric load (e=40)

Mechanical results

The six-brick column 4S2 belongs to the same series of the previous masonry specimen, and thus it suffered 38 ageing cycles before undergo the mechanical test, which was also monitored via DIC. Thus, the testing equipment and set-up were equal to those of 4S1. In this case, however, the compression load was applied with an eccentricity, e , of 40 mm ($e/d \cong 1/6$). Six load/unload cycle were performed, at increasing load levels, until the failure of the specimen at approx. 450 kN (Figure 31).

Both the two central LVDTs underwent to compression, although the displacements recorded from the LVDT on the masonry front face (1.8 mm) were almost twice as those recorded in the rear face (approx. 0.8 mm). As the load was applied at 40 mm from the centre line, towards right, the transducer locate near the right edge recorded the maximum displacements, almost 2.5 mm; on the contrary the LVDT positioned near the left edge of the brick column, registered, as maximum value of vertical displacements, only 1 mm (Figure 32).

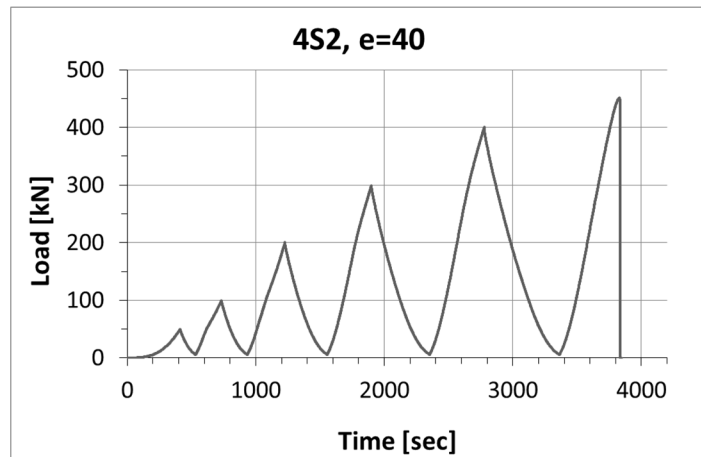


Figure 31: Six-brick column 4S2: load-time history

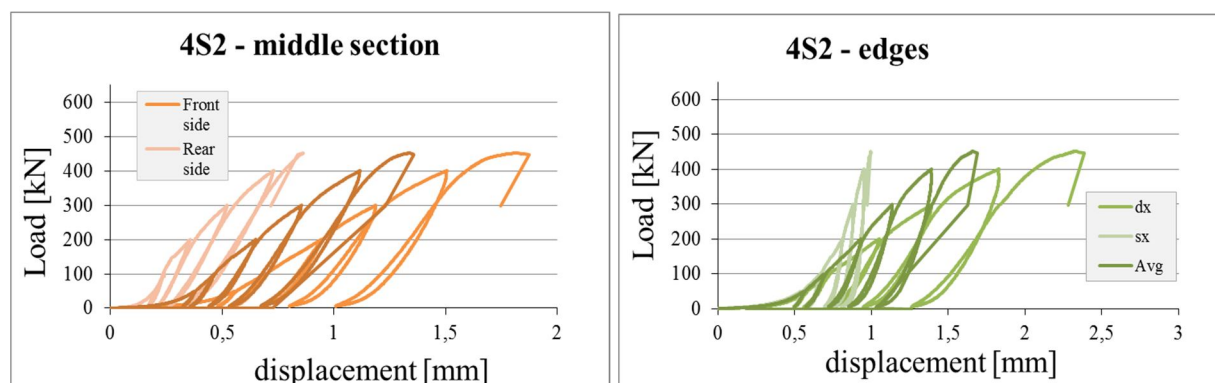


Figure 32: Six-brick column 4S2, load displacement graphs recorded by the two LVDT under the point of load application (left) or near the edges (right)

The not-symmetrical behaviour between the left and right side of the specimen, due to the type of compression test, is underlined by the opening/closing of the mortar joints (Figure 33). Indeed, the mortar joints' displacements recorded from the right side, nearest to the load application point were always negative that means that they were all in compression. The maximum "closing", approx. equal to 0.5 mm, was recorded for both the 2° and 4° mortar joints. On the left side, only two TMLs remained active until the end of the test. It seemed that the 2° mortar joint was compressed and the 3° one in traction, although the movements recorded were of very small entity (near 0.15 mm).

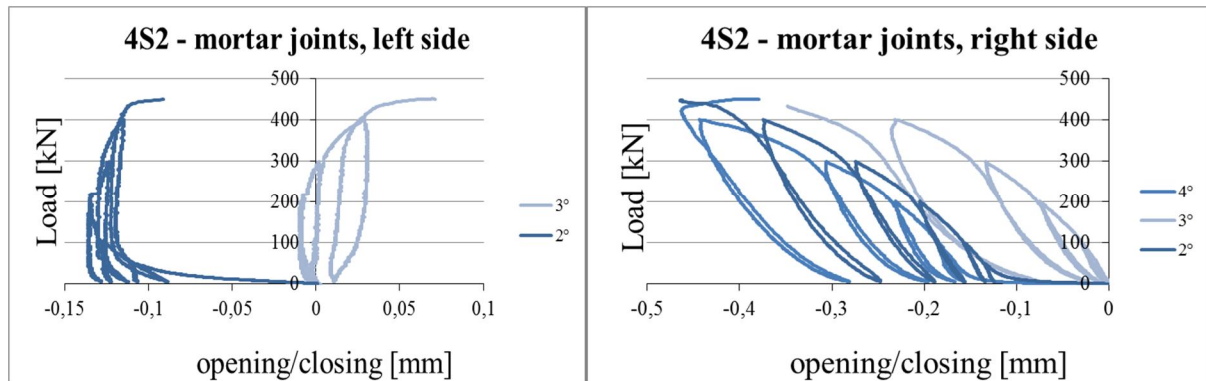


Figure 33: Six-brick column 4S2, movements of the mortar joints, recorded by means of TMLs device

Later, from the values of load, the stresses were calculated taking into account the contribution of the moment due to the eccentricity of the load, according to (eq. 9.2), and obtaining a maximum of 30 MPa. The compressive strains were determined as before, recording a maximum near the right edge of the six-brick column, of about 0.77 %.

Moreover, by using the eq. 9.4, and thus, not neglecting the tensile contribution of masonry, the maximum compressive strength in correspondence of the load application point was determined, obtaining a value of approx. 20 kN.

Finally the stress-strain graphs were visualized (Figure 34) and the modulus of elasticity calculated (Table 9).

Table 7: Six-brick column 4S2, $e=40\text{mm}$, main mechanical parameters

	e [mm]	N_{\max} [kN]	f'_c [MPa]	f_c^{pp} [MPa]	E [MPa]	$\epsilon_{0.4f'_c}$ [%]	ϵ'_m [%]
					LVDTs	LVDTs	LVDTs
4S1	40	451.34	30.39	20.26	10100	0.303	0.74

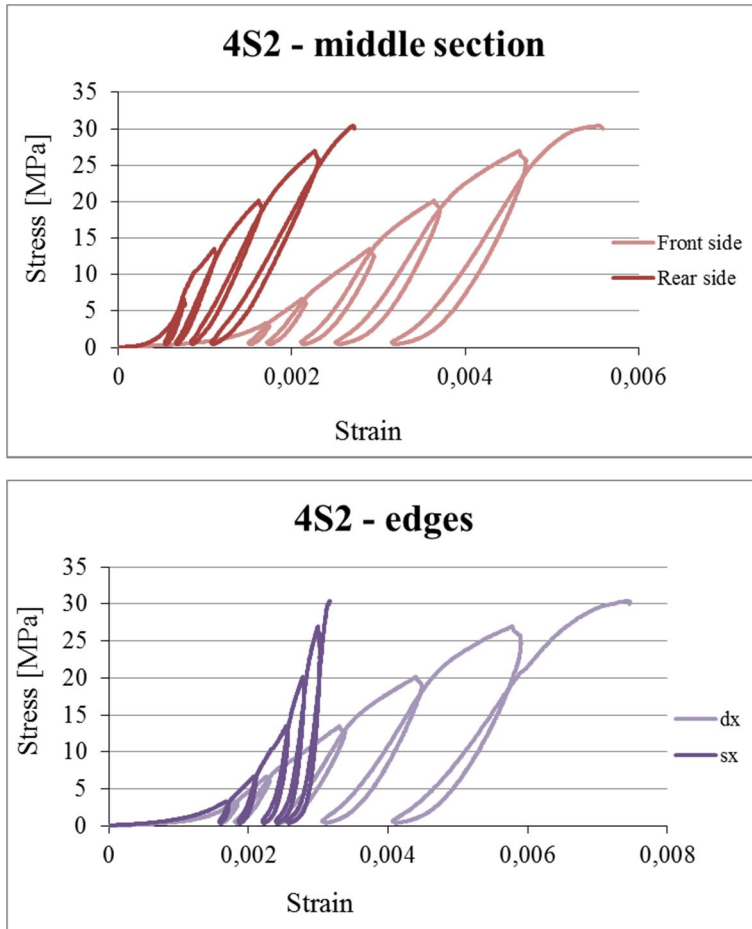


Figure 34: Six-brick column 4S2, stress-strain diagrams

DIC results: data visualization and analysis

The DIC data analysis and visualization was performed as in the previous case (4S1), by individuating the area of interest on which perform the analysis, placing the starting points (Figure 35) and, at the end of the SW image elaboration, remove the rigid motion eventually occurred.

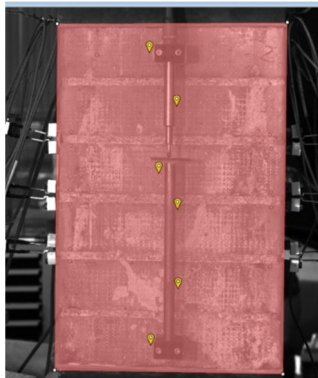


Figure 35: Six-brick column 4S2, AoI and starting points

Since also this was a compression test, main attention was paid to the vertical displacement (direction of load application) and corresponding strains. Thus, coloured maps superimposed to the deformed images representing the variation of strains in the vertical direction, were visualized from the beginning of the test, at increasing load levels, using the same coloured legend (Figure 36, Figure 37).

Prior to starting the test, the deformation was null everywhere. A compression state appeared just after the first loading cycle but, since the end of the 2^o, it was visible only on the 2^o and 4^o mortar joints while the other horizontal joints and the bricks appeared almost undeformed. The compression state of these joints increased at the end of the third load cycle, in which we note also a slight compression in the upper part of the 6th brick, which is in contact with the superior load distribution steel plate.

At the end of the fourth loading cycle, all the mortar joints resulted compressed, although this deformation state was still more accentuated in the external joints. At this load level, a non-symmetrical behaviour between the left and right side of the specimen started to become evident, both on the mortar joints and on the bricks and a greater compression on the right side of the specimen, where the load was applied, compared to the left one was detected. Note that the “specimen right side” is visible on the left side of the images which are referred to the rear side of the brick column. At the end of the sixth loading cycle, at the maximum load, this asymmetrical behaviour is also more evident and the greatest compression state of the mortar joints of the side of load application was recorded. Some local traction states were also visible, especially on the 6th brick due to the exfoliation of the surface in these points (Figure 37 right).

On the contrary, the deformation state along the horizontal direction was almost null for whole the test duration; only at the end of the last loading cycle, a limited, localized traction state was visible in the upper left corner of the specimen (Figure 38).

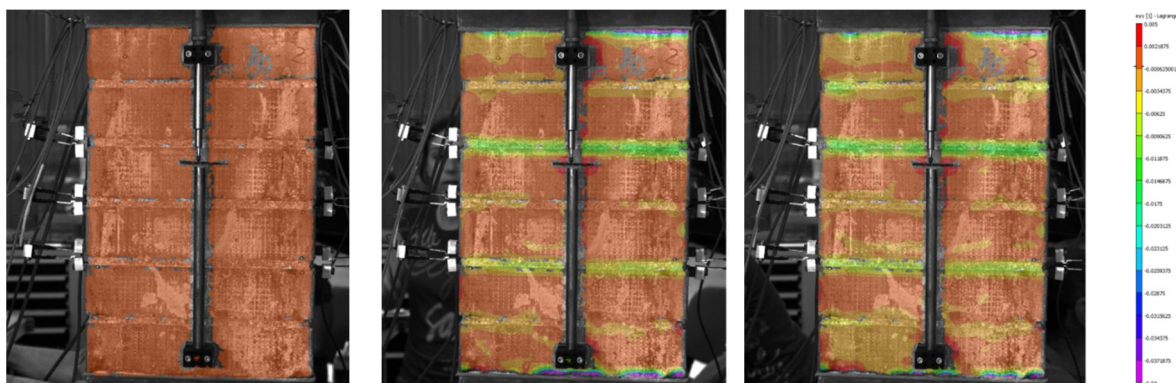


Figure 36: Six-brick column 4S2 ($e = 40$ mm): maps of vertical strain before the load application (left), at the end of the 2nd loading cycle (centre) and at the end of the 3rd loading cycle (right)

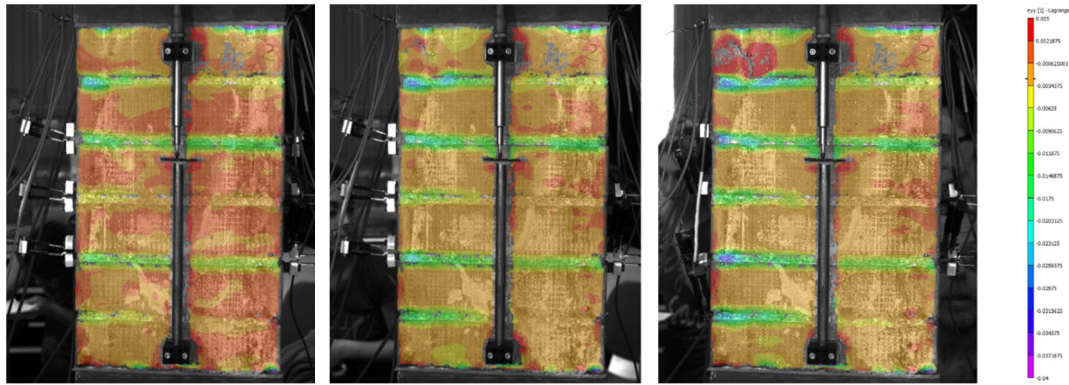


Figure 37: Six-brick column 4S2 ($e = 40$ mm): maps of vertical strain at the end of the 4th (left), 5th (centre) and 6th and last loading cycle (right)

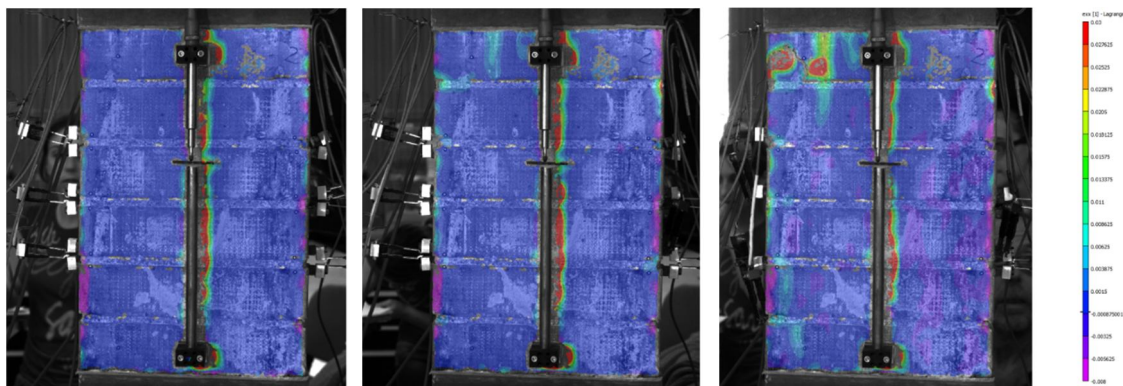


Figure 38: Six-brick column 4S2 ($e=40$ mm), maps of horizontal strains at the end of the 2nd, 4th and 6th (last) loading cycle

After the visualization of the strain maps, a SW post-processing tool, virtual extensometer, was used to quantify the deformations on a particular position, under the load application point, recover the stress-strain diagram and calculate the modulus of elasticity (Figure 39).

The main mechanical parameters calculated traditionally or by means of DIC virtual extensometers are comparable despite some numerical differences (underestimation of E and deformations) which are in the range of measurement accuracy (Table 8).

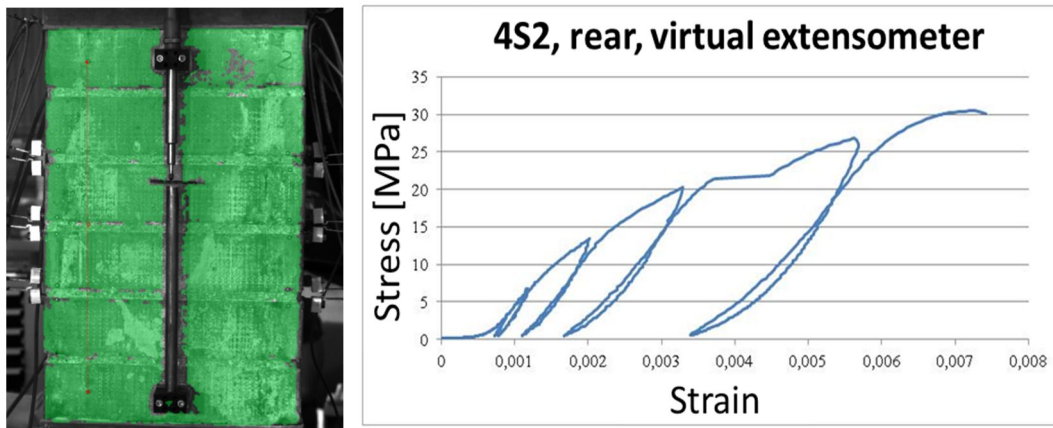


Figure 39: Six-brick column 4S2, ($e=40$ mm): position of a virtual extensometer (left) and corresponding stress-strain graph (right)

Table 8: 4S2: main mechanical parameters, comparison between mechanical values obtained via LVDTs and DIC

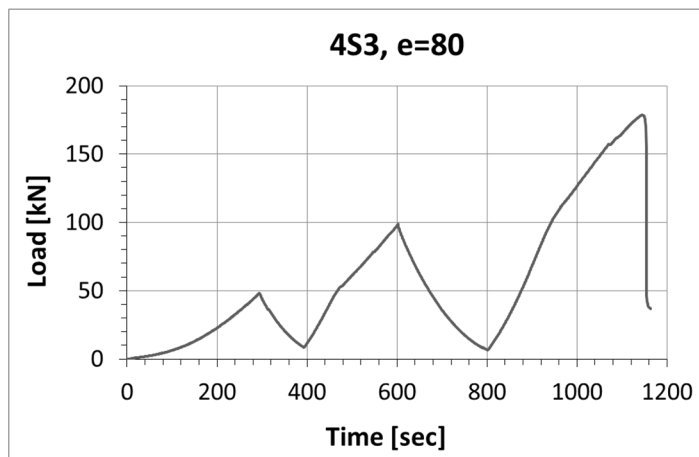
	e [mm]	N _{max} [kN]	f' _c [MPa]	f _c ^{pp} [MPa]	E [MPa]		ε _{0.4f'_c} [%]		ε' _m [%]
					LVDTs	DIC	LVDTs	DIC	LVDTs
4S2	40	451.34	30.39	20.26	10100	9587	0.303	0.184	0.74

9.3.4. Six-brick column 4S3, eccentric load (e=80)

Mechanical results

As a last example, in the following are reported the results of the eccentric compression test carried out on the six-brick column 4S3, where the load was applied with the maximum eccentricity, $e=80$ mm ($e/d > 1/6$).

In this case, only three cycles of loading/unloading were performed as the collapse of the specimen was reached at approx. 180 kN, which is a value two or three times lower than what recorded for the six-brick columns 4S1 and 4S2 (Figure 40).

**Figure 40:** Six-brick column 4S3 (e=80mm), load-time history

The displacements measured by the four vertical LVDTs were plotted against the applied load, as in the previous case (Figure 41). Both the two central LVDTs were compressed almost for the all duration of the test, although an inversion in this tendency was recorded after 100 kN. Instead, the two LVDTs near the edges reacted in a completely different manner: while the device on the rear side (positioned below the load application point) was compressed, the one on the left side was subjected to traction, since the beginning of the test, although this behaviour was more evident at approx. 100 kN. At the maximum load, the values of displacement recorded by these two lateral devices were similar, although opposite in sign. This behaviour is in accordance to the type of compression test performed.

This asymmetrical behaviour (with reference to the vertical axis) was also underlined by the measurement devices installed above the mortar joints. Indeed, a closing tendency was recorded for the three mortar joints of the right side, where the load was applied, while the three joints of the left side were opening (Figure 42).

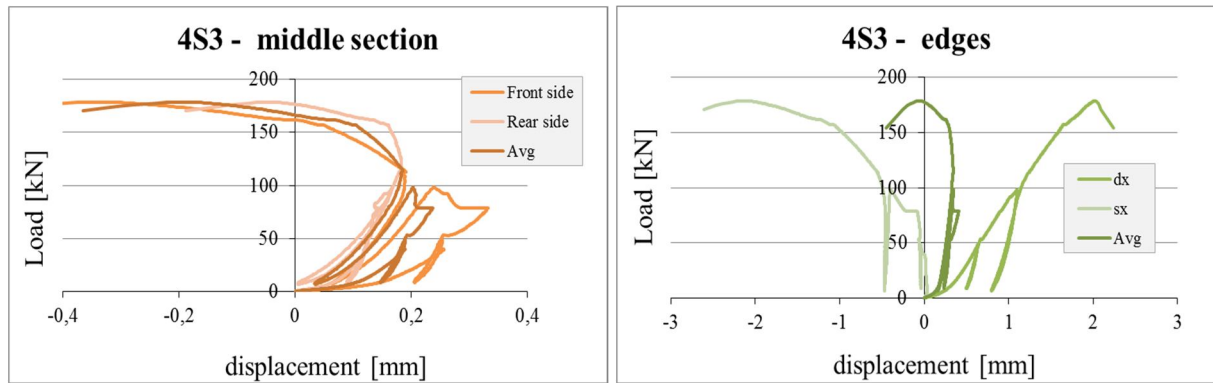


Figure 41: Six-brick column 4S3 ($e=80\text{mm}$) load displacement graphs recorded by the two LVDTs under the load application point (left) or near the edges (right)

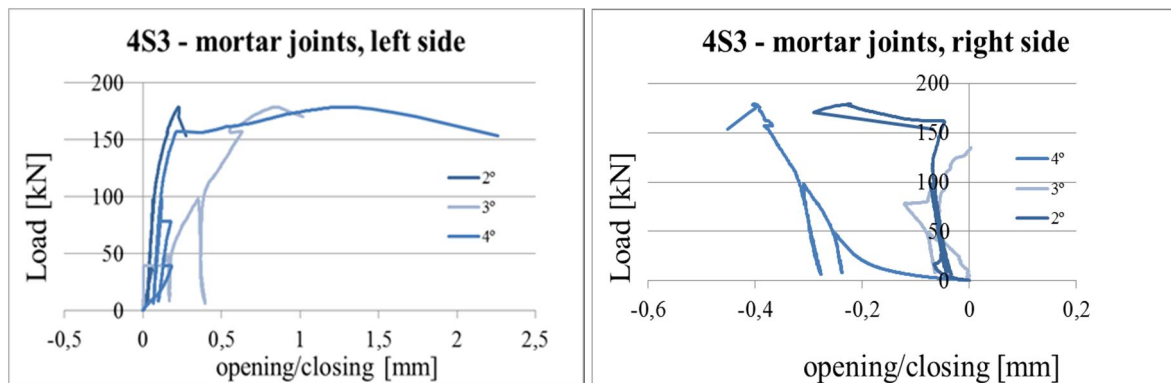


Figure 42: Six-brick column 4S3 ($e=80\text{mm}$), displacements recovered on the mortar joints

The collapse type of this six-brick column appeared also visually evident. In the first two load cycles no cracks appeared while, at about 150 kN, vertical cracks below the load application point were visible both on the front and rear side of the specimen. These cracks were accompanied by the progressive opening of the mortar joints far away from the load application point, which caused, at the end of the test, the detachment of the mortar/brick interfaces in correspondence of the 4th mortar joint (Figure 43).

Anyhow, also in this case, the stress-strain graphs were determined. The values of stresses were firstly determined according to (eq. 9.3), neglecting the tensile contribution of masonry and later, by means of the more general, less simplified eq. 9.4, in order to evaluate the compressive stresses under the load application point as well as the tensile stresses on the opposite side (Figure 44).

Finally, the values of the main mechanical parameters, i.e. maximum compressive strength, tensile strength, modulus of elasticity, etc. were summarized in Table 9.



Figure 43: Six-brick column 4S3 ($e=80$ mm) at the end of the compression test: front (left) and rear side (right). Vertical cracks below the load application point are very evident as well as the mortar joints opening (with detachment from the brick faces) on the opposite side

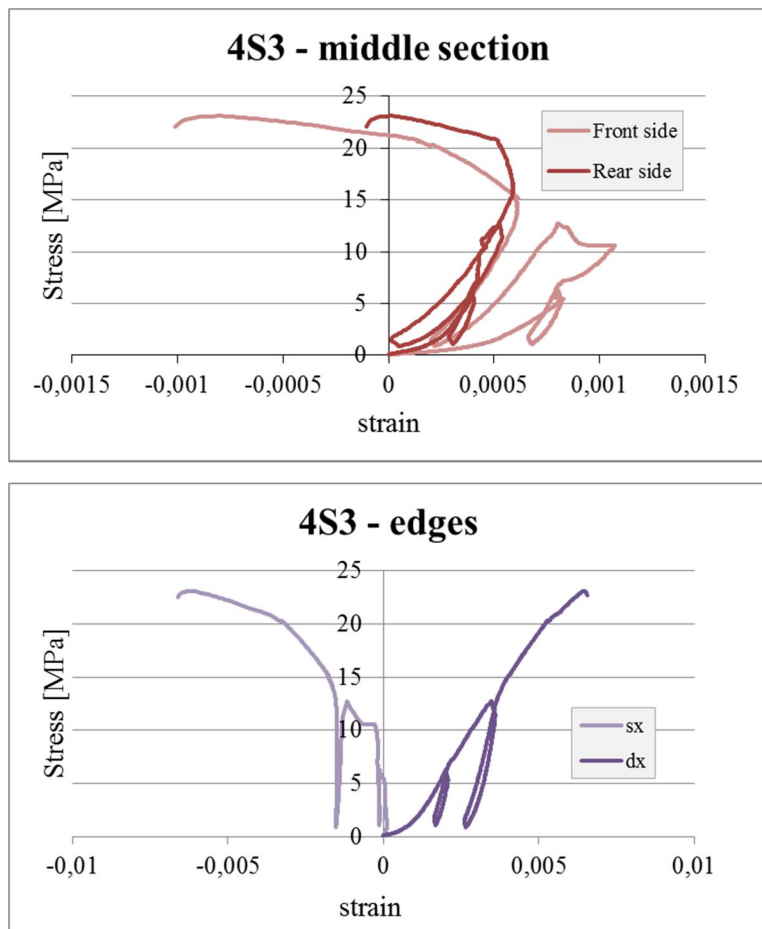


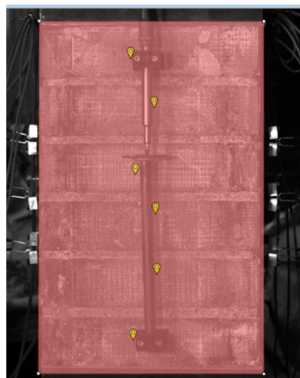
Figure 44: Six-brick column 4S3, resulting stress-strain graphs

Table 9: Six-brick column 4S3 (e=80mm): mechanical results

	e [mm]	N _{max} [kN]	f' _c [MPa]	f ^{pp} _c [MPa]	f' _t [MPa]	E [MPa]		ε _{0.4f'_c} [%]		ε' _m [%]
						LVDTs	DIC	LVDTs	DIC	LVDTs
4S3	80	178.75	23.09	13.74	5.76	6680	/	0.265	/	0.64

DIC results: data visualization and analysis

Analogously to what was performed and explained for the previous six-brick columns (4S1 and 4S2) the sequence of DIC images was analysed after the proper selection of the area of interest (Figure 45).

**Figure 45:** Six-brick column 4S3, AoI and starting points

First of all, the variation of the strains in the vertical direction are displayed as coloured maps (Figure 46, Figure 47). Also in this case, the deformation state at the beginning of the test was null. Then and since the end of the 1st loading cycle, a different state between the left and right side of the specimen was visible, in fact, the part below the load application point was compressed, while the other showed a certain traction state. These strains are, again, more accentuated on the lime mortar joints than on the bricks as the mortar joints are more deformable than the fired-clay bricks composing the six-brick column investigated.

At the end of the second cycle, the different behaviour between the left and right side was more evident and involved all the mortar joints. This difference continued to increase at increasing loading. At the beginning of the 3rd cycle, some vertical crack were detected and at the end of the test, these had caused the detachment of brick portions. On the opposite side, the detachment at the brick/mortar interface of the 4th mortar joint was recorded, as previously seen in the photographs.

The maps of horizontal strains were also visualized at increasing load levels. At the beginning and until about 150 kN were almost null (Figure 48) while later, some appreciable values were detected near the detached areas (Figure 49).

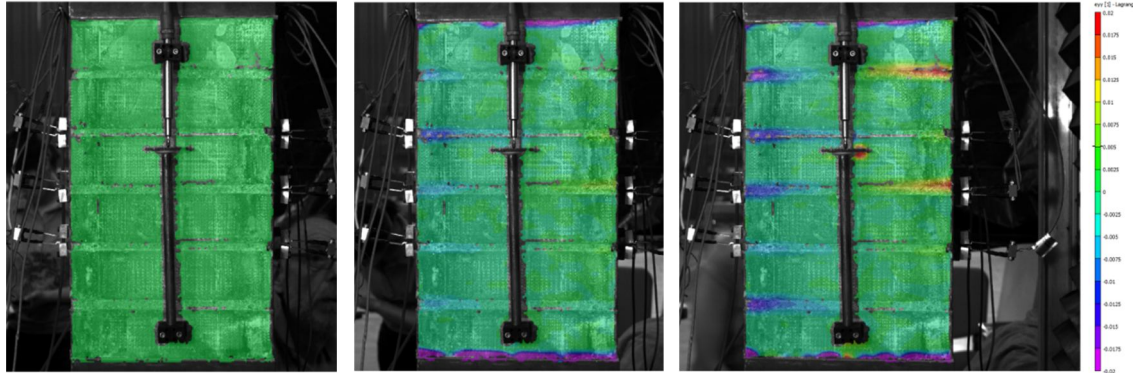


Figure 46: Six-brick column 4S3 ($e=80$ mm): maps of vertical strains at the beginning of the test (left), at the end of the 1st (centre) and 2nd (right) loading cycle

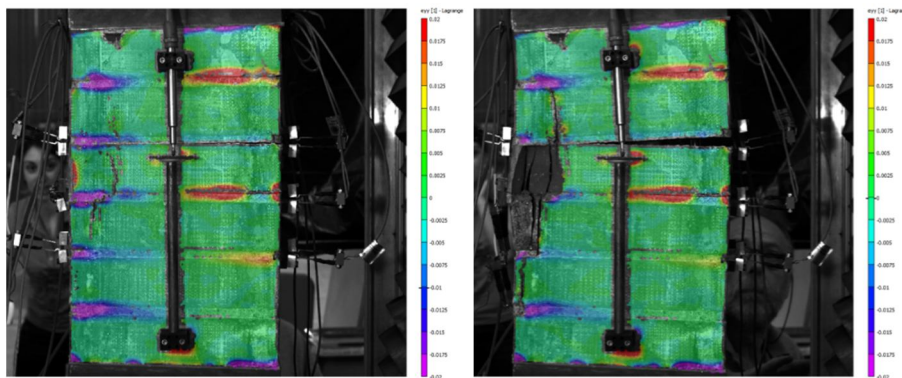


Figure 47: Six-brick column 4S3 ($e=80$ mm): maps of vertical strains at the beginning of the 3rd cycle (left) and at the end of the test (right)

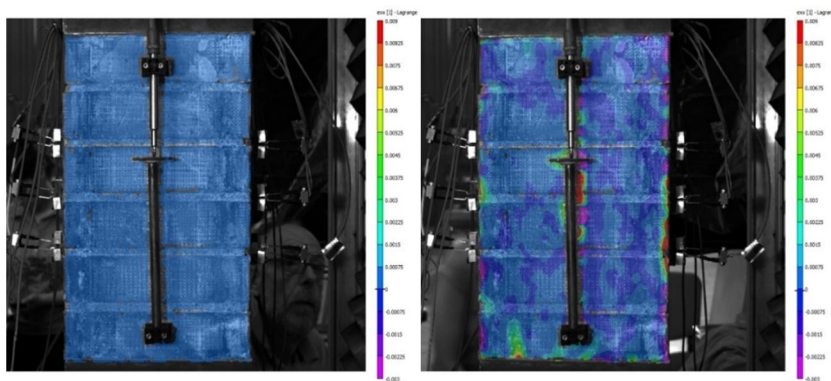


Figure 48: Six-brick column 4S3 ($e=80$ mm): maps of horizontal strains at the beginning of the test (left) and at the end of the 2nd load cycle (right)

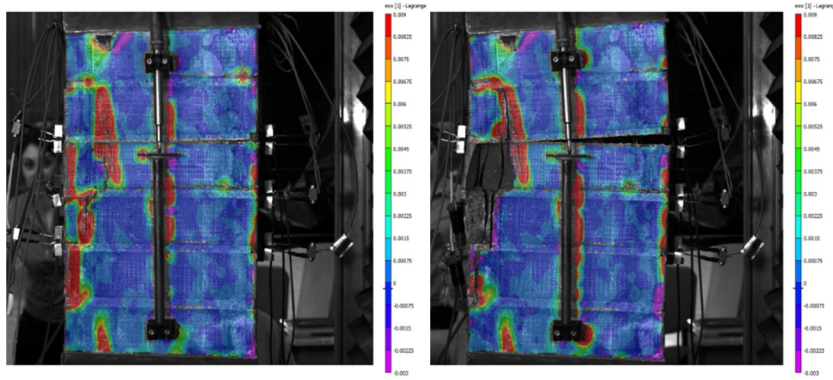


Figure 49: Six-brick column 4S3 ($e=80$ mm): maps of horizontal strains at the beginning of the 3rd cycle (left) and at the end of the mechanical test (right)

Finally, the virtual extensometer was positioned in correspondence of the load application point. Thanks to this SW tool, the stress strain graph in this position was determined and the main mechanical parameters calculated for comparison to those recorded by traditional LVDTs (Figure 50, Table 10), obtaining a good agreement.

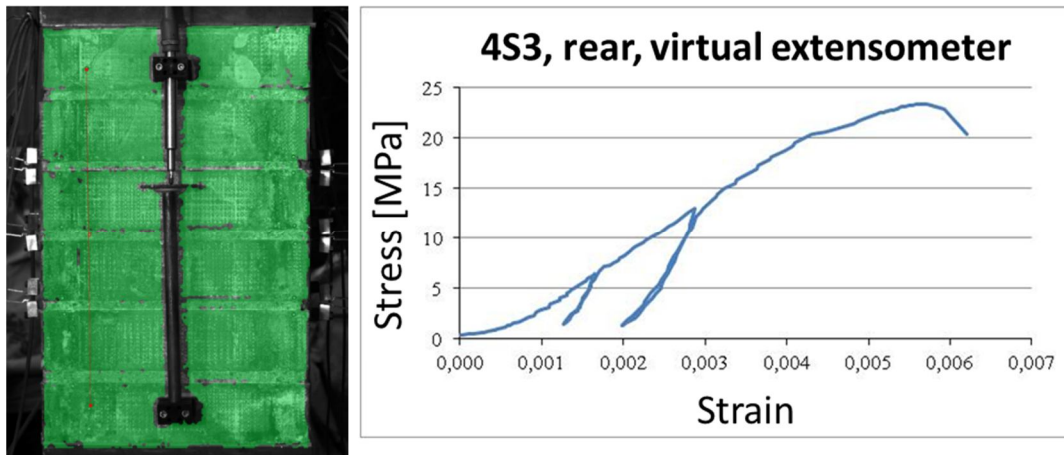


Figure 50: Six-brick column 4S3 ($e=80$ mm): position of the virtual extensometer and recovered stress-strain diagram

Table 10: 4S3: main mechanical parameters, comparison between mechanical values obtained via LVDTs and DIC

	e [mm]	N _{max} [kN]	f' _c [MPa]	f' _c ^{pp} [MPa]	f' _t [MPa]	E [MPa]		ε _{0.4f'_c} [%]		ε' _m [%]
						LVDTs	DIC	LVDTs	DIC	LVDTs
4S3	80	178.75	23.09	13.74	5.76	6680	5190	0.265	0.225	0.64

9.4. Compression tests: discussion of results and comparison

The main mechanical parameters determined by means of traditional wired measurement systems and/or the non-destructive monitoring technique employed are reported in this paragraph for all the six-brick columns of the four series.

The results are summarized in two tables for each series of column, one reporting the values of compressive strength, modulus of elasticity and vertical deformations as well as the values of tensile strength for the eccentric compression tests. Instead, the second summarised the maximum movements of the mortar joints, measured via TMLs devices, in terms of opening/closing.

First of all, the results obtained for the series, 0, that is for the specimens in as-built conditions are reported (Table 11, Table 12). These values are later used as reference values to compare those obtained for similar six-brick columns but subjected to numbers of accelerated ageing cycles.

The concentric compression tests on the brick columns belonging to the 0 series revealed a masonry of good quality as high values of compressive strength were obtained. This aspect was then confirmed by the high values of the same parameters measured during two types of eccentric compression tests. The values of compressive strength calculated are higher than what expected from the mechanical properties of the single masonry constituent materials (§4.2). The theoretical relationships between the compressive strength and the modulus of elasticity reported by the main international standards for the design of new masonry structures (equal to $E=1000f'_c$ [NTC 2008] o $E=600f'_c$ [ASTM]) was not verified, according also to other experimental studies carried out on similar solid brick columns (Brencich 2008). In this case, indeed, the relation which may related the Young's modulus with the compressive strength is approx. $E=500f'_c$.

Table 11: Series 0, six-brick columns in as-built conditions: main mechanical parameters obtained from the compression tests

	e [mm]	N _{max} [kN]	f' _c [MPa]	f' _c ^{PP} [MPa]	f' _t [MPa]	E [MPa]		ε _{0.4f'_c} [%]		ε' _m [%]
						LVDTs	DIC	LVDTs	DIC	LVDTs
0S1	0	473.30	15.78			9633	/	0.15	/	0.25
0S3	0	413.49	13.78			3715	919	0.518	0.63	1.11
0S6	0	603.07	20.1			12052	8119	0.11	0.119	0.35
0S2	40	218.48	28.26	18.21		12492	/	0.56	/	0.57
0S5	40	510.61	33.36	22.25		13848	3379	0.264	0.546	0.00
0S8	40	539.51	35.25	23.51		4374	9416	0.074	0.155	0.47
0S4	80	279.61	34.52	20.77	8.57	20332	8109	0.113	0.254	0.40
0S7	80	354.71	43.79	26.35	10.87	14063	7916	0.079	0.183	0.30

In terms of maximum load, on average there is a reduction with the increasing load eccentricity, due to the fact that a portion of the masonry is subjected to tensile stresses. This evidence is not respected in the values of maximum compressive strength, which increased with the load eccentricity. Anyhow, this tendency is in absolute not correct as it depends upon the simplified constitutive model used to study the behaviour of masonry as demonstrated by other authors (Brencich 2008).

The maximum values of opening/closing of mortar joints recorded during the eccentric load tests, were very variable, ranging from 0.02 to 0.59 mm, and they were always detected in different position on the left and right side, meaning a non-perfect symmetry with respect to the vertical axis (Table 12).

Table 12: Series 0, six-brick columns in as-built conditions, subjected to eccentric compressive loads: average behaviour of the mortar joints measured by wired “omega”

	e [mm]	Ω [mm]		Notes
		opening	closure	
0S2*	40	0.59	-0.39	4° joint sinix, 2° joint dx
0S5	40	0.10	-0.87	2° joint sinix, 3° joint dx
0S8	40	0.02	-0.09	4° joint sinix, 3° joint dx
0S4	80	0.49	-0.14	2° joint sinix, 2° joint dx
0S7	80	0.43	-0.12	3° joint sinix, 2° joint dx

Similarly, in Table 13, Table 14 are reported the mechanical parameters determined throughout axial and eccentric load tests for the series 2 of masonry assemblies, that is for columns subjected to 18 cycles of accelerated ageing.

The reduction of the maximum load with the increasing eccentricities of load application was noted. In this case, however, this reduction is more accentuated than in the case of the reference masonries. Indeed, a difference ranging between 19% and 60% versus a reduction of 14% - 36% measured for the undamaged assemblies.

Table 13: Six-brick columns, series 2, 18° ageing cycles: summary of the main mechanical parameters measured

	e [mm]	N_{max} [kN]	f'_c [MPa]	$f'_c{}^{PP}$ [MPa]	f'_t [MPa]	E [MPa]	$\epsilon_{0.4f'_c}$ [%]	ϵ'_m [%]
						LVDTs	LVDTs	LVDTs
2S3	0	555.72	18.52			6021	0.86	1.12
2S4	0	505.89	16.86			8481	0.78	0.90
2S8	0	510.73	17.02			5041	0.97	1.16
2S1	40	369.96	24.17	16.12		21594	0.25	0.35
2S2	40	483.64	31.60	21.07		19115	0.36	0.50
2S6	40	409.68	26.77	17.85		9064	0.01	1.57
2S5	80	214.91	26.53	15.97	6.59	12448	0.31	0.81
2S7	80	197.25	24.35	14.65	6.05	11463	0.37	0.71
2S9	80	200.52	24.76	14,90	6,15	14051	0.51	0.08

The results of the movements of the central mortar joints on both lateral faces (2°, 3° and 4° joints) in terms of opening/closure are reported only with reference to the six-brick columns subjected to eccentric compression tests because not relevant for the concentric tests. In these cases greater values of opening, up to 0.93 mm and closing, until 1.3 mm, with respect to the values determined for the references columns were detected. Moreover, two of the brick column, 2S1 and 2S5, showed a symmetry respect the vertical axis, as the greater opening, associated to the greater closure were recorded for the 3rd mortar joints.

Table 14: Six-brick columns series 2, 18° ageing cycles, subjected to eccentric loads: average behaviour of the mortar joints measured by means of wired “omega”

	e [mm]	Ω [mm]		Notes
		opening	closure	
2S1	40	0.93	-0.72	3° joint sinix, 3° joint dx
2S2	40	0.29	-0.54	3° joint sinix, 2° joint dx
2S6	40	0.04	-0.63	3° joint sinix, 3° joint dx
2S5	80	0.90	-1.27	3° joint sinix, 3° joint dx
2S7	80	0.62	-0.30	2° joint sinix, 4° joint dx
2S9	80	0.93	-0.05	4° joint sinix, 2° joint dx

Similar considerations arose from the data recorded for the specimens belonging to the serie 3 and 4, subjected respectively to 28 and 38 ageing cycles.

See the following Table 15- Table 18.

Table 15: Six-brick columns, series 3, 28° ageing cycles: summary of the main mechanical parameters measured

	e [mm]	N_{max} [kN]	f'_c [MPa]	$f'_c{}^{PP}$ [MPa]	f'_t [MPa]	E [MPa]	$\epsilon_{0.4f'_c}$ [%]	ϵ'_m [%]
						LVDTs	LVDTs	LVDTs
3S1	0	312.57	10.42			10130	0.65	1.68
3S2	0	557.17	18.57			8682	1.05	1.29
3S7	0	599.68	22.92			8005	0.29	0.51
3S6	40	433.69	28.33	18,90		19143	0.37	0.51
3S11*	40	455.16	29.74	19,78		26394	0.30	0.37
3S9	80	184.25	24.09	14,29	6,01	13610	0.83	1.25
3S10	80	165.39	21.62	12,82	5,40	11184	0.01	1.11

Table 16: Six-brick columns series 3, 28° ageing cycles, subjected to eccentric loads: average behaviour of the mortar joints measured by means of wired “omega”

	e [mm]	Ω [mm]		Notes
		opening	closure	
3S6	40	0.03	/	4° joint sinix
3S11*	40	/	-0.40	2° joint dx
3S9	80	0.75	-1.50	4° joint sinix, 2° joint dx
3S10	80	0.36	-2.11	4° joint sinix, 3° joint dx

Table 17: Six-brick columns, series 4, 38° ageing cycles: summary of the main mechanical parameters measured

	e [mm]	N_{max} [kN]	f'_c [MPa]	f'_c^{PP} [MPa]	f'_t [MPa]	E [MPa]		$\epsilon_{0.4f'_c}$ [%]		ϵ'_m [%]
						LVDTs	DIC	LVDTs	DIC	LVDTs
4S1	0	602	20.32			6811	4351	0.386	0.432	1.00
4S5	0	600.89	20.62			5868	3581	0.495	0.382	1.01
4S6	0	495.07	16.63			6080	1883	0.561	0.730	0.91
4S2	40	451.34	30.39	20.26		10100	9587	0.303	0.184	0.74
4S4	40	449.29	30.26	20.94		11789	7915	0.526	0.494	1.19
4S9	40	322.24	22.76	20.98		7042	2073	0.734	0.694	1.96
4S3	80	178.75	23.09	13.74	5.76	6680	5190	0.265	0.225	0.64
4S7	80	216.72	28	19.04	6.78	10693		0.764		1.45
4S8	80	230.57	29.45	19.97	7.32	6933	4010	0.717	0.511	1.12

Table 18: Six-brick columns series 4, 38° ageing cycles, subjected to eccentric loads: average behaviour of the mortar joints measured by means of wired “omega”

	e [mm]	Ω [mm]		Notes
		opening	closure	
4S2	40	0.07	-0.38	3° joint sinix, 4° joint dx
4S4	40	0.05	-0.40	2° joint sinix, 4° joint dx*
4S9	40	0.13	-0.69	4° joint sinix, 2° joint dx
4S3	80	1.25	-0.40	4° joint sinix, 4° joint dx
4S7	80	2.21	-1.04	3° joint sinix, 3° joint dx
4S8	80	0.83	-0.49	4° joint sinix, 2° joint dx

9.4.1. Compression test, $e=0$

The results of the concentric compression tests on the 4th series of six-brick columns are reported herein.

First of all, the average stress-strain diagrams recorded via LVDTs were reported with reference to all the specimens of the 4 series presenting different health-state conditions, in order to qualitatively compare the behaviours (Figure 51). From these graphs, indeed, the different behaviour of the 4 sets of masonry assemblies is evident, both in terms of maximum load, stiffness, and deformability.

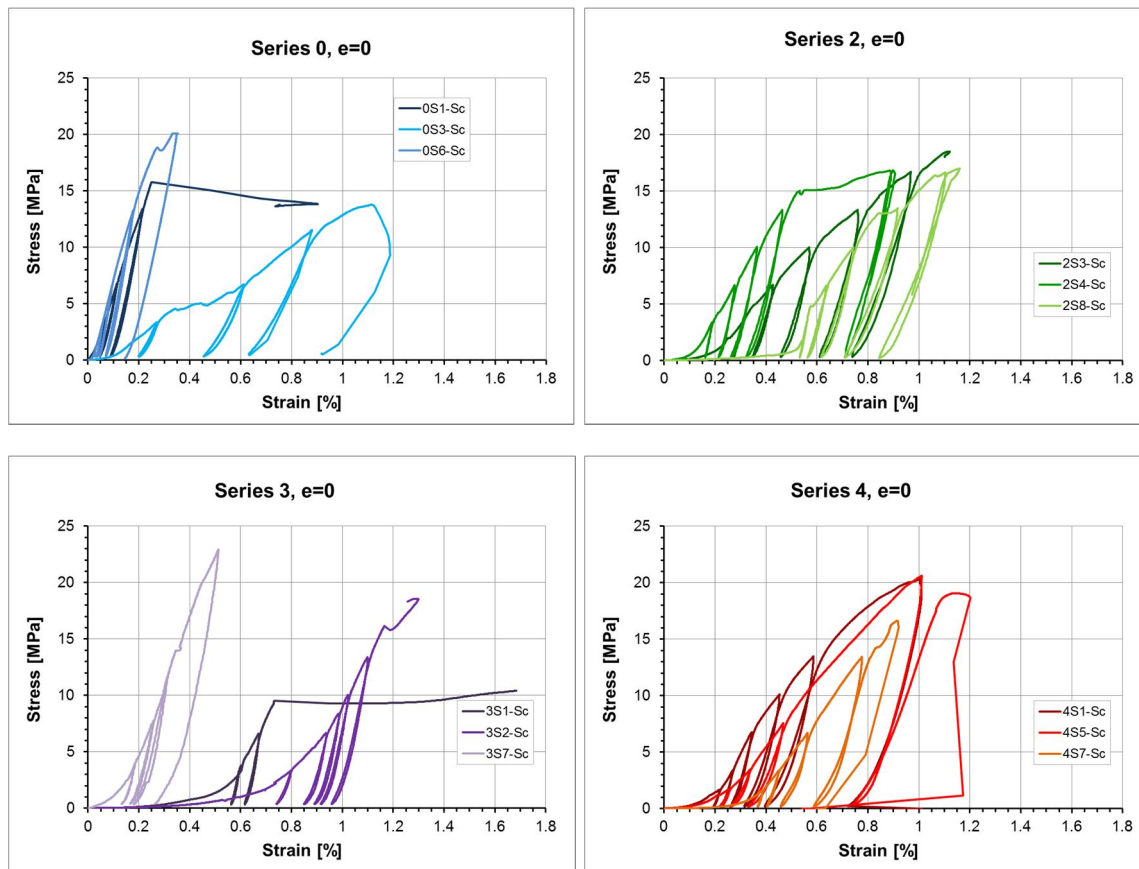


Figure 51: Stress-strain graphs obtained from the concentric load tests for the four series of six-brick columns

More in detail, some differences in the main mechanical parameters recorded arose between the 4 series. First of all, it seems that 18 ageing cycles caused, if compared to the undamaged specimens, an increase of the maximum compression strength, (of about 5%), as well as an increase of the maximum deformations recorded (+70%), while the modulus of elasticity decreased approximately of a 20%. Thus, the six-brick column of the second series appeared more resistant but losing stiffness.

Increasing the number of ageing cycles, at 28 cycles, the mechanical values recorded appeared much dispersed. The maximum compressive strength is greater than for the

undamaged specimens but almost equal to the values measured after 18 cycles. Instead, the maximum strains, increased of about an 80% (10% with reference to the series 2). Differently from what was found before, it was the value of modulus of elasticity as an increase of about a 30% with reference to the series 2 and of about a 5% with respect to the specimens of the series 0 was registered.

Finally, the values recorded for the last series which was subjected to 38 ageing cycles showed a further increase in the resistance (about 10% compared to the aged series 3) and a decrease in the values of maximum strains determined as well as in the values of modulus of elasticity, indicating a lost in stiffness.

Table 19: Summary of the mechanical parameters obtained from the axial compression tests $e=0$ of the six-brick columns belonging to the 4 series

Series	n° of ageing cycles	e [mm]	N_{max}		f'_c		ϵ'_m		E	
			[kN]	CoV [%]	[MPa]	CoV [%]	[%]	CoV [%]	[MPa]	CoV [%]
0 (ref)	0	0	496.62	19	16.55	19	0.57	82	8466	50
2	18	0	524.11	5	17.47	5	1.06	13	6514	27
3	28	0	489.81	32	17.30	37	1.16	51	8939	12
4	38	0	565.99	11	19.19	11	0.97	5	6253	8

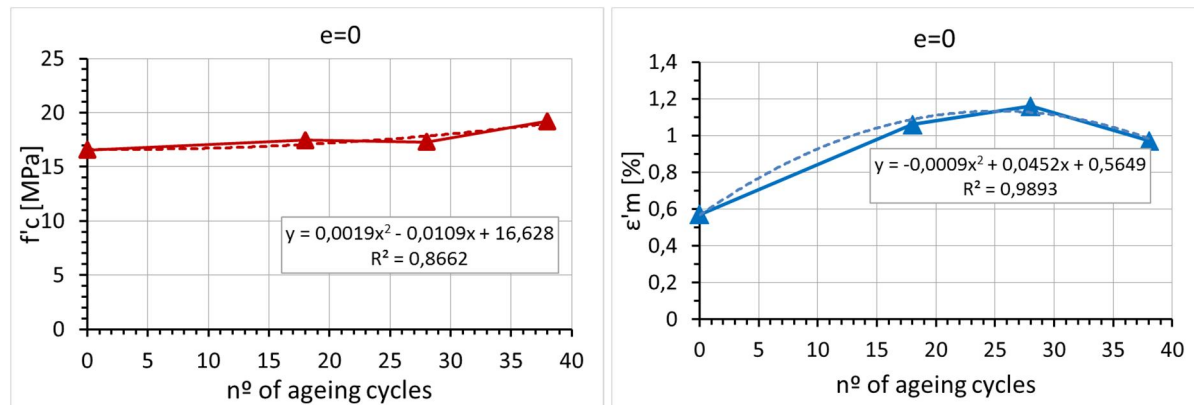


Figure 52: Axial compression tests on the 4 series of six-brick columns: average results in terms of maximum compressive strength (left) and maximum strain under load (right)

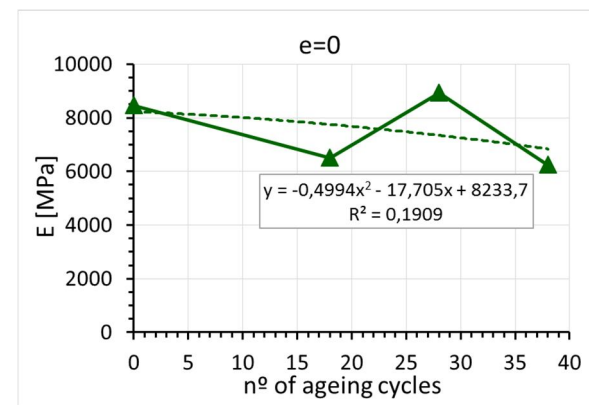


Figure 53: Axial compression tests on the 4 series of six-brick columns: average results in terms of modulus of elasticity

9.4.2. Compression test, e=40 mm

Looking in a whole at the results obtained from the compression tests with eccentricity equal to 40mm ($e/d = 1/6$), a decreasing tendency on the compression strength with the increasing number of ageing cycles is noted.

Table 20: Summary of the mechanical parameters obtained from the eccentric compression tests e=40mm of the six-brick columns belonging to the 4 series

Series	n° of ageing cycles	e [mm]	N_{max}		f'_c		ε'_m		E	
			[kN]	CoV [%]	[MPa]	CoV [%]	[%]	CoV [%]	[MPa]	CoV [%]
0 (ref)	0	40	422.87	42	32,29	11	0,35	87	10238	50
2	18	40	421,09	14	27,51	14	0,81	82	16591	40
3	28	40	444.42	3	29,04	3	0,44	23	22768	22
4	38	40	407.62	18	27,80	16	1,30	47	9644	25

Table 21: Additional mechanical results of the eccentric compression tests (e=40mm) carried out on the six-brick columns belonging to the 4 series

Series	n° of ageing cycles	e [mm]	f'_c^{pp}		Ω			
			[MPa]	CoV [%]	Open [mm]	CoV [%]	Close [mm]	CoV [%]
0 (ref)	0	40	21,32	13	0,24	130	-0,45	-88
2	18	40	18,35	14	0,42	110	-0,63	-15
3	28	40	19,34	3	0,03	49	-0,40	-35
4	38	40	20,73	2	0,085	49	-0,49	-53

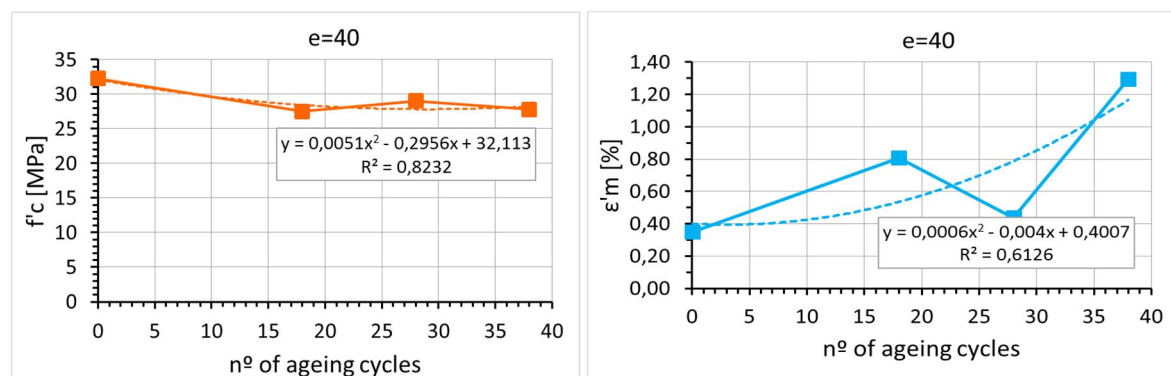


Figure 54: Eccentric compression tests (e=40 mm) on the 4 series of six-brick columns: average results in terms of maximum compressive strength (left) and maximum strain under load (right)

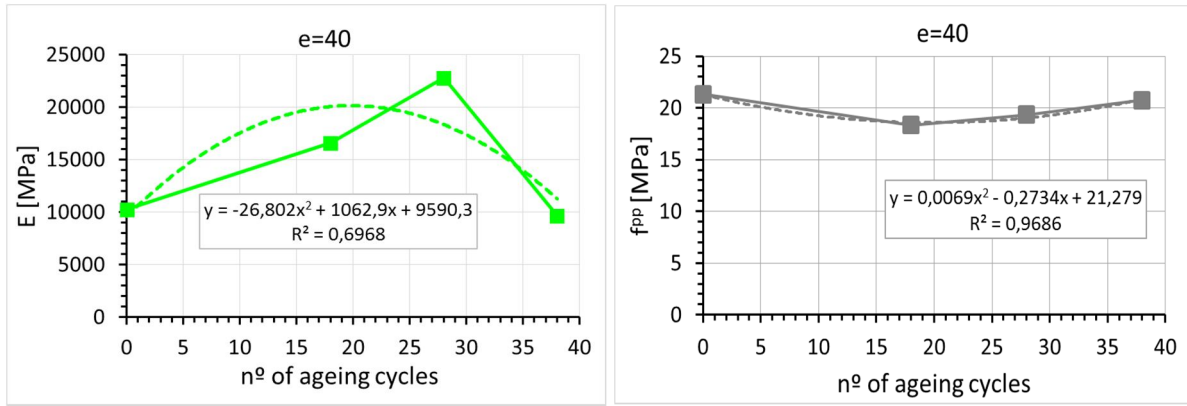


Figure 55: Eccentric compression tests (e=40 mm) on the 4 series of six-brick columns: average results in terms of modulus of elasticity and compressive strength determine according to the parzialization of the resistant section

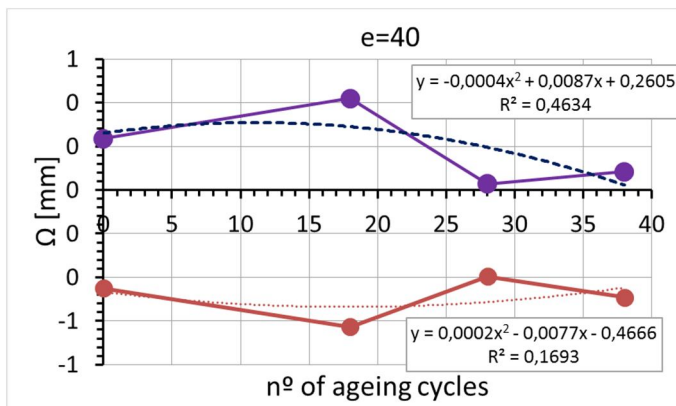


Figure 56: Eccentric compression tests (e=40 mm) on the 4 series of six-brick columns: average values of opening/closing of the mortar joints

9.4.3. Compression test, e=80 mm

In the following a comparison on the main results obtained is shown.

Overall, the maximum compressive strength decreased in with the decreasing values of maximum load registered. The same behaviour is shown by the tensile strength

Table 22: Main mechanical parameters recovered from the eccentric loading tests carried out with the maximum eccentricity, e=80mm

Series	n° of ageing cycles	e [mm]	N _{max}		f' _c		ε' _m		E	
			[kN]	CoV [%]	[MPa]	CoV [%]	[%]	CoV [%]	[MPa]	CoV [%]
0	0	80	317,16	17	39,16	17	0,35	20	17197	26
2	18	80	204,23	5	25,21	5	0,53	74	12654	10
3	28	80	174,82	8	22,85	8	1,18	8	12397	14
4	38	80	208,68	13	26,85	12	1,07	38	8102	28

Table 23: Additional mechanical results of the eccentric compression tests (e=80mm) carried out on the six-brick columns belonging to the 4 series

Series	n° of ageing cycles	e [mm]	f' _c ^{pp}		f' _t		Ω			
			[MPa]	CoV [%]	[MPa]	CoV [%]	Open [mm]	CoV [%]	Close [mm]	CoV [%]
0	0	80	23,56	17	9,72	17	0,46	10	-0,13	-8
2	18	80	15,17	5	6,26	5	0,82	210	-0,54	-120
3	28	80	13,55	8	5,70	8	0,56	49	-1,80	-24
4	38	80	17,58	19	6,62	12	1,43	49	-0,64	-53

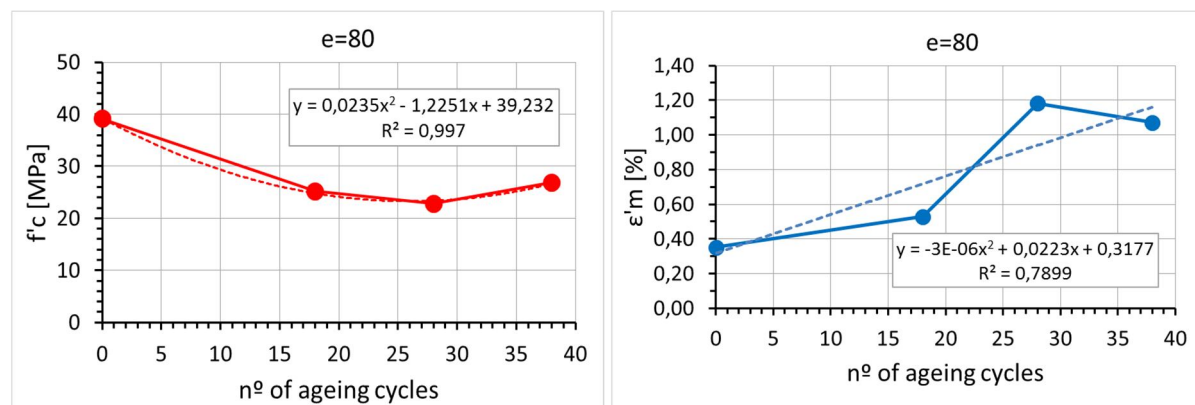


Figure 57: Eccentric compression tests (e=80 mm) on the 4 series of six-brick columns: average results in terms of maximum compressive strength (left) and maximum strain under load (right)

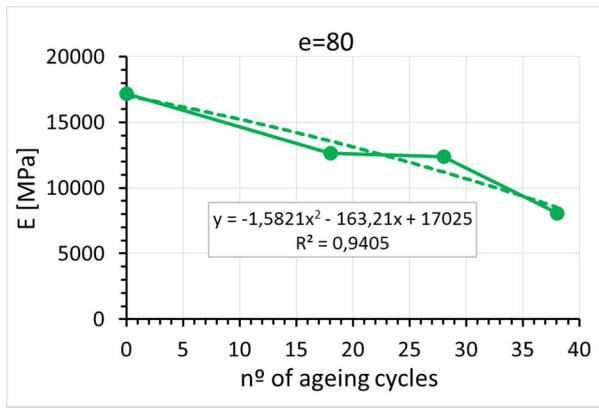


Figure 58: Eccentric compression tests (e=80 mm) on the 4 series of six-brick columns: average results in terms of modulus of elasticity

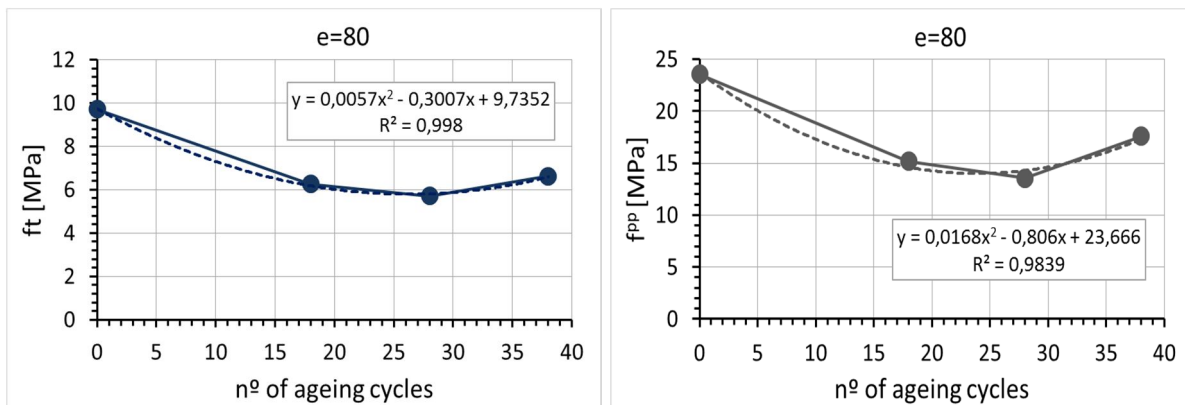


Figure 59: Eccentric compression tests (e=80 mm) on the 4 series of six-brick columns: average results in terms of tensile strength and compressive strength determine according to the parzialization of the resistant section

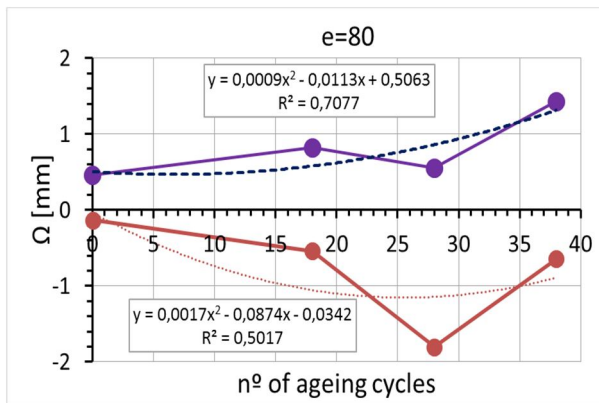


Figure 60: Eccentric compression tests (e=80 mm) on the 4 series of six-brick columns: average values of opening/closing of the mortar joints

In conclusion, it salt weathering decay seemed to have caused an apparent beneficial effect on the compression strength of the brick columns associated with a decreasing in the tension strength.

9.5. Shear tests

In this paragraph, the shear tests carried out on three series of triplets in different starting health-state conditions are reported (series 0, 2 and 3) as the tests on the 6 triplets of the most damaged series, series 4, were not performed. Thus, overall, 18 triplets were considered, in order to have a representative number of specimen on which evaluate the shear strength, as suggested by [30].

Actually, of these large number of specimens, only 10 underwent the mechanical shear test, as the others (in italics in Table 24) were already broken before the test itself. These ruptures, with the exception of three triplets of the series 0, which fell down during their movements, were caused by the artificial ageing cycles to which they underwent. In this last case, there was a “clean” detachment between one or more brick/mortar joints interfaces, with no mortar particles attached to the bricks. Moreover, the detached surfaces of the lime joints presented consistent salt crystals depositions, especially near the edges.

Table 24: Series of triplets prepared for the shear test

Series 0 (reference)	Series 2 (18 ageing cycles)	Series 3 (28 ageing cycles)
0T1	2T10	3T1
0T2	<i>2T10b</i>	<i>3T2</i>
0T3	2T11	3T3
<i>0T4</i>	2T11b	3T4
<i>0T5</i>	<i>2T12</i>	3T5
<i>0T6</i>	<i>2T12b</i>	<i>3T6</i>

The shear tests were carried out according to the *procedure b* indicated in [20] that is without any pre-compression loads. The triplets were thus intended to be tested in vertical, by applying increasing concentrated load on the top part of the central brick, free to scroll down and supporting the bottom part of the two external brick units (Figure 61).

Before performing the tests, the dimensions of the triplets were measured in order to exactly calculate the resistant areas, a crack pattern survey was performed (in order to see previous existing detachments or cracks, i.e. due to the ageing) and, a rough cleaning of the surfaces was carried out. This last procedure, important for the specimens belonging to the decayed series which presented salt depositions on their faces, was performed in order to allow the installation of the bases for two wired transducers. Indeed, each test, although not required by [20], was monitored by means of two LVDTs, measuring displacements until 2mm, one mounted on the front face of the specimen and one on the rear, in order to collect information also about the maximum displacements reached (Figure 62).

The tests were carried out under load control, by means of a universal testing machine Galdabini, with full scale of 100 kN. The velocity of load application was of about 10Kg/sec and the frequency of data acquisition 1data/sec.

During each test, the value of the maximum load, F_{\max} , was recorded and the shear strength, f'_v [MPa] calculated by means of:

$$f'_v = \frac{F_{\max}}{2A} \quad (9.5)$$

Where A is the transversal area of a specimen parallel to the mortar joints [20].

Moreover, the type of rupture was noted, according to the scheme reported in Figure 61, in order to evaluate the location of this collapse (at the interface brick/mortar, inside the mortar joint, in the brick unit or transversally) and thus identify the masonry constituent element less resistant to shear loads.

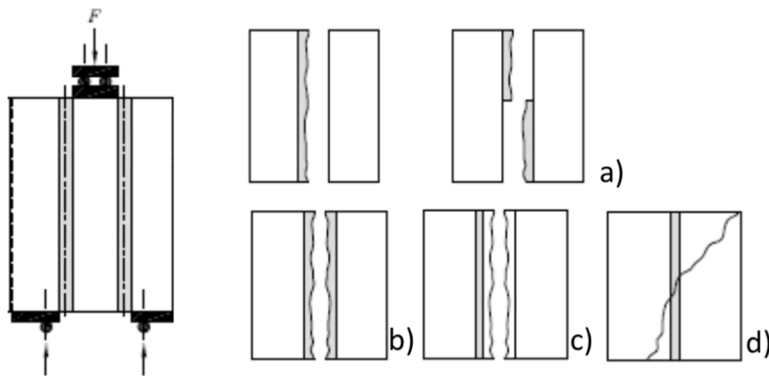


Figure 61: Determination of the shear strength on triplets: testing set-up (left) and types of rupture (right) [20]

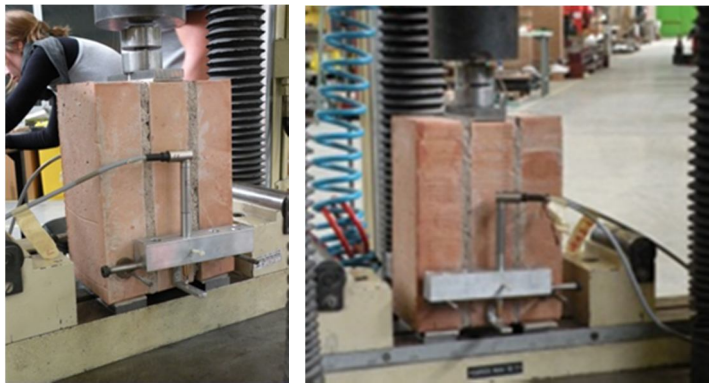


Figure 62: Shear test set-up and measurement devices: view of the triplet front side (left) and rear side (right)

9.5.1. Triplets, series 0, undamaged

The results of the shear tests carried out on the three reference triplets in as-built conditions are reported below.

In these tests, the load was monotonically increased until the collapse of the specimen which occurred at very low load values. The fragile, unexpected rupture occurred for all the three cases at the interface brick/mortar joint (Figure 64, Figure 65, Figure 67). The brick surfaces appeared completely cleaned after the detachment of the joints, index of an initial scarce adhesion at the lime mortar/solid brick interfaces, despite the accurate realization of the specimen.

The maximum values of load and the calculated shear strength are summarised in Table 25, together with the maximum value of displacement measured with the LVDTs. For the three mechanical parameters, the average values and the respective coefficient of variation (in %) are also reported. The dispersion of results is quite high, ranging between 40 - 50%.

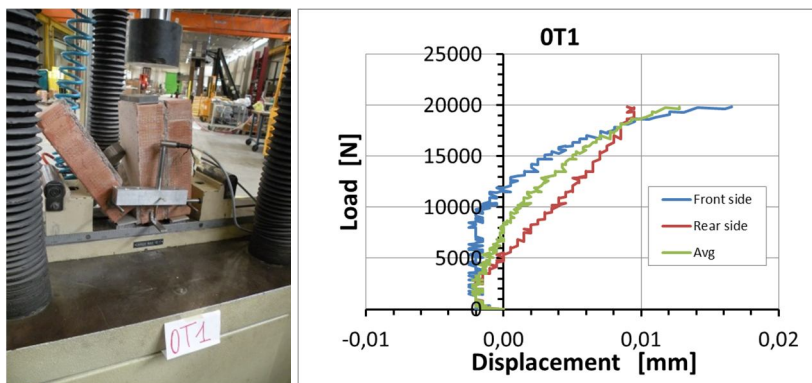


Figure 63: Triplet OS1, end of the test (left), load-displacement graph recorded by the two LVDTs (right)



Figure 64: Triplet OS1, type of rupture: view of both faces

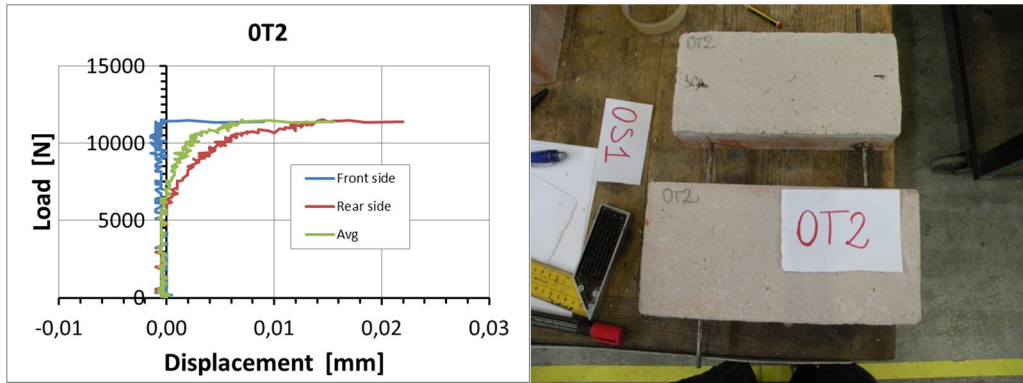


Figure 65: Triplet OS2, load-displacement diagram (left) and photo of the rupture (right)

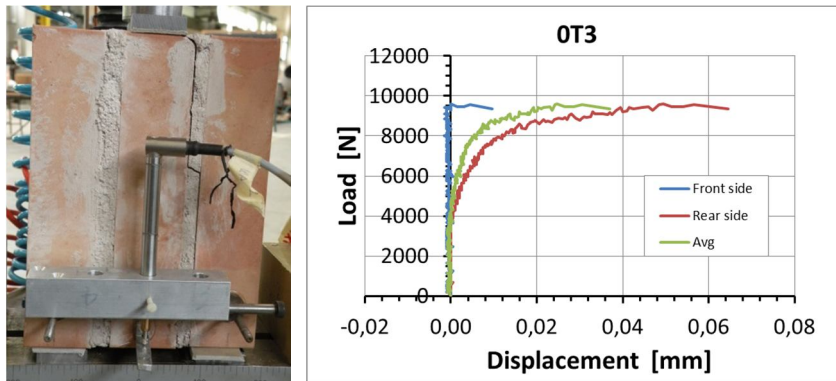


Figure 66: Triplet OT3, final phase of the test (left), load-displacement graph recorded by the two LVDTs (right)



Figure 67: Triplet OT3, type of rupture

Table 25: Results of the shear test on the undamaged triplets

	F_{max} [N]	f'_v [N/mm ²]	Max. Displ.[mm]	Rupture
OT1	19832,58	0,33	0,017	a
OT2	11526,80	0,19	0,015	a
OT3	9602,29	0,162	0,037	a bis
Average	13653,89	0,23	0,02	
<i>DevEst</i>	5436,74	0,09	0,01	
<i>CoV (%)</i>	39,82	39,82	51,81	

9.5.2. Results of the shear tests on the triplets of series 2 (18 ageing cycles)

Similarly to what reported for the previous series of triplets, herein are visualized the results of the shear tests on the six triplets subjected to 18 ageing cycles.

In this case, only 3 specimens were effectively tested, as the rupture of the other three triplets occurred during their preparation, in detail, during their positioning in vertical. The shear test was carried out using the same configuration of the previous tests and the load application was stopped at the failure of the specimen. In these cases, the collapses occurred suddenly, without previous signs, with the exception of triplet 2T11, where a first crack appeared at the superior joint/brick interface just few seconds after the load application.

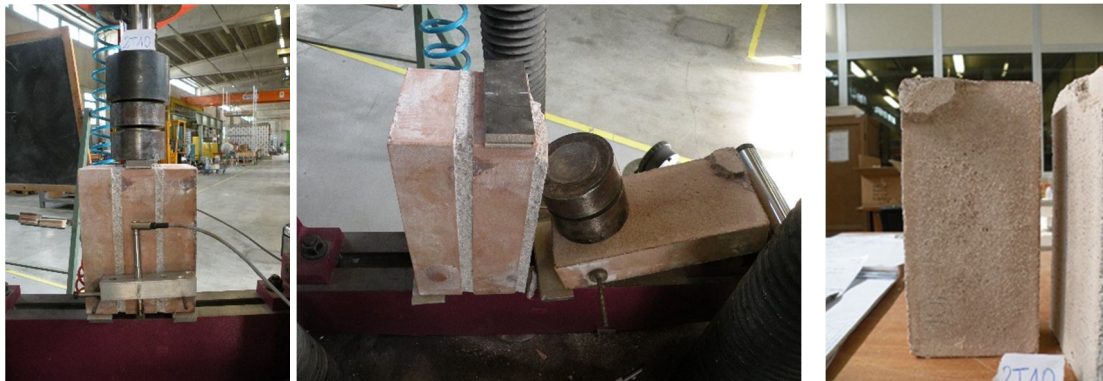


Figure 68: Triplet 2T10, set-up (left) and rupture (centre and right)



Figure 69: Triplet 2T11, first crack (left), general view of the rupture (centre) and detail of the cracks (right)

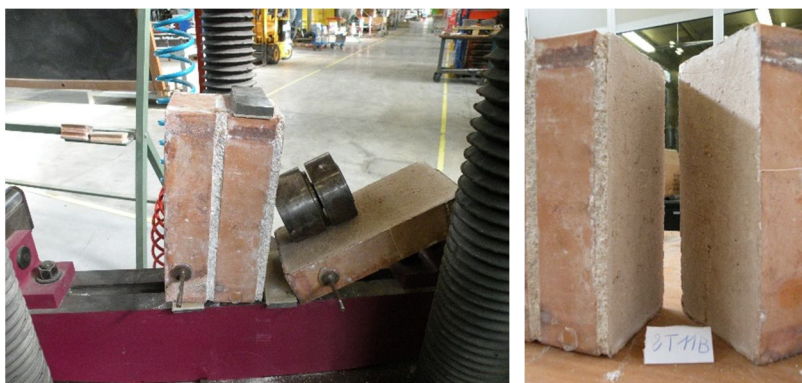


Figure 70: Triplet 2T11b, end of the test (left) and detail of the brick/mortar surfaces after rupture

The rupture of triplets 2T10 and 2T11b (Figure 68, Figure 70) occurred in the same way, with the complete, smooth detachment of one mortar joint from the corresponding brick surface. Instead the collapse of specimen 2T11 occurred with the delamination of both mortar joints; also in this case, the surfaces of the brick remained completely clean with the exception of a little edge (Figure 69).

Finally, the results obtained in terms of maximum load and shear strength were reported (Table 26). They show a high uncertainty in the determination of these mechanical properties due to the dispersion of results (77%). Indeed, the three specimens behave quite differently: while a shear strength of 0.52 MPa was calculated for the triplet 2T10, a value of less than a half, approx. 0.2 MPa for 2T11 and 0.1 Mpa for 2T11b was determined.

Table 26: Results of the shear tests on the triplets of the decayed series 2

	F_{\max} [N]	f'_v [N/mm ²]	Max. Displ.[mm]	Rupture
2T10	31150	0,52	1,20	a
2T11	12525	0,21	1,19	a bis
2T11b	6400	0,11	/	a
Average	16691,67	0,28	1,20	
<i>DevEst</i>	<i>12890,36</i>	<i>0,21</i>	<i>0,01</i>	
<i>CoV (%)</i>	<i>77,23</i>	<i>77,23</i>	<i>0,59</i>	

As the rupture of the triplets 2T10, 2T12 and 2T12b occurred during their preparation, some photos of their actual state were taken. In all the 3 cases, both lime joints resulted completely detached from the corresponding brick and the surfaces of the two construction materials were clean as if they weren't attached at all. This was probably due to a scarce initial adherence worsened by the presence of salt crystals at the interfaces (**Figure 71, Figure 72**).



Figure 71: Triplet 2T10b and 2T12, at the end of the ageing cycles

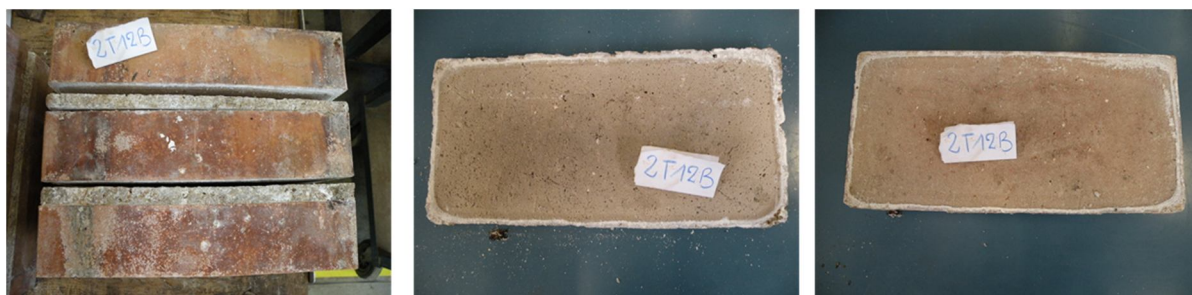


Figure 72: Triplet 2T12b, at the end of the ageing cycle. Salt crystals depositions were detected on the external borders of both mortar (centre) and brick surface (right)

9.5.3. Results of the shear tests on the triplets of series 3 (28 ageing cycles)

At the end of the accelerated ageing treatment, 4 of the 6 triplets belonging to series 3, were still apparently intact. Thus, it was decided to prepare them for the mechanical shear test. Unfortunately, the three triplets (3T1, 3T4 and 3T5), broken during their rotation prior to be positioned under the testing machine from the horizontal configuration (direction parallel to the mortar joints) to the vertical one. From the photos taken, it appeared evident that the detachments of both lime joints from the brick surface was caused by the presence of salt depositions (Figure 73).

Therefore, only one specimen, 3T3, was really tested. Anyhow, in this case, the collapse occurred at a very low load level (120 N) which results in an almost null shear strength (Table 27). The rupture occurred at one mortar/brick interface, type a, as in the previous cases, but the brick surface appeared somehow “dirt”, with a slight layer of salts, more accentuated near the external borders (Figure 74).

Table 27: Results of the shear tests on the triplets of the decayed series 3

	F_{\max} [N]	f'_v [N/mm ²]	Max. Displ.[mm]	Rupture
3T3	120	0,002	/	a

As the rupture of the triplets 2T10, 2T12 and 2T12b occurred during their preparation, some photos of their



Figure 73: State of triplets 3T4, 3T5 and 3T6: one or both mortar joints were completely detached. The brick surfaces appeared clean and smooth with the exception of a thin layer of salt crystals near the external border.



Figure 74: Triplet 3T3, at the end of the mechanical test. Under the load plates (left) and details of the rupture (centre and right)

9.5.4. Comparison and discussion of the shear test results

The shear tests on the series of triplets at different levels of initial decay caused by weathering treatments, were aimed at finding and quantifying possible variations on the shear strength of this specific masonry realized with fired-clay bricks and hydraulic lime mortar joints, in order to complete the mechanical information recovered by means of the concentric and eccentric loading tests.

A first observation arise from this laboratory experience is that the simulated artificial ageing cycles affected the shear strength of masonry, worsening the bond at the mortar joint/brick interfaces. Indeed, the salt crystals tended to deposit in that position breaking the existing weak link (demonstrated by the shear tests on the triplets in as-built conditions) between the two porous materials. Thus, it was necessary only a very small shear force, i.e. just the gravitational force when the triplets were positioned in vertical, to separate them.

After 18 ageing cycles, half of the predisposed specimens collapsed during the rotation from the horizontal position to the vertical one; this number increases at the increasing ageing cycles as this failure occurred for 5 over 6 triplets of the 3rd series which underwent to 28 ageing cycles.

Due to the scarce number of triplets remained available at the end of the ageing tests/preparatory phase of the mechanical test, quantifying the effects of salt decay on the masonry shear strength is quite difficult and not too much reliable. Anyhow, it seemed that this mechanical parameter slightly increased after 18 ageing cycles, if compared to the average values recorded for the undamaged triplets, and then collapsed at the subsequent increasing decay level (28 ageing cycles) becoming almost null (Figure 75).

Further tests and investigations are necessary to recover more and more accurate information related to this mechanical parameter.

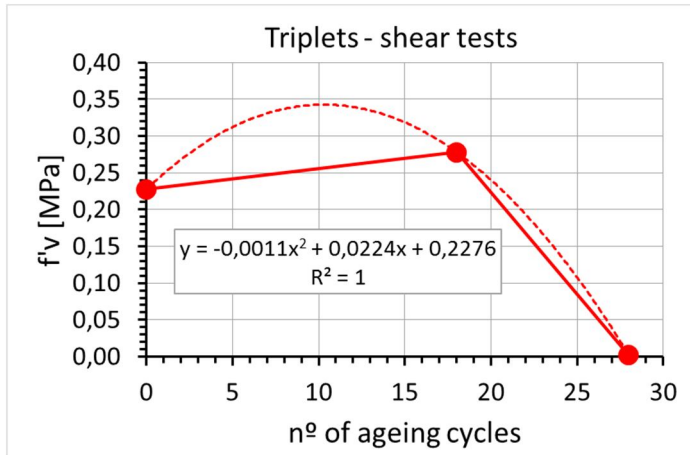


Figure 75: Comparison of the average values of shear strength obtained between the three series of triplets.

10. Discussion and conclusions

This thesis has studied the assessment of environmental decay effects in full-brick masonry. Among the possible weathering processes, the transport of moisture and salts was considered and specifically the damaging effects caused by two salts, sodium chloride and sodium sulphate. A vast experimental laboratory campaign was carried out considering brick masonry walls and small assemblies partly artificially and partly naturally aged through on-purpose own-developed procedures. Numerous integrated testing techniques, either non-destructive or mechanical were applied, also in combination with advanced monitoring techniques.

The experimental approach followed has had two aims: 1) qualitatively and quantitatively evaluate the weathering decay effects and their evolution over time in brick masonry and 2) validate in the lab, holistic approaches and methodologies for future validation on-site on real cases.

The scientific literature was reviewed on the mechanisms responsible for environmental decay in porous masonry materials and consequent damaging effects (chapter 2). It has shown that despite the large number of investigations carried out on this topic, much attention was focused on appearance of superficial decay. From a structural viewpoint, it emerged for example the need to quantify the superficial decay in term of amount of materials losses and to better investigate the consequences of such degradation effects on the masonry's mechanical properties, i.e. variations in the load-bearing capacity of masonry structures. On-site applicable testing and monitoring tools also capable of following the evolution over time of these decay processes since their beginning were also missing.

Taking into account this last need, several non-destructive diagnostic techniques (NDT) and mechanical methodologies with potential for discontinuous/repeated testing of masonry wall elements and suitable for the testing aims of, for example, detecting areas of moisture and salt content and areas of decay were reviewed (chapter 3). Special attention was paid in proposing them in the present study according to tailored procedures of specimen preparation or instrumentation, or of data acquisition or data post-processing thus implementing further development of the techniques themselves. A further step was accomplished in achieving combined application of techniques, either traditional or innovative, sometimes absolutely novel as shown in the experimental chapters of the thesis text. Through the proposition and validation of applicability of techniques exploiting different types of signals or different levels of accuracy, but in general giving favour to image diagnostic methods, on-purpose innovative assessment procedures were developed which allowed a holistic investigation of the decay phenomenon and an improved understanding of its mechanisms with a better knowledge of the state of health of the investigated element. As seen, the reliability and accuracy of the implemented methodologies were critically evaluated throughout the core chapters of the thesis.

In order to know the starting conditions of the two porous materials (fired-clay solid bricks and hydraulic lime mortar) considered in this thesis for construction of the different series of walls and masonry assemblies, a complete physical-chemical and mechanical characterization was performed. In addition to obtaining reference values later to be used against decayed material values, this phase was a good practise for tuning the appropriate modality and numerosity of testing by various techniques. Interesting were the evidences recovered about the presence of considerable amounts of soluble salts within the new or as-produced material units as well as into the tap water of the local aqueduct. This aspect was taken into account in the different phases of the experimental campaign, given that non-intentional salt related damaged may occur. Moreover, the monitored data of the microclimatic parameters (air temperature, relative humidity, rain fall) recorded directly on-site in the open-space laboratory area where the specimens were exposed to climate thanks to a wireless monitoring system installed directly on one large wall were used to estimate the possible hydration/crystallization cycles occurred in the material for the two salts considered. For the first time, this multi-year evaluation has evidenced that, during each ageing summer, the climate of Bologna is greatly favourable to the crystallization of sodium chloride more than of sodium sulphate (chapter 4).

To replicate weathering effects, two different procedures, one called “natural” and one “artificial” were on-purpose designed and established to tests the several series of building materials units, small walls, masonry assemblies and full-scale brick walls realized for the different testing aims.

The outcomes of the vast experimental laboratory campaign performed have addressed several issues relevant for the enhancement of the researches previously conducted in the investigated field.

The different vulnerability of the two porous materials (brick and lime mortar) considered in this thesis, clearly arose from the results of the long-term natural ageing and monitoring on single units of both masonry materials, via visual, non-destructive and mechanical techniques (chapter 5). Overall, mortar prisms showed more evident and severe salt related degradation effects than bricks. On the mortar, increase in superficial roughness, decohesion, pulverization and material losses were visible, while only some cracks at bottom and top faces were recorded on the brick units. These different sensitivity of the two materials was confirmed by the non-destructive ultrasonic tests and mechanical evaluations performed.

The US results obtained for the series of materials units outdoors exposed over three summers and subjected to damp rise from the base via tap water, 0.05% -wt. NaCl or 0.05%-wt. Na₂S₀₄, at the end of each ageing season, were compared to results obtained by means of similar tests carried out on undamaged materials' units. They were somehow unexpected. Indeed, overall, aged materials' units showed values of velocity greater than the reference ones and values of attenuations lower than the values measured before the ageing processes. These increased values of velocity and reduced values of attenuation, if compared to the undamaged ones, suggested an increased density and homogeneity of the aged materials, probably caused by the presence of water and salts within the material pores. This issue was

confirmed by the gravimetric and dimensional analyses, as higher values of density were measured for all the sets of aged materials despite the visible degradations already occurred, i.e. the large amount of material losses (powder) registered at the end of each ageing season for the sets of mortar prisms. Compatible results were also obtained from the mechanical tests as greater values of compressive strength and modulus of elasticity were measured for both porous materials in damaged conditions.

Then, by comparing the non-destructive and mechanical parameters obtained for bricks and mortar prisms subjected to NaCl or Na₂S₀₄ low-concentrated brine rise, at the end of the three ageing summers, NaCl contaminated samples appeared more damaged than the others. Although sodium sulphate is notoriously addressed as a more aggressive salt than sodium chloride for porous materials, the greater decay effects are in line with the estimated numbers of possibly occurred salt hydration/crystallization cycles during each ageing season. Indeed, the microclimatic conditions of Bologna, seemed to have been more favourable to the crystallization of sodium chloride than of sodium sulphate, since the first weathering season.

This phase of the experimental work underlined also the reliability of the high-frequency ultrasound tests in assessing the effects of natural ageing treatments in limited-size samples and their evolution over time since the beginning.

The feasibility and accuracy of several on-site applicable non-destructive diagnostic techniques, applied also in innovative and combined procedures, in detecting moisture and salt transport phenomena as well as environmental decay effects in masonry structures, was evaluated with reference to six on-purpose designed and build full-scale brick walls naturally aged. The techniques employed exploit different physical principle and were addressed to superficial and/or in-depth monitoring. Measurements were repeated at the end of different ageing seasons in order to verify the sensitivity of the testing methods in evaluating the progresses of the simulated weathering effects, obtaining successful or promising results (chapter 6).

The non-destructive sonic tests carried out on the sets of small walls and masonry assemblies, subjected to natural or accelerated ageing have evidenced the potentialities and limitations of this non-destructive methods in evaluating the effects and evolution of environmental decay effects in brick masonry. Indeed, the presence of moisture and salts within the masonry materials was clearly detected since the first stages of ageing, leading to an impossibility in differentiated them. Thanks to variations in direct sonic velocity values, the heights of the moist level in naturally aged small walls have been detected. Defects such as salt crystallizations, cracks or delaminations or bricks are identified, on the majority of the cases, thorough increasing values of attenuation, which seems to be a more sensitive parameter. Anyhow, despite this potentiality, a scarce accuracy in discriminated between the different decay levels was evidenced (chapter 7).

The evaluation of the decay effects due to environment via mechanical tests was carried out on small walls subjected to natural or artificial ageing (chapter 8), on different sets of six-brick columns and triplets accelerated aged (chapter 9). The quantitative evaluation of the variations on the characteristic mechanical property of masonry caused by aggressive environmental agents were evaluated. These mechanical tests were successfully used to validate an innovative non-destructive image monitoring procedure on-purpose implemented, in view of future applications in-situ on historic masonry.

11. References

- Angst, U. et al., 2009, Potentiometric determination of the chloride ion activity in cement based materials, *J. Appl. Electrochemistry*, vol. 40, n°3, pp. 561-573.
- Anzani, A., Binda, L., Lualdi, M., Tedeschi, C., Zanzi, L., 2006, Use of Sonic and GPR Tests to Control the Effectiveness of Grout Injections of Stone Masonry, *Proc. of ECNDT 2006*, Berlin, Germany, September 25-29, Jörg Völker, Dr. Rainer Link, DGZfP, paper Tu.2.4.3.
- Arizzi, A, Viles, H., Cultrone, G. (2012), Experimental testing of the durability of lime-based mortars used for rendering historic buildings, *Construction and Building Materials* 28 (2012) 807–818
- Arnold, A. & Zehnder, K. 1990 “Salt weathering on monuments”, in *The Conservation of Monuments in the Mediterranean Basin: The influence of coastal environment and salt spray on limestone and marble. Proc. of the 1st International Symposium*, 31-58 (1990)
- Augenti, J. *Mater. Civ. Eng.* 2010.22:1102-1111
- Avdelidis N.P., Delegou E.T., Moropoulou A. A thermographic survey for the monitoring of moisture in porous stone, *Proc. of WCNDT 2004 16th World Conference on Non-destructive Testing*, Montreal (Quebec), August 30 - September 3, 2004, CD-ROM ref. 804_avde, *NDT.net - The e-Journal of Non-destructive Testing*, Volume 9, Issue 11 (2004)
- Avdelidis N.P., Moropoulou A. Applications of infrared thermography for the investigation of historic structures, *Journal of Cultural Heritage*, Volume 5, Issue 1 (2004) 119–127
- Benavente, D. et al., 2006, Influence of microstructure on the resistance to salt crystallisation damage in brick, *Materials & Structures*, vol.39, n°1, pp.105-113.
- Benedetti, A. et al., 2010, Mechanical properties of masonry with environmental degradation, 8th Int. Masonry Conference, Dresden.
- Binda, L., Baronio, G., 1998, Crystallization test by total immersion of specimens, *Materials and Structures*, 31, pp.10-15.
- Binda, L., Saisi, A., Tiraboschi, C., 2001, Application of sonic tests to the diagnosis of damaged and repaired structures, in *NDT and E International*, March, Vol. 34, No. 2, 123-138.

Borrelli E., (1999), “Porosity”, in *Consevation of Architectural Heritage, Historic Structures and Materials ARC Laboratory Handbbok vol. 2*, ICCROM, Atel spa, Rome 1999, ISBN 92-9077-157-7, pp. 20

Borrelli E., (1999), vol. 3 “Salts”, in *Consevation of Architectural Heritage, Historic Structures and Materials ARC Laboratory Handbbok*, ICCROM, Atel spa, Rome 1999, ISBN 92-9077-157-7

Brencich A. (2010), *Eng. Struct* 32, 1244-1251.

Brencich, Corradi, Gambarotta (2008), Eccentrically loaded brickwork: Theoretical and experimental results, *Engineering Structures* 30, 3629_3643

Brencich A., de Felice G. (2009), Brickwork under eccentric compression: Experimental results and macroscopic models, *Construction and Building Materials* 23 1935–1946

Brozovsky, J., Zach, J., Brozovsky, J. Jr., 2008, Determine the strength of solid burnt bricks in historical structures, Proc. of 9th International Conference on NDT of Art, Jerusalem Israel, 25-30 May, paper 11.

Bucur, V., 1999, Acoustics as a Tool for The Non destructive Testing of Wood, Proc. of International Symposium on NDT Contribution to the Infrastructure Safety Systems, Torres, RS Brazil, November 22-26, paper 7.

Buj, O., Gisbert, J., 2010, Influence of pore morphology on the durability of sedimentary building stone from Aragon (Spain) subjected to standard salt decay test, *Environ Earth Sciences*, Vol. 61, n°7, pp. 1327-1336.

Camplani, M., Cannas, B., Cau, F., Concu, G., Usai, M., 2008, Acoustic NDT on building materials using features extraction techniques, in *Lecture Notes in Computer Science; Vol 5073, Computational Science and Its Applications, Part II*, Perugia, Italy, June 30-July 03, O. Gervasi, B. Murgante, A. Laganà, D. Taniar, Y. Mun, M. L. Gavrilova, 582-595.

Cappabianca, C., Luprano, V., Tatì, A., 2008, Diagnostic sonic investigation on san giovanni in laterano obelisk, rome, italy, and tomographic reconstruction of same slides project: technology for cultural heritage, Proc. of 9th International Conf. on NDT of Art, Jerusalem Israel, 25-30 May, ISAS International Seminars, paper 74.

Carlomagno G. M., Meola C. Comparison between thermographic techniques for frescoes NDT, *NDT&E International*, Volume 35, Issue 8 (2002) 559–565

Charola, A.E., Weber, J., 1992, The hydration-dehydration mechanism of sodium sulphate, 7th Int. Cong. Deterioration Conservation of Stone, Lab. Eng.Civil, Lisbon, pp.581-590.

Colla C. (2011). Comparative testing for improved diagnosis of historic structures. In: EWCHP- 2011, European Workshop on Cultural Heritage Preservation, Berlin, Germany, September 26-28, ed. Fraunhofer IRB Verlag, 140-147.

Colla C., Largo A., Corvaglia P., Ubertini F. Thermography investigations of Roman archaeological masonry, Proc. of Int. Conf. SACOMATIS 2008, Volume 1, 239-251

Colla, C. (a cura di), (2009), “D5.1 – part 1: Report on test method and former test results”, Smart Monitoring of Historic Structures, SMooHS European Collaborative Research Project (Grant n° 212939), 428 pp.

Colla, C. (a cura di), (2009), “D5.1 – part 2: Report on former tests and former monitoring carried out on project’s case studies”, Smart Monitoring of Historic Structures, SMooHS European Collaborative Research Project (Grant n° 212939), 35 pp.

Colla, C. (Ed.), (2012), “Report D5.2: laboratory and on-site testing activities, Part 1: Brick masonry”, Smart Monitoring of Historic Structures, SMooHS European Collaborative Research Project (Grant n° 212939), 7th FP, 179 pp.

Colla, C. (Ed.), (2012), “Report D5.2: laboratory and on-site testing activities, Part 2: Stone masonry”, Smart Monitoring of Historic Structures, SMooHS European Collaborative Research Project (Grant n° 212939), 7th FP, 67 pp.

Colla, C. (Ed.), (2012), “Report D5.2: laboratory and on-site testing activities, Part 3: Historical timber elements”, Smart Monitoring of Historic Structures, SMooHS European Collaborative Research Project (Grant n° 212939), 7th FP, 60 pp.

Colla, C. (Ed.), (2012), “Report D5.2: laboratory and on-site testing activities, Part 4: Laboratory analyses on materials from test sites”, Smart Monitoring of Historic Structures, SMooHS European Collaborative Research Project (Grant n° 212939), 7th FP, 72 pp.

Colla, C. (Ed.), (2012), “Report D5.2: laboratory and on-site testing activities, Part 5, task WP 5.5: Laboratory ageing tests”, Smart Monitoring of Historic Structures, SMooHS European Collaborative Research Project (Grant n° 212939), 7th FP, 118 pp.

Colla, C. (Ed.), (2012), “Report D5.2: laboratory and on-site testing activities, Part 6: On- site NDT and mechanical testing”, Smart Monitoring of Historic Structures, SMooHS European Collaborative Research Project (Grant n° 212939), 7th FP, 163 pp.

Colla, C. (Ed.), (2012), "Report D5.2: laboratory and on-site testing activities, Part. 7: Laboratory characterization of on-site collected samples", Smart Monitoring of Historic Structures, SMooHS European Collaborative Research Project (Grant n° 212939), 7th FP, 61 pp.

Colla, C. (Ed.), (2012), "Report D5.3: comparative testing", Smart Monitoring of Historic Structures, SMooHS European Collaborative Research Project (Grant n° 212939), 7th FP, 122 pp.

Colla, C., et al., "On site diagnostic investigations for the assessment of the Casa del Tramezzo di Legno in Herculaneum", Proc. Int. Conf. RILEM, Varenna (LC) 1-2 Sept. 2008.

Colla, C., Gabrielli, E., Nardoni, G., Maggioni, M., "Un caso di studio per l'utilizzo del metodo dell'Emissione Acustica su materiale lapideo", Il Giornale delle Prove Non Distruttive Monitoraggio Diagnostica, 1, 28-32 (2008).

Colla, C., Pascale, G., 2007, Prove soniche superficiali per l'indagine dello stato fessurativo di murature in laterizio, Proc. of PnD 2007, Milano, October 11-13, G.M. Gatti, P. Vidali, F.L. Bovio, paper 89.

Collepari M. 1999, Thaumaside formation and deterioration in historic buildings, Cement and Concrete Composites 21, 147-154.

Collepari, M., 1990, Degradation and restoration of masonry walls of historical buildings, Materials and Structures, 23, pp. 81-102

Collepari, M., Collepari, S., Troli, R., 2003, Salt weathering of masonry walls the Venice experiences, Proc. Of CANMET/ACI Int.Conf., Salonicco, Greece, June 2003.

Coppola, L., Collepari, M., 1996, Il ruolo dell'umidità nel degrado dei materiali nelle murature, Il nuovo Cantiere, vol. 6, pp. 44-51, June 1996.

Coppola, L., Troli, R., 1996, Il degrado delle murature causato dai solfati presenti nei laterizi. Analisi di tre case storiche, L'Edilizia, anno IX, n°3/4, pp. 38-47, Milan.

Cultrone G., E. Sebastian 2008 Laboratory simulation showing the influence of salt efflorescence on the weathering of composite building materials. Environmental Geology International Journal of Geosciences, Special issue

Dilek, U., 2007, Ultrasonic pulse velocity in non destructive evaluation of low quality and damaged concrete and masonry construction, in Journal of Performance of Constructed Facilities, Vol. 21, No. 5, 337-344.

- Dimes, F. G., Ashurst, J., (2012), "Conservation of building and stone", Routledge, pp. 468.
- Doehne, E., 1994, In situ dynamics of sodium sulfate hydration and dehydration in stone pores, in: V. Fassina, H. Ott, F. Zezza (Eds.), Proc. of 3rd International Congress on the Conservation of Monuments in the Mediterranean Basin, Graffo, Venice, pp.143± 150.
- Elert K., G. Cultrone, C. Rodriguez-Navarro, E. Sebastian-Pardo 2003 Durability of bricks used in the conservation of historic buildings- influence of composition and microstructure. Journal of Cultural Heritages Vol. 4, 91-99
- Elert, K. et al., 2003, Durability of bricks used in the conservation of historic buildings – influence of composition and microstructure, J. of Cultural heritage, 4, pp. 91-99.
- Fahey, B.D., 1986, A comparative laboratory study of salt crystallization and salt hydration as potential weathering agents in deserts, Geogr Ann Ser A: Phys Geogr, vol. 68, n°1/2, pp. 107± 111.
- Frick, J., Lehmann, F., Menzel, K., Pakdel, H. And Krüger, M. 2011. Monitoring of Salt Content in Mineral Materials using Wireless Sensor Networks. In Proc. of Int. Symposium on Nondestructive Testing of Materials and Structures, NDTMS-2011. Istanbul, Turkey, May 15-18, 2011.
- Garnier, V., Chaix, J., Rossat, M., Payan, C., 2006, Improvement in the Analysis of the Wave's Propagation in Concrete, Proc. of 9th European Conference on NDT, Berlin, Germany September 25-29, paper Th. 4.2.1.
- Grinzato E. Temperature monitors works of art health as human beings, Proc. of WCNDT 2004 16th World Conference on Non-destructive Testing, Montreal (Quebec), August 30 - September 3, 2004, CD-ROM ref. 34_grinzato, NDT.net - The e-Journal of Non-destructive Testing, Volume 9, Issue 11 (2004)
- Hall C., Hoff W.D. (2002) Water transport in brick, stone and concrete. London, UK; New York NY: Taylor & Francis.
- Hall C., Hoff W.D. (2007) Rising damp: capillary rise dynamics in walls. In: Proc. R. Soc. A, 463, 1871-1884.
- Hall, C., Kam-Ming Tse, T., 1986, "Water movement in porous building materials –VII. The sorptivity of mortars", Building and Environment, Vol. 21, issue 2, pp. 113-118
- International Council on Monuments and Sites/International Scientific Committee for Stone, Monuments and Sites (2010): Illustrated glossary on stone deterioration patterns: English-

German version, ICOMOS-ISCS. German transl. of the English-French ed. of 2008, Rolf Snethlage, Stefan Simon, Kurt Heinrichs; 15, 78.S. ISBN 978-3-86568-667-1

Karoglou, M., Moropoulou, A., Giakoumaki, A., Krokida, M.K., 2005, "Capillary rise of some building materials", *Journal of Colloid and Interface Science, Building and Environment*, Vol. 284, issue 1, pp. 260-264

Knacke, O., Von Erdberg, R., 1975, The crystallization pressure of sodium sulfate decahydrate, *Ber Bunsen-Ges Phys Chem*, 79, pp. 653±657

Larsen E.S., C.B. Nielsen 1990 Decay of bricks due to salt. *Materials and Structure* Vol. 23, 16-25

Lockington D.A., Parlange J.Y. (2003) Anomalous water absorption in porous materials. *J. Phys. D: Appl. Phys.* 36: 760–767.

Lubelli, B. et al., 2004, The role of sea salt in the occurrence of different damage mechanisms and decay patterns on brick masonry, *Constr. and Build. Mat.*, 18, pp. 119-124.

Maack, S., Krause, M., 2008, Diagnosis investigations of wooden structures using ultrasonic-echo technique. in *On site assessment of concrete, masonry and timber structures SACoMATiS 2008. Proceeding of the First International RILEM Symposium*, Binda, L., di Prisco, M., Felicetti, R., Vol. 2, 1081-1090.

Michel K., Lavall P. (2001) Experimental evidence and theoretical analysis of anomalous diffusion during water infiltration in porous building materials. *J. Phys. D: Appl. Phys.* 34: 2547–2554.

Moriconi, G., Castellano, M.G., 1994, Mortar deterioration of the masonry walls in historic buildings. A case history: Vanvitelli's Mole in Ancona, *Material and Structures*, vol. 27, n°7, pp.408-414

Mosquera M.J., Benitez, D., Perry, S.H., 2002, Pore structure in mortars applied on restoration effect on properties relevant to decay of granite buildings, *Cement and Concrete Research*, 32, pp. 1883-1888.

Musolino A., M. Raugi, M. Tucci, F. Turcu, 2007 Voids Detection in Brick Masonry Structures by Using Ultrasonic Testing, 2007 IEEE Ultrasonics Symposium 1377-1380

Olivito, R.S., Zuccarello, F. A., "On the shear behaviour of concrete beams reinforced by carbon fibre-reinforced polymer bars: an experimental investigation by means of acoustic emission technique", *Strain*, 46, 470-281 (2010).

- Pagona Maravelaki-Kalaitzaki, 2006, Hydraulic lime mortars with siloxane for waterproofing historic masonry, *Cement and Concrete Research*, vol. 37, issue 2, February 2007, pp. 283-290.
- Pelt L., Kopingaj K., Bertram G. and Langt G. (1995) Water absorption in a fired-clay brick observed by NMR scanning. *J. Phys. D: Appl. Phys.* 28: 675-680.
- Rirsch, E., Zhang, Z., 2010, "Rising damp in masonry walls and the importance of mortar properties", *Construction and Building Materials*, Vol. 24, issue 10, pp. 1815-1820
- Rodriguez-Navarro C., E. Doehne, E. Sebastian 2000 How does sodium sulphate crystallize? Implications for the decay and testing of building materials. *Cement and Concrete Research* Vol. 30, 1527-1534
- Rodriguez-Navarro, C., Doehne, E., 1999, Salt weathering: influence of evaporation rate, supersaturation and crystallization pattern, *Earth Surf Processes Landforms*, pp. 24191± 209.
- Rodriguez-Navarro, C., Doehne, E., Sebastian, E., Ginell, W.S., 1996, Saltgrowth in capillary and porous media, *Proc. of 3rd Int. Cong. Of Restoration of Buildings and Architectural Heritage*, in: E.M. Sebastian, E.Valverde, U. Zezza, pp. 509-514.
- Russo, S., Boscato, G., Massaria, L., 2004, Non-destructive test of structural rehabilitation. The cases of Devil's and S. Donato's masonry bridges in Venice, *Proc. of 16th WCNDT 2004 World Conference on NDT, Montreal, Canada, Aug 30 - Sep 3, CD-ROM*, paper 659.
- S. Martinez-Ramirez, F. Puertas, M.T. Blanco-Valera, G.E. Thompson 1997, Studies in degradation of lime mortars in atmospheric simulation chamber. *Cement and Concrete Research* Vol. 27, 5, 777-784
- S. Martinez-Ramirez, F. Puertas, M.T. Blanco-Valera, G.E. Thompson 1998 Effects of dry deposition of pollutants on the degradation of lime mortar with sepiolite. *Cement and Concrete Research* Vol. 28, 1, 125-133
- Sabbioni, C., Bonazza, A., Zappia, G., 2002, Damage on hydraulic mortars: the Venice Arsenal, *Journal of Cultural Heritage*, 3, pp. 83-88.
- Sabbioni, C., Zappia, G., e alt., 2000, Atmospheric deterioration of ancient and modern hydraulic mortars, *Atmospheric Environment*, vol. 35, issue 3, pp. 539-548.
- Silva, B., Prieto, B. et al., 2004, Addition of cement to lime based mortars: effect on pore structure and vapor transport, *Cement and concrete research*, vol.36, n°9, pp. 1635-1642.

Sperling, C.H.B., Cooke, R.U., 1985, Laboratory simulation of rock weathering by salt crystallization and hydration processes in hot, arid environments, *Earth Surf Processes Landforms*, 10 pp. 541±555.

Theoulakis P, Moropoulou M. 1997 Microstructural and Mechanical parameters determining the susceptibility of porous building stones to salt decay. *Construction and Building Materials* Vol. 11, 1, 65-71

Theoulakis, P., Moropoulou, A., 1997, Microstructural and mechanical parameters determining the susceptibility of porous building stones to salt decay, *Construction and Building Materials*, vol. 11, n°1, pp.65-71

Theoulakis, P., Moropoulou, A., 1999, Salt crystal growth as weathering mechanism of porous stone on historic masonry, *J. of porous materials*, 6, pp.345-358.

Van Hees, R.P.J., Brocken, H.J.P., 2004, Damage development to treated brick masonry in a long-term salt crystallization test, *Constr. and Build. Mat.* 18, pp. 331-338.

VIC-3D Manual & Testing Guide, www.correlatedsolutions.com

W Ko, W. C., and Yu, C. W. “Study of Kaiser Effect in Concrete Material Under Cyclic Loading”, In *Proceedings of IAES-19: 295-302*, Kyoto, Japan (2008).

Warke, P.A., Smith, B.J. 2000. Salt distribution in clay-rich weathered sandstone. *Earth Surface Processes and Landforms*. 25, 1333-1342.

Winkler, E.M., Singer, P.C., 1972, Crystallization Pressure of Salts in Stone and Concrete, *Geological Society of America Bulletin*, v.83, p. 3509-3514, November 1972.

National and international standards

ASTM C 1403 (2006). Standard test method for rate of water absorption of masonry mortars.

ASTM C 88-90, 1997, Standard test method for soundness of aggregate by use of sodium sulfate or magnesium sulfate, *Annu Book ASTM Stand 4.2*, pp. 37± 42.

D.M. 14 gennaio 2008, *Nuove Norme tecniche per le costruzioni*, (2008).

DIN 52111. 1990. Testing on natural stone and mineral aggregates. Crystallisation test with sodium sulfate. In German.

DIN EN 13755:2002, Natural stones test methods; determination of water absorption at atmospheric pressure

DIN EN 1925: 2000, Natural stones test methods; determination of water absorption coefficient by capillarity

DIN EN 1936

RILEM PEM/25 (1980). V. tentative recommendations – Test No.II.6 Water absorption coefficient.

RILEM PEM/25. 1980. V. Durability tests. Test No. V.1a, Crystallisation test by total immersion (for untreated stone). Test No. V.2 Crystallisation test by partial immersion (for stone).

RILEM TC 127-MS. 1998. MS-A-2 Uni-directional salt crystallization test for masonry units. *Material and Structures*, vol.31, pp.10-11 (January-February, 1998).

RILEM TC 127-MS.1998 MS-A-1 Determination of the resistance of wallettes against sulphates and chlorides. *Material and Structures*, vol.31, pp.2-9 (January-February, 1998).

UNI EN 1015-11:2007

UNI EN 1015-18 (2004). Methods of test for mortar for masonry. Determination of water absorption coefficient due to capillary action of hardened mortar.

UNI EN 1052-1, Metodi di prova per muratura: determinazione della resistenza a compressione, UNI, Milano, Italia (2001).

UNI EN 12370. 2001. Metodi di prova per pietre naturali-Determinazione della resistenza alla cristallizzazione dei sali. (Natural stone test methods – Determination of resistance to salt crystallization). In Italian.

UNI EN 13919. 2004. Metodi di prova per pietre naturali-Determinazione della resistenza all'invecchiamento dovuto a SO₂ in presenza di umidità. (Natural stone test methods – Determination of resistance to ageing by SO₂ action in the presence of humidity). In Italian.

UNI EN 14580, Test methods for natural stones: determination of elastic static modulus (2005), In Italian language

UNI EN 772-1, Test methods for masonry: determination of compression resistance, (2002)

UNI EN ISO 13755 (2008). Natural stones test methods: determination of water absorption at atmospheric pressure.

UNI EN ISO 15148:2002, Hygrothermal performances of building materials and products. Determination of water absorption coefficient by partial immersion

UNI EN ISO 15801 (2010). Conservation of cultural property. Test methods: determination of water absorption by capillary.

UNI EN ISO 1925 (2000). Natural stones test methods: determination of water absorption coefficient by capillarity.

UNI-EN 13412-2006

VDI 3797-1. 1980. Testing of the presumable resistance of preserved and not preserved natural stone against air pollutants. Sodium sulfate crystallisation test. In German.

Annex I - List of publications

1. Colla, C., Gabrielli, E., Pascale, G., (2011), “Experimental diagnosis of structural and material deterioration affecting historic structures due to environment”, Atti di *AIMETA 2011 – XX Congresso dell’Associazione Italiana di Meccanica Teorica e Applicata*”, Bologna, Italia, 12 - 15 settembre, idn 403, 10 pp., ISBN 978-88-906340-1-7.
2. Gabrielli, E., Colla, C., Strojceki, M., Lukomski, M., (2011), “Valutazione non distruttiva del degrado meccanico e ambientale in strutture murarie”, Atti di *AIMETA 2011 – XX Congresso dell’Associazione Italiana di Meccanica Teorica e Applicata*”, Bologna, Italia, 12 - 15 settembre, idn 393, 10 pp., ISBN 978-88-906340-1-7.
3. Castellazzi, G., Colla, C., de Miranda, S., Gabrielli, E., Formica, G., Molari, L., Ubertini, F., (2011), “A simplified model for salt diffusion and crystallization in historical masonry”, In *Cultural Heritage Preservation*, Atti di *European Workshop on Cultural Heritage Preservation EWCHP-2011*, Berlin, Germany, September 26-28, ed. M. Krüger, Fraunhofer IRB Verlag, ISBN 978-3-8167-8560, pp. 232 - 239.
4. Strojceki, M., Lukomski, M., Bratasz, L., Colla, C., Gabrielli, E., (2011), “The Kaiser effect in wood – does historic wood have a stress memory?”, In *Cultural Heritage Preservation*, Atti di *European Workshop on Cultural Heritage Preservation EWCHP-2011*, Berlin, Germany, September 26-28, ed. M. Krüger, Fraunhofer IRB Verlag, ISBN 978-3-8167-8560, pp. 171 – 176.
5. Colla, C., Gabrielli, E., Largo, A., Angiuli, R., (2011), “Experimental studies by combined NDT of capillary rise monitoring in masonry specimens”, In *Cultural Heritage Preservation*, Atti di *European Workshop on Cultural Heritage Preservation EWCHP-2011*, Berlin, Germany, September 26-28, ed. M. Krüger, Fraunhofer IRB Verlag, ISBN 978-3-8167-8560, pp. 131 - 139.
6. Colla, C., Gruener, F., Gabrielli, E., Frick, J., (2011), “Monitoring of salt content and mobility in masonry materials”, In *Cultural Heritage Preservation*, Atti di *European Workshop on Cultural Heritage Preservation EWCHP-2011*, Berlin, Germany, September 26-28, ed. M. Krüger, Fraunhofer IRB Verlag, ISBN 978-3-8167-8560-6, pp. 210 - 217.
7. Colla, C., Gabrielli, E., Pascale, G., Di Tommaso, A., Ubertini, F., (2012), “Masonry assessment for the seismic risk evaluation of historic structures”, *Developing the future of masonry*, atti di *15th International Brick and Block Masonry Conference (15th IB²MaC)*, Florianopolis, Brazil, June 3th – 6th, ISBN 978-85-63273-10-9, 10 pp.

8. Gabrielli, E., Colla, C., Gruener, F., 2012, "Evaluation of damage evolution in masonry due to environmental parameters and salt capillary rise", *Developing the future of masonry*, atti di 15th Intern. Brick and Block Masonry Conference (15th IB²MaC), Florianopolis, Brazil, June 3th – 6th, ISBN 978-85-63273-10-9, 10 pp.
9. Marani, F., Gabrielli, E., Colla, C., 2012, "Bricks vulnerability to detrimental reactions promoted by salt contaminated solutions in natural environment: experimental evidences", 28 Conv. Intern. Scienza e Beni Culturali, *La conservazione del patrimonio architettonico all'aperto*, Bressanone, 10-13 luglio, pp. 901-911, ISBN 978-88-95409-16-0
10. Molari, L., Castellazzi, G., Colla, C., de Miranda, S., Gabrielli, E., Ubertini, F., (2012), "A 3D model for salt diffusion and crystallization in masonry structures", Atti di 6th European Congress on Computational Methods in Applied Sciences and Engineering, ECCOMAS 2012, Vienna, September 10th -14th, Vienna, Vienna University of Technology, ISBN: 978-3-9502481-9-7 (CD-ROM).
11. Paci, G., Gabrielli, E., Colla, C., 2012, "On-site dynamic wireless sensor monitoring in the historic building of Palazzina della Viola, Bologna, Italy", In *Cultural Heritage Preservation*, Atti di 2nd European Workshop on Cultural Heritage Preservation, EWCHP 2012, Kjeller, Norway, 24th -26th Sept., ISBN 978-82-425-2525-3, pp. 74 – 81.
12. Frick, J., Colla, C., Gabrielli, E., Gruener, F., 2012, "Seasonal Monitoring of Salt Movement in Masonry Materials", In *Cultural Heritage Preservation*, Atti di 2nd European Workshop on Cultural Heritage Preservation, EWCHP 2012, Kjeller, Norway, 24th -26th September, ISBN 978-82-425-2525-3, pp. 27 - 34.
13. Colla, C., Gabrielli, E., Krueger, M., Lehmann, F., 2012, "Experience of acoustic emissions of masonry", In *Cultural Heritage Preservation*, Atti di 2nd European Workshop on Cultural Heritage Preservation, EWCHP 2012, Kjeller, Norway, 24th - 26th September, ISBN 978-82-425-2525-3, pp. 207 - 215.
14. Gabrielli, E., Marani, F., Colla, C., 2012, "Ir thermography to compare the evaporation fluxes in brick masonry", In *Cultural Heritage Preservation*, Atti di 2nd European Workshop on Cultural Heritage Preservation, EWCHP 2012, Kjeller, Norway, 24th - 26th September, ISBN 978-82-425-2525-3, pp. 216 - 223.
15. Colla, C., Gabrielli, E., Krueger, M., Lehmann, F., Bastianini, F., 2012, "On-site loading test in the historic building of Malvezzi Palace, Bologna, Italy: experience integrating traditional measurements tools with wireless sensor systems", In *Cultural Heritage Preservation*, Atti di 2nd European Workshop on Cultural Heritage Preservation, EWCHP 2012, Kjeller, Norway, 24th -26th September, ISBN 978-82-425-2525-3, pp. 198 - 206.

16. Gabrielli, E., Colla, C., 2012, “Laboratory investigation of damp rise in porous masonry construction materials”, In *Structural analysis of historical constructions*, Atti di *Int. Conf. on Structural Analysis of Historical Constructions, SAHC 2012*, Wroclaw, Poland, October 15th -17th, ISBN 978-83-7125-216-7, pp. 659 – 667.
17. Bitelli, G., Colla, C., Gabrielli, E., Girardi, F., Ubertini, F. (2012). “Quantitative monitoring of superficial decay evolution in plastered and unplastered outdoors masonry”, In *Structural analysis of historical constructions*, Atti di *Int. Conf. on Structural Analysis of Historical Constructions, SAHC 2012*, Wroclaw, Poland, October 15th -17th, ISBN 978-83-7125-216-7, pp. 2288 – 2296.
18. Colla, C., Rajcic, V., Gabrielli, E., et al. 2012, “Integrated approach for on-site assessment of conservation state of a historical masonry building: Malvezzi Palace, Italy”, In *Structural analysis of historical constructions*, Atti di *Int. Conf. on Structural Analysis of Historical Constructions, SAHC 2012*, Wroclaw, Poland, October 15th - 17th, ISBN 978-83-7125-216-7, pp. 2367 – 2375.
19. Strojceki, M., Łukomski, M., Colla, C., Gabrielli, E., (2012), “Acoustic emission as a non-destructive method for tracing damage: from laboratory testing to monitoring historic structures”, RILEM Bookseries, vol. 6, *Proc. of NDTMS-2011, Istanbul Technical University*, Istanbul, Turkey, May 15-18, Springer, ISBN: 978-94-007-0722-1, ISBN 978-83-7125-216-7, pp. 1131-1136.
20. Colla, C., Molari, L., Gabrielli, E., de Miranda, S., (2012), “Damp and salt rising in damaged masonry structures: numerical modelling and NDT monitoring”, RILEM Bookseries, vol. 6, *Proc. of NDTMS-2011 Istanbul Technical University*, Istanbul, Turkey, May 15-18, Springer, ISBN 978-94-007-0722-1, pp. 1151-1156.
21. Bishara, A., Plagge, R., Hernandez, J.L., Reeb, S., Paci, G., Garrecht, H., Garcia, D., Gabrielli, E., Colla, C., Krick, B. (2013), “Development of new systems and technologies for sustainable refurbishment of Europe’s built heritage”, Atti di *3rd European Workshop on Cultural Heritage Preservation, EWCHP 2013*, Bolzano, September 16th -18th, ed. A. Troi, E. Lucchi, EURAC, ISBN 978-88-88307-26-8, pp. 143 – 152.
22. Colla, C., Polei, R., Gabrielli, E., (2013), “Innovative non-destructive investigation of problematics in historical ceramic tilings via acoustic and electromagnetic techniques”, Atti di *12th European Meeting on Ancient Ceramics, EMAC 2013*, Padova, Italy, September 19th – 21st, ed. R. Piovesan, L. Maritan, C. Grifa, p.80.
23. Colla, C., Gabrielli, E., Polei, R., Ubertini F. (2013), “Indagini innovative in laboratorio di problematiche in rivestimenti e pavimentazioni ceramiche: metodi non distruttivi elettromagnetici e acustici”, Atti di *AIPnD 2013, 15° Conferenza Nazionale sulle Prove*

- non Distruttive Monitoraggio Diagnostica*, Trieste, 23/26 Ottobre 2013, ISBN 978-88-89758-14-4, IDN 59, pp.10.
24. Gabrielli, E., Colla, C. (2013), “La tecnica della correlazione digitale di immagini per il monitoraggio di provini di muratura sottoposti a prove meccaniche”, *Atti di AIPnD 2013, 15° Conferenza Nazionale sulle Prove non Distruttive Monitoraggio Diagnostica*, Trieste, 23/26 Ottobre 2013, ISBN 978-88-89758-14-4, IDN 61, pp. 10.
25. Castellazzi, G., Colla, C., de Miranda, S., Formica, G., Gabrielli, E., Molari, L., Ubertini, F., (2013), “A coupled multiphase model for hygrothermal analysis of masonry structures and prediction of stress induced by salt crystallization”, *Construction & Building Materials*, vol. 41, pp. 717-731.
26. M. Strojecki, C. Colla, M. Łukomski & E. Gabrielli (2013) “Kaiser effect in historic timber elements” *European Journal of Wood and Wood Product*, vol. 71, n°6, pp. 787–793, DOI 10.1007/s00107-013-0738-8.
27. Bitelli, G., Colla, C., Gabrielli, E., Girardi, F., Ubertini, F. "Quantitative monitoring of superficial decay evolution in plastered and unplastered outdoors masonry", *Journal of Architectural Heritage* (accepted).